

THE UNIVERSITY OF HULL

**Development of a Continuous Flow Microreactor for Chemical
synthesis with In-line Catalysis, Heating and Detection**

being a Thesis submitted for the Degree of

Doctor of Philosophy

in the University of Hull

by

Grant Thomas Robert Chaplain

MChem (University of Hull)

May 2013

Abstract

The development of a micro fluidic flow organic synthetic system incorporating heterogeneous catalysis, novel heating regimes and in-line spectroscopic detection is described. The reactions used to model the flow synthesis include Suzuki and acetylation reactions using heterogeneous immobilised palladium and tungstosilicic acid catalyst respectively. Catalyst immobilisation was carried out on silica monoliths made using Tetraethyl orthasilicate (TEOS) as a precursor which produced surface areas of $240 \pm 9 \text{ m}^2 \text{ g}^{-1}$ and porosities between 0.65 and 0.70 with nano pore diameters of $1100 \pm 20 \text{ nm}$. Functionalisation of the TEOS monoliths with palladium was achieved through the formation of palladium nano clusters within the nano pores of the monolith. Once immobilised, the palladium bound monolith was placed into a flow stream as a capillary monolithic reactor (CMR). Microwave and conventional oven heating were applied to the catalyst as the reactants 4-bromobenzonitrile and phenyl boronic acid to produce 4-cyanobiphenyl flowed through with different residence times and temperatures. Under microwave heating, the monolithic structure and the tube connections present in the microwave were observed to break down, an effect thought to be associated with very high localised heating of the palladium. Heating however using convection from a column heater proved to be more successful and facilitated the continuous flow of reactants without flow disruption. In-line Raman spectroscopy was placed in to the flow system as a detection method replacing off-line gas chromatography-mass spectrometry (GC-MS). Calibration using Raman spectra was achieved using partial least square regression (PLSR) which gave results within $\pm 10\%$ to those obtained using the GC-MS method. Using the flow system with in-line Raman analysis, the reaction was optimised and kinetic studies were performed. For the reaction conditions used, the overall 2nd order rate constant k was $4.45 \times 10^{-3} \text{ M}^{-1} \text{ s}^{-1}$, and

the optimal flow rate for 4-cyanobiphenyl production was 0.30 mL min^{-1} producing 53 g h^{-1} (with a 14% conversion). The optimal conversion under the flow parameters performed was at 0.02 mL min^{-1} showing 61% conversion (producing 17 g h^{-1}).

The reaction was then altered to accommodate an acetylation reaction. Tungstosilicic acid was immobilised on the surface of TEOS monoliths and the CMRs were actively catalysing the reaction between 4-bromophenol and acetic anhydride to produce 4-bromophenyl acetate. Unfortunately, leaching of the tungstosilicic acid was observed from the monolith surface which interfered with Raman spectroscopic observations making detection of reactants and products difficult.

In conclusion the overall project was a successful venture. It allowed fast optimisation procedures for reaction scaling, and produced a significant amount of molecular data for each reaction ran. This model set-up was appropriate and versatile for the objectives of this project. Areas within the research to address were improving the catalyst immobilisation techniques, and different heating mechanisms. Despite this, the flow reaction system was an advance towards developing a fully automated flow synthetic optimisation system.

Acknowledgements

I would like to thank my supervisors Professor Stephen J. Haswell, Professor Paul D.I. Fletcher and Professor Steve M. Kelly for their guidance and assistance throughout the project. I am appreciative of the contributions made by Dr. Ping He, Mr. Andrew Mansfield, Dr. Stuart Kitney and Mr. Dean Moore.

I would also like to thank the Analytical Group at the University of Hull for their help and positive encouragement throughout this PhD project. In particular I would like to thank Dr. Kevin Welham, Dr. Vincent Rocher and Mr. Tony Sinclair for their technical support and data interpretation advice.

I am grateful to the University of Hull Chemistry Department, Flow Synthetic Group at Pfizer Inc and CEM Inc for allowing me to use their facilities and equipment. Special thanks to the E.P.S.R.C. grant number: EP/G027765/1, for their funding.

A final thanks to the three people who supported me throughout these studies; Dr. Tomasz Lemanski, Dr. Peter Docker and my loving wife Mrs. Emma Chaplain. To whom I dedicate this thesis.

Abbreviations

BBN	4-bromobenzonitrile
BET	Brunauer Emmett Teller
CBP	4-cyanobiphenyl
CMR	Capillary monolithic reactor
DCM	Dichloromethane
DMF	Dimethylformamide
ECD	Electron capture detector
EDX	Energy dispersive X-ray spectroscopy
FID	Flame ionisation detector
FPD	Flame photometric detector
GC	Gas chromatography
GC-MS	Gas chromatography-mass spectrometry
HPA	Heteropoly acid
HPLC	High performance liquid chromatography
IR	Infrared
MS	Mass spectrometry
MTMOS	Methyltrimethoxysilane
NMF	N-methylformamide
NMR	Nuclear magnetic resonance
NPD	Nitrogen phosphorous detector
PC	Principal component
PCA	Principal component analysis
PEEK	Polyetheretherketone
PEO	Polyethylene oxide
PLS	Partial least squares

PLSR	Partial least square regression
PTFE	Polytetrafluoroethylene
RID	Refractive index
SEM	Scanning electron microscopy
SERS	Surface enhanced Raman spectroscopy
TCD	Thermal conductivity detector
TEM	Transmission electron microscopy
TEOS	Tetraethyl orthasilicate
THF	Tetrahydrofuran
TLC	Thin layer chromatography
TMOS	Tetramethyl orthasilicate
UV	Ultra violet

Acknowledgements	iii
Abbreviations	iv
List of Figures	xii
List of Reaction Schemes	xv
List of Tables	xvi
List of Equations	xvii
1 Introduction	1
1.1 Overview	1
1.2 Flow chemistry	1
1.3 Reagent flow	2
1.4 Flow organic synthesis	9
1.5 Flow Suzuki reactions	14
1.6 Flow Acetylation reactions	17
1.7 Microwave theory and Microwave Suzuki flow reactions	19
1.8 Heterogeneous palladium catalysis and immobilisation methods	22
1.9 Heterogeneous enzyme-based catalysts in flow	26
1.10 Flow reaction analysis	27
1.11 Raman spectroscopy theory	29
1.12 Comparing IR and Raman	32
1.13 Raman spectroscopy and Fluorescence	33
1.14 Raman flow reaction monitoring	33
1.15 Pre-spectral processing for quantification	34
1.16 Raman spectral pre-processing	36
1.17 Raman spectral processing	37
1.18 PLS Regression	38
1.19 Aims	40

2	Silica monolith generation, characterisation and functionalisation	42
	Experimental	43
2.1	Monolith generation	43
2.2	Method 1 - Tetramethyl orthosilicate (TMOS) and methyltrimethoxysilane (MTMOS)	43
2.3	Method 2 - Potassium silicate	43
2.4	Method 3 - Tetramethyl orthosilicate (TMOS)	44
2.5	Method 4 - Tetraethyl orthosilicate (TEOS)	44
2.6	Monolith characterisation	45
2.7	Porosity testing	45
2.8	Surface area analysis	46
2.9	Microscopic analysis	46
2.10	Catalyst loading	47
2.11	Palladium acetate deposition in THF	47
2.12	Palladium acetate deposition in DMF	47
2.13	Palladium bis(dibenzylideneacetone) deposition	48
2.14	Sodium tetrachloropalladate deposition	48
	Results	49
2.15	Monolith generation	49
2.16	Potassium silicate monolith	53
2.17	Tetramethyl orthosilicate (TMOS) monolith	58
2.18	Tetraethyl orthosilicate (TEOS) monolith	60
2.19	Varying Monolith size	63
2.20	Catalyst loading	66
2.21	Summary	73

3	Monolithic flow, CMR design and heating	75
	Experimental	76
3.1	Flow regime design	76
3.2	Flow system design A	76
3.3	Flow system design B	77
3.4	Flow system design C	78
3.5	Flow system design D	78
3.6	Flow system design E	79
3.7	Flow system design F	80
3.8	Flow reactor design	80
3.9	Flow reactor design 1	80
3.10	Flow reactor design 2	81
3.11	Microwave chamber mapping	81
3.12	GC-MS analysis of flow regimes	82
	Results	83
3.13	Flow regime design	83
3.14	Pump flow rate calibrations	83
3.15	Microwave wattage calibration	86
3.16	IR fibre optic temperature probe calibration	86
3.17	Column heater temperature calibration	88
3.18	Flow system design	89
3.19	Microwave chamber heating zone	96
3.20	Summary	98

4	Suzuki reaction chemistry with Raman spectroscopic monitoring	100
	Experimental	100
4.1	GC-MS analysis of Suzuki reactions	100
4.2	GC-MS analysis A	100
4.3	GC-MS analysis B	101
4.4	Suzuki reaction chemistry	102
4.5	Batch Suzuki reaction - DMF and Dioxane using palladium on activated charcoal	102
4.6	Batch Suzuki reaction - Silica 60 mesh beads	103
4.7	Batch Suzuki reaction - CMR	103
4.8	Flow Suzuki reaction - NMF carrier solvent	103
4.9	Flow Suzuki reaction 1 - pure reaction mixture flow	104
4.10	Flow Suzuki reaction 2 - pure reaction mixture flow	104
4.11	Flow Suzuki reaction 3 - pure reaction mixture flow	105
4.12	Raman spectroscopic analysis	105
4.13	Raman spectra	108
4.14	Raman pressure testing	108
4.15	Raman flow testing	109
4.16	Raman spectral calibration A	109
4.17	Raman spectral calibration B	110
4.18	Raman spectral calibration C	111
4.19	Raman spectral calibration D	113
4.20	Raman spectral calibration E	114
	Results	115
4.21	Suzuki reaction	115
4.22	Batch Suzuki reactions	116

4.23	Batch Suzuki reaction results - DMF and Dioxane	116
4.24	Batch Suzuki reaction results -Silica 60 mesh beads and CMR	117
4.25	Flow Suzuki reactions	120
4.26	Flow Suzuki reactions and Raman spectroscopic analysis	121
4.27	Raman spectral calibration A - results	122
4.28	Raman spectral calibration B - results	131
4.29	Raman flow cell flow and pressure testing	142
4.30	Flow reaction monitoring	145
4.31	Microwave power vs Reaction conversion	149
4.32	Raman spectral calibration C - results	151
4.33	GC-MS analysis calibration	156
4.34	Raman spectral calibration C validation	158
4.35	Raman spectral calibration D - results	166
4.36	Raman spectral calibration E - results	172
4.37	Flow reaction monitoring - Flow system design F	179
4.38	Summary	188
5	Acetylation reactions with Raman spectroscopic monitoring	190
	Experimental	190
5.1	Acetylation reaction chemistry	190
5.2	Catalyst preparation - HPA	191
5.3	Catalyst characterisation	192
5.4	Raman analysis conditions	192
5.5	Batch acetylation reaction	192
5.6	Flow acetylation reaction	193
5.7	Acetylation Raman spectral calibration - A	193

5.8	Acetylation Raman spectral calibration - B	193
5.9	HPA influence on Raman spectra	194
	Results	195
5.10	Acetylation reaction	195
5.11	Tungstosilicic acid immobilization	196
5.12	Batch acetylation reaction - results	200
5.13	Acetylation reaction Raman spectra	200
5.14	Acetylation Raman spectral calibration - A results	202
5.15	Acetylation Raman spectral calibration - B results	210
5.16	HPA influences on Raman spectra - results	213
5.17	Summary	218
6	Conclusion	219
7	Further Work	223
8	Publications and Presentations	225
9	References	226
10	Appendix	238

List of Figures

1.1 Laminar flow diagram	4
1.2 “F-shaped” channel design	7
1.3 Electroosmotic flow design	8
1.4 Lithiation and Murahashi flow reaction	10
1.5 Immobilised palladium catalysts	24
1.6 Energy states of IR and Raman	32
1.7 Principles of PLSR	40
2.1 Optical cross section of a glass capillary with a monolith from 2.2	51
2.2 Optical side view of a glass capillary with a monolith from 2.2	52
2.3 Optical cross section of a glass capillary with a monolith from 2.3	54
2.4 Optical side view of a glass capillary with a monolith from 2.3	55
2.5 SEM Image a monolith from 2.3	56
2.6 BET results for nitrogen adsorption and desorption of a monolith from 2.3	57
2.7 SEM Image a monolith from 2. 4	59
2.8 SEM Image a monolith from 2.5	61
2.9 BET results for nitrogen adsorption and desorption of a monolith from 2.5	62
2.10 SEM image of varying monolith sizes from 2.5	65
2.11 SEM image of a monolith generated from 2.3 and 2.12	67
2.12 SEM-EDX image of Figure 2.11	68
2.13 EDX analysis of monolith from 2.3 and 2.12	71
2.14 Photograph of monoliths with and without palladium immobilisation	71
2.15 TEM image of monolith from 2.5 and 2.14	72
3.1 Final flow schematic design	76
3.2 Flow schematic design from 3.2	77
3.3 Flow schematic design from 3.3	77

3.4 Flow schematic design from 3.4	78
3.5 Flow schematic design from 3.5	79
3.6 Flow schematic design from 3.6	79
3.7 Photograph of monolith inside a glass capillary	81
3.8 Calibration graph of syringe pump flow	84
3.9 Calibration graph of HPLC pump flow	85
3.10 Calibration graph of IR fibre optic temperature probe	87
3.11 Calibration graph of the column heater	88
3.12 Photograph of reaction set-up from 3.6	95
3.13 Temperature graph of microwave cavity	97
4.1 Raman flow cell and schematic	107
4.2 Molecular structure of NMF and DMF	121
4.3 Raman spectrum of 4-cyanobiphenyl	124
4.4 Raman spectrum of 4-bromobenzonitrile	125
4.5 Raman spectrum of phenyl boronic acid	126
4.6 4-bromobenzonitrile Raman calibration in dioxane	128
4.7 phenyl boronic acid Raman calibration in dioxane	129
4.8 4-cyanobiphenyl Raman calibration in dioxane	130
4.9 4-bromobenzonitrile Raman calibration in DMF	132
4.10 phenyl boronic acid Raman calibration in DMF	133
4.11 4-cyanobiphenyl Raman calibration in DMF	134
4.12 Pressure effects on the Raman spectrum	143
4.13 Flow effect on Raman spectrum	144
4.14 Reaction mixtures Raman spectrum in dioxane and DMF	146
4.15 Microwaves effect on Suzuki reaction conversion	150
4.16 Raman spectrum of increasing concentrations of 4-cyanobiphenyl	152

4.17 Calibration graph of 4-bromobenzonitrile and 4-cyanobiphenyl from 4.18	154
4.18 Raman spectra of solutions used for Figure 4.17	155
4.19 GC-MS calibration of 4-bromobenzonitrile and 4-cyanobiphenyl	157
4.20 Raman spectra of reaction in Table 4.10	163
4.21 Calibration graph of 4-bromobenzonitrile and 4-cyanobiphenyl from 4.19	167
4.22 Raman spectra of calibration used for Figure 4.21	168
4.23 Raman spectra of reactions displayed in Table 4.10	171
4.24 Calibration graph of 4-bromobenzonitrile and 4-cyanobiphenyl from 4.20	175
4.25 Kinetic graph for determining order of reaction	183
4.26 Optimum flow rate graph for Suzuki reaction	184
4.27 Kinetic plot for Suzuki reaction	185
4.28 Heterogeneous catalyst mechanisms	187
5.1 SEM-EDX image of monolith with HPA	198
5.2 EDX analysis of image in Figure 5.1	199
5.3 Raman spectra of acetylation reaction compounds	201
5.4 Calibration of 4-bromophenyl acetate and 4-bromophenol	204
5.5 Raman spectra of flow acetylation reactions and original mixture	205
5.6 Raman spectra of calibration solutions from Table 5.1	208
5.7 Raman spectra of calibration solutions from Table 5.2	209
5.8 Calibration of acetylation reaction using PLSR	211
5.9 Optimum flow rate graph of acetylation reaction	212
5.10 Raman spectra of batch acetylation reactions varying HPA concentrations	215
5.11 Graph of HPA effect on Raman peak area	216
5.12 Graph of HPA effect on the 4-bromophenyl acetate concentration	217

List of Reaction Schemes

1.1 Homogeneous Suzuki reaction mechanism	13
1.2 Homogeneous acetylation reaction mechanism	18
2.1 Hydration and condensation summary of TMOS and MTMOS	50
2.2 Formamide hydrolysis in potassium silicate solution	53
4.1 Model Suzuki reaction	102
5.1 Model acetylation reaction	191
5.2 Model acetylation reaction mechanism	196

List of Tables

2.1 Characterisation of 2.5 monoliths of varying diameter	64
3.1 Summary of reaction conversion and conditions used in Chapter 3	99
4.1 Suzuki analyte calibration solution concentrations	112
4.2 Suzuki reaction conversions from 4.7	119
4.3 Statistics summary of 4-bromobenzonitrile calibrations	136
4.4 Statistics summary of phenyl boronic acid calibrations	137
4.5 Statistics summary of 4-cyanobiphenyl calibrations	138
4.6 t-test results of 4-bromobenzonitrile Raman response	139
4.7 t-test results of phenyl boronic acid Raman response	140
4.8 t-test results of 4-cyanobiphenyl Raman response	141
4.9 Suzuki reaction conversions using microwave heating	148
4.10 Suzuki reaction conditions A-E	160
4.11 Conversion predictions from 4.18 and 4.3	162
4.12 Conversion predictions from 4.19 and 4.3	170
4.13 Conversion predictions from PLSR and 4.3	176
4.14 Averages of Table 4.13 for conversion predictions	178
4.15 Results of Suzuki reaction at different flow rates	181
5.1 Acetylation analyte calibration concentrations	203
5.2 Acetylation analyte calibration concentrations with purchased product	207

List of Equations

1.1 Reynolds number determination	3
1.2 Einstein's equation of Brownian motion	5
1.3 Equation of Joule heating	21
1.4 Polarisability of a molecule	30
1.5 Expansion of Equation 1.4	31
1.6 Expansion of Equation 1.4	31
1.7 Expansion of Equation 1.4	31
1.8 Expansion of Equation 1.4	31
1.9 Determination of Raman signal	31
1.10 Simplified version of Equation 1.9	31
1.11 Mean centring of data	36
1.12 Autoscaling of data	36
2.1 Porosity determination	46
3.1 Actual microwave output equation	86
4.1 Peak area determination summary	113
4.2 Total peak area determination	113
4.3 Baseline peak area determination	114
4.4 Summary of Equations 4.1, Equation 4.2 and Equation 4.3	114
4.5 Rate law for Suzuki reaction	183
4.7 Reaction kinetic equation for overall second order reaction kinetics	184

1.0 Introduction

1.1 Overview

The purpose of this research was to explore possible flow, heating and detection techniques to control and monitor organic synthetic reactions. Once generated this flow reaction system would be able to easily alter reaction time and temperature to provide data that could be used to understand the reaction kinetics and optimise the system with a possibility of automation. The flow reaction design developed incorporates heterogeneous catalysis, microwave heating and Raman spectroscopy. A review of the literature confirmed the benefits associated with flow systems i.e. reaction control and selectivity and supported the approach found in this work. The proposed model reaction used to develop the methodology was a Suzuki reaction due to its complexity, catalyst tolerance, air tolerance and well practised synthesis in the academic and industrial sectors of chemistry.

1.2 Flow chemistry

Flow chemistry is a branch of chemistry that has been growing for the past 20 years¹⁻⁷. It has been classed as both meso flow and micro flow during over this time and used for both organic and inorganic synthesis as well as providing advantages for modern analytical techniques. The conventional idea of flow for synthetic reactions is to provide a continuous flow of reactants to produce product as apposed to the more conventional batch, stop and start reaction chemistry. As with any reaction, scale-up is always an issue. Scale-up of flow reaction chemistry offers the advantage over batch reaction chemistry of scale through volume flow whilst monitoring fast reaction times,

more efficient and effective control of reaction conditions, efficient reagent mixing, minimal waste, additional reactions in tandem, analysis and purification in tandem, automation of conditions and there is minimal chemical exposure^{6, 8-11}.

The ability to shunt from scalable micro flow reaction conditions is attractive mainly due to the low level reagent/waste generated and high control of reaction parameters, as a result with diffusive mixing under laminar flow high surface area to volume ratio that can not only explore physical environmental effects but also surface interactions with the reaction flow and effect mass and heat transfer¹². One of the challenges of scale-up is the difficulty in maintaining reaction conditions throughout a flow reaction for example temperature differences from the outer flow maybe different to the temperature of the inner flow. Sacks et al. demonstrated this concept in polymerisation in large scale batch reactors¹³. To avoid the possibility of losing reaction control whilst scaling up it is important to maintain the advantages of micro flow without compromising the control of reaction conditions¹⁴.

1.3 Reagent flow

One of the underlying advantages of micro flow is that reagent flow profiles can be used to dictate the behaviour, mixing and separation of the flow. This phenomenon attributes to fluid mechanics and is classified by Reynolds number¹⁵. Different flow types can be characterised laminar, transient and turbulent flow. Laminar flow is popular amongst micro fluidic chemists as it permits liquids to run side by side one another without mixing. Laminar flow is usually expressed at a low Reynolds number below 2300. Turbulent flow is what is usually observed everyday where there is no order to the flow, just molecules moving randomly in the direction of flow. It is usually expressed at a high Reynolds number above 4000. If the Reynolds number should lie

between 2300 and 4000 then the fluid is to be transient; neither turbulent nor laminar but a mixture of the two¹⁶. Reynolds number is determined by the fluid velocity, channel diameter, fluid density and fluid viscosity¹⁷ (Equation 1.1). Figure 1.1 shows the flow regime of a low Reynolds number (laminar) fluid flow where the fluid is separated into streams running parallel with one another and the channel surface interaction with the moving fluid is shown¹⁸. The slowest flow is at the walls of the channel, this is due to viscous interaction between the fluid and the walls. This creates a parabolic flow profile that is distinct to laminar flow. Turbulent flow behaviour does not follow this flow regime but does adopt an irregular flow pattern that allows rapid mixing¹⁹.

$$Re = \frac{\rho V D_H}{\mu} \qquad \text{Equation 1.1}$$

Where Reynolds number (Re) for a cylindrical channel would be determined by fluid density (ρ) kg/L, fluid velocity (V) m/s, chamber diameter (D_H) m and the fluid viscosity (μ) Ns/m².

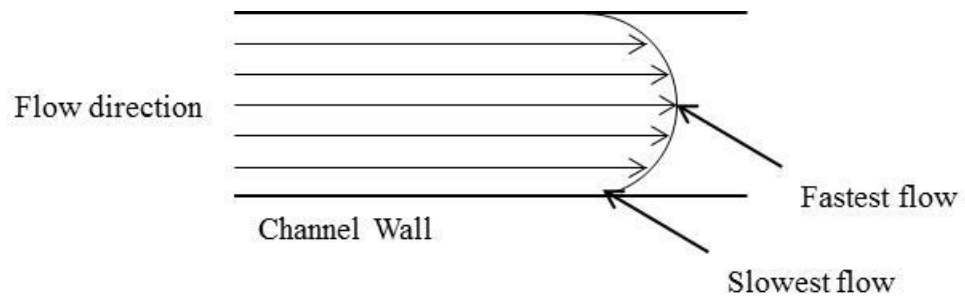


Figure 1.1 Laminar flow regime demonstrating the effect of a low Reynolds number flow in a channel.

Control of mixing in the flow channels has been the subject of much work in the evaluation of micro fluidic devices. In the field of analytical chemistry, the micro flow brought laminar flow into perspective as some techniques were dependant on laminar flow in order to perform multiple washing and analyte tagging¹⁷. Mixing in laminar flow is solely dependent on diffusion and can be explained through Einstein's equation of Brownian motion²⁰ (Equation 1.2). It states that the distance travelled in relation to time and the diffusion constant of that molecule²¹.

$$x = \sqrt{2D\tau} \quad \text{Equation 1.2}$$

Where the diffusion of a molecule in a pressure driven flow is determined by the root mean square distance a molecule has travelled (x) in relation to the diffusion constant (D) and diffusion time (τ).

This dependency on diffusion for laminar flow has been utilised by Peyman et al. to effectively tag analytes with magnetic particles that are pulled through laminar flow streams of buffer solution, fluorescent tagging reagent and then buffer solution until the magnetic particle, analyte and fluorescent tag reach a detector channel²². This same procedure was also used for DNA hybridisation²³.

Other authors have tried to mix within laminar flow in order to completely or partially activate or react compounds. Most methods involve the use of a serpentine channel which increases the channel to fluid interface creating fast and slow moving fluid within a channel band. This promotes mixing as two flow streams side by side in the channel would vary in speed and the resulting change would yield a higher Reynolds number for one stream and a lower Reynolds number for the other. This variation promotes the mixing of the two streams through chaotic advection²⁴. Another method for mixing has been demonstrated by Kim et al. where stream splitting and recombination of streams was performed using an "F-shaped" channel design that

generated a chaotic advection when the two streams met in flow again (Figure 1.2). This appeared to be an adaptation to the serpentine design in that the splitting and recombination of two streams lowered and then raised the Reynolds numbers very slightly to enhance the mixing²⁵.

Pressure driven flow has been widely used in relation to micro fluidics due to its ease to operate and simplistic set up whilst electroosmotic flow has been used a lesser extent. This technique of flow pumping occurs when an applied voltage is introduced to an electrolyte medium within a micro channel that has a charged surface, this enables the solution to be drawn through the channel²⁶. The medium consists of ions of different charge to the surface of the channels which create a double charge layer. The counter ion with the opposing charge to the wall is attracted to the wall. The counter ion which is free to flow will then move toward the cathode or anode (dependant on if the ions are cations or anions) when a potential difference is introduced along the channel. This generates a bulk movement of the electrolyte in solution towards the direction of the counter ion's flow²⁷. The flow profile is described in Figure 1.3. A notable difference between the electroosmotic flow profile and the hydrodynamic pressure driven flow profile is the shape of the front of the flow. This is due to the absence of the pressure differences across the diameter of the channel. In pressure driven flow the slow and fast flow result in molecules moving at different velocities, however for the electroosmotic flow the flow of the bulk solution is at the same velocity (with exception to the far edges of the flow which are interacting with the channel surface).

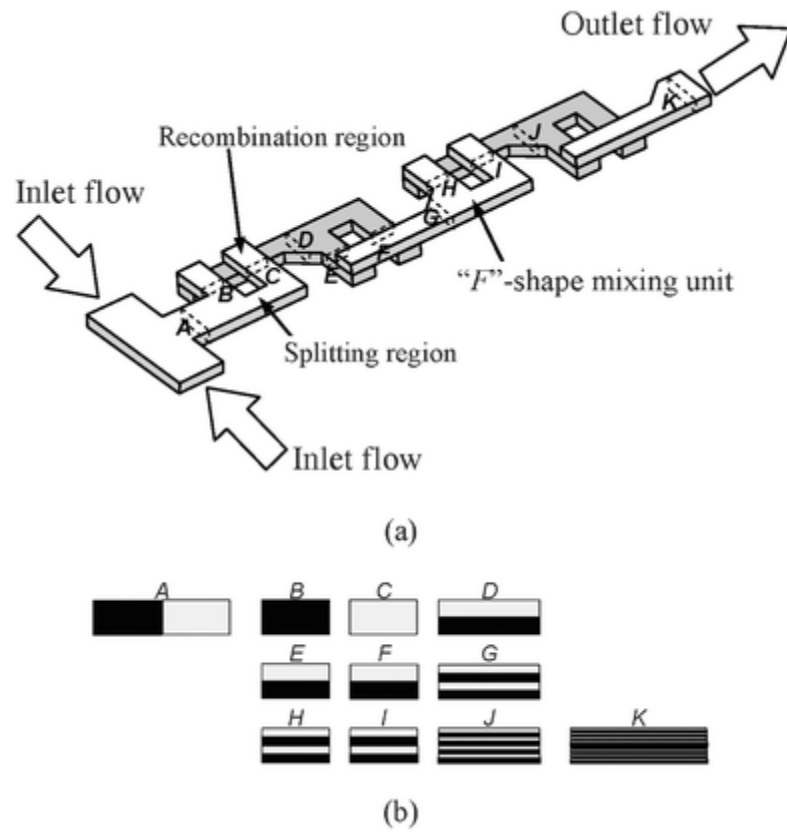


Figure 1.2 The “F-shaped” channel design described by Kim et al.²⁵, where the serpentine mixer (a) demonstrates different flow profiles in different sections (b).

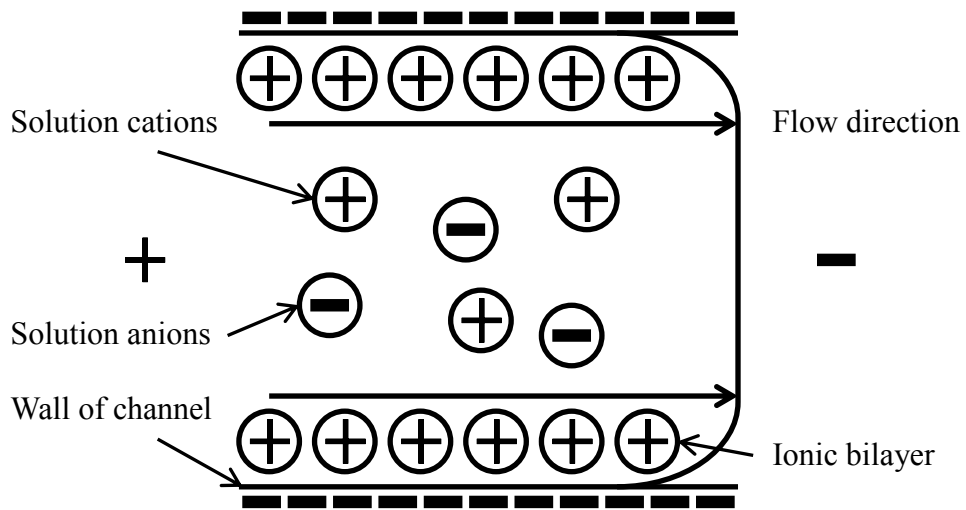


Figure 1.3 Electroosmotic flow example of the movement of an electrolyte solution with cations as the bilayer to a negatively charged surface showing the flow direction of solution towards the cathode.

1.4 Flow organic synthesis

Organic synthesis has benefitted through flow reaction techniques in that it provides improvements in reaction yields, product selectivity and scalability^{1, 28-29}. The advantages of flow chemistry have been exploited where high control of reaction conditions is beneficial and increased surface area interactions can be used to adapt reactions and provide a suitable environment that would otherwise be considered unsafe³⁰⁻³². Reactions such as polypyridine synthesis, acetylation, acylation, amide synthesis, Knoevenagel condensation, Heck coupling, Suzuki coupling, Kumada–Corriu coupling and Sonogoshira coupling have been used previously in flow reactions to improve and provide a novel synthetic method of synthesis³³⁻⁴¹. Nagaki et al. have used a micro flow reactor to control reaction conditions that would otherwise be deemed hazardous for a lithiation and Murahashi coupling in tandem⁴². Their flow reactor design allowed a temperature change of 0 °C for the lithiation and 50 °C for the Murahashi reaction in a very short space of time. This permitted the use of continuous flow to produce two reactions that would eventually lead to the formation of biaryl products (Figure 1.4). When their method was compared to a standard millilitre batch technique, it was observed that the flow reaction had an increase in yield from 73% to 93% demonstrating the effective use of flow reaction chemistry over batch.

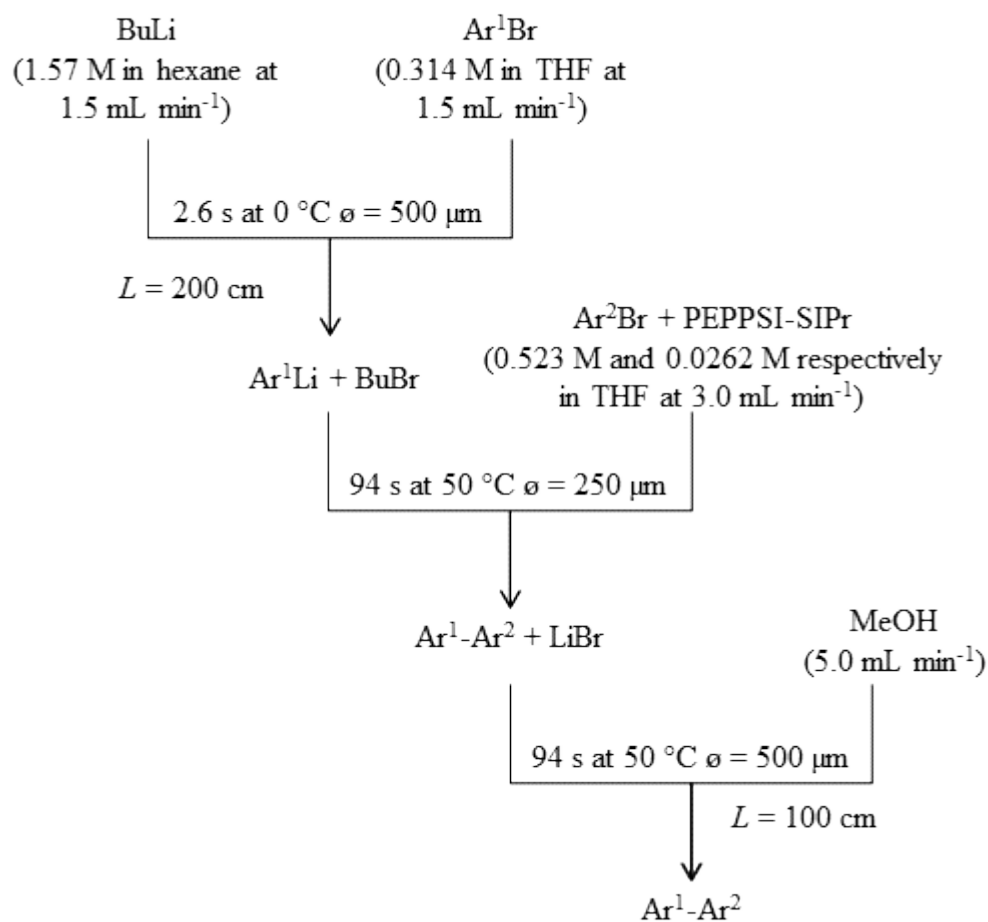
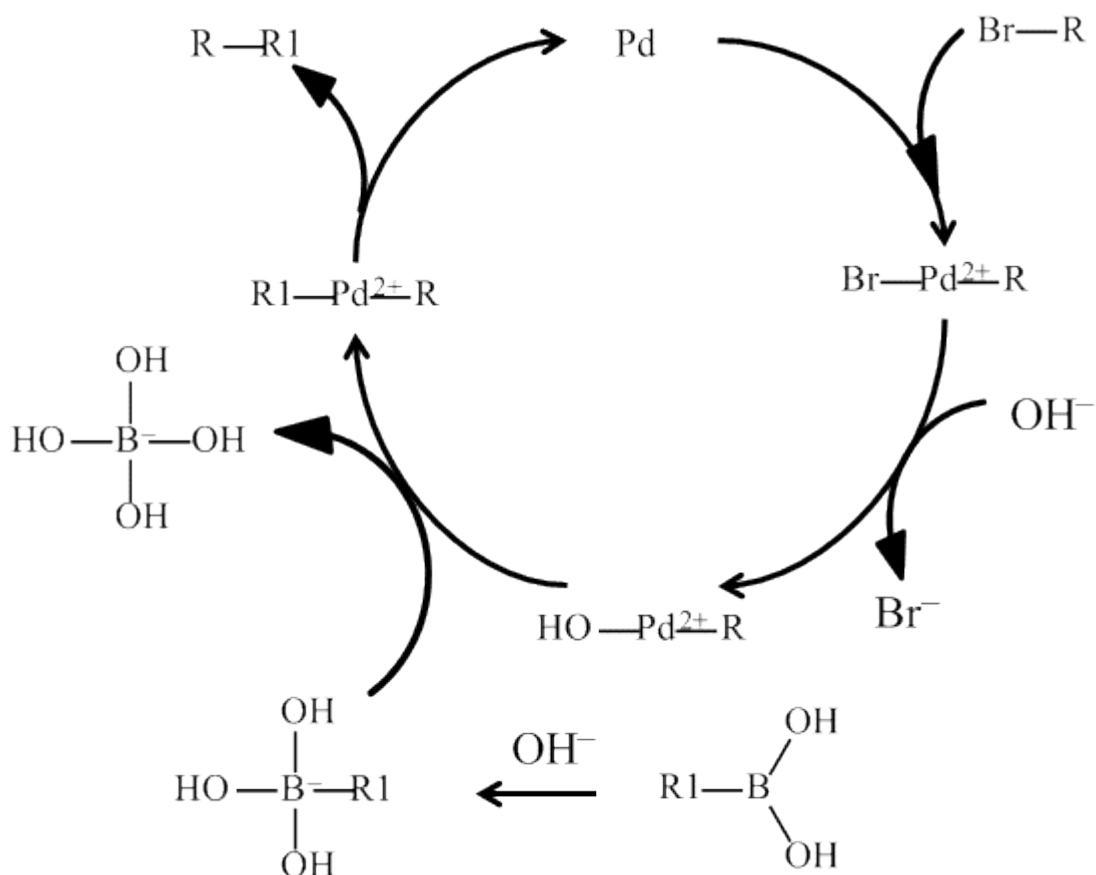


Figure 1.4 Nagaki et al . proposed reaction schematic of the lithiation and Murahashi reaction in a pressure flow driven reaction system⁴².

Another example of increased reaction activity was observed by Greenway et al. for the Suzuki reaction between 4-bromobenzonitrile and phenyl boronic acid¹⁴. An interesting observation occurred during this study in that with the use of electroosmotic flow was not only producing pumping in the micro channels but also generate hydroxide ions. For the Suzuki reaction to occur, a source of hydroxide ions is required to replace the halide on the palladium catalyst and create the boronic salt required in the mechanism (See Reaction Scheme 1.1). The energy output of the electrodes was enough to ionise the water molecules present in the solvent by providing electrons with high enough energy to break the H-OH bond resulting in free protons and free hydroxide ions. These free hydroxide ions were available for the Suzuki reaction. Comparing the batch reaction to the micro flow reaction under the same conditions had a yield increase from 10% to 60% providing more confirmation that micro flow or base introduction can increase the efficiency and effectiveness of reactions. However one of the drawbacks of using electroosmotic flow for organic synthesis is that the production of product can be hindered by back pressure effects, which slow the flow and negate the advantage of high reaction control by disrupting the flow of reagents or causing unwanted mixing⁸. Despite these back pressures, electroosmotic pumping is still a useful tool in the field of flow organic chemistry.

The mechanism for the Suzuki cross-coupling reaction consists of four stages of palladium species. The first state is palladium which then undergoes oxidative addition from the organohalide (C-X). This changes the oxidation state of the palladium from 0 to II. The C-X bond is added to the palladium and forms a C-Pd^{II}-X complex. The base (B) present in solution exchanges with the halide and the halide is removed from the complex leaving C-Pd^{II}-B. A side reaction which occurs during the oxidative addition and base exchange is associated with the formation of the organic boronic salt (formed from the boronic acid reaction with the base). The organic boronic salt replaces the base

of the palladium complex with the organic group of the salt by intermolecular transmetallation to form C-Pd^{II}-C. The drive of this step is from the stability of the base with the boronic salt. The final stage of the mechanism is called reductive elimination in which the palladium species is reduced when the organic substituent form a new C-C bond, the palladium oxidation state returns to Pd⁰ to start the cycle again⁴³. Reaction Scheme 1.1 illustrates the proposed homogeneous Suzuki reaction mechanism.



Reaction Scheme 1.1 Homogeneous Suzuki reaction mechanism commonly proposed⁴³. R and R1 are relative organic substituents.

Pressure driven pumping is still a favoured method of organic flow synthesis due to its controlled flow and prospects of ease of scale-up and simplicity in design in comparison to other techniques. Despite its simplicity, it can accommodate a wide variety of processes that would be difficult to integrate into other types of flow systems. Sahoo et al. have used physical means of purification and three reaction steps to convert an acid chloride to a carbamate using the Curtius rearrangement of isocyanates⁴⁴. The reactions used glass chips that had a mixing zone, reaction channels and a phase separator that was used to separate aqueous and organic phases as well as a gas-liquid phase. The design uses the density and immiscibility of two phases to carefully remove the waste. This reaction set up is necessary in order to prevent reaction intermediate decomposition of the azide which is a common problem for this reaction in conventional batch chemistry⁴⁵. The use of the multiple reaction design shows great potential in applications in other chemical organic synthetic reactions.

1.5 Flow Suzuki reactions

The Suzuki reaction is a preferential reaction amongst many organic synthetic chemists since its first publication in 1979⁴⁶. It consists of an organic halide reacting with an organic boronic acid/ester to generate a carbon-carbon bond between the two organic substituents. The popularity of this reaction stems from its tolerance to atmospheric conditions, low waste, non-toxic, high yielding, and ease of purification⁴⁷. It is of particular interest in pharmaceutical and liquid crystal chemistry⁴⁸⁻⁴⁹. It involves the use of organometallics traditionally with palladium however it has been known to use metals such as nickel, platinum, copper and ruthenium⁵⁰⁻⁵³. Suzuki cross-coupling reactions have been performed by Leadbeater et al. that contain no metallic catalyst⁵⁴. The group used microwave heating in batch to promote the reaction of various

organohalides with phenyl boronic acid in the presence of sodium carbonate. They observed cross-coupling products with no palladium present. The results were reassessed and it was observed that up to 50 ppb of palladium could initiate the Suzuki reaction accounting for impurities that are present in commercially available sodium carbonate⁵⁵.

The mechanism for the Suzuki cross-coupling reaction consists of four stages of palladium species. The first state is palladium which then undergoes oxidative addition from the organohalide (C-X). This changes the oxidation state of the palladium from 0 to II. The C-X bond is added to the palladium and forms a C-Pd^{II}-X complex. The base (B) present in solution exchanges with the halide and the halide is removed from the complex leaving C-Pd^{II}-B. A side reaction which occurs during the oxidative addition and base exchange is associated with the formation of the organic boronic salt (formed from the boronic acid reaction with the base). The organic boronic salt replaces the base of the palladium complex with the organic group of the salt by intermolecular transmetallation to form C-Pd^{II}-C. The drive of this step is from the stability of the base with the boronic salt. The final stage of the mechanism is called reductive elimination in which the palladium species is reduced when the organic substituent form a new C-C bond, the palladium oxidation state returns to Pd⁰ to start the cycle again⁴³. Reaction Scheme 1.1 illustrates the proposed homogeneous Suzuki reaction mechanism.

The Suzuki reaction has been used in flow organic synthesis to emphasise advantages in micro reactor design. Noël et al. have used multistep synthesis involving Suzuki reaction chemistry and purification techniques to fully incorporate Suzuki reaction cross-coupling of phenols⁵⁶. The method of synthesis consisted of two main reaction steps. Trifluoromethanesulfonic anhydride was used, produced by reacting the phenol replacing the alcohol group with a triflate functionality⁵⁷. This acts as a strong electron withdrawing group and is considered just as effective as the organohalide equivalent. The second stage of the flow reaction was the reaction with aromatic boronic acids in a biphasic system. The reaction flow system used stainless steel beads in a packed bed reactor to enhance the mixing of the bilayer and increase the reagent interface.

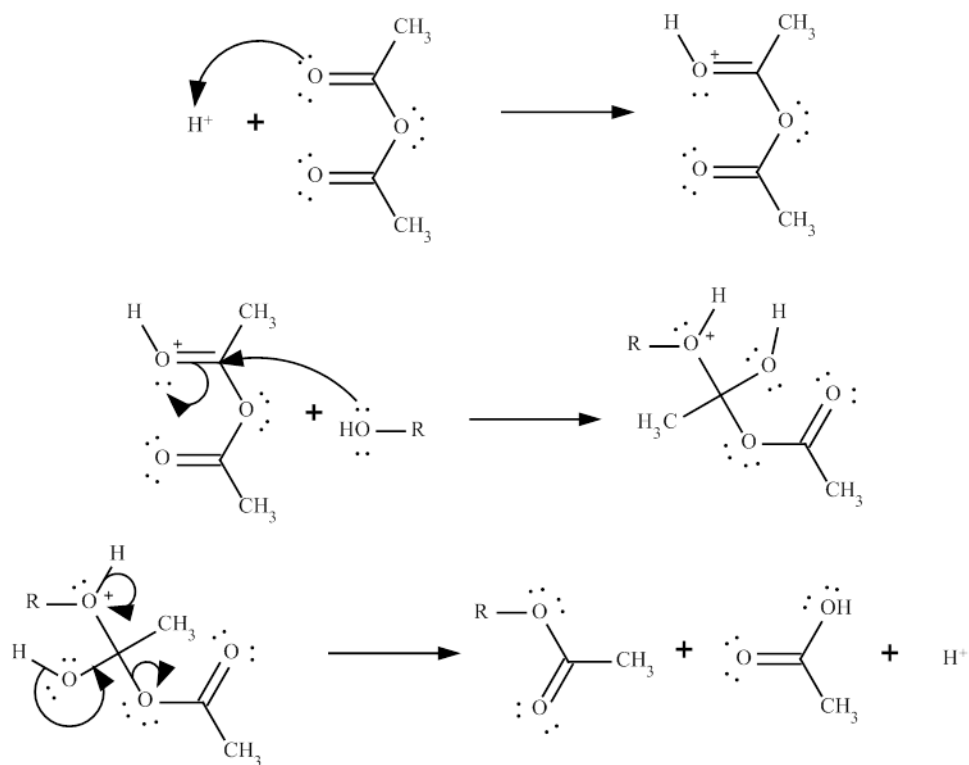
Other examples of Suzuki reaction chemistry have been used to demonstrate stability of reactions and demonstrate that the milder flow conditions are applicable to flow synthesis. A study conducted by Mennecke et al. used Suzuki and Heck reactions to demonstrate the stability of their heterogeneous palladium catalyst support⁵⁸. Their study showed how after multiple reaction cycles for the Heck reaction between 4-iodoacetophenone and styrene showed no decrease in catalyst activity after 10 cycles producing above 90% yield. They also cycled their catalyst through 10 cycles of the Suzuki reaction between 4-bromotoluene and phenyl boronic acid. For the Suzuki reaction there was a much greater instability in their yield after cycling, however it was claimed that due to it being isolated yields, deviations may have resulted from the work up. Lee et al. used immobilised palladium acetate in polyurea to perform similar reactions to Mennecke et al. except with greater success⁵⁹. In this case they report that with the use of this catalyst some of those Suzuki reactions observed product even at reaction temperatures at 40 °C. This shows highly efficient reaction yields using this

methodology and demonstrates that the use of heterogeneous catalysis in flow reaction chemistry can be advantageous.

1.6 Flow Acetylation reactions

Acetylation reactions are widely used in the industrial sector for the production of pharmaceuticals and biodiesel⁶⁰⁻⁶³. In the pharmaceutical industry it allows intermediate steps to promote a reaction to its completion⁶⁴. For example in conjunction with Suzuki reaction chemistry, the acetylation of phenols in the para-position alters the electron donating properties of the alcohol as it is converted to an ester. This in turn promotes the Suzuki reaction as esters have lower electron donation properties than the alcohol⁶⁵. The mechanism for this conversion from an alcohol to an ester is generally catalysed by Brønsted-Lowry bases or acids⁶⁶⁻⁶⁷. The catalysis by acids is performed by activating the acetylating reagent which is usually either acetic acid or acetic anhydride. The mechanism for the acetylation reaction is displayed in Reaction Scheme 1.2⁶⁸.

Catalyst separation from the organic reagents and products has proven difficult for most synthetic methods. The most popular is batch liquid-liquid separation especially when producing biodiesel. This is because the long chain alkanes and alkenes provide an organic phase. For pharmaceutical applications however, many compounds are soluble in the aqueous phase⁶⁹. Some research groups have used acetylation reaction in flow chemistry to improve separation of catalyst from the reaction mixture. One possible way to do this is by generating a fluorous phase catalyst. Yoshida et al. have done precisely this, by pumping an organic alcohol through the fluorous phase catalyst they have produced an efficient phase separating system generating highly yielding products⁷⁰. Other methods of separation in flow chemistry are in the form of immobilised heterogeneous acid catalysts⁷¹⁻⁷².



Reaction Scheme 1.2 homogeneous acetylation reaction mechanisms via acidic catalyst commonly proposed. R is the organic substituent of the alcohol.

1.7 Microwave theory and Microwave Suzuki flow reactions

There has been a growing use of microwaves over the past 50 years in organic synthesis⁷³. They provide an alternative heating mechanism to the conventional conduction of a flame or oil bath. Microwave energy is defined as a region of the electromagnetic spectrum between 300 MHz and 300 GHz, however domestic use is limited to 2.45 GHz (corresponding to a 12.24 cm wavelength) in order to not interfere with microwaves used in communication⁷⁴. The idea of its use in heating stems from its interaction with water and other polar molecules.

Microwaves can be artificially generated by a magnetron. A high powered cylindrical cathode is placed in the centre surrounded by a gap and an outer anode. As the cathode is powered, a permanent magnetic field in place permits electrons to be attracted to the anode in a spiral fashion. As the electrons move, they pass openings in the anode that causes a turbulent effect that resonates the electrons. Resonance causes a high energy radiofrequency within the magnetron in which waveguides select and transport the microwave to their destination. The wavelength design is specific to one wavelength meaning no wavelength shorter or larger can pass. They are made from metal that reflects microwaves through its channel for communication (pulse production of microwaves) or heating (continuous production of microwaves)⁷⁵.

Continuous microwave production can result in heating effects of some molecules. Microwaves do not have the energy requirements to break, rotate or stretch bonds but they do have the energy to rotate molecules. This is the principle mechanism by which they induce heating into chemical reactions. Polar molecules in a microwave field align with the field and can freely rotate in low energy microwaves. As the energy increases and the frequency of waves increases the polar molecules struggle to maintain their complete rotations and drop back into a relaxed state. This causes molecules to no

longer be synchronised with one another and leads to them moving in different directions. Friction is then induced and the molecules heat up, this is called dipolar polarisation. The lack of synchronisation occurs over a range of a frequency until it reaches its peak at which the majority of molecules cannot completely relax and the molecules then begin stop rotating freely and no longer absorb microwave energy. The relaxation is reflected in the dielectric constant of molecules. This is explained fully by the Debye model corresponding to the reorientation of the dipolar moments of the molecules (relaxation time) ⁷⁶. Microwave heating is not only caused by dipolar polarisation but also by ionic conduction. Ionic conduction occurs when disassociated ions in solution move with the microwave (as the electrons of the polar molecules do). Opposing ions move to opposite ends of the wave and a net movement of these ions introduces electrostatic friction between the ions generating heat. This is dispersed rapidly to the surrounding solution increasing the mobility of the ions and thus increasing the temperature further ⁷⁷.

Indirect microwave heating also occurs in non-earthed metals. Metals are used in microwave waveguides to reflect the wave to its desired location with little or no absorption of the microwaves. Microwaves however can heat a metallic surface by charging. Electrons on the metallic shell can move with the introduction of a magnetic wave. Microwaves provide a magnetic wave on the surface of a metal and the electrons follow through the metallic surface generating a current. These are called *Eddy currents*. An increase in microwave power increases the microwave amplitude and increases the distance the current travels. Resistance is directly proportional to the distance the current travels. An increase in resistance is directly proportional to the heating of the metallic surface and is called Joule heating (see Equation 1.3). This connects the microwave heating effects to Joule heating⁷⁸.

$$Q = I^2 \cdot R \cdot t \quad \text{Equation 1.3}$$

Where Joule heating (Q) is determined by the square of the current (I), the resistance (R) and the time (t).

The use of microwave heating has advantages in organic synthesis in that it has been reported to generate super-heated “hot spots” in solution that rapidly disperse to surrounding solution effectively heating inside out rather than outside in⁷⁹. This temperature increase is rapid and allows higher energy states to be attained faster. Accomplishing these higher energy states promotes quicker and cleaner reaction conditions as less by-products are produced⁸⁰⁻⁸¹. However the most attractive feature of microwave heating is the significantly reduced reaction time. The reaction rates of the Suzuki reaction using microwave energy increase dramatically with the introduction of microwave heating. Baxendale et al. found a 48-fold rate increase in a batch Suzuki reaction between 1-bromo-4-methoxybenzene and phenyl boronic acid⁸². Their research continued to use microwave reaction chemistry for flow reaction synthesis. A heterogeneous palladium catalyst (Pd EnCat-30TM) was subjected to microwaves under flow conditions whilst a homogeneous solution of many organic halides and many organic boronic acids were flowed through separately with tetrabutylammonium acetate. In many of their cases comparison of batch microwave chemistry to flow microwave chemistry showed a yield improvement. This was possibly due to the limitations of the penetrating ability of microwaves. The decrease in surface area to volume ratio of the batch reaction meant less of the reaction mixture was exposed than the flow. Dependant on the solution contents, microwaves may not penetrate the surface of the solution deep enough as it is readily absorbed.

Flow Suzuki microwave heated reactions were also performed by Leadbeater et al. A batch stop-flow method was used in order to performed Suzuki and Heck

reactions⁸³. The batch stop-flow method was successfully scaled-up using microwave synthesis without losing production yields for Suzuki and Heck reactions whilst re-optimising their approaches. Using the same system set-up, Leadbeater et al. demonstrated that not only the optimisation procedure could be found but also the reaction composition⁸⁴. They used organic bases to successfully prove that the organic bases were comparable to inorganic bases for the Suzuki reaction. Rather than a batch stop-flow mechanism, He et al. compared continuous flow Suzuki reactions between batch and flow. Two different heterogeneous catalysts were immobilised in glass capillaries coated with gold³³. Their research found that the integration of the heterogeneous palladium capillary coated in a gold film could produce yields above 70% in 15 seconds demonstrating that reaction effects on the reaction could be assessed swiftly.

1.8 Heterogeneous palladium catalysis and immobilisation methods

Most Suzuki reaction chemistry involves palladium catalysis. The discovery of the Suzuki reaction in 1979 used the homogeneous catalyst tetrakis(triphenylphosphine)palladium to catalyse the reaction between boranes and halides⁴⁶. Since the first reported work many palladium species have been developed in order to catalyse the Suzuki reaction⁸⁵⁻⁸⁸. An adaptation to the catalyst design was immobilisation. Immobilisation can occur by means of non-covalent adsorption and desorption, ionic exchange/interaction, covalent bonding, cross-linking and entrapment through a gel/ capsule/ zeolite^{7, 89-92}. It has advantages over the traditional homogeneous catalysis in that purification is much simpler, ease of catalyst recycling, waste reduction and increased catalyst stabilisation.

Palladium immobilisation on silica has been a favoured method of immobilisation for many years⁹³⁻⁹⁵. The methods of immobilisation are characteristic to the oxidation state of the palladium. This oxidation state can be advantageous for the proposed reaction. Karimi et al. have used palladium catalyst immobilisation to perform aerobic oxidation of alcohols⁹⁶. The immobilisation procedure uses silica gel modified with 3-aminopropyltrimethoxysilane to create an active surface to react with 2,2'-dipyridyl ketone, 2-acetylpyridine or 2,2'-bipyridylamine (Figure 1.5). These three different immobilised molecules on silica gel provided amine bidentate ligands for palladium acetate. In turn this backbone provided a catalyst for a range of aerobic oxidations of alcohols turning them into ketones or aldehydes. This type of bidentate ligand approach was also adopted by Sandee et al. with the exception that instead of amines as ligand, phosphine ligand complexes were formed⁹⁷. Bis(dibenzylideneacetone)palladium was bound co-ordinately with the phosphine ligands and allowed different allylic alkylation reactions to be performed successfully. The palladium complex was recycled with minimal metal leaching and was observed to have increased selectivity for one of the immobilised catalysts due to the rigid structure of the ligand permitting a greater bite angle specifying the mechanism of reaction. This demonstrates the importance of correct ligand selection for desired product, as a correct ligand can instigate a particular mechanism for the reaction.

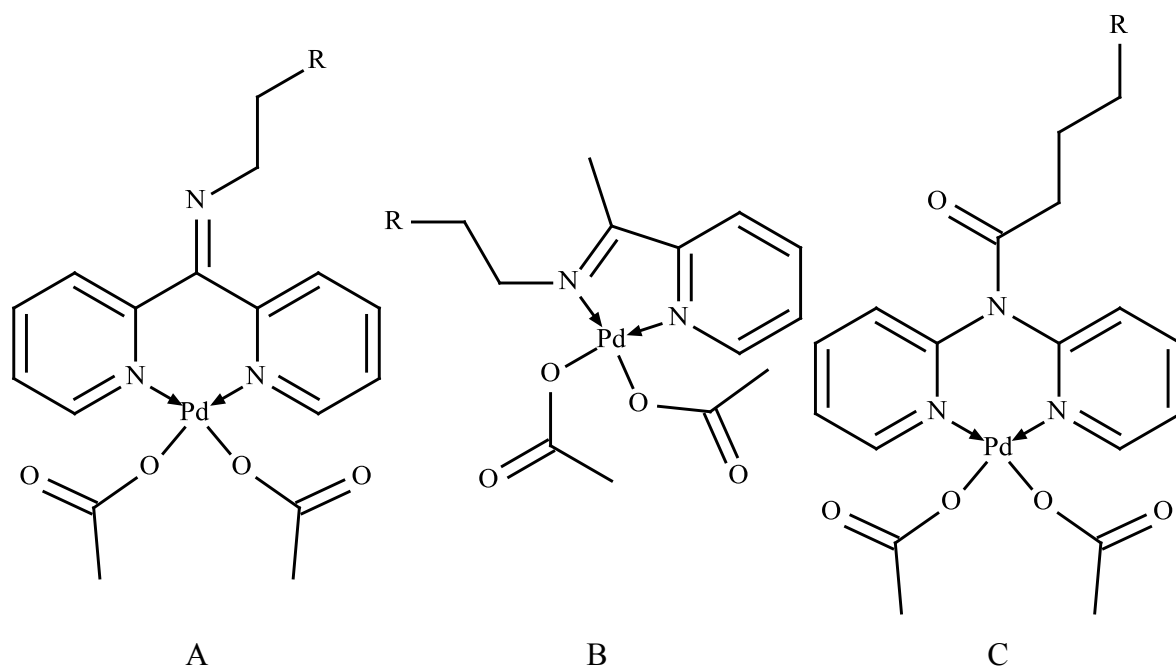


Figure 1.5 The immobilised palladium catalysts and their cross-linkers described previously⁹⁶ where R represents the silica support.

It is a well-known that thiols have been observed to poison palladium catalysts in certain reactions (especially methane oxidation). The sulphur containing compounds produce strong sulphate coordinate bonding to the palladium. This alters the capability of the palladium as a catalyst⁹⁸. Nevertheless, immobilised thiols have been demonstrated to effectively scavenge palladium and be useful for carbon-carbon forming reaction chemistry⁹⁹⁻¹⁰⁰. Successful Suzuki and Heck reactions have been reported to occur above 98% conversion by Richardson et al. and Crudden et al. with minimal leaching⁹⁹⁻¹⁰⁰. This demonstrates that although sulphur containing compounds can poison the palladium catalysts in some reactions, it can also act as a very useful immobilisation cross-linker at retaining the catalyst with minimal leaching.

Not only is co-ordinate bonding mechanisms of palladium immobilisation on solid supports possible, but encasing them is too. Encasing palladium and physically entrapping the catalyst has attracted keen interest. This methodology anchors the palladium within the solid support, usually without the use of a cross-linker. By encasing the palladium it is unable to escape from the solid support whilst still providing pores to permit reagents and products to move freely into and out of the pore. He et al., for example, demonstrated the locking of palladium within the nano pore structure of a sol-gel silica monolith¹⁰¹. Palladium entrapped within these pores was used effectively with microwave heating to instigate flow Suzuki cross-coupling reactions. The catalyst supported by this methodology also showed effective flow reaction catalyst scale-up. Another method of trapping palladium in silica was reported by Das et al.¹⁰². Nano porous silica was generated and palladium placed inside the structure through absorption where it was reduced from Pd^{II} to Pd⁰. This had palladium particles cluster together inside the nano pores trapping them. The immobilised palladium was then able to catalyse the Suzuki reaction and showed minimal leaching from its support.

1.9 Heterogeneous enzyme-based catalysts in flow

Catalyst immobilisation has been used to enhance enzyme-based reactions in flow reactors. Richter et al. have used glass as an immobilisation medium for binding the enzymes Xanthine oxidase and Horseradish peroxidase¹⁰³. Their methodology required the use of a cross-linker, 3-aminopropylsilane-glutaraldehyde, and demonstrated that the ease of preparation and the multi-stepping properties of their reaction system were highly advantageous. However a problem was observed from an increase in back pressure. These advantages and disadvantages were also observed with polystyrene and agarose as a media for immobilisation¹⁰⁴⁻¹⁰⁵.

Other immobilisation media have been reported based on polymer and silica monoliths¹⁰⁶⁻¹⁰⁷. Unlike the glass, polystyrene and agarose, these monoliths provide a low pressure backbone for immobilisation. They also have distinct advantages in that they provide a more stable environment for the catalysts and have been shown to improve the reaction efficiency. Although the organic polymer and silica monoliths can have their surface chemistry altered to provide anchoring, a popular method of immobilisation is trapping these large molecules within the pores of the monolith effectively caging the catalyst within^{101, 106-107}. A disadvantage of monoliths as an immobilisation medium is their preparation which requires a number of practical steps. This is the same for both organic and silica monoliths. Silica monoliths do have an advantage over organic monoliths in that they can reach temperatures exceeding 300 °C without charring or burning and they are solvent tolerant. Organic monoliths swell in the presence of certain solvents whilst silica does not. A different inorganic immobilisation material to silica was used by Heule et al.¹⁰⁸. Horseradish peroxidase was immobilised on the surface of aluminium oxide using the cross-linker

3-aminopropylsilane-glutaraldehyde. Their research showed that the aluminium oxide provided a vast surface area due to its high porosity, thus increasing the catalyst contact with the substrates. Disadvantages of their work led to the conclusion that the procedure for preparation was complex and that large scale processing using aluminium oxide was not applicable to this methodology.

All the immobilisation methods mentioned so far required an anchoring mechanism whether physical or chemical to enable incorporation into a flow system. Nomura et al. used a different anchoring mechanism in the form of magnetic beads¹⁰⁹. A magnetic field holds the beads with the catalyst embedded on the surface in micro flow channels and can be quickly manipulated into releasing and capturing the heterogeneous catalyst just by the removal and placement of a magnetic field. Use of magnetic beads for immobilisation was demonstrated by Nomura et al. to be simple, however it did have a disadvantage in that the contact of the catalyst with its reagents was limited as the magnetic beads could block the flow.

1.10 Flow reaction analysis

Flow reaction monitoring was initially performed using offline techniques. Sampling of the flow reaction mixture would be then subjected to pre-analysis off-line techniques in order to ascertain the right composition for analyte analysis. For gas chromatography (GC) this is usually a liquid-liquid extraction to separate polar and non-polar molecules, in particular, volatile solvent. Other such techniques like high performance liquid chromatography (HPLC) usually require that the injection mixture be the same composition of the mobile phase of the HPLC needing once again pre-analysis techniques. The use of chromatographic techniques is often necessary as most detectors cannot be specific to one compound within a mixture. HPLC and GC have

been used in countless research¹¹⁰⁻¹¹⁹. Both rely on the interaction of the mixture of analytes and the solid phase of a separation column. HPLC separates by promoting the affinity of the analytes with the stationary phase and mobile phase (column and carrier liquid). By altering the composition of the mobile phase or altering the stationary phase surface functionality; the analyte separate. GC is similar to HPLC but the mobile phase is a gas. It does not depend on the affinity of the analytes dissolution into the gas phase but more so their volatility as the analytes are in a constant fluctuation with their affinity to be a free moving gas and their affinity with the stationary phase¹²⁰. Despite their similarity in separation, they differ in that for quantitative analysis HPLC can use internal and external standards but GC uses only internal standards. This is because the injection volumes of a HPLC are a liquid in a pre-designated injection loop and are always constant. GC injects a liquid that vaporises to a gas in a constant injector volume, the partial pressures of the gas generated can vary between each injection and the concentration of analytes would vary considerably if an internal standard was not used¹²¹. An important part of GC or HPLC analysis is the detection. GC detectors include flame ionisation (FID), electron capture (ECD), nitrogen phosphorous (NPD), thermal conductivity (TCD), flame photometric (FPD), infrared spectrometry (IR), ultraviolet spectrometry (UV) and mass spectrometry (MS). HPLC detectors include refractive index (RID), electrochemical, conductivity, infrared spectrometry (IR), ultraviolet spectrometry (UV), fluorescence spectrometry and mass spectrometry (MS)¹²⁰.

Nuclear magnetic resonance (NMR) and mass spectrometry (MS) are popular detectors amongst organic chemists as it gives structural information on the compounds in the reaction mixture. A cheaper detector than NMR and MS is UV spectroscopy for organic analytes. However UV detection can only occur if the organic analytes contain a UV active chromophore. Chromophores are an atom or group of atoms within a

molecule that show activity at certain wavelengths of the electromagnetic spectrum. A UV chromophore is usually broad and non-specific to a particular compound. Despite the lack of specificity, research has gone into using UV active compounds for fluorescence detection. Tang et al. have used fluorescent tagging of organic thiols to demonstrate the sensitivity and specificity in conjunction with HPLC separation¹²². Fluorescence detection can also be used in on-line analysis rather than having to use off-line HPLC separation. One such type of analysis was performed by Liang et al.¹²³. They describe their fluorescence and UV detection flow cell that was coupled with capillary electrophoresis.

On-line analysis has advantages over the conventional and traditional off-line analysis. In particular IR and Raman spectroscopic analysis can give structural information within seconds of application on the composition of a flow reaction mixture without the need of purification. This distinct advantage removes further time consuming stages and in process monitoring can be invaluable in showing a reaction has gone to completion or if there is a problem. Monitoring reactions using on-line analysis are greatly favoured in industry for this reason. Another advantage of using IR or Raman on-line monitoring is the need for no physical sampling. NMR, MS and other detection techniques all required a separated invasive sample into reaction mixtures. Spectroscopic analysis using IR, Raman, UV or fluorescence are non-invasive and can be performed using a window into the reaction mixture.

1.11 Raman spectroscopy theory

Raman spectroscopy was first predicted by Smekal in 1923 but was not until 1928 that it was first observed¹²⁴. It is dependent on the inelastic scattering of photons from an incident light source on to a Raman active molecule. The concept of this

scattering is determined by the polarisability of a molecule. If a molecule has a strong permanent dipole then its polarisability is low as the electric field is already shifted across a bond. Equation 1.4 shows the effect of polarisability and electric field strength has on an induced dipole. Nevertheless the size of the electric field interaction is dependent on the vibration or rotation of a molecule. If the vibration or rotation fluctuate the polarisability of the molecule, it can be regarded as Raman active. Rotation Raman spectroscopy provides information on bond lengths of a molecule¹²⁵. Vibration Raman spectroscopy provides information about the molecular composition. A vibration of a bond that changes in its displacement coordinate (bond length or bond angle) in relation to its change in polarisability is considered Raman active.

$$\mu = \alpha E \qquad \text{Equation 1.4}$$

Where μ is the induced dipole moment, α is the polarisability and E is the electric field strength.

Raman scattering occurs when the incident light source shifts the electron cloud of a bond towards one side of a bond inducing a dipole, and as it shifts back photons are scattered in all directions. The majority of the scattered light is scattered as elastic scattering also known as Rayleigh scattering. The Raman scattering however occurs as in-elastic scattering in the form of Stokes scattering. Equation 1.4 can be expanded to include Equation 1.5, Equation 1.6, Equation 1.7 and Equation 1.8. This generates Equation 1.9 giving an equation to derive the Raman signals. Simplifying Equation 1.9 segments out different sections of the equation that correspond to Rayleigh, Stokes and Anti-Stokes scattering (Equation 1.10). $\alpha_0 E_0 \cos 2\pi \gamma t$ shows the Rayleigh scattered band, $\cos 2\pi(\gamma - \gamma_v)t$ shows the Stokes scattering and $\cos 2\pi(\gamma + \gamma_v)t$ shows the Anti-Stokes scattering¹²⁶⁻¹²⁷.

$$\mu = \alpha E_0 \cos 2\pi\gamma t \quad \text{Equation 1.5}$$

$$E = E_0 \cos 2\pi\gamma t \quad \text{Equation 1.6}$$

$$Q = Q_0 \cos 2\pi\gamma_v t \quad \text{Equation 1.7}$$

$$\alpha = \alpha_0 + \frac{\delta\alpha}{\delta Q} Q_0 \cos 2\pi\gamma_v t \quad \text{Equation 1.8}$$

$$\mu = \alpha_0 E_0 \cos 2\pi\gamma t + \frac{\delta\alpha}{\delta Q} Q_0 E_0 (\cos 2\pi\gamma_v t) (\cos 2\pi\gamma t) \quad \text{Equation 1.9}$$

$$\mu = \alpha_0 E_0 \cos 2\pi\gamma t + \frac{\delta\alpha}{\delta Q} \frac{Q_0 E_0}{2} [\cos 2\pi(\gamma - \gamma_v)t + \cos 2\pi(\gamma + \gamma_v)t] \quad \text{Equation 1.10}$$

Where the induced dipole moment (μ) would be determined by the polarisability (α) and electric field strength (E). The polarisability could be observed as being affected by the initial polarisability (α_0) of the molecule, the normal coordinate (central gravity point of the electron cloud, Q), the normal coordinate constant (for a maximum normal coordinate, Q_0), the vibration frequency of the molecule (γ_v) and time (t). The electric field could be observed as being affected by the electric field constant at a maximum of the field (E_0), the incident radiation frequency (γ) and time.

Rayleigh, Stokes and Anti-Stokes scattering occur at different frequencies. This phenomenon can be expressed in the form of an energy state diagram (Figure 1.6). The frequency of the occurrence of scattering is highest with Rayleigh, then Stokes and then Anti-Stokes. Anti-Stokes occur the least as a vibration energy state must have been reached to allow the energy to be absorbed to the virtual energy levels. The higher vibration energy states occur less frequently than the ground vibration energy state of the molecule which means Stokes scattering occurs more frequently. Rayleigh scattering occur the most frequently because more molecules have a higher probability of returning to the ground state from their excited state. If temperature was increased

however, the Stokes and Anti-Stokes likelihood of occurring would increase as the vibration energy levels would be reached more frequently.

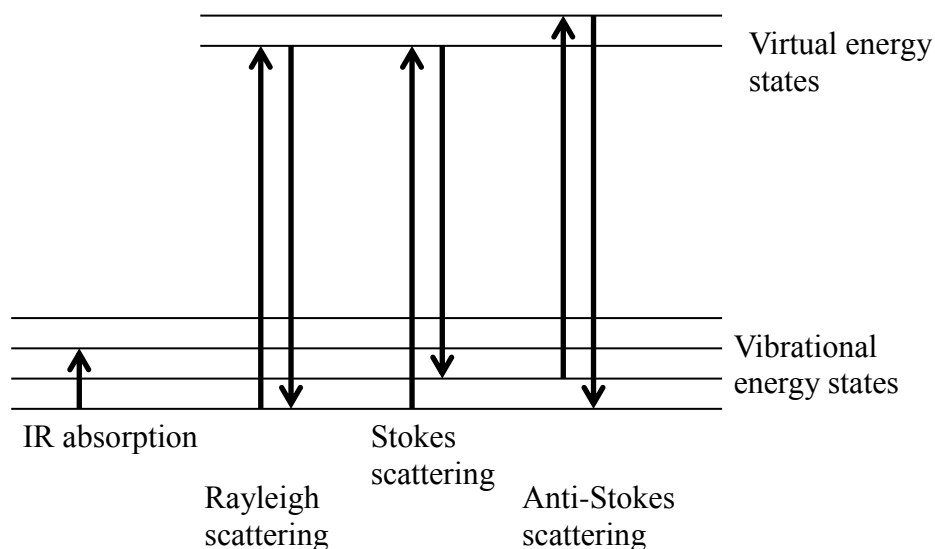


Figure 1.6 The separate energy states of absorption and scattering of IR absorption, Rayleigh, Stokes and Anti-Stokes scattering.

1.12 Comparing IR and Raman

IR and Raman spectroscopy both use vibrations within molecular bonds to distinguish between molecules. Generally IR active bonds are not Raman active bonds and Raman active bonds are not IR active bonds (this is not the case of all molecules). IR is dependent on the polarity of a bond containing a permanent dipole. As a molecular bond vibrates it absorbs energy from the incident beam. The remaining beam is detected and the absorbed wavelengths are observed. The absorbed wavelength is dependent on the type of bonds present producing a fingerprint spectrum of that particular molecule. This is similar to Raman spectroscopy, however unlike Raman, IR spectra have broad peaks that can often over mask or shadow other peaks. Other advantages that Raman spectroscopy are that it accommodates a small sample size, ease of sample preparation,

water tolerance (water shows weak Raman activity), solvent tolerance, sensitivity and low cost¹²⁸⁻¹²⁹.

1.13 Raman spectroscopy and Fluorescence

Fluorescence interferes greatly with Raman spectroscopic signals. It floods the spectrum and can make Raman signals almost impossible to distinguish. This is due to the increased probability of molecules fluorescing rather than in-elastic scattering. This does not occur for all molecules however, only for molecules that are fluorescently active. There are methods to avoid fluorescence in Raman spectra. Methods to prevent fluorescence include careful selectivity of the laser wavelengths, fluorescent filters and fluorescent quenching substances¹³⁰⁻¹³¹. Another method of fluorescent removal is in the form of chemometric analysis, effectively removing the variation in the spectra contributed by the fluorescence from the raw spectra. Ampiah-Bonney et al. performed such a chemometric method called principal component analysis (PCA) on Raman spectra obtained for acetylation reactions between ethanol and acetic acid¹³². This provided pure Raman spectra for the reaction.

1.14 Raman flow reaction monitoring

Flow reaction chemistry has used Raman spectroscopy in order to present immediate on-line analysis of a reaction composition. This provides not only identification of compounds but can also be used in reaction quantification. This invaluable technique in recent process monitoring has been used by Fletcher et al. to demonstrate flow profiling in micro fluidic channels between ethanol and acetic acid, as well as the position of the acetylation product ethyl acetate¹³³. A Raman microscope

was used to map the position of each chemical within the channels by monitoring specific peaks that correspond to ethanol, acetic acid and ethyl acetate. The Raman intensities of these compounds were calibrated in order to generate accurate concentration profiles of the reagents and products spatially located within a micro fluidic channel at different time intervals during a flow reaction.

Quantification in Raman reaction monitoring is careful and selective due to the changes in flow composition affecting the signal response. Bubbles can be a cause of such variation in response, however it has been found that as long as the flow is still sampled in the flow reaction chamber the bubbles/gas interactions are negligible¹³⁴. Examples of quantification of Raman spectroscopy are not simple to obtain unless simpler reactions were chosen. Most of these reactions involve compounds that are less likely to fluoresce; examples include acetylation reactions of non-aromatics and some Knoevenagel reactions¹³⁵⁻¹³⁶. Most reaction monitoring using Raman spectroscopy is purely qualitative and is used to identify the presence of compounds. Lee et al. demonstrated the use of Raman spectroscopic flow reaction monitoring for the identification of the imine benzylideneaniline¹³⁷. This technique was used to map the flow dimensions to provide diffusion information on the flow system as well as to provide a peak ratio variation to determine the end point of the reaction. Direct quantification from peak intensity or peak area to concentration using larger molecules is difficult as these compounds can possess fluorescing characteristics.

1.15 Pre-spectral processing for quantification

Raman spectroscopy has many factors that can affect the intensity of its peaks. As its molecular count contributing to the Raman signalling is much less than the fluorescing nature of compounds it can often be difficult to obtain pure Raman spectra.

However sometimes even slight fluorescent changes can alter the quantification of Raman spectra rather than masking it. Other factors contributing or altering Raman spectra stem from the exact chemical composition of the solution passing through the detection window, any phase shifting passing through the flow (solid, liquid and gaseous phases), window movement, sample colour, refractive index, and liquid temperature¹³⁸. These factors all alter the Raman signal that makes quantification difficult. The exact chemical composition can increase or decrease the signal by either promoting the vibration of the bond and give more molecular counts or hinder it by reducing the energy available for scattering, furthermore if the chemicals absorb radiation in the spectral window of interest this can give false readings in the data. This leads to colour that can also affect the signal, partially in the visible region of the spectrum, where certain wavelengths could be absorbed and once again alter the Raman signal. The temperature of the liquid passing by the Raman window is an important factor in influencing the Raman signal intensity. The temperature of solution alters the amount of molecules present in the Stokes and Anti-Stokes pathways. An increase in temperature increases the amount of molecules in an already excited vibration state promoting Anti-Stokes scattering. Another effect of increasing temperature is a shift in Raman frequency¹³⁹. Especially for solids, the expansion in intermolecular bonds with the increase in temperature reduces the frequency that the photons are scattered.

Shifting phases in solution can greatly alter the spectra. An example of this is observed in surface enhanced Raman spectroscopy (SERS); where the surface interactions between a solid and a liquid or gas within the Raman window amplify Raman signalling. Mabbott et al. have used a SERS system for positive identification of illegal drugs by generating silver nano particles on the surface of a British 2 pence coin¹⁴⁰. This amplified the Raman signal making concentrations as low as 0.0001 M of

drugs capable of detection. During this methodology as with most Raman detection and quantification techniques, multivariate and data pre-processing was required.

1.16 Raman spectral pre-processing

Data pre-processing of Raman spectra is usually required in order to identify the significance of variance in the spectra and confirm the contributions to the change in spectra. In order to ascertain this, the spectra must undergo certain data processing in order to make spectra comparisons equivalent. In almost all spectral pre-processing mean centring is instigated (Equation 1.11). Mean centring helps normalise the data preventing a large variant magnitude from completely engulfing the first line of variance called the First Principal Component¹⁴¹.

$$X_{cen} = X_{raw} - \bar{X} \quad \text{Equation 1.11}$$

Where the mean centred intensities (X_{cen}) are determined by the raw spectral intensity (X_{cen}) minus the average of all the spectra intensities (\bar{X}).

A variation of the mean centring exists called Auto-Scaling (Equation 1.12). This forces the intensity values to have equal significance rather than just reducing the magnitude of the variation¹⁴¹.

$$X_{auto} = \frac{X_{raw} - \bar{X}}{\sigma} \quad \text{Equation 1.12}$$

Where the auto-scaled intensities (X_{auto}) are determined by the raw spectral intensities (X_{cen}) minus the average of all the spectra intensities (\bar{X}), divided by the standard deviation of all the spectral intensities (σ).

If spectral conditions are not ideal, baseline correction maybe instigated. This can set all points to a reference point which is then taken as zero. This allows the spectra to become unified and defines specific variations from one spectra with another.

1.17 Raman spectral processing

After adjusting data to capture variance and remove scale effects; it can then be placed into different algorithms in order to determine outliers and/or carry out calibration modelling. There are many types of processing analysis within univariate and multivariate analysis. Univariate analysis involves the monitoring and analysis of one particular wavelength and observing its change over a range of spectra. This is ideal in spectra that are not affected by external influences on the molecule spectra of interest. Multivariate analysis is more complex as a range of wavelengths is monitored which are calculated into different vectors called scores and loadings.

Scores and loadings are measurements of variations in the independent variable (for example concentration) and dependant variables (for example Raman spectral intensities) respectively. Initial understandings of this concept originated from the idea that a change in the independent variables would influence the dependant variable values. Multivariate analysis uses the scores and loadings extracted from the raw data to provide an underlying analysis of the structure of the data. Principal component analysis (PCA) and partial least squares (PLS) are two multivariate techniques that break the raw data into scores and loadings and use them to determine how different samples relate to one another. PCA can be used as an outlier detection tool to identify trends in a reaction system that is not obvious from the raw data¹⁴². It is based on finding the greatest variation in data and setting it as a new set of variables. This plots a new configuration in that the data has then accounted for the greatest variation in the data set. From here

the data can be subjected to another component analysis to find the second greatest variation in the spectra. This new set of plotted variables makes up the second principle component. The PCs can be extended until they account for all the variation in the data. For Raman spectra this can be in the form of the concentration of chemicals present, the noise of the instrument or the fluorescence interference¹³². This means that certain aspects of the Raman processed spectra can be singled out and possibly removed to permit pure spectral influences of the desired observation, for example, observing reactant and product concentrations.

PLS is similar to PCA analysis in that it uses variations in the spectra in order to distinguish a pattern. PLS differs from PCA in that it has unsupervised variation detection. PCA will not distinguish variation contributions made by either the independent or dependant variables. PLS provides a supervised reduction technique that compares loadings and scores against predicted loadings and scores for the greatest variation in the spectra. For Raman analysis of a reaction mixture this greatest variation is usually concentration¹⁴³. Therefore PLS can distinguish the greatest variation in spectra and plot this against a set of known concentration. This provides as much information as possible but distinguishes between any other variations present in the spectra, focussing its primary attention on the concentration variances affect on the scores. By observing this effect, PLS can be subject to regression and provide predictive capability for latent variables embedded within Raman spectra which would not be accessible using univariate approach due to complex spectral interaction.

1.18 PLS Regression

PLS regression (PLSR) is based on the idea of finding the latent variables of the spectral data sets and comparing the scores, deducing the relationship between the

independent and dependant variables. Figure 1.7 shows the relationship between scores and loadings to the original spectra. The spectral data and the concentrations of the samples can be decomposed into their components. A common component of both is the scores. By plotting the scores obtained against concentration for calibration spectra and in conjunction with spectra of unknown concentrations, it is possible to establish the concentration of the unknowns. This methodology of calibration has been successfully implemented by Barnes et al.¹⁴⁴. Micro fluidic devices were used to initiate a polymerisation reaction by UV activation and were monitored using a Raman microscope. The Raman data was analysed using PLSR and provided conversion information for the reaction between benzyl methacrylate monomers and the cross-linker 1,6-hexanediol dimethacrylate. The PLS monitored region of the spectra was between 1500 cm^{-1} and 1800 cm^{-1} Raman shifts. Other examples of PLSR have been used to find soil organics using Vis-NIR spectroscopy, quantification of blood serum contents by Raman spectroscopy, water analysis for polyaromatic compounds using fluorescence spectroscopy and DNA analysis of multicomponent markers from different microbes through electropherograms¹⁴⁵⁻¹⁴⁸. PLSR can be used in a wide variety of techniques to establish unique and quantitative analysis models that can distinguish chemical differences in a wide variety of media.

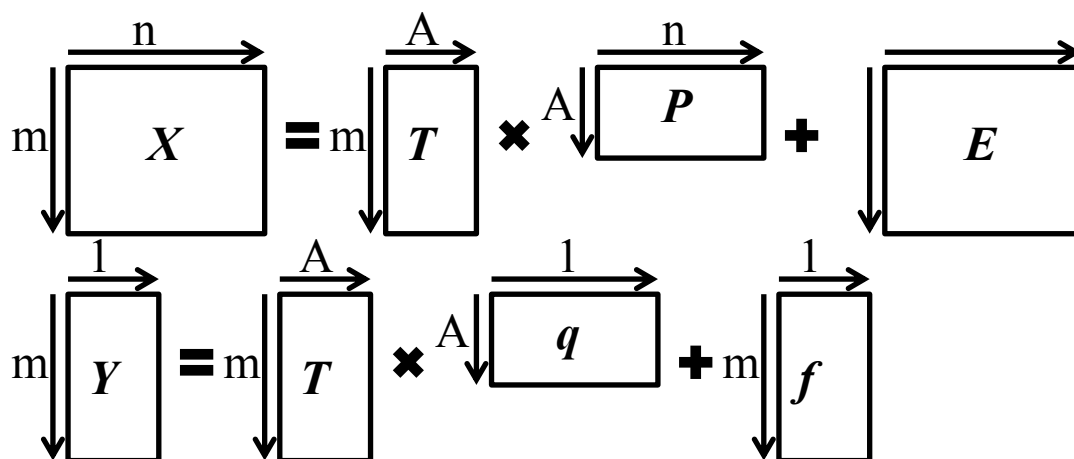


Figure 1.7 Principles of partial least squares regression (PLSR) where X is the original spectral data that is decomposed into scores (T) and loadings (P) with an error matrix (E). Y is the original concentration data of the test samples. This can be decomposed into its own scores and a loading vector (q). The number of latent variables can be stated as A , and the error matrix of Y is f .

1.19 Aims

This project represented a part of a larger EPSRC funded project focussed on flow synthetic chemistry projects in collaboration with Pfizer Inc. The research was aimed at exploring methods of flow chemistry that could be applied to an industrial research environment with prospects of production scale-up. This has been shown to be a highly desired area within the pharmaceutical industry and much investment has been offered into using flow chemistry for drug synthesis.

The aim of the work described in this thesis was to produce a method of flow reaction chemistry that can utilise microwave heating over a heterogeneous catalyst under a flow regime with on-line detection of reactants and products. The stages of development were catalyst preparation, flow reaction design, heating regimes, catalyst

incorporation into the flow design, executing and monitoring flow reaction, reaction quantification, and adaptability to other flow reactions. The example flow reaction chosen was a Suzuki reaction; a well versed reaction in pharmaceutical chemistry. Another desired trait of the system was automation, the ability to generate a library of compounds using this flow methodology thus expanding the knowledge needed to compile likely compounds to form appropriate drug candidates.

Characterisation and Functionalisation - Experimental

2.0 Silica monolith generation, characterisation and functionalisation

The catalysts required for this flow project were required to be heterogeneous and porous in nature. This led to the generation of silica monoliths. Their solid support backbone, ease of surface modification from silanol groups, and high porosity made them an ideal for a solid support structure. The monoliths themselves consist of two significant formations; the micro pores and the nano pores. The micro pores lower the back pressure and permitted flow through the monolith without compromising its structure making silica monoliths a feasible option for the flow system. The nano pore structures contributed to the surface area of the silica and allowed palladium nano clusters formation in the pores locking them onto the surface making the chemical nature of the silica monolith essential for the proposed Suzuki reaction. Eventually by incorporating the silica monolith embedded with palladium into a flow reaction system, this allowed the possibility of an automated optimisation flow reaction system.

The silica monoliths specification that enabled them to be potential candidates for immobilised palladium required high surface areas, high porosity, high reproducibility and ease of modification. From the monolith design the final stage was palladium addition to produce viable clusters of palladium on the surface of the silica for catalysis. This meant the palladium would not leach from the silica and cover the entire surface of the monolith allowing an even spread of reaction sites.

Characterisation and Functionalisation - ExperimentalExperimental*2.1 Monolith generation*

The generation of silica monoliths was evaluated using four methods all of which were based on a change in the pH of the reaction media. The four methods which used different pre-cursors were named accordingly.

2.2 Method 1 - Tetramethyl orthosilicate (TMOS) and methyltrimethoxysilane (MTMOS)

18 μL of TMOS (98% Sigma Aldrich) and 69 μL of MTMOS (98% Sigma Aldrich) (1:4 molar ratio) was added to diluted hydrochloric acid (0.1 M Sigma Aldrich) (8 μL of 1 mM hydrochloric acid, in 13.2 μL of water). The resultant sol solution was mixed thoroughly and a 4.2 μL aliquot was then added to 17.8 μL of water. 22 μL of 0.2 M Tris-HCl buffer (pH 7 Sigma Aldrich) brought the solution to pH 7. The buffered solution was added to glass capillary (25 μL 612-1405 VWR) moulds and rolled by hand until the solution appeared “milky”. The capillary was left for 15 hours at 20 °C for monolith polymerisation. Reduced pressure removed any remaining fluid.

2.3 Method 2 – Potassium silicate

A ratio by volume of 1:10 formamide (99% Sigma Aldrich) to potassium silicate (10% Sigma Aldrich) solution respectively was formed by adding 100 μL of formamide to 900 μL potassium silicate. An aliquot of this mixture (25 μL) was then placed in a

Characterisation and Functionalisation - Experimental

glass capillary (25 μ L 612-1405 VWR)). The capillary was plugged at each end and heated in an oven (Hotbox size 1 GallenKamp) for 24 hours at 80 °C. The resulting monolith was washed with ethanol (99% Sigma Aldrich) and then water. *Ostwald ripening* was carried out by subjecting the monolith to 0.1 N ammonium hydroxide (Volumetric 5.0 N Sigma Aldrich) at 40°C for 48 hours. The monoliths were washed with water and kept under vacuum for 4 days.

2.4 Method 3 - Tetramethyl orthosilicate (TMOS)

0.432 g of polymer F127 (12600 Mw Sigma Aldrich) and 4 mL of 0.02 M acetic acid (99% Sigma Aldrich) were mixed at 0 °C until homogeneous. 2 mL of TMOS (98% Sigma Aldrich) was placed in the solution and stirred vigorously for 30 minutes. The resultant bubble free homogeneous sol-gel was poured into various glass capillary moulds (diameters of 4.8 mm and 8.2 mm with lengths of 60 mm and 50 mm respectively), and plugged with PTFE tape. The mould was heated at 40 °C for 48 hours. The monolith produced was washed with water and dried in an oven at 60 °C for 24 hours. The monolith was subjected to *Ostwald ripening* with 1 N ammonium hydroxide (Volumetric 5.0 N Sigma Aldrich) for 24 hours at 85 °C. After washing with water the monolith was dried at 60 °C for 24 hours. The final monolith was then calcinated at 550 °C for 6 hours.

2.5 Method 4 – Tetraethyl orthasilicate (TEOS)

0.282 g of poly ethylene oxide (PEO, 100000 Mw Sigma Aldrich), 2.537 mL of 1 N nitric acid (1 N volumetric standard Sigma Aldrich) and 0.291 mL of water were mixed at 0 °C until homogeneous. 2.256 mL of TEOS (98% Sigma Aldrich) was placed

Characterisation and Functionalisation - Experimental

in the solution and stirred vigorously for 30 minutes. The resultant bubble free homogeneous sol-gel was poured into various plastic moulds (sizes ranging from 4.8 – 19.1 mm diameter) and plugged with PTFE tape. The mould was heated at 40 °C for 72 hours. The resultant monolith was washed with water and subjected to *Ostwald ripening*. 0.1 N ammonium hydroxide (Volumetric 5.0 N Sigma Aldrich) was added in excess to the monolith and heated 24 hours at 80 °C. Once treated the monolith was washed with water and dried at 40 °C for 48 hours and then 100 °C for 24 hours. The final monolith was then calcinated at 550 °C for 3 hours.

2.6 Monolith characterisation

The monoliths generated were analysed using various techniques measuring porosity, surface area and microscopic imaging. Surface area was determined using a Porosimeter (Tristar3000 Micromeritics). Microscopic analysis was performed using a scanning electron microscope and an optical microscope. The scanning electron microscope (EVO 60 Carl Zeiss) required a sputter coater (SC7640 Polaron) and a vacuum cabinet (E12E Edwards High Vacuum). The optical microscope (Axiovert S100, Carl Zeiss) required no pre-treatment equipment.

2.7 Porosity testing

Porosity was measured by weighing the mass of the monolith with and without water absorbed. This gave the exact mass of water in the void pore volume of the monolith. Assuming the monolith structure was cylindrical and all the micro and nano

Characterisation and Functionalisation - Experimental

pores were filled with water when absorbed, estimations were produced for the monolith porosity using Equation 2.1.

$$\frac{W_T - W_M}{dLr^2\pi} = \varphi \quad \text{Equation 2.1}$$

Where porosity (φ) was determined based on the dry weight of the monolith (W_M), total weight of the monolith filled with water (W_T), the density of water (d), the length of the monolith (L) and the radius (r).

2.8 Surface area analysis

Surface area analysis was performed by Brunauer Emmett Teller surface area analysis (BET). The analysis equipment used to measure the partial pressures was a Porosimeter (Tristar3000 Micromeritics). Samples were prepared by pre-weighing a monolith into the glass tubes and fitting them into the analyser. Liquid nitrogen was used as the adsorption gas at 77.3 K with an equilibrium interval of 5 seconds. Data obtained was used for surface area analysis and nano pore diameter analysis. This was repeated thrice for monoliths described in 2.19.

2.9 Microscopic analysis

Two types of microscopic analysis were performed; optical microscopy (Axiovert S100, Carl Zeiss) and Scanning Electron Microscopy (SEM, EVO 60 Carl Zeiss).

For SEM analysis, monolith samples were dried, cut through the cross section of the silica and attached to aluminium SEM mounts with super glue. Sputtering (SC7640 Polaron) was then performed on the monolith samples by coating with carbon particle in a high vacuum (E12E Edwards High Vacuum) and using a sputter coater. Coatings of

Characterisation and Functionalisation - Experimental

up to 10 nm of carbon were added and the sample was then placed in the scanning electron microscope for imaging and analysis.

2.10 Catalyst loading

Catalytic loading was performed with varying precursors to inevitably produce Pd(0) nano particles on the silica monolith surface. Four methods of palladium immobilization were performed.

2.11 Palladium acetate deposition in THF

0.0200 g (8.909×10^{-5} moles) of palladium acetate (98% Sigma Aldrich) in 0.5 mL THF (99% Sigma Aldrich) was pipetted onto the monolith. The monolith was heated at 80 °C for 48 hours. Once cool, it was washed with dry THF and reduced using 1 M hydrazine in THF (1 M Sigma Aldrich) for 24 hours at room temperature. The monolith was then washed with THF and then water until no colour change was observed. The monolith colour changed from brown to black after reduction.

2.12 Palladium acetate deposition in DMF ¹⁴⁹

0.1000 M of palladium acetate (98% Sigma Aldrich) in dimethylformamide (DMF, 99% Sigma Aldrich) was pipetted onto the monolith (volume in accordance with monolith void volume) and heated to 150 °C for 30 minutes and the immediately rinsed with cool DMF. The palladium filled monolith was then heated to 400 °C for 1 minute and washed immediately after with DMF. This washing process was repeated three

Characterisation and Functionalisation - Experimental

times. Eventually the cool DMF became transparent and the monolith colour changed to black.

*2.13 Palladium bis(dibenzylideneacetone) deposition*¹⁵⁰

0.0160 g (2.783×10^{-5} moles) palladium bis(dibenzylideneacetone) (Sigma Aldrich) in 8.1 mL of dry tetrahydrofuran (THF, 99% Sigma Aldrich) was mixed with 20 mL of dry THF. The monolith was then fully submerged into mixture. The mixture was left standing for 24 hours at room temperature. Hydrogen reduction followed for 24 hours at 172.37 kPa at room temperature using an autoclave. THF was removed from the monolith by negative pressure and washed with DCM (99.8% Sigma Aldrich). The residual DCM was then removed by negative pressure.

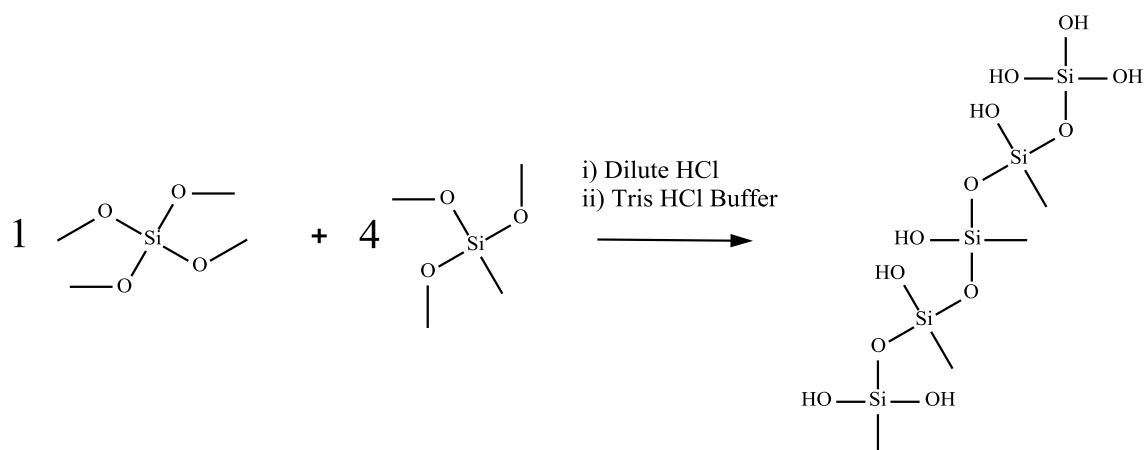
*2.14 Sodium tetrachloropalladate deposition*¹⁰¹

0.0500 g (1.6995×10^{-4} moles) of sodium tetrachloropalladate in a 0.5 mL aqueous solution was added to the monolith by pipette prior calcination. The solution was left on the monolith for 6 hours, washed with water and dried at 40 °C for 24 hours. The monolith was subjected to further drying at 100 °C for 24 hours and calcinated at 550 °C for 3 hours. The monolith was then washed with water and dried at 40 °C for 24 hours. After drying the palladium on the monolith was reduced to Pd(0) using hydrogen at 172.37 kPa at 340 °C for 3 hours at a ramp of 2 °C min⁻¹.

Characterisation and Functionalisation – Results and DiscussionResults*2.15 Monolith generation*

All monoliths produced were subject to some or all of the characterisation procedures described previously (2.6). This characterisation was used to assess whether the silica monolith structure would form a beneficial backbone sustaining low back pressure flow whilst supporting the immobilised catalyst. It permits a finer detail into the micro pore and the nano pore structure. Pore analysis of the silica monoliths helped determine which monoliths would have a lower back pressure (caused from the micro pores) and which have a higher likelihood of catalyst-silica modification (caused from the nano pores surface contributions). The initial starting monolith produced was derived from *monolith 2.2*.

Using *monolith 2.2*, the formation of a silica monolith was based on the hydration and condensation of Si-O bonds present in both the TMOS and the MTMOS. The acidic conditions used to generate the Si-OH (silinol) monomer groups. The pH was then adjusted to a neutral point using Tris-HCl buffer solution. Reducing the amount of free protons in solution caused the reduction of hydrogen's on the silinol groups which caused in turn the condensation of the Si-O⁻ groups on the monomers which formed a more stable dimer and eventually a polymer as groups of dimmers and polymer bridged together in their gel form. This process is shown in Reaction Scheme 2.1 which shows the hydration and condensation of the silica monomers on a 1:4 ratio of TMOS:MTMOS.

Characterisation and Functionalisation – Results and Discussion

Reaction Scheme 2.1 The hydration and condensation summary reaction between tetramethyl orthosilicate and methyltrimethoxysilane with a 1:4 molar ratio (method described in *monolith 2.2*).

The product formation produced a “milky” appearance during the rolling process in the glass capillary. Optical microscopy of the monolith once formed indicated two distinct microscopic structures. A hollow bore or a “half and half” type structure from either excess or lack of rolling (Figure 2.1 and Figure 2.2). This type of monolith appeared to stick to the walls of the glass capillary with little shrinking observed. The heat of the hands were thought to contribute to the activation of the formation of the monolith structure by heating the glass walls of the capillary initiating a faster rate of reaction at the sol-glass interface. This would explain the excess rolling/excess heating to form the hollow bore type monoliths (Figure 2.1). Using the same theory a lack of rolling would cause less of activation for the polymerisation at the surface and would cause polymer generation to be subjected to gravity so the product is seen forming in the lower half of the cylindrical capillary (Figure 2.2).

Characterisation and Functionalisation – Results and Discussion

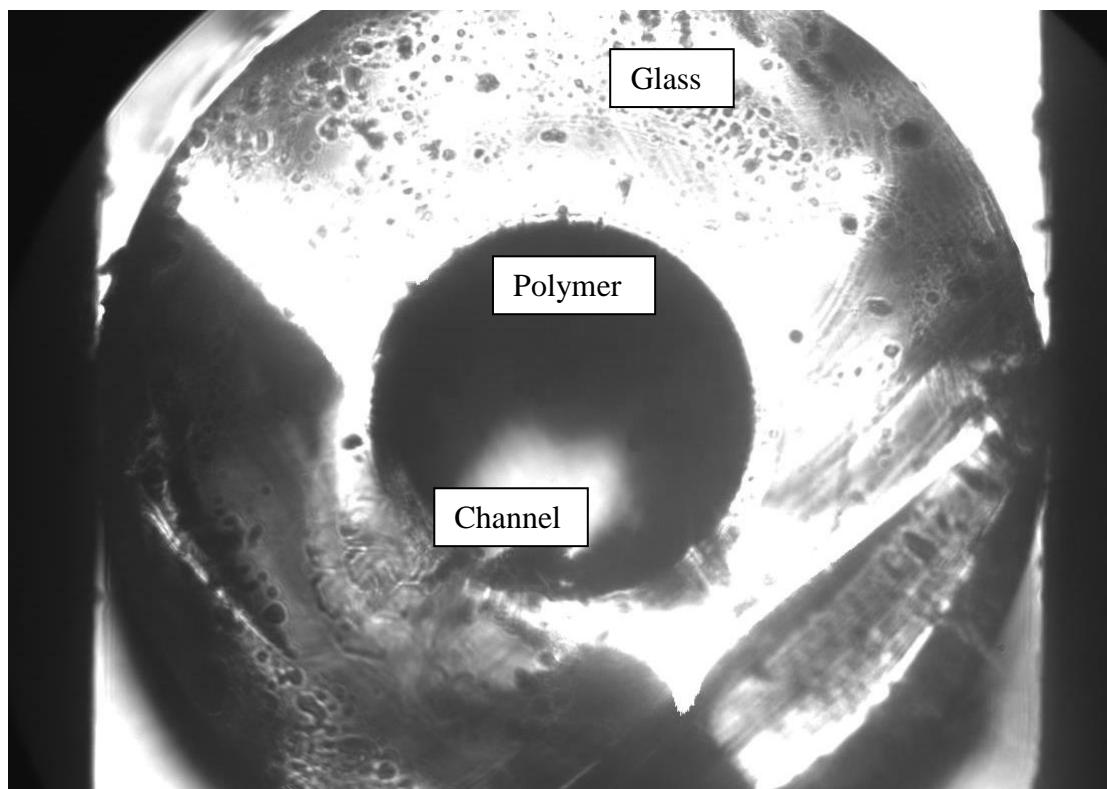


Figure 2.1 An image obtained using the optical microscope of the cross section of a 25 μL glass capillary (internal diameter of 0.3 μm) containing a monolith formed from *monolith 2.2* demonstrating excess rolling.

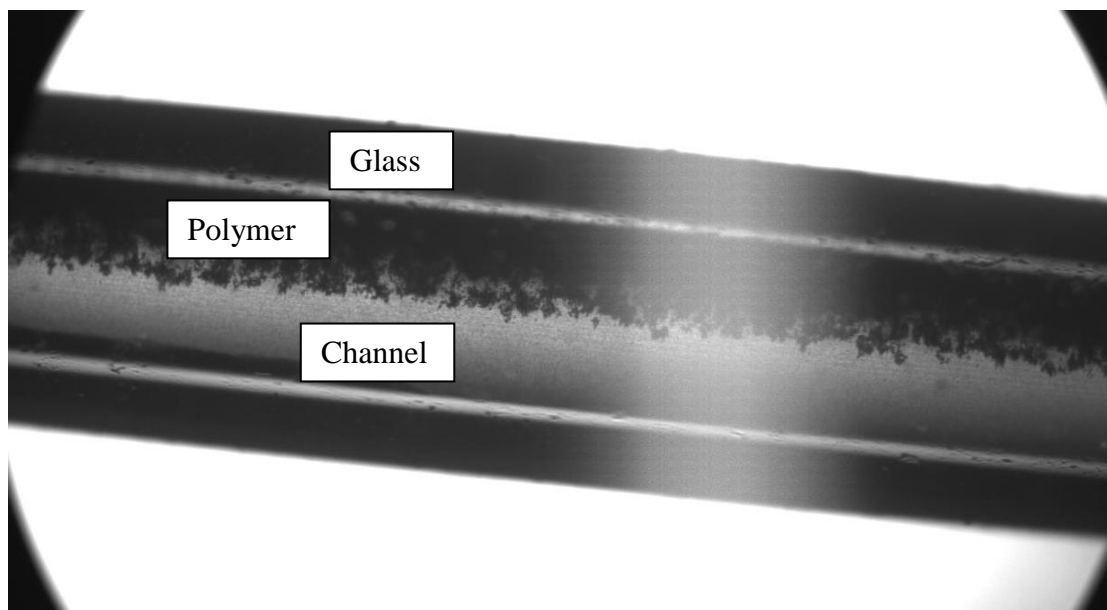
Characterisation and Functionalisation – Results and Discussion

Figure 2.2 An image obtained using the optical microscope of the side view of a 25 μL glass capillary (internal diameter of 0.3 μm) containing a monolith formed from *monolith 2.2* demonstrating a lack of rolling.

Attempts were made to rectify and create a capillary full of monolith that would allow liquid to flow through the monolith. Increasing the aliquot concentrations of the sol solution was considered by varying the amount of aliquot used of the concentrated monomers. Aliquots varied from 4.2, 8.4, 12.6, 16.8 and 21.0 μL . The results were an appearance of denser monolith formation but still the problem of a hollow bore or “half and half” formation occurred. Another variation in methodology to form a full monolith capillary was changing the resting position of the monolith from a horizontal base to a vertical stand. This resolved any “half and half” monolith formation however it also generated cracked and non-uniform monoliths (visually observed). Nevertheless, one monolith was formed successfully with no hollow bore or “half and half” formation.

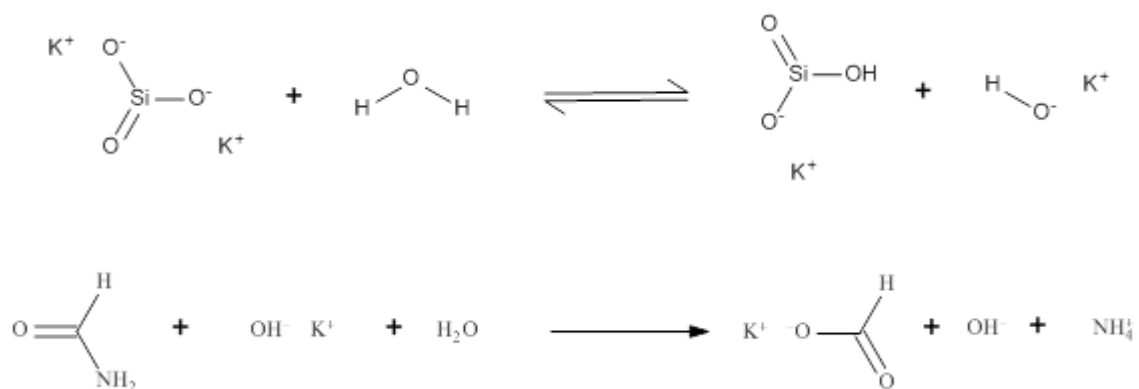
Characterisation and Functionalisation – Results and Discussion

This method of monolith preparation could not be repeated. The porosity of the one successful monolith was calculated from Equation 2.1 and found to be 0.71.

No surface area analysis (BET) or SEM analysis was performed on the monolith due to its lack of reproducibility.

2.16 Potassium silicate monolith

The monolith was formed based on the potassium silicate disassociation in water to produce potassium bisilicate and potassium hydroxide. The potassium hydroxide and water present from the potassium silicate solution hydrolysed the formamide into potassium formate and ammonium hydroxide (Reaction Scheme 2.2). This gradual change to ammonium hydroxide altered the pH from 11.8 to 10.8 resulting in condensation of the potassium bisilicate in the initial disassociation to polymerise with each other and form the silica backbone¹⁵¹.



Reaction Scheme 2.2 The reaction showing the hydrolysis of formamide in basic potassium silicate solution to produce ammonium hydroxide.

Analysis of the monolith formed from *monolith 2.3* was compared to the previous monolith formed from *monolith 2.2* using optical microscopy and porosity.

Characterisation and Functionalisation – Results and Discussion

Additionally due to its repeatable manufacture of this monolith BET surface area analysis and SEM imaging were used to characterise the monolithic surface.

Optical microscopy provided a recognised insight into the filling of the monolith within the glass capillary channels. The monoliths produced from *monolith 2.3* are shown in Figure 2.3 and Figure 2.4 confirming the complete seal of the monolith to the walls of the capillary. Not only can this comparison be seen as advantageous but the porosity of these types of monoliths was averaged at 0.79, a slightly higher porosity to that previously described.

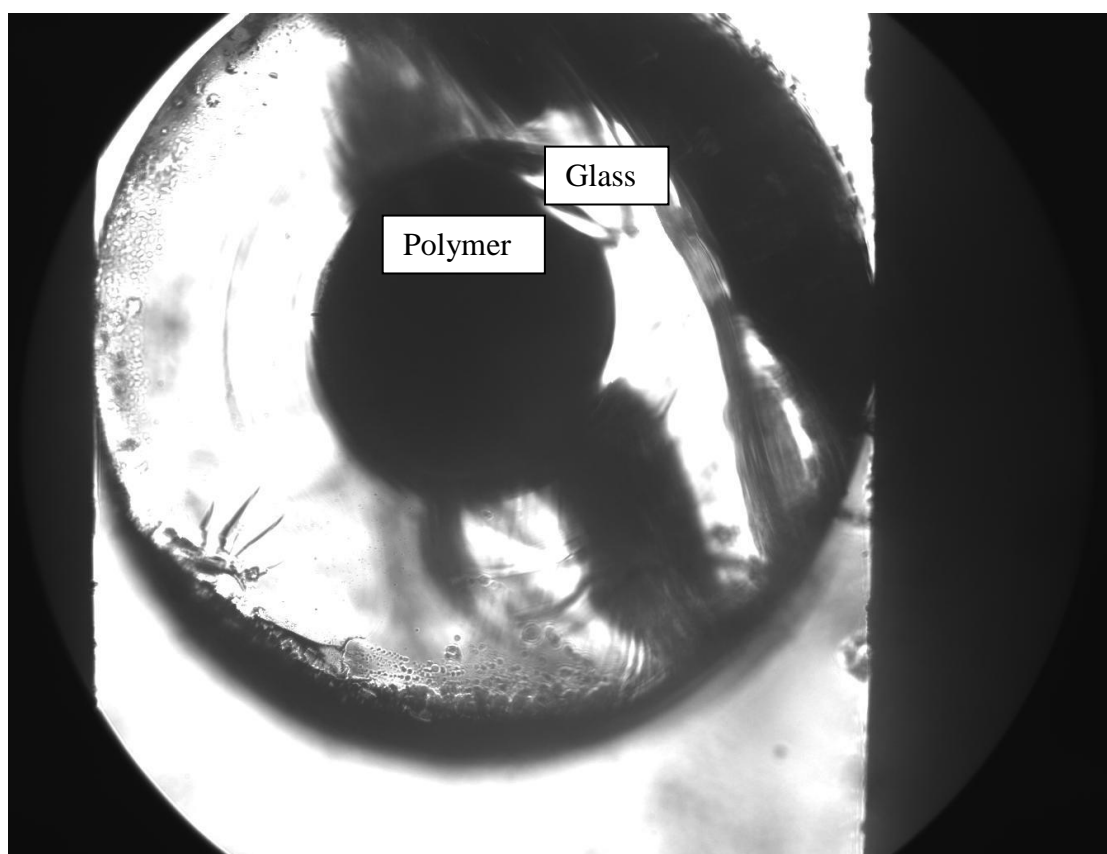


Figure 2.3 An image obtained using the optical microscope of the cross section of a 25 μL glass capillary (internal diameter of 0.3 μm) containing a monolith formed from *monolith 2.3*.

Characterisation and Functionalisation – Results and Discussion

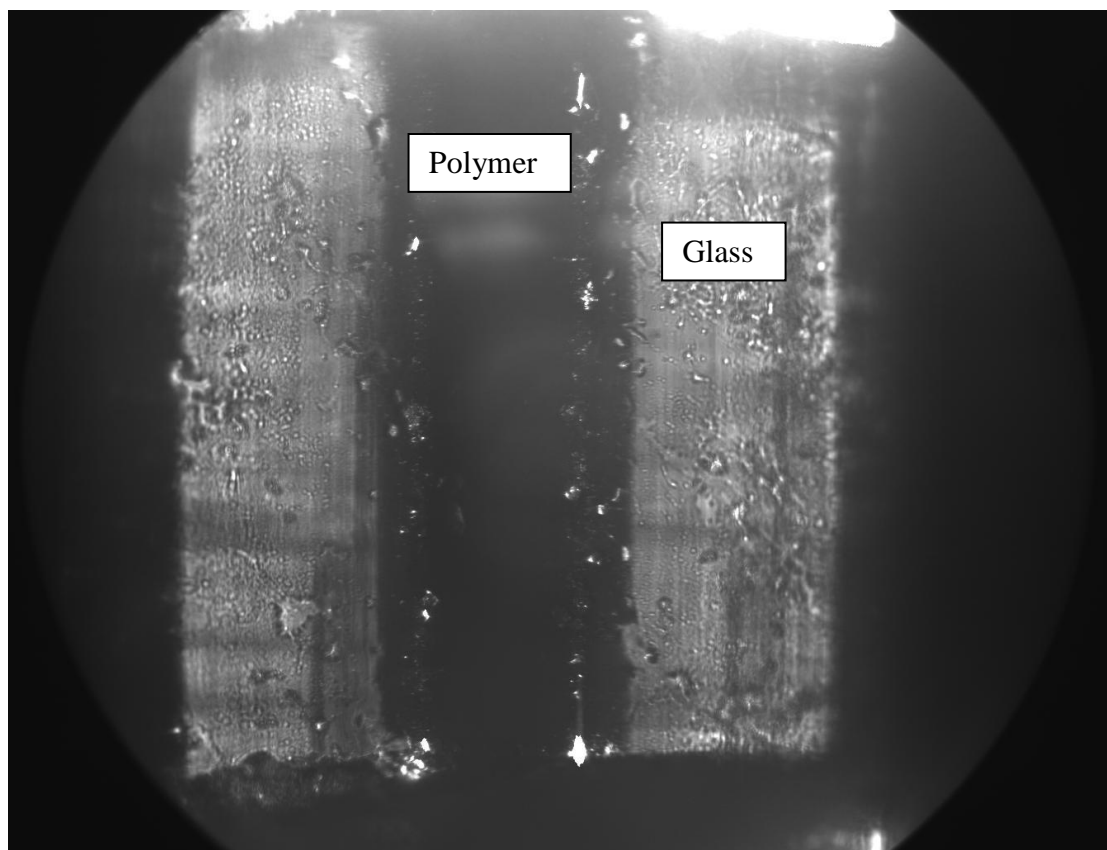


Figure 2.4 An image obtained using the optical microscope of the side view of a 25 μL glass capillary (internal diameter of 0.3 μm) containing a monolith formed from *monolith 2.3*.

Characterisation and Functionalisation – Results and Discussion

The monolith showed promise for use as an immobilising backbone for catalysis. SEM imaging of the monolith shows a jagged porous structure with fine bridging between bulk silica (Figure 2.5). The micro pore size can be observed to be between 2 - 3 μm in diameter. This size of micro pore would have still lead to high back pressures which was observed in the system during reactions. In theory the fewer the micro pores or the finer the size of the micro pores, the more liquid is forced to flow through a confined space, the greater the back pressure.

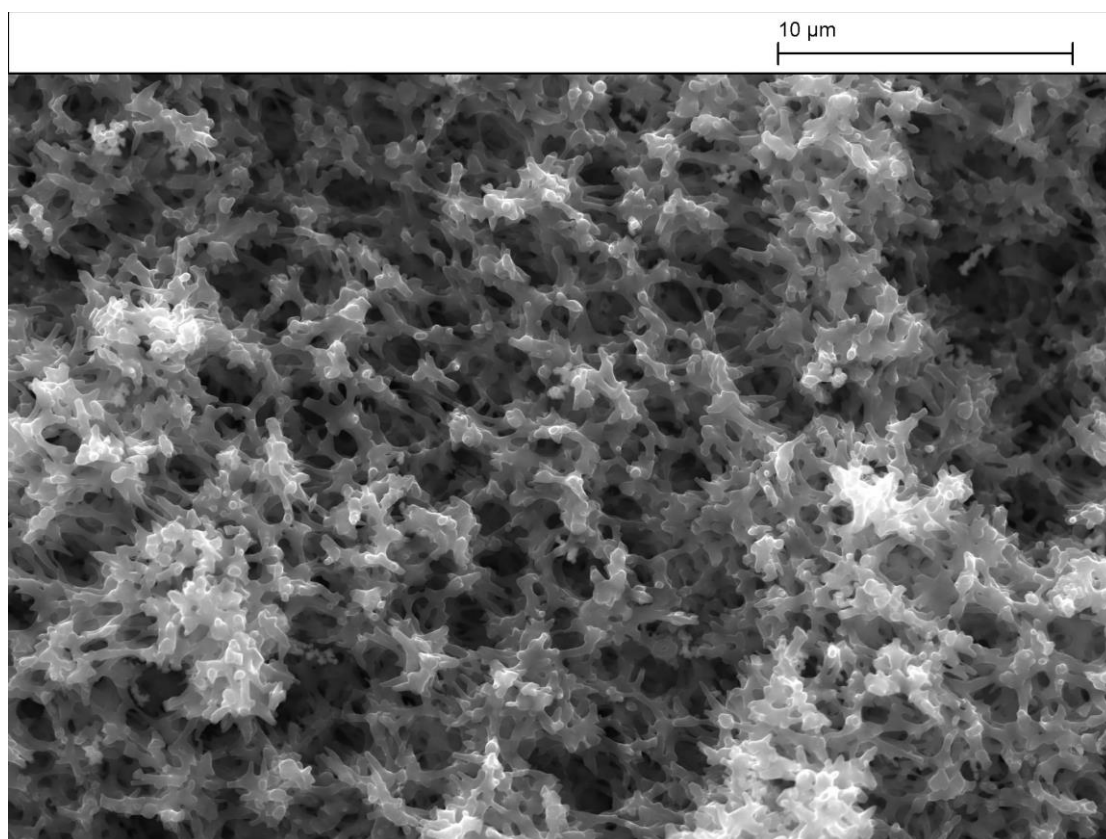


Figure 2.5 SEM imaging of a monolith produced by *monolith 2.3*.

Characterisation and Functionalisation – Results and Discussion

Further determination of the pore sizes of the monolith was obtained for the nano pore dimensions from BET surface area analysis. Figure 2.6 demonstrates that there is no definitive nano pore structure relating to these monoliths and the peaks observed toward the lower end of the scale are possibly due to nano cracks. The deficiency of nano pores ultimately suggests that anchoring of the catalyst onto these monoliths would be less favourable. Despite this lack of nano pore structure the surface area could be determined at $15 \text{ m}^2 \text{ g}^{-1}$. This surface area value is significantly lower than previous reports for other types of sol-gel monoliths¹⁵²⁻¹⁵⁵. This poor surface area from a lack of nano pore was not sufficient to support the functionalisation of the catalyst, therefore less suitable to provide large enough contact for organic synthesis.

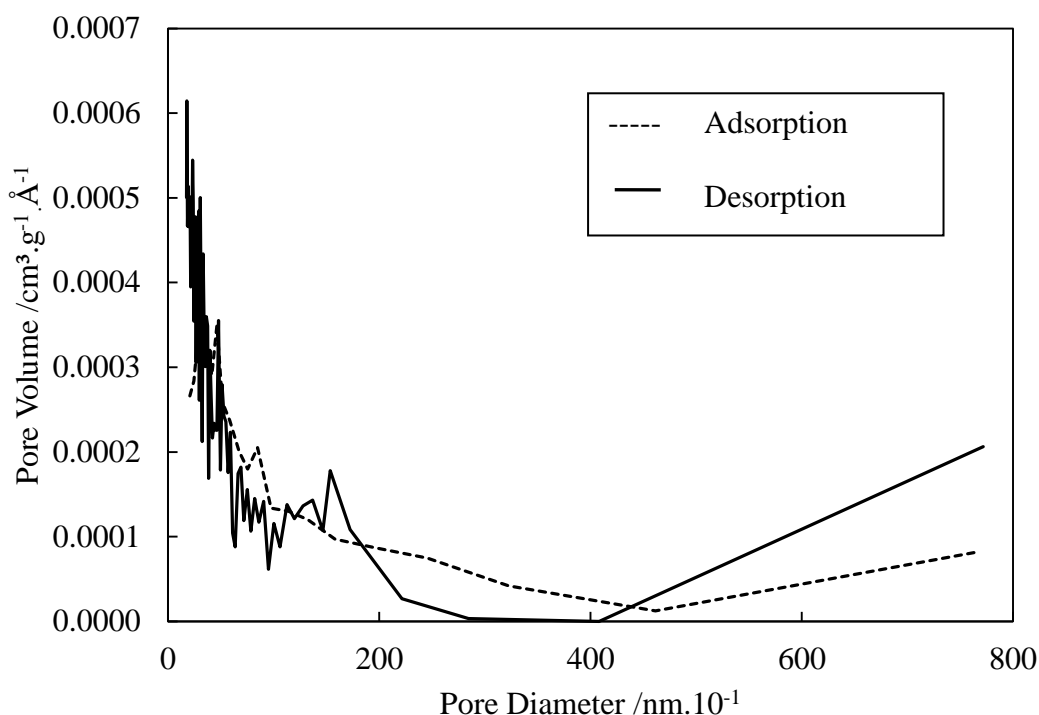


Figure 2.6 BET results for adsorption and desorption of nitrogen to find nano pore diameter of monoliths produced from *monolith 2.3*.

Characterisation and Functionalisation – Results and Discussion*2.17 Tetramethyl orthosilicate (TMOS) monolith*

The formation of the TMOS monoliths were similar to the TMOS and MTMOS monoliths in that an acid is used to hydrolyse the Si-O-Me groups present on the TMOS. However instead of a change in pH due to a buffer, the condensation reaction proceeded with an increase in temperature to initiate the polymerisation of the TMOS monomers. A weaker acid (acetic acid) could therefore be used to catalyse the polymerisation. The weaker acid resulted in a slower hydrolysis reaction and lead to the formation of a stable silica monolith. The presence of polymer F127 provided a hydrophilic and hydrophobic micelle type phase¹⁵⁶. It contains polyethylene oxide chains at both ends of the polymer (PEO, 100 monomers in length each) with a polypropylene oxide chain in the middle (PPO, 65 monomers in length). The PEO chains act more hydrophilically than the PPO chain creating a micelle structure in aqueous solution. With this present within solution, the polymer acts as a template (or porogen) for the monolith and the silica moulds around these micelles. The removal of polymer F127 by washing and heating causes voids within the monolith which produces micro pores.

The formation of a large surface area is however critical for a high catalyst loading. Improving the surface area with these monolith types was carried out using *Ostwald ripening*. The addition of ammonium hydroxide gently heated with the monolith caused a dissolution and reprecipitation process in which gentle etching of the monolith surface was occurring. This generated nano voids in the monolith surface called nano pores. These nano pores present throughout the silica monolith provided surface areas much higher than that achieve from the monolith produced from *monolith* 2.3.

Characterisation and Functionalisation – Results and Discussion

On formation of the monolith within glass capillaries, visual inspection under the microscope did not indicate the presence of hollow bore or “half and half” formation. In this case however unlike previous monoliths fabricated, the monolith was observed to be completely unbound to the glass capillary. So whilst a continuous monolith was produced an alternative method of placing the monolith into a flow system was going to be required. The unbound monoliths were configured for flow by using polytetrafluoroethylene (PTFE) heat shrink tubing. The porosity of this monolith was 0.73 which concurs with literature values¹⁵². From the same literature surface area of this monolith formation was approximately $200 \text{ m}^2 \text{ g}^{-1}$ with a nano pore size of 13.5 nm. Also SEM imaging concludes that the micro pore diameter was between 2 - 3 μm (Figure 2.7).

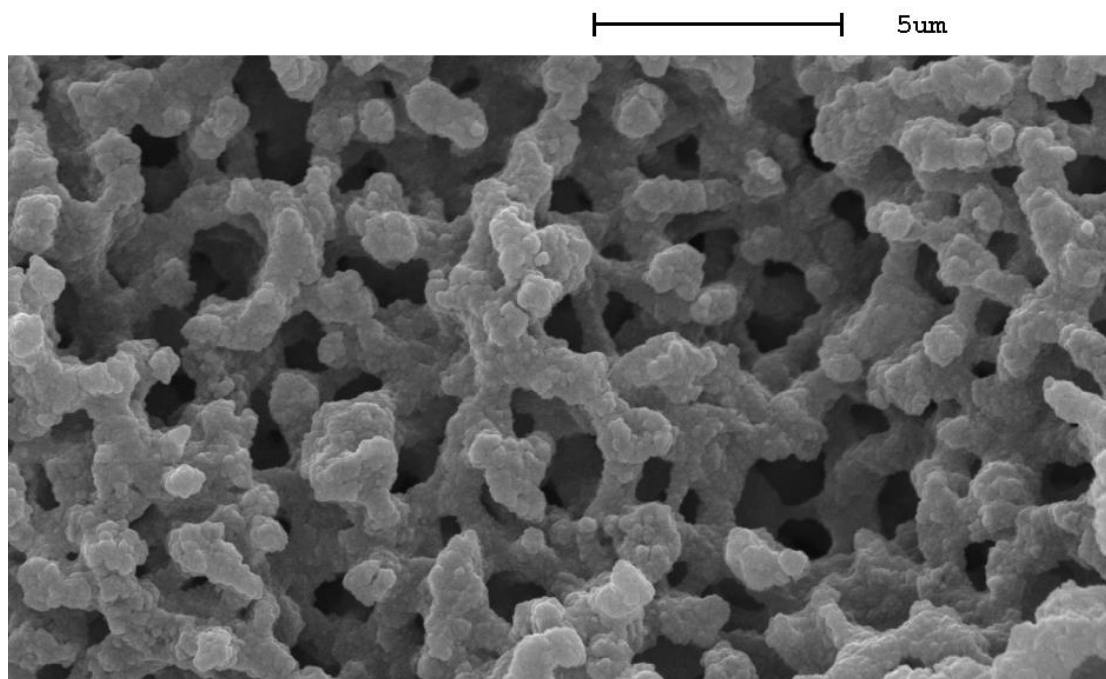


Figure 2.7 SEM imaging of a monolith produced by *monolith 2.4*¹⁵².

Characterisation and Functionalisation – Results and Discussion*2.18 Tetraethyl orthasilicate (TEOS) monolith*

The sol-gel process for generating the TEOS monolith was very similar to that used from *monolith 2.4*. However, even though the basic mechanism is the same for hydrolysis and condensation polymerisation, there are differences. The catalyst and porogen used for the silica formation were changed. Polyethylene oxide was used as a porogen and nitric acid as the catalyst. The reason why these were changed from polymer F127 and acetic acid is that the TEOS contains ethoxy functionality on the surface as opposed to methoxy. The increase in carbon chain in the TEOS had an inductive effect on the Si-O-C bonds. The spread of electron density over an extra hydrocarbon made the Si-O bond less prone to react. Hence the use of a stronger acid was required to protonate the oxygen present. The change in porogen was performed due to the solubility of TEOS being lower in aqueous phase of the synthesis. Not only did the porogen permit micro pore generation, it also permitted increased solubility of the monomer¹⁵⁷.

Imaging of the 2.5 monolith was possible through the SEM (Figure 2.8). Micro pore size from this image was observed to be between 4 - 20 μm in diameter. Porosity data of TEOS manufactured monoliths were in the range of 0.65 to 0.70. Nano pore size was estimated by BET analysis to be 11 nm in diameter (using average pore width from Figure 2.9). Surface area was determined to be $240 \text{ m}^2 \text{ g}^{-1}$.

Characterisation and Functionalisation – Results and Discussion

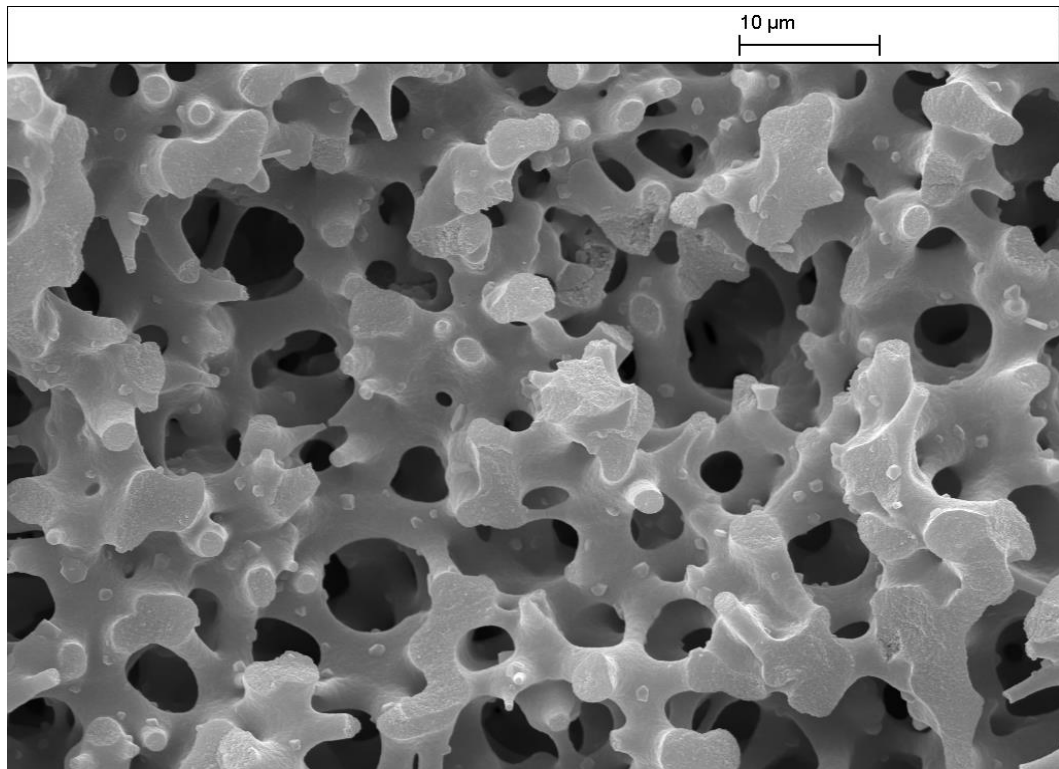


Figure 2.8 SEM imaging of a monolith produced by 2.5.

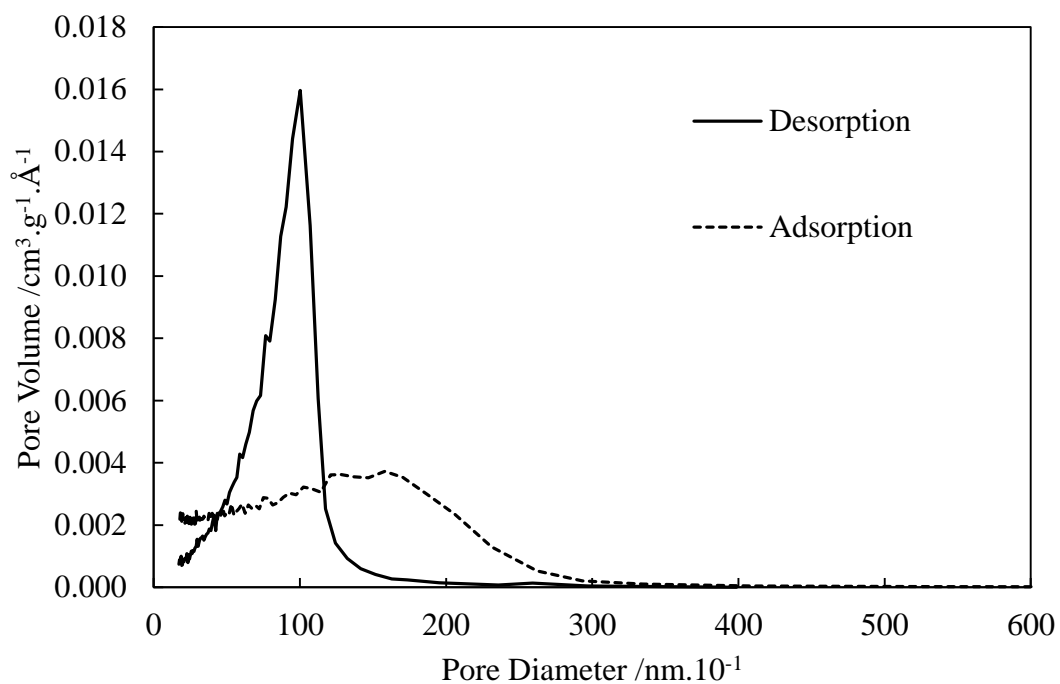
Characterisation and Functionalisation – Results and Discussion

Figure 2.9 BET results for adsorption and desorption of nitrogen to find nano pore diameter of monoliths produced from *monolith 2.5*.

Characterisation and Functionalisation – Results and Discussion*2.19 Varying Monolith size*

The 2.5 monolith was varied in size to generate higher volumes of catalytic monolith reactors (CMR) whilst retaining its micro and nano pore geometry. By producing a larger volume CMR, increased flow rates for reactions permitted the same reaction time but having an increase in productivity. There are basically two methodologies to increase the monolith volume; increasing the length or the width of the monolith which would allow a larger volume for the monolith contact. By varying either the length or the width had no consequence to the monolithic structure. Table 2.1 shows there is negligible difference between the monolith shrinking, surface area and nano pore diameter. Not only are the surface areas and the nano pore sizes reproducible at increasing monolith diameter sizes but the micro pore sizes and monolith structure are too (Figure 2.10). This lack of variation and trend from increasing monolith diameter size meant that increasing the amount of product produced per unit time was highly likely. Potentially the increase in diameter meant that the reactants would have a longer time to react with the catalyst and each other for the same void monolith volume of a longer CMR. The advantage of this for the reaction over the longer thinner CMRs would be that the flow reactants and products would occupy a compact space for the same volume, and therefore offer more applications fitting into smaller spaces.

Characterisation and Functionalisation – Results and Discussion

Monolith Mould Diameter /mm	Monolith diameter /mm	Monolith shrinking /%	Average surface area /m ² g ⁻¹	Average nano pore diameter /nm
4.8	3.4	28.87	249.56	1118.5
8.7	6.6	23.79	242.68	1084.7
12.1	9.0	25.37	227.33	1121.5
14.5	10.8	25.52	235.52	1108.0
19.1	14.5	24.20	247.91	1091.8

Table 2.1 BET surface area and pore size analysis of varying 2.5 monolith diameters formulated from the same sol-solution.

Characterisation and Functionalisation – Results and Discussion

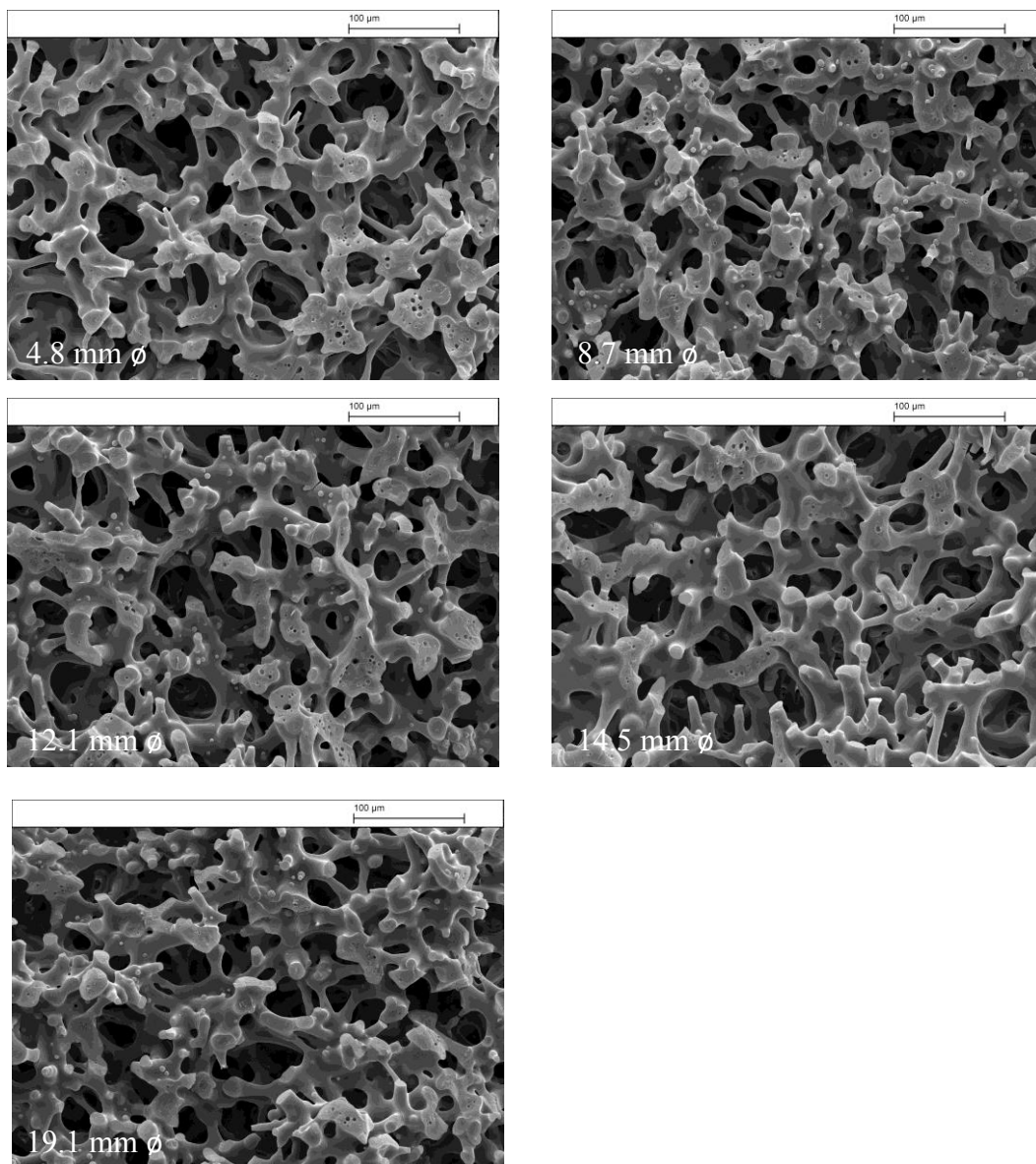


Figure 2.10 SEM imaging analysis of varying 2.5 monolith diameters formulated from the same sol-solution.

Characterisation and Functionalisation – Results and Discussion*2.20 Catalyst loading*

The palladium was immobilized on the surface of the silica through physical adsorption rather than ionic, covalent or co-ordination bonding. The methods of the palladium deposition were designed to produce nano particles of palladium (0) on the surface of the silica. Palladium coating was apparent on the monoliths as the colour changed from a white to black when wet.

The palladium deposition method from 2.11 was applied to a *monolith 2.2*. Palladium was reduced (observed from a brown to black colouration) by the hydrazine used. This was used later in flow synthesis and was observed to be unsuitable due to high leaching of palladium (See *Flow System design 3.18*).

The *palladium loading 2.12* method had more success. Palladium was loaded onto monoliths formed by *monolith 2.3*. Once formulated the monoliths appear dark grey/black when wet suggesting the palladium had been successfully converted from palladium(II) acetate to palladium(0). The catalyst was analysed by SEM and EDX imaging. SEM analysis (Figure 2.11) indicated that there was no definitive change in shape or structure of the monolith integrity at this microscopic level (by comparison to Figure 2.5). Energy Dispersive X-ray spectroscopy (EDX, INCA System 350, Oxford Instruments) imaging of Figure 2.11 showed clusters of a heavier element, palladium (Figure 2.12). This revealed that the method of palladium deposition may have only developed clusters of palladium for catalysis rather than total coverage. EDX spectroscopic area analysis of a non-cluster area however showed traces of palladium (Figure 2.13). The presence of palladium on a non-cluster area suggests total coverage

Characterisation and Functionalisation – Results and Discussion

of the monolith surface. The authors who describe such synthesis of the porous palladium layer suggest it is 6 μm thick with total coverage¹⁴⁹.

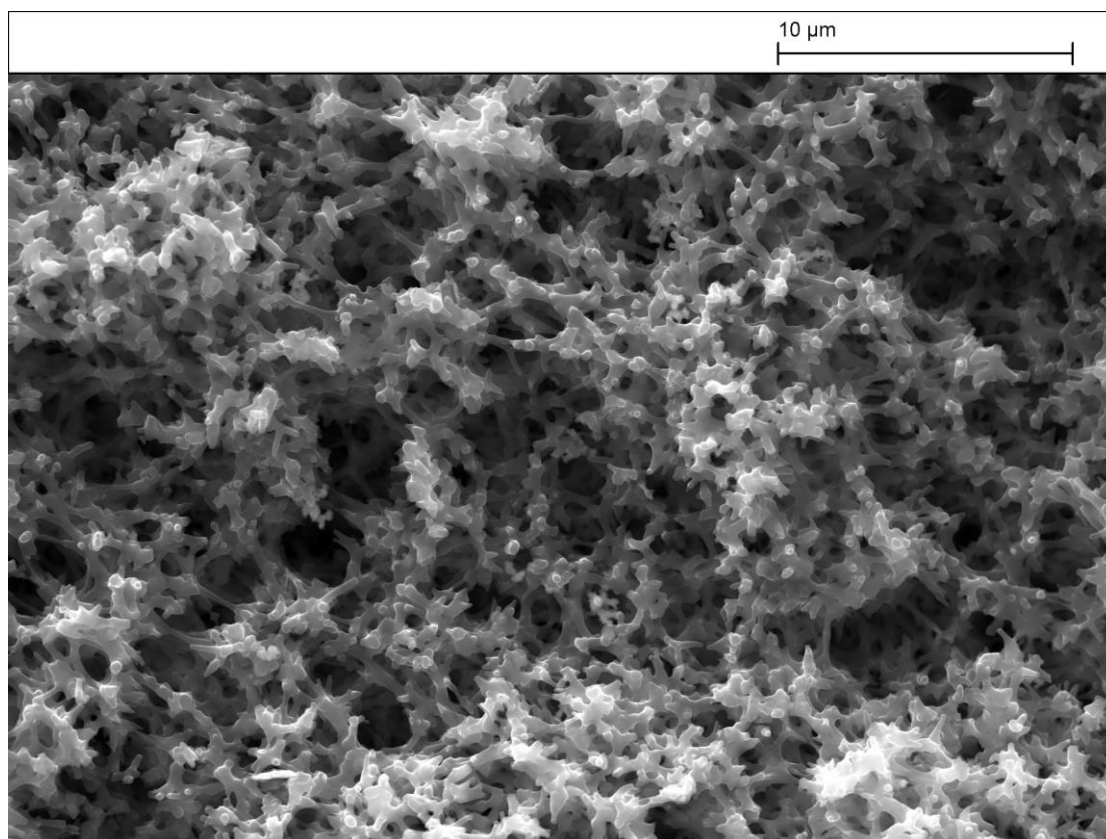


Figure 2.11 SEM imaging of a monolith generated using *monolith 2.3* and *palladium loading 2.12*.

Characterisation and Functionalisation – Results and Discussion

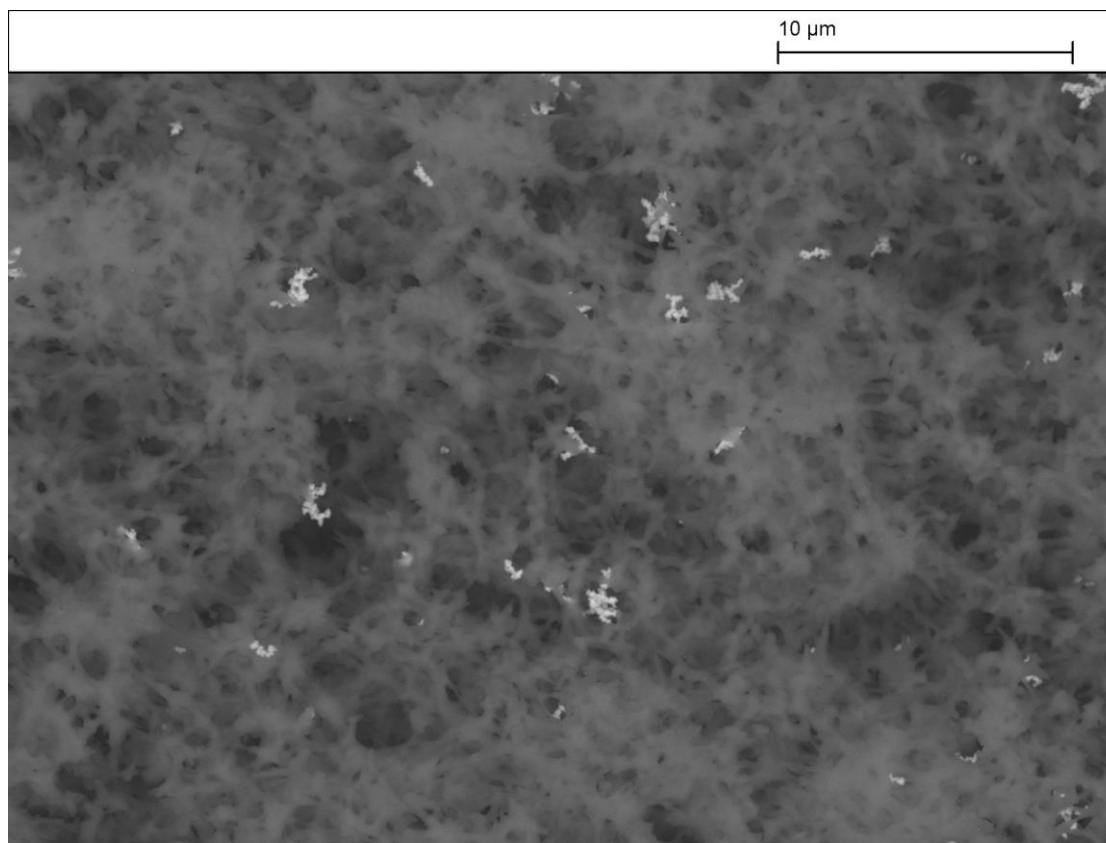


Figure 2.12 SEM-EDX imaging of a monolith generated using *monolith 2.3* and *palladium loading 2.12*. The palladium clusters are observed in white.

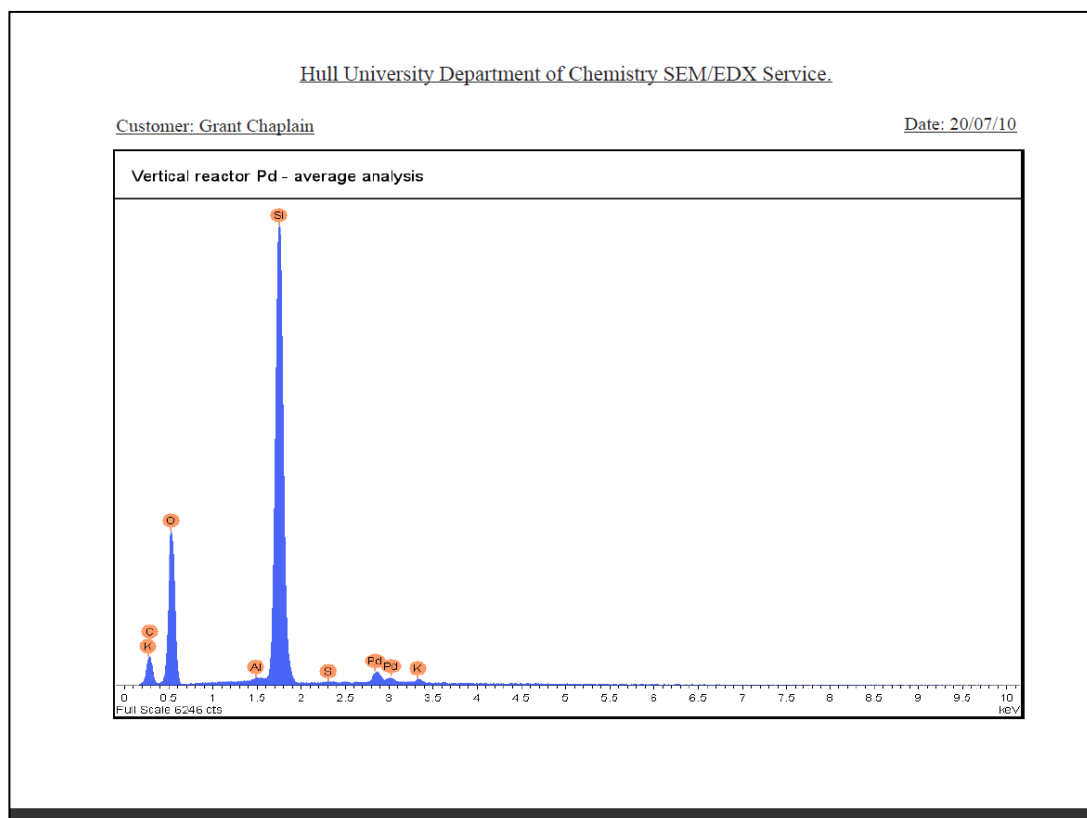
Characterisation and Functionalisation – Results and Discussion

Figure 2.13 EDX area analysis of a non-cluster surface of the monolith generated using *monolith 2.3* and *palladium loading 2.12*.

Characterisation and Functionalisation – Results and Discussion

Palladium immobilisation using *palladium loading 2.13* was assessed. Palladium was deposited onto the monoliths formed from *monolith 2.3*. Colour changes were observed however the colour density was varied throughout the monolith. This suggests an uneven distribution of palladium on the silica. The lack of uniform palladium meant this method of palladium deposition was discounted.

The most successful deposition of palladium was introduced using *palladium loading 2.14* onto monoliths from 2.5. These type of catalytic monoliths were described in literature as having good conversions and low palladium leaching¹⁰¹. Once again, the monoliths changed colour (Figure 2.14). Unlike the other catalytic monoliths produced, these Na₂PdCl₄-TEOS monolithic reactors were uniform with high surface areas. Nano pore presence had already been observed (Figure 2.9) but the palladium can also be observed in the nano pores from TEM (transmission electron microscopy, Figure 2.15). With a size of approximately 10 nm, the palladium clusters bares a very similar resemblance to the nano pore size of the monoliths.

Characterisation and Functionalisation – Results and Discussion

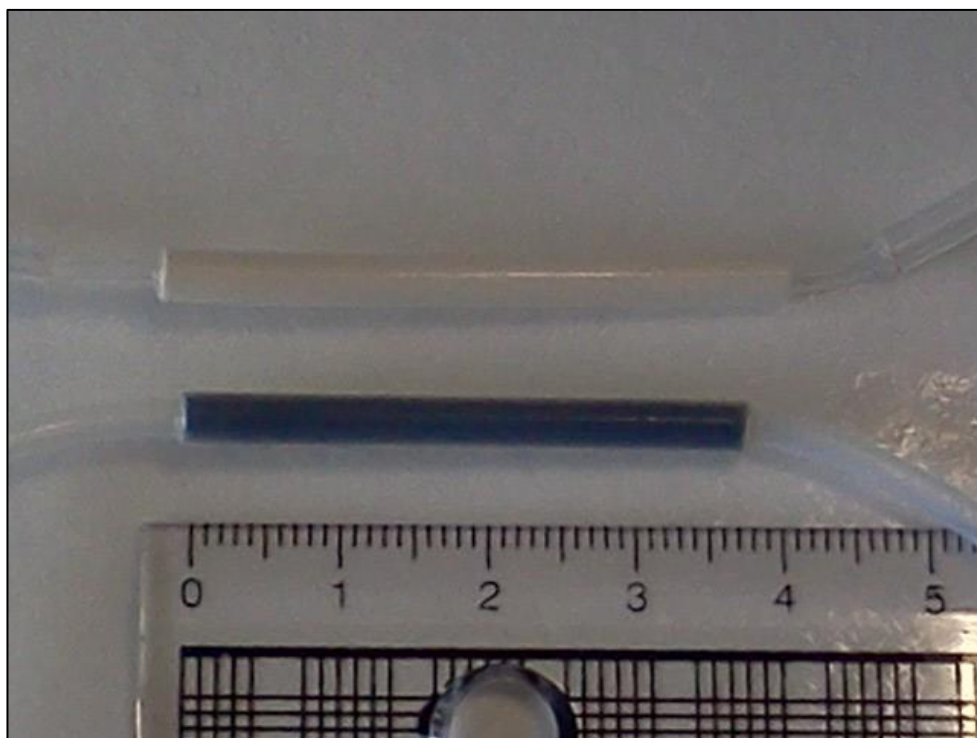


Figure 2.14 Photograph demonstrating the colour difference between a monolith with palladium (black) and without palladium (white/cream).

Characterisation and Functionalisation – Results and Discussion

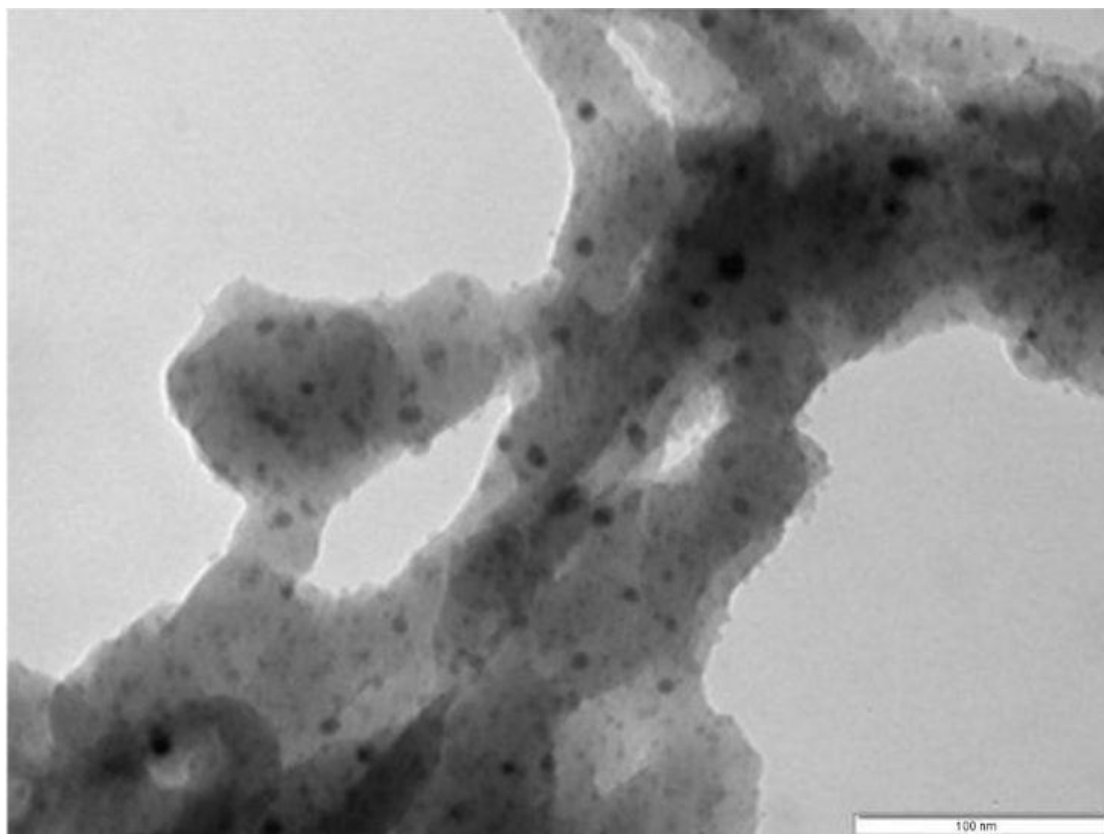


Figure 2.15 TEM imaging of a monolith formed by similar methods to *monolith 2.5* with *palladium loading 2.14*¹⁰¹. Palladium clusters are observed as dark black spots.

Characterisation and Functionalisation – Results and Discussion*2.21 Summary*

Each method produced a silica monolithic structure. The final monolith used for flow reaction evaluation was the monoliths formed according to the information in *monolith 2.5*. The method for immobilising palladium onto the monolith is given in *palladium loading 2.14*. The monoliths produced from *monolith 2.2* were irreparable and could not be investigated further. Nano pore structure of the monoliths produced from *monolith 2.3* was not seen, although the micro pore size would have permitted sufficient flow with little back pressure, the anchoring of the catalyst and the exposed residence time for a reaction would have been insufficient. Despite *monolith 2.3* monoliths having a low surface area, they were easy to reproduce. The sol-gel methods of monolith manufacture were better suited to the requirements of the CMR. Monoliths produced from *2.4* demonstrated potential during characterisation, however the monoliths produced from *2.5* demonstrated even better properties, such as high surface areas, high porosity and nano pore generation. These properties were also observed not to change as the diameter was changed leading to the prospect of increasing product output through volume of scaling up.

Palladium immobilisation from *palladium loading 2.14* had a distinct advantage over the other four methods tested. The method described in *palladium loading 2.11* had a significant disadvantage to do with mass leaching of palladium, this would prove damaging to the flow system (see *Flow System design 3.18*). Method *palladium loading 2.13* had inconsistent palladium(0) through the cross section of the monolith; the uneven distribution was not acceptable for a CMR. The palladium deposition from *palladium loading 2.12* showed promise for immobilisation but was improved by the *palladium*

Characterisation and Functionalisation – Results and Discussion

loading 2.14 method that demonstrated complete coverage, a higher palladium loading and palladium nano clusters within the monolith nano pores.

The monolith generation, characterisation and functionalisation, showed a monolith and immobilisation method that corresponded to the requirements of the CMR. The methods were from monoliths from 2.5 and palladium immobilisation from *palladium loading 2.14*.

and Heating - Experimental

3.0 Monolithic flow, CMR design and heating

Flow reaction technology has distinct advantages that have high potential in an industrial setting. When implemented, flow synthesis can act like a conveyer belt for production producing a high amount of product without pause (as would be for batch synthesis). Its main advantage is using surface area affects enhance synthetic chemistry through physical and chemical interaction. This was the reason for the production of CMRs.

Reactions require heat to occur. This could be performed by a range of methods, however only two methods were considered. Microwave heating is a method that penetrates a reaction liquid and heats from the inside out. The advantage of this with flow synthesis is that by varying the microwave power, a very fast change in temperature can be observed that's capable of controlling a reaction temperature quickly. This would make optimisation and library construction swift and simple. A second method of heating was column heating, heating from the outside in and allowed controlled equivalent heating throughout the reactions. This method is slow by comparison to the microwave heating and more likely to produce reaction by-products as microwaves can reach higher temperature faster that could promote wanted product formation.

The construction of the CMR was incorporated into 6 different flow systems each with its own advantages and disadvantages which then proceeded to a modification on the previous flow method. Adapting these flow methods in conjunction with the CMRs and microwave/column heating showed great potential in assembling a viable flow system for the Suzuki reaction between 4-bromobenzonitrile and phenyl boronic

and Heating - Experimental

acid. The ideal flow system would contain continuous flow, a stable CMR, resistance to fracture by pressure and external heating, and a fully integrated detection system.

Experimental

3.1 Flow regime design

The flow design for the reaction system included a number of parameters to accommodate continuous liquid flow, the presence of a heterogeneous catalyst and a localised heating mechanism. As the flow regime developed more components were placed in the flow system including back pressure valves, glass capillary connectors, column heating and a Raman flow cell. The final flow set-up is shown in Figure 3.1.

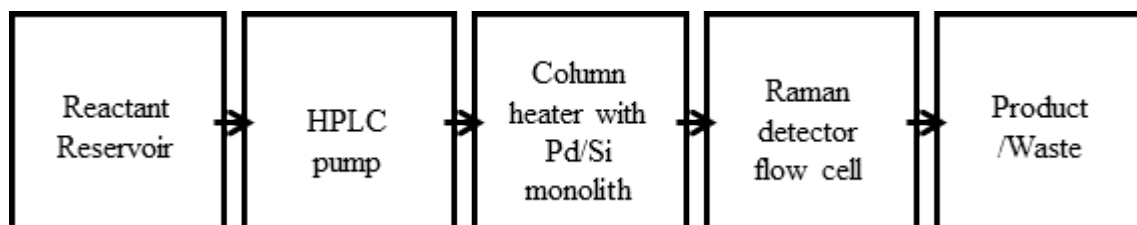


Figure 3.1 Final flow schematic design from *flow design 3.7*.

3.2 Flow system design A

A syringe pump (KDScientific) pumped N-methylformamide (NMF, 99% Sigma Aldrich) through 1/16 PEEK tubing into an injection loop (6 valves Rheodyne) of 44.5, 65.8 or 2144.3 μL . The 4-bromobenzonitrile (99% Sigma Aldrich), phenyl boronic acid (95% Sigma Aldrich) and potassium carbonate (99% Sigma Aldrich) in 66.7% aqueous DMF (99% Sigma Aldrich) or NMF carrier solvent entered under the

and Heating - Experimental

microwave cavity (Discovery CEM) into the vertically standing CMR connected in flow. The plug of reactants passed out the top of the microwave cavity for sampling product or waste collection (Figure 3.2).

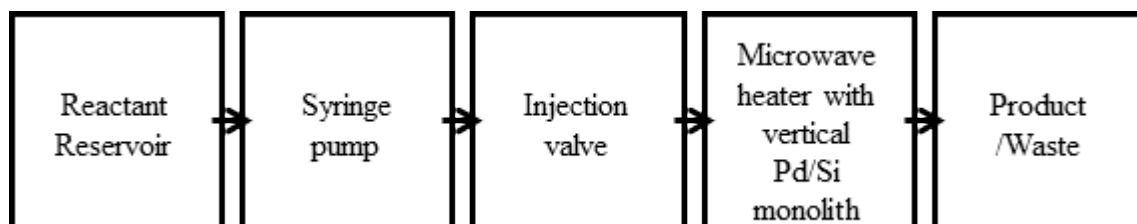


Figure 3.2 Flow schematic design from *flow design 3.2*.

3.3 Flow system design B

A syringe pump (KDScientific) pumped a homogeneous mixture of 4-bromobenzonitrile (99% Sigma Aldrich), phenyl boronic acid (95% Sigma Aldrich) and potassium carbonate (99% Sigma Aldrich) in 66.7% aqueous DMF (99% Sigma Aldrich) through the 1/16 PEEK tubing. This would enter under the microwave cavity (Discovery CEM) into the vertically standing CMR connected in flow. The reactants passed out the cap of the microwave cavity for sampling or waste collection (Figure 3.3).

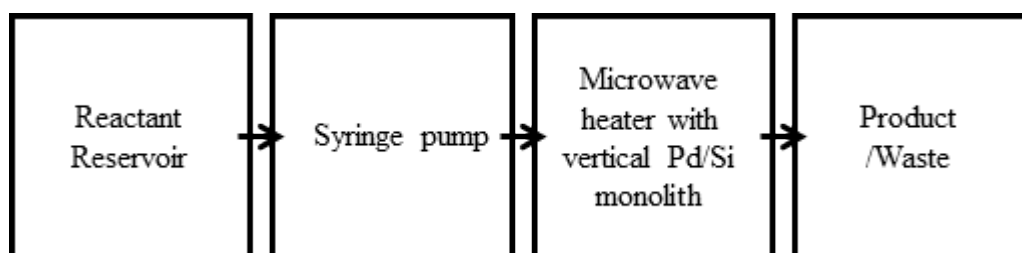


Figure 3.3 Flow schematic design from *flow design 3.3*.

and Heating - Experimental*3.4 Flow system design C*

A HPLC pump (Pu-1580 Jasco) pumped a homogeneous mixture of 4-bromobenzonitrile (99% Sigma Aldrich), phenyl boronic acid (95% Sigma Aldrich) and potassium carbonate (99% Sigma Aldrich) in 66.7% aqueous DMF (99% Sigma Aldrich) through the 1/16 PEEK tubing. This would enter under the microwave cavity (Discovery CEM) into the horizontal standing CMR connected in flow. The reactants passed out the base of the microwave cavity for sampling or waste collection (Figure 3.4).

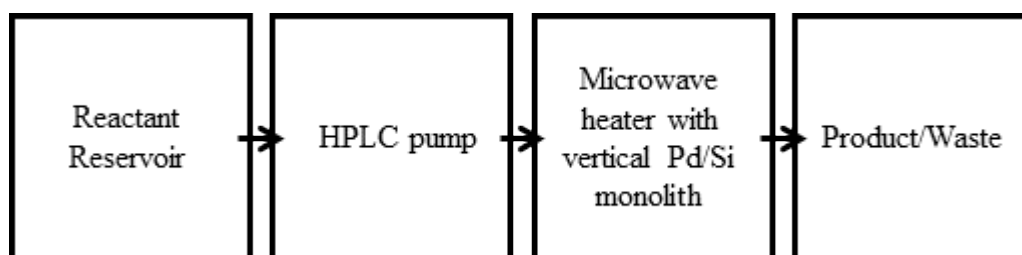


Figure 3.4 Flow schematic design from *flow design 3.4*.

3.5 Flow system design D

A HPLC pump (Pu-1580 Jasco) delivered a homogeneous mixture of 4-bromobenzonitrile (99% Sigma Aldrich), phenyl boronic acid (95% Sigma Aldrich) and potassium carbonate (99% Sigma Aldrich) in 66.7% aqueous DMF (99% Sigma Aldrich) through the 1/16 PEEK tubing. This entered under the microwave cavity (Discovery CEM) into the horizontal standing CMR connected in flow. The reactants passed out the base of the microwave cavity through a 275.79 kPa back pressure valve (UpChurch Scientific) for sampling or waste collection (Figure 3.5).

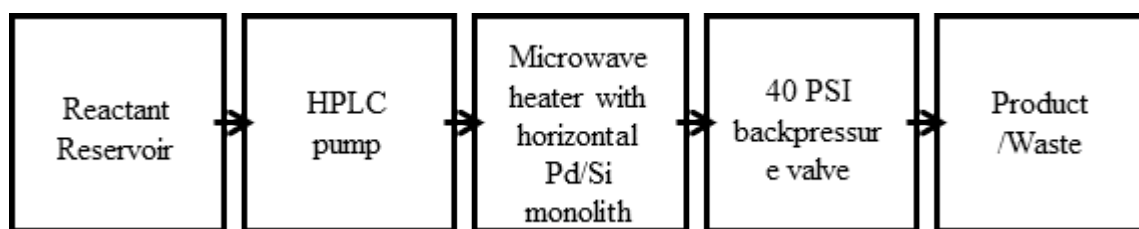
and Heating - Experimental

Figure 3.5 Flow schematic design from *flow design 3.5*.

3.6 Flow system design E

A HPLC pump (Pu-1580 Jasco) delivered a homogeneous mixture of 4-bromobenzonitrile (99% Sigma Aldrich), phenyl boronic acid (95% Sigma Aldrich) and potassium carbonate (99% Sigma Aldrich) in 66.7% aqueous DMF (99% Sigma Aldrich) through the 1/16 PEEK tubing. This would enter under the microwave cavity (Discovery CEM) into the horizontal standing CMR connected in flow. The reactants passed out the base of the microwave cavity through a 275.79 kPa back pressure valve (UpChurch Scientific). The flow passed through the Raman flow cell fitted with a Raman probe (RIP-RPB-785-SS Ocean Optics), laser (785 nm at 350 mV Ocean Optics) and spectrometer (QE65000 Ocean Optics). The final stage of the flow regime was sampling or waste (Figure 3.6).

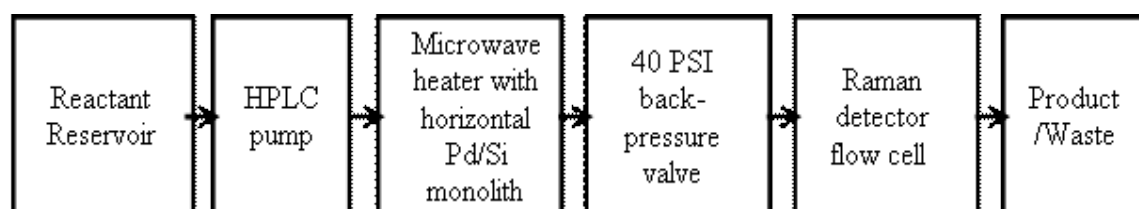


Figure 3.6 Flow schematic design from *flow design 3.6*.

and Heating - Experimental*3.7 Flow system design F*

A HPLC pump (Pu-1580 Jasco) delivered a homogeneous mixture of 4-bromobenzonitrile (99% Sigma Aldrich), phenyl boronic acid (95% Sigma Aldrich) and potassium carbonate (99% Sigma Aldrich) in 66.7% aqueous DMF (99% Sigma Aldrich) through the 1/16 PEEK tubing. This entered the column heater (Column Block Heater Jones Chromatography) which was pre-set to temperature. From the column heater, the flow passed through the Raman flow cell fitted with a Raman probe (RIP-RPB-785-SS Ocean Optics), laser (785 nm at 350 mV Ocean Optics) and spectrometer (QE65000 Ocean Optics). The final stage of the flow regime was sampling or waste (see Figure 3.1).

3.8 Flow reactor design

The flow reactor incorporated a palladium catalyst impregnated onto the silica monolith either anchored to the flow system by glass capillaries or by PTFE heat shrink tubing.

3.9 Flow reactor design I

The CMR was suspended in the flow system by anchoring to glass. Monoliths produced from *monolith 2.3* were bound to the surface of the 25 μ L glass capillaries (612-1405 VWR) by bonding to silinol groups present on the capillary surface (Figure 3.7). After palladium preparation the glass capillaries fitted to 1/16 ferrules and into the corresponding PEEK connectors.

and Heating - Experimental

Figure 3.7 A 25 μL glass capillary containing a monolith coated in palladium from methods *monolith 2.3* and *palladium loading 2.12*.

3.10 Flow reactor design 2

The CMR generated from *monolith 2.3*, *monolith 2.4* and *monolith 2.5* were locked in PTFE heat shrink tubing (Adtech). The tubing was shrunk around glass connectors at both ends of the CMR to incorporate the monolith in flow. The glass connectors and CMR were heated to 340 °C for 15 minutes to facilitate shrinking of the tubing (Figure 2.14). Other longer monoliths developed required the use of a heat gun due to their inability to fit into the furnace.

3.11 Microwave chamber mapping

The microwave (Discovery CEM) was thermally “mapped” vertically and horizontally. Initial testing involved cutting a glass TLC plate saturated in cobalt chloride (97% Sigma Aldrich) solution to the diameter and height of the microwave cavity. The plate was moistened without loss of any cobalt chloride and placed vertically in the microwave cavity. The plate was then heated at 100 W for 10 seconds. This was repeated with the plate moistened and heated at 100 W for 5 seconds.

and Heating - Experimental

Temperature testing was then performed by placing an IR fibre optic temperature probe (Picosens OpSens) into a 1/8 PTFE tube (15 mm in length with an ID of 2.4 mm) filled with water and sealed with PTFE tape. This was lowered from the centre of the cavity from the top at regular intervals. The probe was then heated for 60 seconds at 300 W and temperature differences recorded.

3.12 GC-MS analysis of flow regimes

GCMS (Perkin Elmer Gas Chromatograph and GCMS, Varian Saturn 2000) analysis was performed to evaluate the progress of the reaction. The products of the reaction were sampled at the end of the flow and subject to liquid-liquid extraction in DCM (99.8% Sigma Aldrich). The contents were washed with 1 mL of 1 M sodium hydroxide (≥ 98 Sigma Aldrich) and washed with 10 mL of water 3 times. Magnesium sulphate (ReagentPlus $\geq 99.5\%$ Sigma Aldrich) was used to dry the analyte solution. The GCMS conditions were an injector temperature of 230 °C with a 1:20 split injection, a carrier gas of nitrogen (Energas) at 1 mL min⁻¹. Oven temperature was 100 °C for 2 minutes and ramped by 20 °C min⁻¹ to 270 °C with a hold time of 9.5 minutes. Column used for the separation was a Phenomenex Zebron ZB-5 capillary column 30 m in length and an ID of 0.25 mm.

and Heating – Results and DiscussionResults*3.13 Flow regime design*

The various designs for the flow system were modified in in order to accommodate reactions and reaction mixture flow testing. Before any flow assumptions were made calibrations were performed on the flow instrumentation. These calibrations include the pumps used, microwave wattage, IR temperature probe and column heater temperature.

3.14 Pump flow rate calibrations

The syringe pump was calibrated by pumping water at room temperature for 5 minutes and collecting the eluent. This eluent was weighed, over a range of 0.005, 0.020, 0.050, 0.100 and 0.200 mL min⁻¹. The weight of water obtained was used to predict the observed flow rate. These were correlated and a calibration graph formed for the syringe pump flow rate (Figure 3.8). It was concluded that the syringe pump value given on the instrument was correctly labelled to the flow rate observed. However the HPLC pump did suggest a problem with calibration. The weight of water was recorded at room temperature every 30 seconds for 2.5 minutes and the average flow rate for the 30 seconds was recorded. The HPLC pump calibration was linear, however had some discrepancies. The flow rate values observed were different to the values set on the HPLC pump screen (Figure 3.9). This is thought to be due to the fact that during cleaning of the instrument one of the steel tubes was replaced with a longer piece of steel tubing. This made the total volume of the tubing in the pump larger and the pump

and Heating – Results and Discussion

would pump less liquid for the same apparent flow rate. Also the change in variation of the flow rates between Figure 3.8 and Figure 3.9 was noted. This increase in variation was explained by the smaller volumes/weights recorded for the water in Figure 3.9 meaning that there is more significance in noise and error effects.

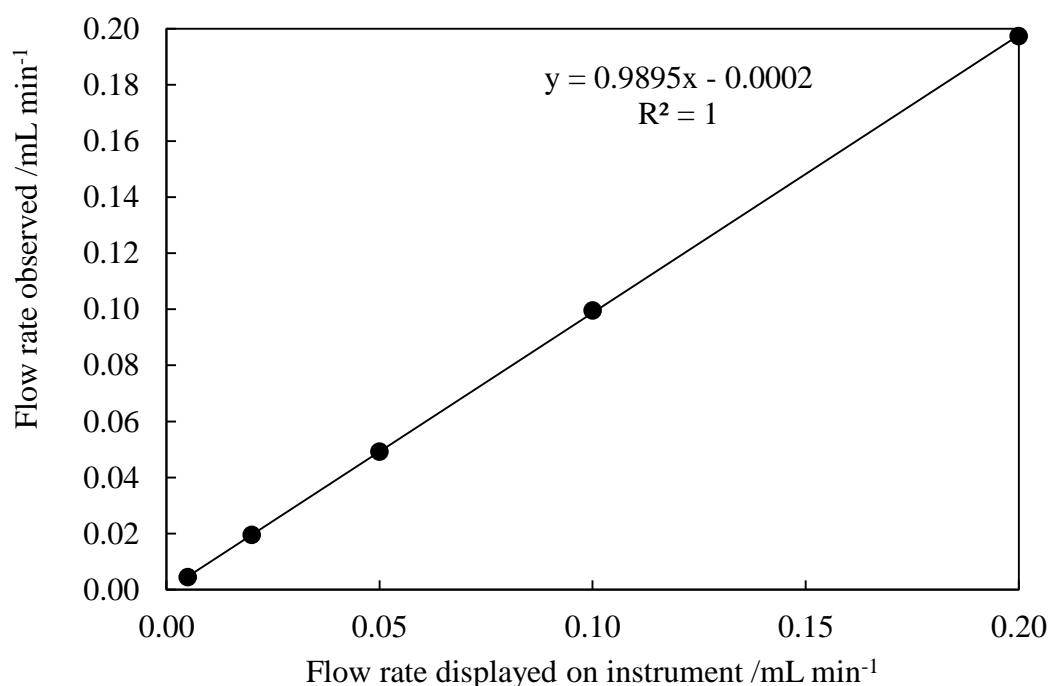


Figure 3.8 Calibration graph of the syringe pump used for the flow regime. Weights of water pumped were measured after 5 minutes at room temperature. Flow rates used were 0.005, 0.020, 0.050, 0.100 and 0.200 mL min⁻¹.

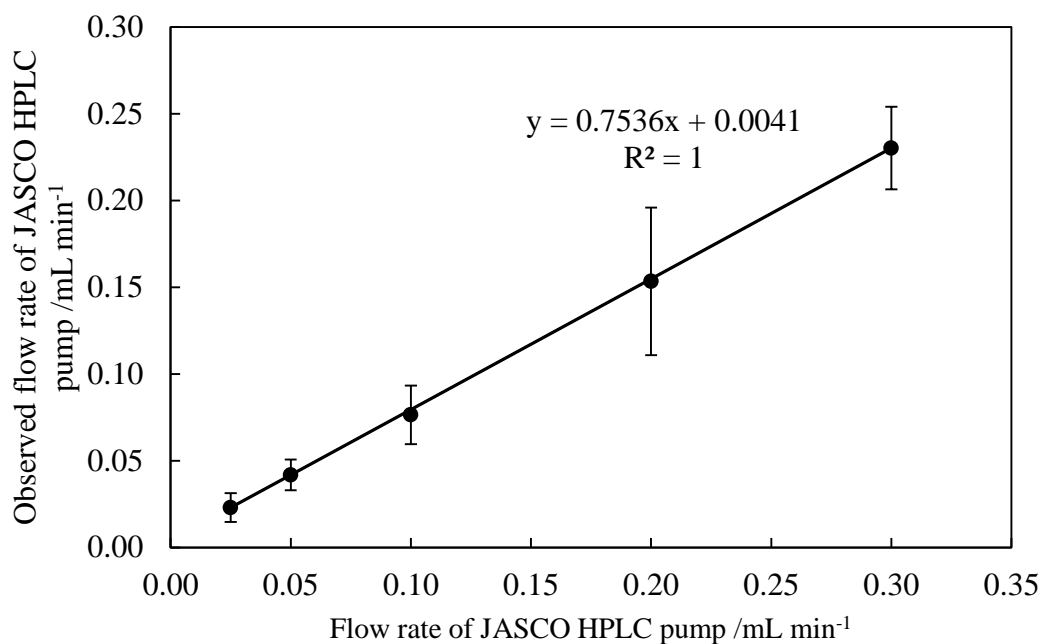
and Heating – Results and Discussion

Figure 3.9 Calibration graph of the HPLC pump used for the flow system. Weight of water was recorded at room temperature every 30 seconds for 2.5 minutes. Flow rates used were 0.025, 0.050, 0.100, 0.200 and 0.300 mL min⁻¹.

and Heating – Results and Discussion*3.15 Microwave wattage calibration*

The microwave wattage was determined by setting the instrument to maximum power (300 W) and monitoring the temperature increase of 100 mL water in a round bottom flask placed in the microwave cavity for 1 minute. The resulting temperature was measured and compared to the temperature before heating. The temperatures were applied to an equation provided by CEM to give the maximum power outage (Equation 3.1). The maximum power output was set to 300 W.

$$\text{Actual microwave output} = 6.97 \left(\frac{\text{Temperature before heating}}{\text{Temperature after heating}} \right) \quad \text{Equation 3.1}$$

The actual microwave output equation for the CEM microwave Discovery¹⁵⁸.

3.16 IR fibre optic temperature probe calibration

The IR fibre optic temperature probe was calibrated by measuring a range of temperatures of water between 20 and 70 °C and comparing this value to a mercury thermometer (Figure 3.10). The linearity of the calibration with little variance demonstrated a positive correlation and a good calibration. The advantage of using this type of probe was that it adsorbs little microwave energy when in the chamber and was contactless.

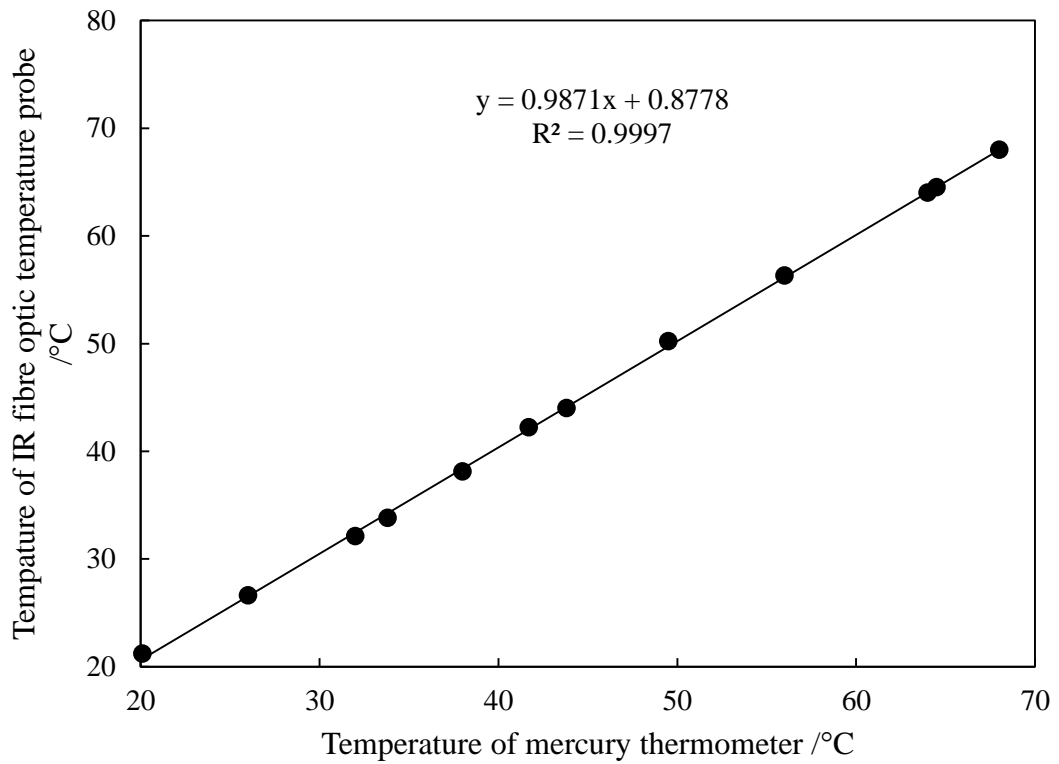
and Heating – Results and Discussion

Figure 3.10 Calibration of the IR fibre optic probe with a mercury thermometer. Water was used as a testing medium with temperatures between 20 and 70 °C.

and Heating – Results and Discussion*3.17 Column heater temperature calibration*

The column heater (Column Block Heater Jones Chromatography) was calibrated using the IR fibre optic temperature probe. Temperatures between 50 and 90 °C were used. The temperatures were left for 10 minutes to stabilise before the temperature was recorded. The column heater setting demonstrated high linearity in temperature in conjunction with the temperature probe. A maximum difference of 1 °C was observed between the temperature probe and the column heater for one reading. All other readings were less than 1 °C difference. The calibration is shown in Figure 3.11. During reactions involving the column heater, the value viewed on the instrument was assumed to be the temperature of the reaction.

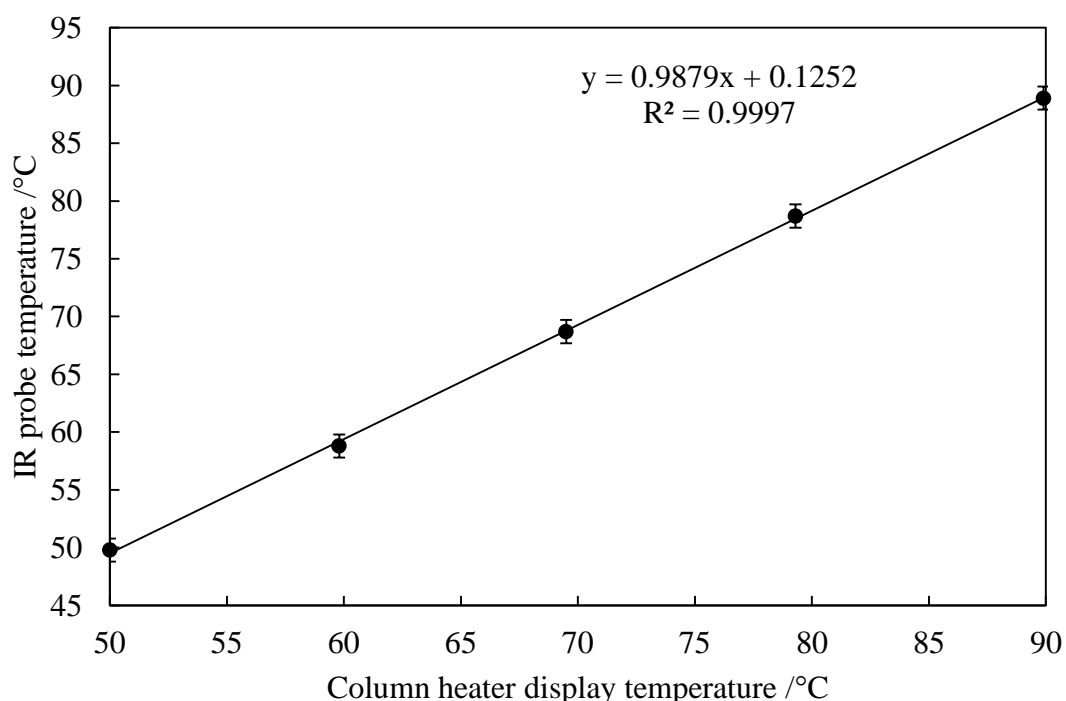


Figure 3.11 Calibration of the column heater display temperature with the observed column heater temperature recorded with the IR fibre optic temperature probe.

and Heating – Results and Discussion*3.18 Flow system design*

The initial design for the flow system was to take an approach similar to a HPLC apparatus set-up (*flow design 3.2*). However due to the low volumes of the monolithic catalyst very low flow rates were required (CMR volumes below 25 μL). Most HPLC pumps could not reliably deliver the values required for the flow reaction system. Syringe pumps therefore offered a possible alternative. Also incorporated into its design was an injection loop.

The idea of an injection loop gave the option of automating an injection of reagents into the flow system to provide a plug of reaction solution. One of the promising possibilities of this was providing a library of compounds produced by this one system. The injection loop sizes of 44.5, 65.8 or 2144.3 μL were used for the flow system. The two smaller injection loops of 44.5 and 65.8 μL were thought to be insufficient in providing enough material for the reaction. Nevertheless dispersive (or dilution) effects in the carrier solvent (NMF) meant that the reaction was less likely to take place. To resolve this, a much larger injection loop was introduced at 2144.3 μL .

In conjunction with the flow system described in *flow design 3.2* the initial CMR produced from methods *monolith 2.2* with *palladium loading 2.11* was tested for flow. The initial flow heating showed the CMR melting to the Teflon connectors within a few seconds of activating the microwave. The palladium had leached massively from the CMR and generated arcing within the flow system. Observing the effect of the arcing had completely destroyed the connectors and blocked the flow system. This CMR design was not used for further experiments due to its lack of safety and lack of flow.

Suzuki reactions were performed in this flow system with CMRs formed from *monolith 2.3* with *palladium loading 2.12*. 0.1 M 4-bromobenzonitrile, 0.12 M phenyl

and Heating – Results and Discussion

boronic acid and 0.25 M potassium carbonate in 66.7% aqueous DMF was injected into the flow system, through a 6 way valve. Reaction conditions of catalyst residence time and microwave power were varied; 3.9 and 7.9 minutes at 80 W, 3.9 minutes at 200 W and 7.9 minutes at 300 W. All times and microwave wattages were found to give no conversion (Appendix 1, Appendix 2, Appendix 3, Appendix 4).

A batch reaction test was performed to determine if the NMF was affecting the reaction. A simulation of a flow reaction was done by flowing NMF over the same type of monolithic reactor. The NMF was then replaced with a solution of 0.025 M 4-bromobenzonitrile, 0.026 M phenyl boronic acid and 0.121 M potassium carbonate in 66.7% aqueous DMF. The reactant loaded CMR was placed in an oven for 120 minutes at 80 °C. A comparative experiment without NMF flow prior to reaction was also performed under the same conditions. Appendix 5 and Appendix 6 show the GC-MS results of the NMF coated and the non-NMF coated monoliths. The product 4-cyanobiphenyl was observed at approximately 8.44 minutes. Comparing the two reactions it is obvious that flowing NMF prior to reaction affects the reaction considerably. This clarified the reason why the reaction was not working for all flow loops. This new information proves the previous assumption that the reagents are dispersing beyond the plug was not the cause for the lack of reactive activity.

The lack of activity from the carrier solvent NMF lead to the reconsideration of the role of the carrier solvent for this reaction system. In addition to this, a loop injection system was thought to be unnecessary. Instead of a continuous flow of carrier solvent was replaced with a continuous flow of reactants. The reaction solution was placed directly into the syringe pump. The reaction solvent at this point had been 66.7%

and Heating – Results and Discussion

aqueous DMF. The reaction solvent was compared to 66.7% aqueous dioxane. Palladium on charcoal was used as a catalyst for the batch reaction. 0.025 M 4-bromobenzonitrile, 0.026 M phenyl boronic acid and 0.121 M potassium carbonate were reacted for 120 minutes at 80 °C. GC-MS results of the reaction demonstrated a much higher area ratio for 4-cyanobiphenyl to 4-bromobenzonitrile in the dioxane solvent than the DMF (Appendix 7 and Appendix 8). Both reaction solvents provided the product 4-cyanobiphenyl. However, the activity with this catalyst and these reaction conditions shows that dioxane as a reaction solvent increased 4-cyanobiphenyl production.

The changes described led to the formulation of *flow design 3.3*. This design was used briefly. Still using the same CMRs formed from *monolith 2.3* with *palladium loading 2.12*, other difficulties had arisen with this methodology. Using the syringe pump directly coupled to the monolithic reactor had back pressures that exceeded the syringe pump pressure limits at the flow rates used. This produced inconsistent flow rates throughout the flow system.

In addition a potential problem was observed when using the microwave. A Suzuki reaction was performed using 0.025 M 4-bromobenzonitrile, 0.026 M phenyl boronic acid and 0.121 M potassium carbonate at 100 W with a residence time of 22.6 minutes. This produced 4-cyanobiphenyl product (GC-MS peak 8.46 minutes, Appendix 9). Little 4-cyanobiphenyl production indicated that there was another contributing factor for the reaction. This was tested and mapped by the microwave heating zone present in the cavity (See 3.19). The conclusion was that the heating was not vertical and consistent throughout the chamber as expected. The focus of the microwaves was at the centre of the microwave chamber along the horizontal axis. An

and Heating – Results and Discussion

adaptation of the catalyst reactor design had to be formulated to accommodate the change in flow direction.

The difficulties encountered for *flow design 3.3* were adapted leading to *flow design 3.4*. The high back pressures observed, which caused irregular pumping, were resolved by replacing the syringe pump with a HPLC pump that could reach lower flow rates. The JASCO Pu-1580 HPLC pump could pump at flow rates of $5 \mu\text{L min}^{-1}$. This proved capable in controlling the residence time of the reactants on the catalyst at higher pressures.

The other amendment to the procured from the design of *flow design 3.3* was to the position of the CMR in the microwave chamber. The results of the heating zones of the chamber meant that the heating of the CMR was only a fraction of what was expected. To resolve this issue, holes were drilled in the base of the microwave cavity, large enough for tubing and connectors but small enough to prevent microwave discharge from the chamber. This made fixing the CMR reactor in the horizontal position much simpler than previously possible. A Teflon block was used to hold the CMR 45 mm from the base. This point was half the height of the cavity and found to be the maximum heating zone. Placing the CMR in the horizontal position made flow connection to and from the CMR difficult. Certain types of Teflon connectors were not possible to use due to the presence of rubber “O” rings that melted when subjected to microwave energy. The limitations of using the microwave due to connector limitations, meant that the material used had to be non-metal and transparent to microwave energy. Teflon was the primary connector material available however with the change into horizontal CMR positioning and available space, glass connectors were manufactured

and Heating – Results and Discussion

and used to connect the CMR to the flow system. Nevertheless the glass did conduct the microwave energy but was non-destructive in terms of the fitting and did not influence the flow of liquid.

The change from vertical positioning to horizontal positioning was necessary to maximise the CMR exposure to microwave energy. Previous working on the monolith development in the flow system was changing the residence time of the reaction. This could be done by two methods; varying the flow rate and varying the CMR volume. The CMR volume was varied initially for the monoliths made from *monolith 2.3* by increasing the length of the capillary. The increase in length was not an option in the horizontal cavity position due to the limitations of the microwave chamber walls. The other method for increasing the CMR volume was to increase its diameter. Trying to increase the diameter of the *monolith 2.3* monoliths could not be achieved as attempts at increasing the mould diameter resulted in cracked and deformed monolith formation. CMRs formed from *monolith 2.5* monoliths could be increased in diameter size, making them ideal for the horizontal position CMR.

A difficulty arose with *flow design 3.4*. The presence of bubbles was observed within the CMR under microwave heating. This was thought to be due to high localised temperatures on the CMR that produced boiling of either water or dioxane in the reaction solution (similar boiling points). The boiling produced bubbles within the CMR and the rapid expansion of gas caused physical monolithic damage and fragmentation. The CMR destruction released silica and palladium chunks. To prevent the formation of bubbles a 275.79 kPa back pressure valve was placed in the flow line after the microwave chamber. The increase in pressure within the monolith and capillaries helped

and Heating – Results and Discussion

prevent bubbles from being formed during a reaction. The back pressure valve in the flow system represents the adaptation from *flow design 3.4* to *flow design 3.5*.

The method described in *flow design 3.6* became *flow design 3.5* by the addition of a PTFE Raman flow cell. The Raman flow cell was placed in-line after the back pressure valve and permitted a window into the reaction system giving Raman spectroscopic details of the flow of product solution out of the CMR. The full microwave heating Raman spectroscopic flow system is shown in Figure 3.12. This flow system incorporated continuous reagent flow, high pressures, a focal microwave heating zone, glass capillary adapters, Teflon connectors and a low pressure Raman flow cell.

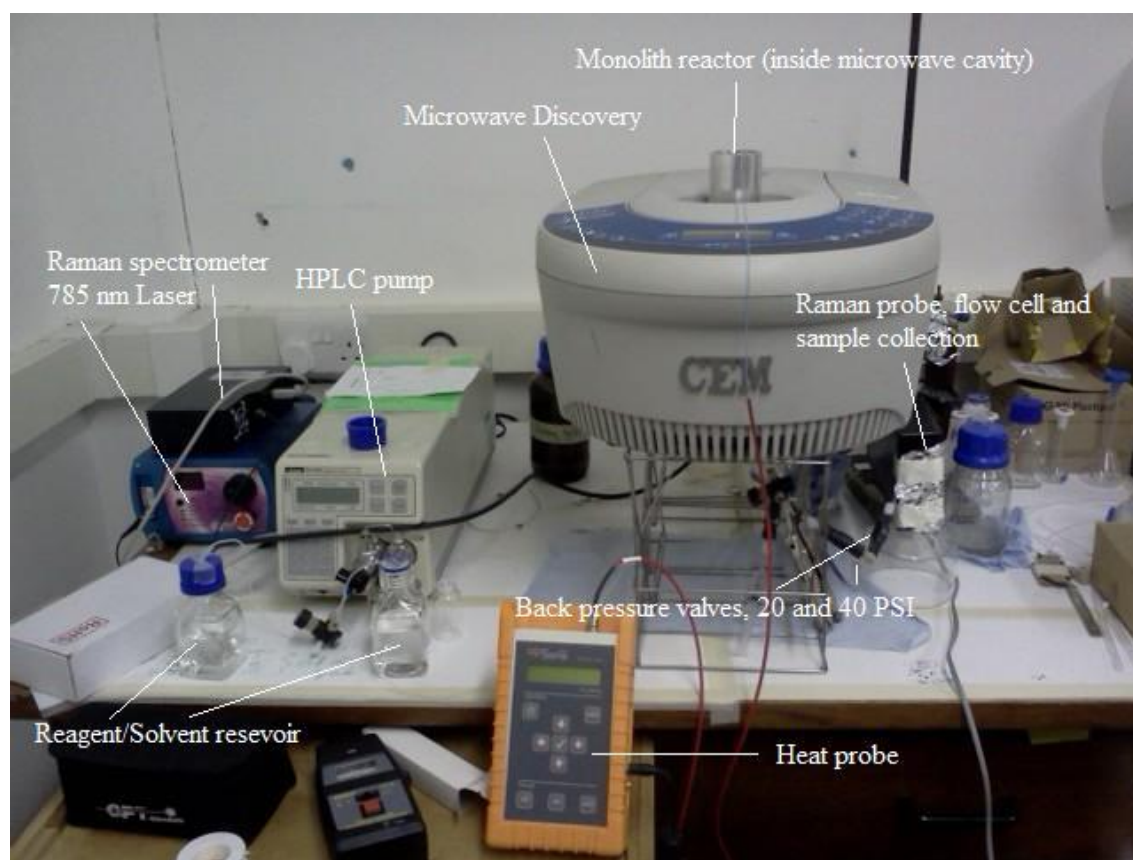
and Heating – Results and Discussion

Figure 3.12 A photograph of *flow design 3.6* incorporating reagent/solvent reservoir, HPLC pump, Microwave Discovery, heat probe, monolith reactor position, Raman flow cell and back pressure regulator valves

Over time the bubble formation in the monolith was still occurring and this was jeopardising the CMR structure. Not only were the bubble formations destroying the catalyst they were also causing difficulties in the Raman spectra. Bubbles interfered with the laser interaction with the reaction solution. Assuming localised heating from the microwave energy was the cause, the microwave was replaced with a column heater and the back pressure valve was removed. The withdrawal of the microwave meant that instead of heating inside the CMR out, the column heater would heat outside in. The advantages of using the microwave for reactions were promising from a high yields and

and Heating – Results and Discussion

purity points of view (previously reported ¹⁵⁹⁻¹⁶¹) but the effect of bubble formation from the reaction required an adaptation to the heating mechanism. On using the column heater without the back pressure valve, no bubbles were formed which meant that the flow system was converted to a simpler design. One final change in the flow system was the size of the CMR. No longer was it only possible to just increase the diameter of the CMR for an increased CMR volume but also the length could be variable too. Increased volume of the CMR permitted higher flow rates equivalent to the same catalyst residence time. Using this methodology it was possible to increase the amount of 4-cyanobiphenyl produced per unit time. The final flow system designed using these adaptations were *flow design 3.7* (see previously Figure 3.1).

3.19 Microwave chamber heating zone

The microwave chamber heating was mapped using hydrated cobalt chloride saturated into a silica TLC plate. Hydrated cobalt chloride is pink and when dehydrated is blue. On heating in the microwave cavity the highest regions of heating changed from pink to blue. Initially the experiment was carried out at 100 W of microwave power for 10 seconds and the plate colour was immediately observed. However on doing this the plate was heated enough to lose any mapping capability as the centre of the plate horizontal and vertical were blue. A more focussed point of microwave heating was observed when the time was reduced to 5 seconds. A blue section was observed approximately 20 mm from the top and base of the chamber. A darker, denser blue colouration was observed over a 10 mm diameter approximately 45 mm from the base of the cavity. 45 mm was approximately the centre of the cavity and the blue colouration surrounding this area extended up to 20 mm from the walls of the cavity

and Heating – Results and Discussion

which implies a focal heating point at 45 mm. The microwave heating focal point was confirmed by measuring the difference in water temperature in a 10 mm 1/8 2.4 mm PEEK tube with the IR fibre optic temperature probe sealed inside with PTFE tape at 300 W for 60 seconds. The PEEK tube was lowered horizontally from the top of the chamber and temperatures were recorded (Figure 3.13). The highest temperature difference was observed 40 mm from the top of the chamber confirming there was a focal point in the microwave chamber. This information was used to alter the flow system from *flow design 3.4* to *flow design 3.5*.

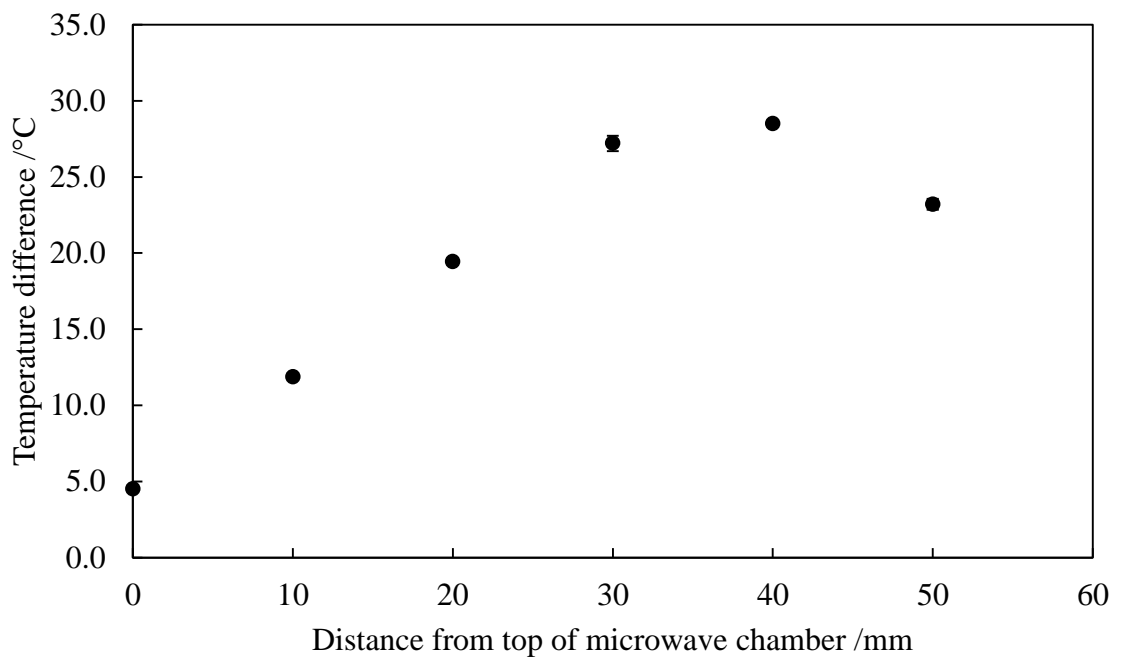


Figure 3.13 Graph of temperature difference from start of heating at 22 °C to the final temperature recorded after 60 second in relation to depth into the microwave chamber at 300 W. Water contained in 10 mm 1/8 2.4 mm PEEK tubing fitted with the IR fibre optic temperature probe was used in a horizontal position down the centre of the chamber.

and Heating – Results and Discussion*3.20 Summary*

The final flow system developed incorporated a flow of reagents, a stable CMR and a fully integrated Raman detection system. The flow of reagents was developed by changing the introduction of reagents into the flow system from a carrier solvent to a pure reagent driven flow. This removed an external factor that was found to be affecting the catalyst activity. Further development led to the change from a syringe pump to a HPLC pump. A HPLC pump could handle the back pressures generated by the CMR that the syringe pump could not. With this increasing pressure and need for integrating the CMR into the flow, the flow design was altered to accommodate CMR positional change and the higher flow rates of the HPLC pump. Glass connectors and PTFE heat shrink tubing effectively sealed the CMR and glass connectors within the flow forcing the flow of reagents through the CMR. Despite its successful integration, the CMR irradiated by the microwave underwent physical damage leading to palladium leaching. The heating mechanism was changed to a column heater that proved to be more reliable and less destructive than the microwave heating.

The detection system was successfully placed after the reaction zone in the flow and could then be used further in the Suzuki reaction between 4-bromobenzonitrile with phenyl boronic acid and potassium carbonate. Conversions up to 79% were observed in batch and for a much lower residence time, it was observed in flow at 7% (Table 3.1). The final flow design shown in Figure 3.1 can be used to perform and assess organic reactions effectively and efficiently.

and Heating – Results and Discussion

Aqueous 66.7% solvent	Flow/ Batch	Reaction/ Residence time /min	Temperature /°C	Microwave power /W	Catalyst	Conversion /%
DMF	Batch	120	80	N/A	CMR*	0 ⁺
DMF	Batch	120	80	N/A	CMR*	79
DMF	Batch	120	80	N/A	Pd/C	18
Dioxane	Batch	120	80	N/A	Pd/C	72
Dioxane	Flow	23	N/A	100	CMR*	7

* CMRs made from monolith 2.3 with palladium loading 2.12

⁺ NMF flowed through CMR pre-reaction

Table 3.1 Summary reaction conversions and conditions involved in formulating the CMR design and reaction heating.

Raman Spectroscopic Monitoring - Experimental

4.0 Suzuki reaction chemistry with Raman spectroscopic monitoring

The Suzuki reaction is a favoured reaction amongst many organic synthetic chemists as its air tolerant, potentially very clean, and straightforward to set-up and does not take more than a few hours to complete (dependant on reaction conditions). This was used in the flow reaction system and analysed by GC-MS. Later the reactions were monitored by Raman spectroscopy to give immediate details of the consistency of the reaction mixture within the flow system. Monitoring the flow showed it is possible to determine the concentration of the product and reagents passing by the Raman focal point. This can give kinetic details of the reaction and automisation of the flow reaction system to find an optimum flow rate and temperature. The objectives of using the Suzuki reaction in the flow system with Raman spectroscopic monitoring here to determine if the proposed Suzuki reaction is possible in a round bottom flask, if the proposed Suzuki reaction is possible in flow, if Raman monitoring was possible, if Raman monitoring could provide concentration details and if the concentration details could be used to optimise the flow system.

Experimental*4.1 GC-MS analysis of Suzuki reactions**4.2 GC-MS analysis A*

GC-MS (Perkin Elmer Gas Chromatograph, Varian Saturn 2000) analysis was performed to evaluate the progress of the reaction. The products of the reaction were

Raman Spectroscopic Monitoring - Experimental

sampled and subject to liquid-liquid extraction in DCM (99.8% Sigma Aldrich). The contents were washed with 1 M sodium hydroxide ($\geq 98\%$ Sigma Aldrich) and washed with water 3 times. Magnesium sulphate (ReagentPlus $\geq 99.5\%$ Sigma Aldrich) was used to dry the analyte solution. The GC-MS conditions were an injector temperature of 230 °C with a 1:20 split injection, a carrier gas of nitrogen (Energas) at 1 mL min⁻¹. Oven temperature was 100 °C for 2 minutes and ramped by 20 °C min⁻¹ to 270 °C with a hold time of 9.5 minutes. Acetone (GC grade $\geq 99.9\%$ Sigma Aldrich) was used as a wash solvent. Column used for the separation was a Phenomenex Zebron ZB-5 capillary column 30 m in length and an ID of 0.25 mm.

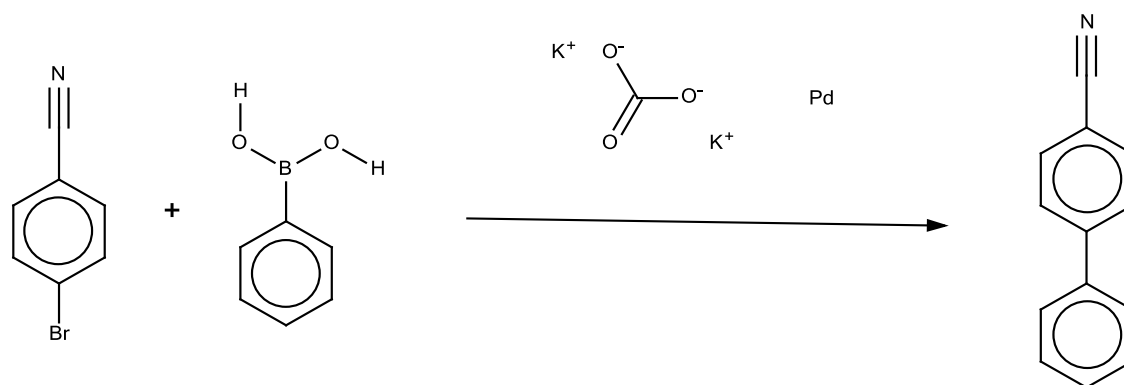
4.3 GC-MS analysis B

GC-MS (Perkin Elmer Gas Chromatograph, Varian Saturn 2000) calibration and reaction analysis were performed after liquid-liquid extraction in DCM (99.8% Sigma Aldrich) and water. 10 μ L of decane (99% Sigma Aldrich) was added as an internal standard to 400 μ L of the standard or sample. Liquid – liquid extraction was performed with 2 mL DCM and 10 mL water. The standard or sample was washed 3 times with 10 mL of water and then dried over magnesium sulphate (ReagentPlus $\geq 99.5\%$ Sigma Aldrich). The sample was then filtered and placed into GC-MS. The GC-MS conditions were an injection temperature of 50 °C with a 1:50 split. Nitrogen (Energas) gas was flowed at 1 mL min⁻¹. Oven temperatures were 50 °C with a ramp of 35 °C min⁻¹ to 70 °C for 7.23 minutes, then ramped to 20 °C min⁻¹ to 250 °C and held for 6 minutes. Acetone (GC grade $\geq 99.9\%$ Sigma Aldrich) was used as the washing solvent. Column used for the separation was a Phenomenex Zebron ZB-5 capillary column 30 m in length and an ID of 0.25 mm.

Raman Spectroscopic Monitoring - Experimental

4.4 Suzuki reaction chemistry

The Suzuki cross-coupling reaction used in the evaluation of the flow system is shown in Reaction Scheme 4.1. 4-Bromobenzonitrile is reacted with phenyl boronic acid to produce 4-cyanobiphenyl in the presence of potassium carbonate and palladium.



Reaction Scheme 4.1 The Suzuki reaction used in the flow and batch reactions. The limiting reagent for the reaction was always 4-bromobenzonitrile. The solvent for the reactions was varied between 66.7% aqueous DMF and 66.7% aqueous dioxane.

4.5 Batch Suzuki reaction – DMF and Dioxane using palladium on activated charcoal

0.025 M 4-bromobenzonitrile (99% Sigma Aldrich), 0.026 M phenyl boronic acid (95% Sigma Aldrich) and 0.121 M potassium carbonate (99% Sigma Aldrich) were placed in a 66.7% aqueous DMF (99% Sigma Aldrich) in a 100 mL round bottom flask. Once homogeneous at 80 °C, palladium on activated charcoal (10% Pd Johnson and Matthey) was added. The reaction proceeded for 120 minutes. A sample at the end of the reaction was subjected to GC-MS analysis using *GC-MS analysis 4.2*. This was repeated for 66.7% aqueous dioxane (99% Sigma Aldrich).

Raman Spectroscopic Monitoring - Experimental*4.6 Batch Suzuki reaction – Silica 60 mesh beads*

0.025 M 4-bromobenzonitrile (99% Sigma Aldrich), 0.026 M phenyl boronic acid (95% Sigma Aldrich) and 0.121 M potassium carbonate (99% Sigma Aldrich) were placed in a 66.7% aqueous dioxane (99% Sigma Aldrich) in a 100 mL round bottom flask. Once homogeneous at 80 °C, palladium on 60 mesh silica beads (BDH for GC) was added to the reaction mixture. The palladium on silica beads was produced by *palladium loading 2.12*. The reaction was performed for 120 minutes and 10 minutes. Both reactions were subjected to GC-MS analysis using *GC-MS analysis 4.2*.

4.7 Batch Suzuki reaction – CMR

CMR formed from *monolith 2.3* with *palladium loading 2.12* was used in a glass capillary as a reaction vessel. 0.025 M 4-bromobenzonitrile (99% Sigma Aldrich), 0.026 M phenyl boronic acid (95% Sigma Aldrich) and 0.121 M potassium carbonate (99% Sigma Aldrich) were placed in a 66.7% aqueous dioxane (99% Sigma Aldrich) and loaded onto the CMR. Batch reaction times of 6, 8, 10, 15, 30 and 120 minutes were performed at 80 °C. Sampling was performed by pushing the equivalent volume of the monolith reactor through the monolith to displace the reaction mixture. Reaction solutions were subjected to GC-MS using *GC-MS analysis 4.2*.

4.8 Flow Suzuki reaction – NMF carrier solvent

NMF (99% Sigma Aldrich) was used with a loop injector flow system to pump a reaction mixture through a microwave cavity (previously described in *flow design 3.2*). 0.1 M 4-bromobenzonitrile (99% Sigma Aldrich), 0.12 M phenyl boronic acid (95% Sigma Aldrich) and 0.24 M potassium carbonate (99% Sigma Aldrich) in 66.7%

Raman Spectroscopic Monitoring - Experimental

aqueous DMF (99% Sigma Aldrich) was flowed as a homogeneous reaction mixture. The reaction mixture was pumped through the flow system at flow rates of 5 and 10 $\mu\text{L min}^{-1}$ resulting in catalytic residence times of 7.9 and 3.9 minutes respectively. Reaction conditions of catalyst residence time and microwave power were 3.9 and 7.9 minutes at 80 W, 3.9 minutes at 200 W and 7.9 minutes at 300 W. The CMR used was generated from *monolith 2.3* with *palladium loading 2.12*. Each reaction was analysed using GC-MS from *GC-MS analysis 4.2*.

4.9 Flow Suzuki reaction 1 – pure reaction mixture flow

These reactions were performed using the experimental flow system described in *flow design 3.3*. 0.025 M 4-Bromobenzonitrile (99% Sigma Aldrich), 0.026 M phenyl boronic acid (95% Sigma Aldrich) and 0.121 M potassium carbonate (99% Sigma Aldrich) were placed in a 66.7% aqueous dioxane (99% Sigma Aldrich) were pumped with no carrier solvent through a CMR generated from *monolith 2.3* with *palladium loading 2.12*. The catalyst residence time was 22.6 minutes at 100 W of microwave power for a flow rate of 1 $\mu\text{L min}^{-1}$. Reaction solutions were subjected to GC-MS analysis using *GC-MS analysis 4.2*

4.10 Flow Suzuki reaction 2 – pure reaction mixture flow

These reactions were performed using the flow system described in *flow design 3.4*, *flow design 3.5* and *flow design 3.6*. 0.1 M 4-Bromobenzonitrile (99% Sigma Aldrich), 0.12 M phenyl boronic acid (95% Sigma Aldrich) and 0.24 M potassium carbonate (99% Sigma Aldrich) in a homogeneous solution of either 66.7% aqueous dioxane (99% Sigma Aldrich) or 66.7% aqueous DMF (99% Sigma Aldrich) were

Raman Spectroscopic Monitoring - Experimental

used for the reaction. Varying wattages and flow rates were used and described in the results. Reaction solutions were subjected to Raman spectroscopic analysis and GC-MS analysis using *GC-MS analysis 4.2* or *4.3*.

4.11 Flow Suzuki reaction 3 – pure reaction mixture flow

These reactions were performed using the flow system described in *flow design 3.7*. 0.10 M 4-Bromobenzonitrile (99% Sigma Aldrich), 0.12 M phenyl boronic acid (95% Sigma Aldrich) and 0.24 M potassium carbonate (99% Sigma Aldrich) in a homogeneous solution of 66.7% aqueous DMF (99% Sigma Aldrich) . The temperature for the reaction was 80 °C. Flow rates of the reaction were 27, 42, 60, 80, 95, 110, 140, 170, 245 and 381 $\mu\text{L min}^{-1}$. The CMR used generated from *monolith 2.5* with *palladium loading 2.14*. Reaction solutions were subjected to Raman spectroscopic analysis and GC-MS analysis using *GC-MS analysis 4.3*.

4.12 Raman spectroscopic analysis

Raman spectroscopic analysis was performed on the flowing solution post reaction. Initial calibrations were carried out in order to determine the concentration of both reactants and products. The calibration was performed in 66.7% aqueous dioxane (99% Sigma Aldrich) and 66.7% aqueous DMF (99% Sigma Aldrich). All calibrations were performed with the Raman flow cell and its design shown in Figure 4.1. A laser (785 nm at 350 mV Ocean Optics) at 785 nm was focused 7.5 mm from the lense with a spot size of was 135 μm with an approximate depth of field of 2.2 mm into the flow cell. A quartz window was used to separate the probe (Raman probe, RIP-RPB-785-SS Ocean Optics) from the liquid. The Raman scattered photons were collected through the

Raman Spectroscopic Monitoring - Experimental

same probe and passed back to the spectrometer (QE65000 Ocean Optics). Every spectral recording was observed at 20 °C.

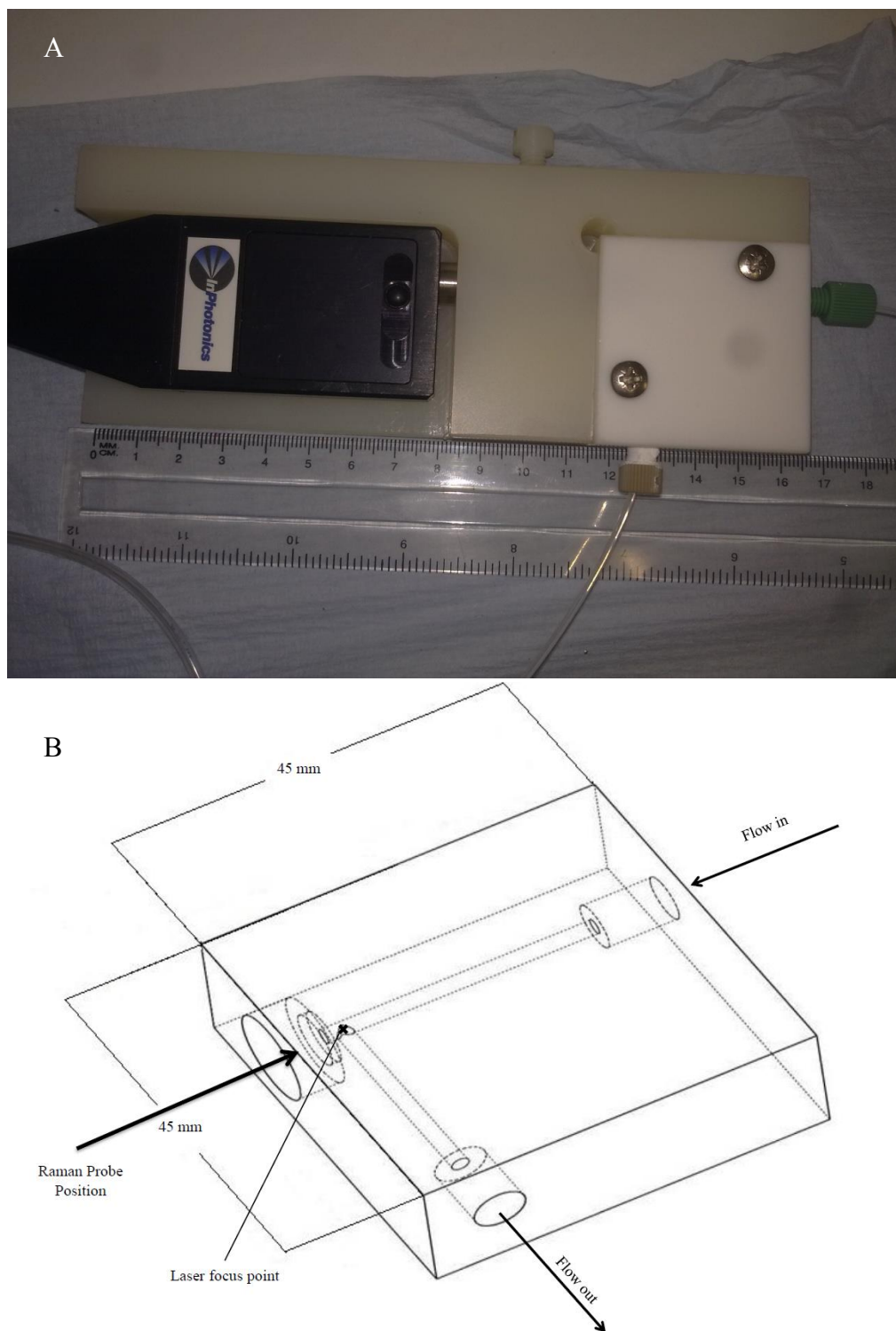
Raman Spectroscopic Monitoring - Experimental

Figure 4.1 A) The PTFE Raman flow cell incorporating the Raman fibre optic probe, the inline quartz window and the flow stream. The direction of flow was from the right to the bottom of the flow cell. B) A schematic of the inside of the Raman flow cell

Raman Spectroscopic Monitoring - Experimental

demonstrating the flow direction, the Raman laser focal point, the dimensions of the flow cell and the position of the Raman probe.

4.13 Raman spectra

Raman spectra were obtained for 4-bromobenzonitrile (99% Sigma Aldrich), phenyl boronic acid (95% Sigma Aldrich), 66.7% aqueous dioxane (99% Sigma Aldrich), 66.7% aqueous DMF (99% Sigma Aldrich) and 4-cyanobiphenyl (95% Sigma Aldrich). 66.7% aqueous dioxane was pumped through the Raman flow cell at $20 \mu\text{L min}^{-1}$. This was set to dark spectrum and subtracted for a zero baseline. 0.2 M 4-Bromobenzonitrile, 0.2 M phenyl boronic acid and 0.2 M 4-cyanobiphenyl in 66.7% aqueous dioxane were pumped separately through the Raman flow cell. Spectra were obtained using an integration time of 200 ms averaged 3 times with electrical and stray light correction default from the software (SpectraSuite Ocean Optics). The 66.7% aqueous DMF spectrum was observed under the same conditions except without any subtraction of the background.

4.14 Raman pressure testing

The Raman flow cell was tested for pressure effects on the Raman signal. A variable pressure valve (JR-BPR1 VICI Jour) was placed after the Raman flow cell and pressure increased and monitored using an in house built pressure device. 66.7% aqueous DMF (99% Sigma Aldrich) was monitored in flow at $20 \mu\text{L min}^{-1}$. The Raman area signal was obtained between Raman shifts of 870.98 and 873.16 cm^{-1} and a noise range between 899.21 and 901.37 cm^{-1} . The noise was subtracted from the signal for the contributing 66.7% aqueous DMF peak area. The spectral conditions used to obtain the

Raman Spectroscopic Monitoring - Experimental

data were a 200 ms integration time averaged 3 times with electrical and stray light correction default from the software (SpectraSuite Ocean Optics).

4.15 Raman flow testing

Raman spectral data was obtained by flowing 0.1004 M 4-cyanobiphenyl in 66.7% aqueous dioxane (99% Sigma Aldrich) at flow rates of 0, 20, 40, 50, 100 and 120 $\mu\text{L min}^{-1}$. The spectra were integrated between Raman shifts of 1291.08 and 1300.69 cm^{-1} subtracting a noise area between Raman shifts 1264.02 and 1273.71 cm^{-1} . The spectral conditions used to obtain the data were a 200 ms integration time averaged 3 times with electrical and stray light correction default from the software (SpectraSuite Ocean Optics). A 66.7% aqueous dioxane spectrum was used as a dark spectrum and subtracted from the original spectra.

4.16 Raman spectral calibration A

Raman spectra were obtained for concentrations of 4-cyanobiphenyl (95% Sigma Aldrich), phenyl boronic acid (95% Sigma Aldrich) and 4-bromobenzonitrile (99% Sigma Aldrich) in 66.7% aqueous dioxane (99% Sigma Aldrich). Each analyte was in a separate solution. 4-Cyanobiphenyl concentrations were 0.0020, 0.0100, 0.0199, 0.0498, 0.0697, 0.0996, 0.1494 and 0.1992 M. Phenyl boronic acid concentrations were 0.0098, 0.0196, 0.0491, 0.0688, 0.0982, 0.1474, and 0.1965 M. 4-Bromobenzonitrile concentrations were 0.0100, 0.0199, 0.0498, 0.0697, 0.0996, 0.1494 and 0.1992 M. Subtraction of a background noise area was performed from the peak of interest and the contributed peak of the analyte was observed. 4-Cyanobiphenyl was observed using a background noise between the Raman shift

Raman Spectroscopic Monitoring - Experimental

1264.02 - 1273.71 cm^{-1} subtracted from the peak area of the signal between Raman shifts 1291.08 - 1300.69 cm^{-1} . The phenyl boronic acid had a noise subtraction between the Raman shifts 749.04 - 751.29 cm^{-1} from the signal peak between Raman shifts 778.23 - 780.47 cm^{-1} . 4-Bromobenzonitrile had a noise subtraction between the Raman shifts 749.04 - 751.29 cm^{-1} from the signal peak between Raman shifts 730.95 - 733.22 cm^{-1} . Subtracting the background noise area from the analyte peak area gave only the pure analyte peak area without background interferences. Each calibration solution was pumped at 20 $\mu\text{L min}^{-1}$. The spectral conditions used to obtain the data were a 200 ms integration time averaged 3 times with electrical and stray light correction default from the software (SpectraSuite Ocean Optics). A 66.7% aqueous dioxane spectrum was used as a dark spectrum and subtracted from the original spectra.

4.17 Raman spectral calibration B

Raman spectra were obtained for concentrations of 4-cyanobiphenyl (95% Sigma Aldrich), phenyl boronic acid (95% Sigma Aldrich) and 4-bromobenzonitrile (99% Sigma Aldrich) in 66.7% aqueous DMF (99% Sigma Aldrich). The solvent change is an adaptation of *Raman calibration 4.16*. Each analyte was in a separate solution.

4-cyanobiphenyl concentrations were 0.0100, 0.0200, 0.0500, 0.0999 and 0.1499 M. Phenyl boronic acid concentrations were 0.0198, 0.0504, 0.0715, 0.1002 and 0.1505 M. 4-Bromobenzonitrile concentrations were 0.0194, 0.0502, 0.0699, 0.1000 and 0.1513 M. Subtraction of a neutral background area was performed from the peak of interest and the contributed peak of the analyte was observed. 4-Cyanobiphenyl was observed using noise between the Raman shift 1264.02 - 1273.71 cm^{-1} subtracted from the peak

Raman Spectroscopic Monitoring - Experimental

area of the signal between Raman shifts 1291.08 - 1300.69 cm^{-1} . The phenyl boronic acid had a noise subtraction between the Raman shifts 749.04 - 751.29 cm^{-1} from the signal peak between Raman shifts 778.23 - 780.47 cm^{-1} . 4-Bromobenzonitrile had a noise subtraction between the Raman shifts 749.04 - 751.29 cm^{-1} from the signal peak between Raman shifts 730.95 - 733.22 cm^{-1} . Each calibration solution was pumped at 20 $\mu\text{L min}^{-1}$. The spectral conditions used to obtain the data were a 200 ms integration time averaged 3 times with electrical and stray light correction default from the software. A 66.7% aqueous DMF spectrum was used as a dark spectrum and subtracted from the original spectra.

4.18 Raman spectral calibration C

Raman spectra were obtained for concentrations of simulated reaction mixtures in 66.7% aqueous DMF (99% Sigma Aldrich) . The reaction mixtures were replicas of what the concentration of reagents and products would have been at different conversions during synthesis allowing analysis of all the components of the solution, as opposed to *Raman calibration 4.16* and *Raman calibration 4.17* which involved a singular component being analysed. 4-Bromobenzonitrile (99% Sigma Aldrich), phenyl boronic acid (95% Sigma Aldrich), potassium carbonate (99% Sigma Aldrich) and 4-cyanobiphenyl (95% Sigma Aldrich) were added in different ratios. Table 4.1 demonstrates the concentrations used to simulate the Suzuki reaction conversion. 4-Bromobenzonitrile and 4-cyanobiphenyl were analysed by using the peak areas observed between Raman shifts 1591.81 - 1597.04 cm^{-1} and 1616.15 - 1621.34 cm^{-1} respectively. Background noise area subtraction for both peaks was between Raman shifts 1570.78 - 1576.05 cm^{-1} . Each calibration solution was flowed at 80 $\mu\text{L min}^{-1}$. The

Raman Spectroscopic Monitoring - Experimental

spectral conditions used to obtain the data were a 1 s integration time averaged 3 times with electrical and stray light correction default from the software (SpectraSuite Ocean Optics). No dark spectra were recorded, and all calibration spectra used the original raw spectra.

Conversion /%	Concentration /M			
	4-bromobenzonitrile	Phenyl boronic acid	Potassium carbonate	4-cyanobiphenyl
0	0.0994	0.1156	0.2485	0.0000
20	0.0764	0.0957	0.2544	0.0220
40	0.0579	0.0802	0.2440	0.0391
60	0.0397	0.0677	0.2394	0.0598
80	0.0193	0.0413	0.2400	0.0797
100	0.0000	0.0205	0.2438	0.0989

Table 4.1 The concentration of 4-bromobenzonitrile, phenyl boronic acid, potassium carbonate and 4-cyanobiphenyl used for Raman spectroscopic calibration in relation to simulated conversion.

Raman Spectroscopic Monitoring - Experimental

4.19 Raman spectral calibration D

Raw Raman spectra were used previously from *Raman calibration 4.18* and were calibrated using manual baseline correction. 4-Bromobenzonitrile (99% Sigma Aldrich) and 4-cyanobiphenyl (95% Sigma Aldrich) were analysed for their individual peak and baseline correction was performed manually. A line of best fit was generated to assume the baseline through the analyte peak, and the integral of the resulting trapezoid was subtracted from the total area of each individual trapezoid between the two Raman shifts. Equation 4.1 is the simple summary of the integration where A_{peak} represents the area of the analyte peak, A_{total} represents the total area under the peak and $A_{baseline}$ represents the area under the baseline. Equation 4.2 and Equation 4.3 explain how the areas were established where k_n represents the higher Raman shift number, k_m represents the lower Raman shift number, k_1 represents the Raman shift at the start of the peak, k_2 represents the Raman shift at the end of the peak, R_{sn} represents the Raman signal intensity at the higher Raman shift number, R_{sm} represents the Raman signal intensity at the lower Raman shift number, R_{s1} represents the Raman signal intensity at k_1 , and R_{s2} represents the Raman signal intensity at k_2 . Equation 4.4 incorporates the equations together. 4-Cyanobiphenyl was measured between Raman shifts of 1250.40 – 1321.73 cm^{-1} . 4-Bromobenzonitrile was measured between Raman shifts 760.29 – 793.86 cm^{-1} .

$$A_{peak} = A_{total} - A_{baseline} \quad \text{Equation 4.1}$$

Summary equation of the *Raman calibration 4.19* for area determination.

$$A_{total} = \sum_{k_1}^{k_2} \frac{(k_n - k_m)(R_{sn} + R_{sm})}{2} \quad \text{Equation 4.2}$$

Determination of total spectral peak area.

Raman Spectroscopic Monitoring - Experimental

$$A_{baseline} = \frac{(k_2 - k_1)(R_{S1} + R_{S2})}{2} \quad \text{Equation 4.3}$$

Determination of baseline trapezoid peak area.

$$A_{peak} = \left[\sum_{k_1}^{k_2} \frac{(k_n - k_m)(R_{Sn} + R_{Sm})}{2} \right] - \left[\frac{(k_2 - k_1)(R_{S1} + R_{S2})}{2} \right] \quad \text{Equation 4.4}$$

Combined equations of Equation 4.1, Equation 4.2 and Equation 4.3.

4.20 Raman spectral calibration E

Previous Raman spectra obtained from *Raman calibration 4.18* but were calibrated differently to *Raman calibration 4.18* and *Raman calibration 4.19*. Partial least square regression (PLSR) was used to calibrate the spectral change between Raman shifts 1560.22 - 1631.69 cm^{-1} . Spectral pre-processing was performed using row-mean centring and smoothing with a moving average of 5 points. PLSR was then applied to the spectral data through Pychem (Python. Bioinformatics) software to 5 factors accounting for over 99% of the variance. 5 spectra were used to make the regression model (0 – 80% conversion) and 1 spectra was used for validation (100% conversion). Testing the model on individual reaction samples required using the same PLSR process inputting the model used each time.

Raman Spectroscopic Monitoring - Results and DiscussionResults*4.21 Suzuki reaction*

The chosen reaction for testing the flow system was the Suzuki reaction between 4-bromobenzonitrile and phenyl boronic acid to produce 4-cyanobiphenyl. This model reaction had the potential to be useful in synthesis of complex organic molecules for pharmaceutical or material chemistry.

The reaction used for testing the flow system was the reaction between 4-bromobenzonitrile and phenyl boronic acid with potassium carbonate to produce 4-cyanobiphenyl. The 4-bromobenzonitrile species contained a high electron withdrawing species in the para position. This nitrile group drew electrons from the benzene ring providing a favourable attacking point at the carbon bound to the bromide. This provided a more effective initial binding of the halide species in the Suzuki reaction mechanism¹⁶². Another reason for choosing the reagents and products carefully for this reaction is the homogeneity of the reaction solution. Unlike most round bottom flask Suzuki reactions, the use of a flow system required a homogeneous mixture to prevent any blockage in the flow and promote non-surface dependant steps (except for the catalyst). Having non-homogeneous solutions would inherently be dependent on surface area and dissolution rather than just the catalytic residence time. For the Suzuki reaction to occur, water can be present in the solvent in order to promote the formation of the boronic salt and the dissolution of the base. For this reaction, the 4-cyanobiphenyl and 4-bromobenzonitrile had a low solubility in water. A mixture of water and an organic solvent was therefore required. Dioxane and DMF were chosen due to their solubility in

Raman Spectroscopic Monitoring - Results and Discussion

water, their extensive use in microwave chemistry and Suzuki reaction chemistry¹⁶³⁻¹⁷⁵.

4.22 Batch Suzuki reactions

Three different heterogeneous palladium catalysts were used to establish Suzuki reaction activity. The same model reaction was used to produce 4-cyanobiphenyl with all three catalysts (Reaction Scheme 4.1). The three catalysts used were palladium on activated charcoal, palladium deposited onto glass beads and palladium deposition onto a silica monolith. Gradual modification of catalyst support permitted a greater flexibility and potential for the palladium deposition and catalytic activity.

4.23 Batch Suzuki reaction results – DMF and Dioxane

The first Suzuki reactions performed were carried out to demonstrate that the reaction can work on a catalyst known to be used for Suzuki reaction chemistry. The method described in *Batch Suzuki reaction 4.5* used palladium on charcoal to identify a solvent affects. The results of this reaction were described previously in *Flow System design 3.18*. It specified that the 66.7% aqueous DMF showed less activity than the 66.7% aqueous dioxane (Appendix 7 and Appendix 8 respectively). This was possibly due to the nature of the homogeneous reagents and heterogeneous catalyst. Accordingly solubility is the key for catalyst contact. The polar DMF was likely to promote 4-bromobenzonitrile adsorption to the surface of the catalyst. However, this promotion may not be the same for the phenyl boronic salt. Further possible explanation for the lower activity in DMF is that DMF's polar nature did not favour 4-cyanobiphenyl leaving the catalyst surface, due to the possibly of coating the catalyst with 4-cyanobiphenyl which would inhibit activity. A less complicated explanation could

Raman Spectroscopic Monitoring - Results and Discussion

simply be that DMF was coating the catalyst surface inhibiting the reagent-catalyst binding, which was plausible as previously discussed when NMF was seen to prevent the reaction in flow (*Flow System design 3.18*). Dioxane being less polar helped promote the solubility of 4-bromobenzonitrile and 4-cyanobiphenyl. This does not favour the 4-bromobenzonitrile adsorption to the surface of the catalyst but promoted the removal of 4-cyanobiphenyl from the catalyst. Accordingly there are many reasons for the 66.7% aqueous dioxane increase in Suzuki reaction activity but these were not investigated in detail in this work. The fact that 66.7% aqueous dioxane favoured the production of 4-cyanobiphenyl over 66.7% aqueous DMF with conversions of 72% and 18% respectively.

4.24 Batch Suzuki reaction results –Silica 60 mesh beads and CMR

Following the batch Suzuki reactions performed with palladium on activated charcoal, other catalysts were examined. Palladium was immobilized onto glass beads (described in *Batch Suzuki reaction 4.6*) and onto a monolith (described in *Batch Suzuki reaction 4.7*). GC-MS results were obtained using 4.2 and compared with the other catalysts used. The palladium immobilized on silica beads was used as a step toward silica monolith functionality. By testing this method of immobilization on silica beads, it showed the palladium catalytic activity without having to develop a method for a silica monolith if the immobilization activity was low. Fortunately the immobilization onto beads demonstrated a very promising conversion for the Suzuki reaction. Appendix 10 shows the chromatograph from the resulting solution for the reaction and yielded 95% conversion after 120 minutes compared to the Suzuki reaction results obtained from *Flow system design 3.18*. In reality however the reaction or catalyst

Raman Spectroscopic Monitoring - Results and Discussion

residence time within the flow system was much shorter than 120 minutes, and the batch reaction was reduced to 10 minutes. The palladium on silica beads still proved highly effective with a conversion of 70% after 10 minutes (Appendix 11). With this new knowledge of catalyst activity, it was adapted to incorporate a silica monolith in place of the silica beads.

A monolith was produced using the methodology described previously (see *monolith 2.3*). These monoliths were produced and kept in a glass capillary. The capillary and CMR became the reaction vessel. The same experiment was used previously to demonstrate NMF's effect on the Suzuki reaction in flow (see *Flow System design 3.18*). The CMR was loaded with the homogeneous reagent solution (described in *Batch Suzuki reaction 4.7*) and the glass capillary plugged and heated. For the same reaction time of 120 minutes, a conversion of 79% was observed (Appendix 6). The ratio or peak area between 4-cyanobiphenyl and 4-bromobenzonitrile was lower for the CMR than the silica beads but was nevertheless still relatively high. To see the effect of time on the conversion, the same reaction was repeated at 6, 8, 10, 15 and 30 minutes (Appendix 12, Appendix 13, Appendix 14, Appendix 15 and Appendix 16 respectively). These chromatograms showed no sign of 4-cyanobiphenyl production until 15 minutes (Table 4.2).

Raman Spectroscopic Monitoring - Results and Discussion

Reaction time /min	Conversion /%
6	0
8	0
10	0
15	5
30	10
120	79

Table 4.2 The conversions of the Suzuki reaction described in *Batch Suzuki reaction 4.7*. The CMR was formed from *monolith 2.3* with *palladium loading 2.12* was used in a glass capillary as a reaction vessel. 0.025 M 4-bromobenzonitrile, 0.026 M phenyl boronic acid and 0.121 M potassium carbonate were placed in a 66.7% aqueous dioxane and placed in an oven at 80 °C.

A possible reason for the observed lower activity for the CMR in comparison to the silica beads was possibly due to palladium leaching from the monolith after each loading. The high surface area of the monolith in comparison to the silica beads should permit greater contact of the palladium to the reaction solution. This higher area however increases the likelihood of not only catalysis but of palladium loss from the solid support. Repeating the reaction consecutively especially after 120 minutes reaction time, then 6, 8, 10, 15, and 30 minutes would have had a diminishing return effect as palladium leached from the CMR. Another plausible explanation is that the leached palladium was in fact the catalyst for the reaction rather than the solid supported palladium. If this was the case then after the first 120 minutes it is likely that no activity

Raman Spectroscopic Monitoring - Results and Discussion

would have been observed at all. There was activity seen still after a total of 144 minutes for both the 15 minute and 30 minute reactions. Applying this reaction in a flow mode was therefore becoming more feasible as flow rates could be adjusted and amended to allow a catalyst residence time up to 30 minutes. Coupled with the efficiency of microwave heating it was assumed that reaction would take place and produce even higher reaction conversions.

4.25 Flow Suzuki reactions

Initial flow reaction studies were performed with a HPLC type set up and were described previously using NMF as a carrier solvent (see 3.18). It was shown previously that the NMF was inhibiting the Suzuki reaction in flow and this was verified by using a CMR for a batch Suzuki reaction developed using *monolith 2.3* and *palladium loading 2.12*. The reasons for the inhibition were not explained thoroughly. One possible effect the NMF had for the reaction was the varying solubility as residues remained after flowing the reagents onto the CMR. This coating could prevent either one of the reagents from adsorbing the catalyst surface and thus preferentially cause the reagents to stay in the 66.7% aqueous DMF solution. Another possibility was that the NMF generated a sterically hindered barrier to the reaction mixture. The structures of NMF and DMF are shown in Figure 4.2. The lone pairs on the nitrogen of the NMF are much more freely available and could of co-ordinate bonded to the palladium and so block the access to the ligand. DMF has the potential to be a ligand to the palladium however because of the extra methyl group present on the nitrogen; it is likely that the methyl group hinders the co-ordination sterically and electronically. The increase of the spread of the electron density through the 2 methyl groups, the electron density at the lone pair

Raman Spectroscopic Monitoring - Results and Discussion

would have been broader than that for the 1 methyl group of NMF. This effect of co-ordinate bonding from the NMF would explain the inhabitation of the reaction. With the potential of DMF co-ordination to palladium, this also could explain the increased activity for the Suzuki reaction when solvents were compared between 66.7% aqueous DMF and 66.7% aqueous dioxane.

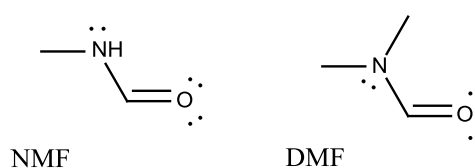


Figure 4.2 The molecular structures of NMF and DMF showing the lone pairs of the solvents.

The two stage development of switching from NMF carrier solvents to pure reaction mixture flow, and changing the reaction mixture from DMF to dioxane was explained previously in *Flow System design 3.18*. Factors that led to further adaptation of the flow system was also explained which directed the reaction from *Flow Suzuki reaction 4.9* to *Flow Suzuki reaction 4.10*.

4.26 Flow Suzuki reactions and Raman spectroscopic analysis

In addition to the flow Suzuki reaction chemistry, on-line monitoring was also included in the flow system. This meant reaction products could be analysed by Raman spectroscopy. The Raman spectroscopic window into the flow system was shown in Figure 4.1. This window allowed specific spectra to be obtained for each Raman active

Raman Spectroscopic Monitoring - Results and Discussion

component in the reaction mixture. Obtaining these spectra permitted calibration graphs to be constructed relating to concentration and reaction conversion.

4.27 Raman spectral calibration A - results

Raman spectra were obtained by the method described in *Raman calibration 4.16*. Each of the analytes were placed in 66.7% aqueous dioxane and the spectra obtained for 0.2 M of each one separately. A dark background subtraction of flowing 66.7% aqueous dioxane showed that there were specific peaks present for 4-cyanobiphenyl, 4-bromobenzonitrile and phenyl boronic acid. The flow rate used for analysis was $20 \mu\text{L min}^{-1}$ at $20 \text{ }^\circ\text{C}$. 0.2 M 4-cyanobiphenyl (Figure 4.3) gave an intense peaks at around 1190 , 1290 and 1614 cm^{-1} . The peaks were considered for calibration; however comparison between 4-cyanobiphenyl, 4-bromobenzonitrile and phenyl boronic acid needed to be carried out. Spectra of 4-bromobenzonitrile (Figure 4.4) and phenyl boronic acid (Figure 4.5) indicated that peaks at 278 , 411 , 778 , 1076 , 1185 and 1595 cm^{-1} for 4-bromobenzonitrile and 730 , 1005 and 1607 cm^{-1} for phenyl boronic acid. Although all the peaks were at different wavenumbers, they had the potential to overlap and cause interference with one another when analysing their peak area; for example, the peaks for 4-cyanobiphenyl at 1614 cm^{-1} could have overlapping areas with 4-bromobenzonitrile at 1595 cm^{-1} and phenyl boronic acid at 1607 cm^{-1} .

In selecting peaks for analysis however; it was not only the area under these peaks alone that would determine the calibration. Comparison of Figures 4.3, 4.4 and 4.5 showed a definitive change in background between the compounds. Separately calibrating the peaks may have proven any calibrations incorrect especially when contrasted with the change of compounds in a reaction. The rise in baseline as the

Raman Spectroscopic Monitoring - Results and Discussion

reaction proceeded would have made concentration determination potentially orders of magnitudes out from its actual value. Baseline subtraction was the solution to gaining the actual peak area and thus the actual concentration/conversion for a reaction. Baseline subtraction offered performed by subtracting a background noise area near to and the same width apart as the peak area of interest. 4-Bromobenzonitrile and phenyl boronic acid used the same background noise subtraction between the Raman shifts 749.04 - 751.29 cm^{-1} . 4-Cyanobiphenyl had a noise subtraction between the Raman shifts 1264.02 - 1273.71 cm^{-1} . The peaks of interest for 4-bromobenzonitrile, phenyl boronic acid and 4-cyanobiphenyl were chosen to be between the Raman shifts of 730.95 - 733.22 cm^{-1} , 778.23 - 780.47 cm^{-1} and 1291.08 - 1300.69 cm^{-1} respectively. These peaks were selected primarily because of their independence of interference with one another.

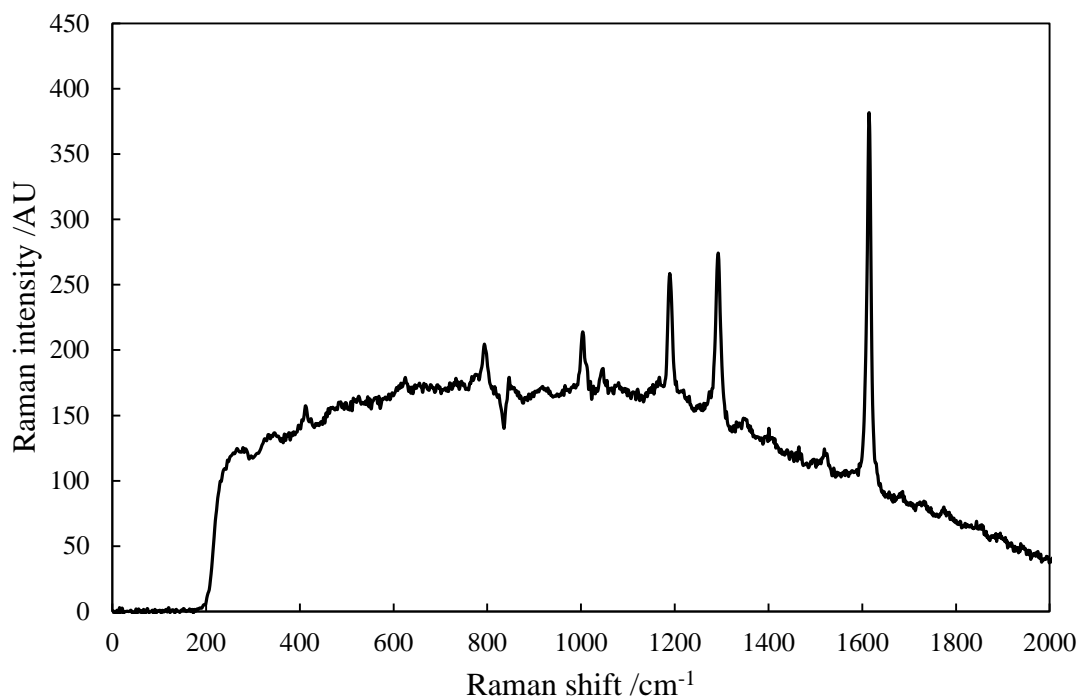
Raman Spectroscopic Monitoring - Results and Discussion

Figure 4.3 Raman spectrum of 0.2 M 4-cyanobiphenyl in 66.7% aqueous dioxane at $20 \mu\text{L min}^{-1}$ and $20 \text{ }^\circ\text{C}$. 66.7% aqueous dioxane was used as a dark spectrum and subtracted from the spectrum. An acquisition time of 200 ms was used and averaged from 3 spectra. Laser power was set to 340 mV and in built stray light and electric dark correction was active and set to the default factory settings.

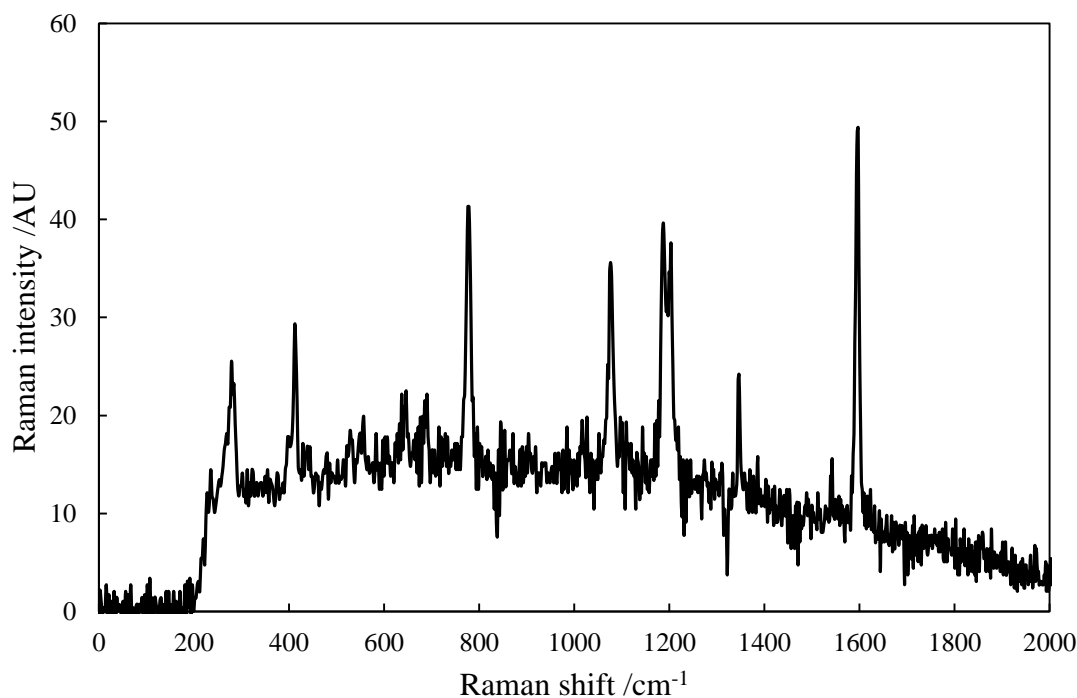
Raman Spectroscopic Monitoring - Results and Discussion

Figure 4.4 Raman spectrum of 0.2 M 4-bromobenzonitrile in 66.7% aqueous dioxane at $20 \mu\text{L min}^{-1}$ and $20 \text{ }^\circ\text{C}$. 66.7% aqueous dioxane was used as a dark spectrum and subtracted from the spectrum. An acquisition time of 200 ms was used and averaged from 3 spectra. Laser power was set to 340 mV and in built stray light and electric dark correction was active and set to the default factory settings.

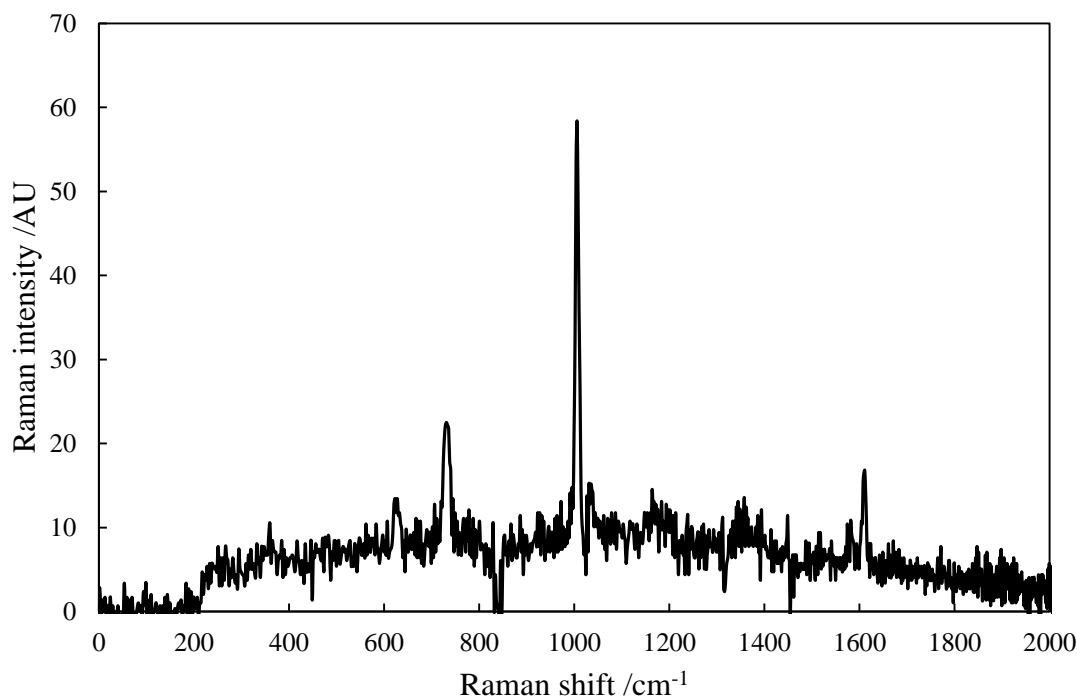
Raman Spectroscopic Monitoring - Results and Discussion

Figure 4.5 Raman spectrum of 0.2 M phenyl boronic acid in 66.7% aqueous dioxane at $20 \mu\text{L min}^{-1}$ and $20 \text{ }^\circ\text{C}$. 66.7% aqueous dioxane was used as a dark spectrum and subtracted from the spectrum. An acquisition time of 200 ms was used and averaged from 3 spectra. Laser power was set to 340 mV and in built stray light and electric dark correction was active and set to the default factory settings.

Raman Spectroscopic Monitoring - Results and Discussion

The calibration of these Suzuki reaction components was linear and each point coincides within 1 standard deviation for 4-bromobenzonitrile, phenyl boronic acid and 4-cyanobiphenyl (Figure 4.6, 4.7 and 4.8 respectively). This was not strictly true for 4-cyanobiphenyl, however, if the 200 mM Raman intensity result were seen as anomalous, the line of best fit would fit within one standard deviation of the spectra obtained. Deriving the line of best fit for each of the graphs demonstrated a strong correlation between concentration and Raman peak area intensity, by obtaining the equation for the line of best fit; these calibrations were used to predict Suzuki reaction conversions.

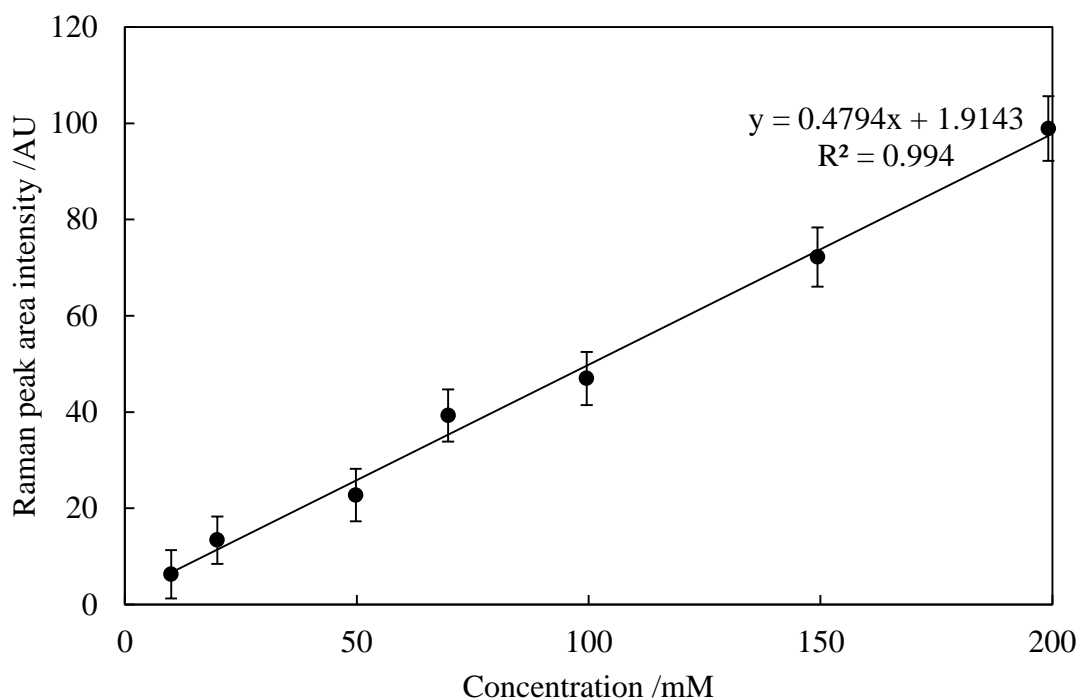
Raman Spectroscopic Monitoring - Results and Discussion

Figure 4.6 Raman spectra calibration of 4-bromobenzonitrile in 66.7% aqueous dioxane with a dark spectrum background subtraction of 66.7% aqueous dioxane. Concentrations of 0.0100, 0.0199, 0.0498, 0.0697, 0.0996, 0.1494 and 0.1992 M were used for the calibration flowing at $20 \mu\text{L min}^{-1}$ at $20 \text{ }^\circ\text{C}$. An acquisition time of 200 ms was used and averaged from 3 spectra. Laser power was set to 340 mV and in built stray light and electric dark correction was active and set to the default factory settings. The peak area of interest analysed was between Raman shifts $778.23 - 780.47 \text{ cm}^{-1}$ with noise subtraction between Raman shifts $749.04 - 751.29 \text{ cm}^{-1}$.

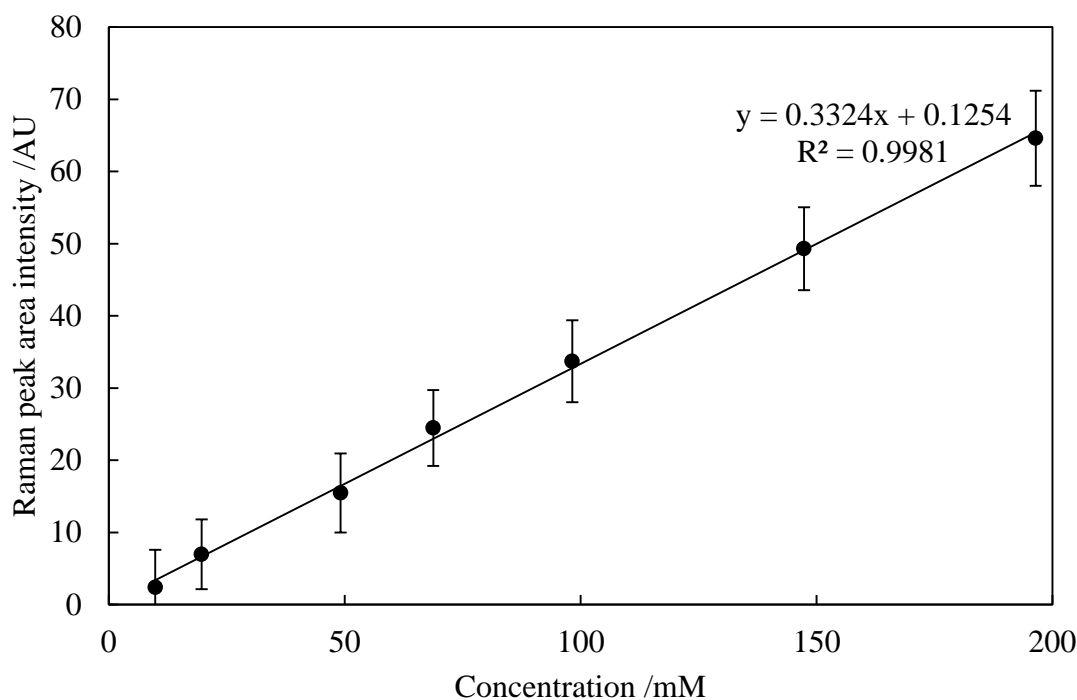
Raman Spectroscopic Monitoring - Results and Discussion

Figure 4.7 Raman spectra calibration of phenyl boronic acid in 66.7% aqueous dioxane with a dark spectrum background subtraction of 66.7% aqueous dioxane. Concentrations of 0.0098, 0.0196, 0.0491, 0.0688, 0.0982, 0.1474, and 0.1965 M were used for the calibration flowing at $20 \mu\text{L min}^{-1}$ at $20 \text{ }^\circ\text{C}$. An acquisition time of 200 ms was used and averaged from 3 spectra. Laser power was set to 340 mV and in built stray light and electric dark correction was active and set to the default factory settings. The peak area of interest analysed was between Raman shifts $730.95 - 733.22 \text{ cm}^{-1}$ with noise subtraction between Raman shifts $749.04 - 751.29 \text{ cm}^{-1}$.

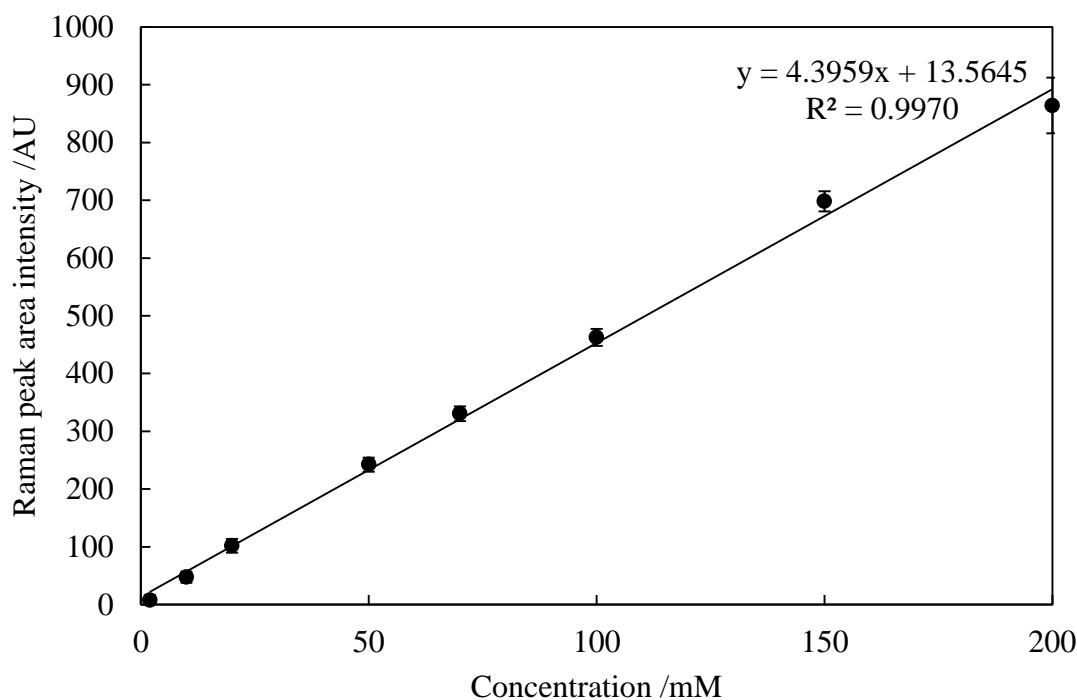
Raman Spectroscopic Monitoring - Results and Discussion

Figure 4.8 Raman spectra calibration of 4-cyanobiphenyl in 66.7% aqueous dioxane with a dark spectrum background subtraction of 66.7% aqueous dioxane. Concentrations of 0.0020, 0.0100, 0.0199, 0.0498, 0.0697, 0.0996, 0.1494 and 0.1992 M were used for the calibration flowing at $20 \mu\text{L min}^{-1}$ at 20°C . An acquisition time of 200 ms was used and averaged from 3 spectra. Laser power was set to 340 mV and in built stray light and electric dark correction was active and set to the default factory settings. The peak area of interest analysed was between Raman shifts $1291.08 - 1300.69 \text{ cm}^{-1}$ with noise subtraction between Raman shifts $1264.02 - 1273.71 \text{ cm}^{-1}$.

Raman Spectroscopic Monitoring - Results and Discussion*4.28 Raman spectral calibration B - results*

This method of calibration was basically the same as *Raman calibration 4.16* except the solvent was changed from 66.7% aqueous dioxane to 66.7% aqueous DMF. The reason for the change was that, whilst dioxane did give a higher activity than DMF in the Suzuki reaction, DMF heated more readily in a microwave due to its polar nature. Its significantly higher dielectric constant compared with dioxane (36.7 compared to 2.25) permits dielectric heating when subjected to microwave radiation. This suggests that the heating of DMF occurs much faster than dioxane and increases the rate of reaction in theory permitting shorter reaction times for the same amount of product.

Calibrating the analyte solutions is described in *Raman calibration 4.17*. The calibrations were shown to be highly linear once again. 4-Bromobenzonitrile, phenyl boronic acid and 4-cyanobiphenyl were calibrated in separate solutions of 66.7% aqueous DMF. Concentrations used were 0.0194, 0.0502, 0.0699, 0.1000 and 0.1513 M for 4-bromobenzonitrile, 0.0198, 0.0504, 0.0715, 0.1002 and 0.1505 M for phenyl boronic acid, and 0.0100, 0.0200, 0.0500, 0.0999 and 0.1499 M for 4-cyanobiphenyl. After positioning a line of best fit on each of the calibrations (Figure 4.9, 4.10, 4.11), it was clear that a directly proportional relationship was present between Raman peak area intensity and concentration of analyte in 66.7% aqueous DMF.

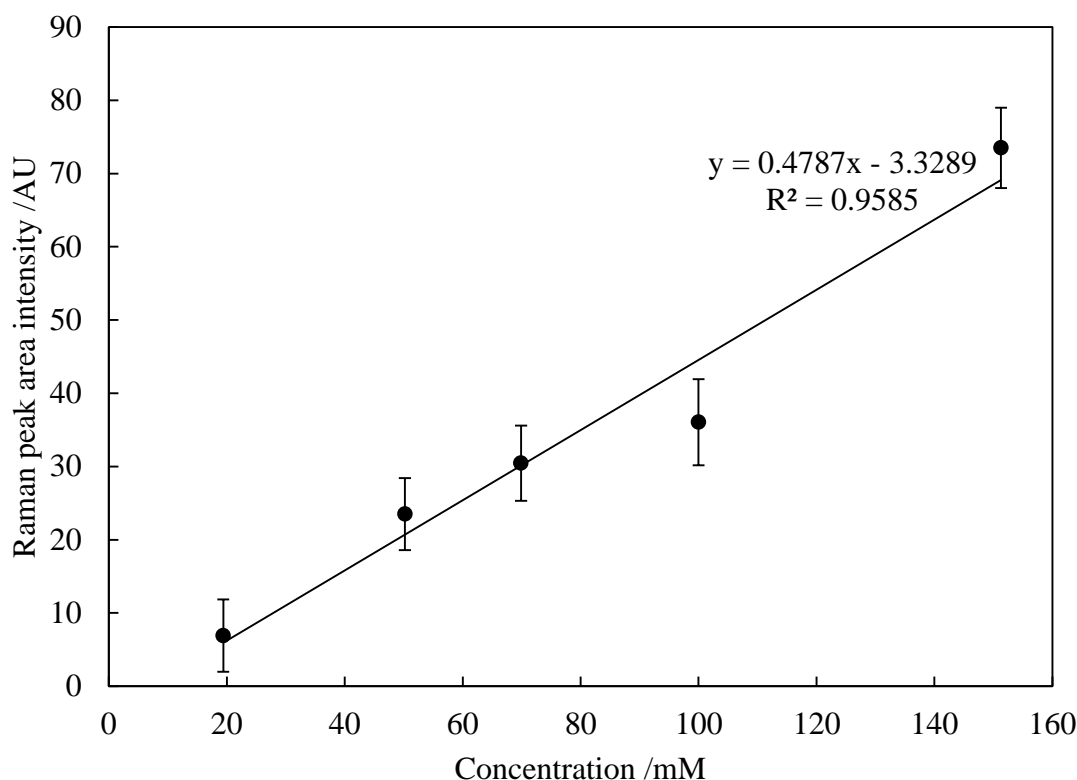
Raman Spectroscopic Monitoring - Results and Discussion

Figure 4.9 Raman spectra calibration of 4-bromobenzonitrile in 66.7% aqueous DMF with a dark spectrum background subtraction of 66.7% aqueous DMF. Concentrations of 0.0194, 0.0502, 0.0699, 0.1000 and 0.1513 M were used for the calibration flowing at $20 \mu\text{L min}^{-1}$ at $20 \text{ }^\circ\text{C}$. An acquisition time of 200 ms was used and averaged from 3 spectra. Laser power was set to 340 mV and in built stray light and electric dark correction was active and set to the default factory settings. The peak area of interest analysed was between Raman shifts $778.23 - 780.47 \text{ cm}^{-1}$ with noise subtraction between Raman shifts $749.04 - 751.29 \text{ cm}^{-1}$.

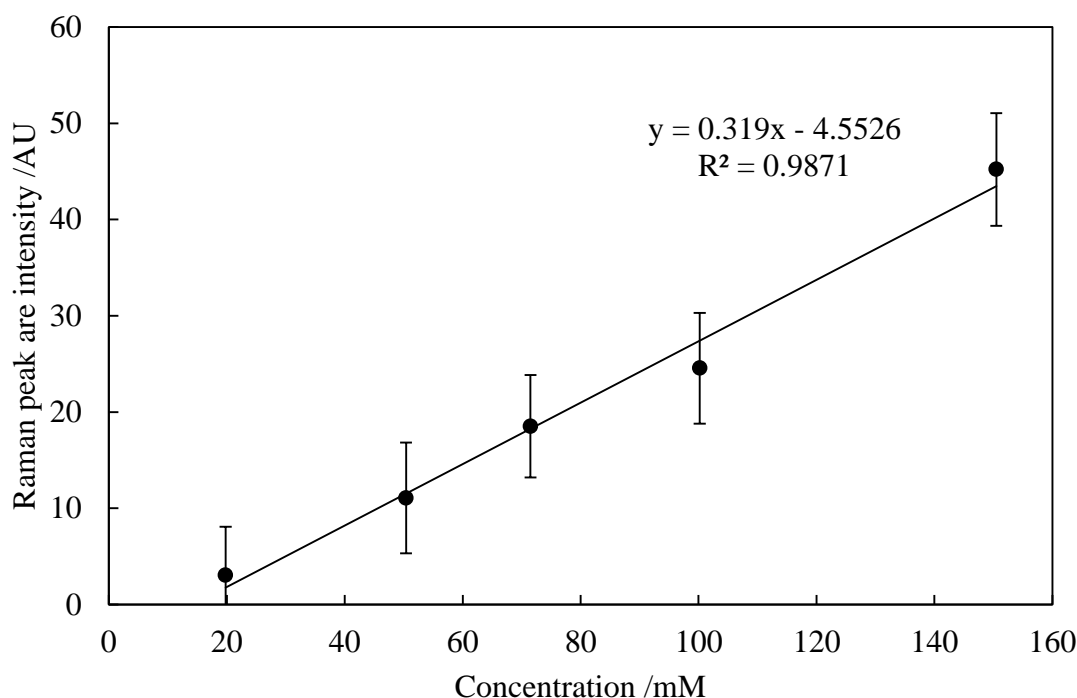
Raman Spectroscopic Monitoring - Results and Discussion

Figure 4.10 Raman spectra calibration of phenyl boronic acid in 66.7% aqueous DMF with a dark spectrum background subtraction of 66.7% aqueous DMF. Concentrations of 0.0198, 0.0504, 0.0715, 0.1002 and 0.1505 M were used for the calibration flowing at $20 \mu\text{L min}^{-1}$ at $20 \text{ }^\circ\text{C}$. An acquisition time of 200 ms was used and averaged from 3 spectra. Laser power was set to 340 mV and in built stray light and electric dark correction was active and set to the default factory settings. The peak area of interest analysed was between Raman shifts $730.95 - 733.22 \text{ cm}^{-1}$ with noise subtraction between Raman shifts $749.04 - 751.29 \text{ cm}^{-1}$.

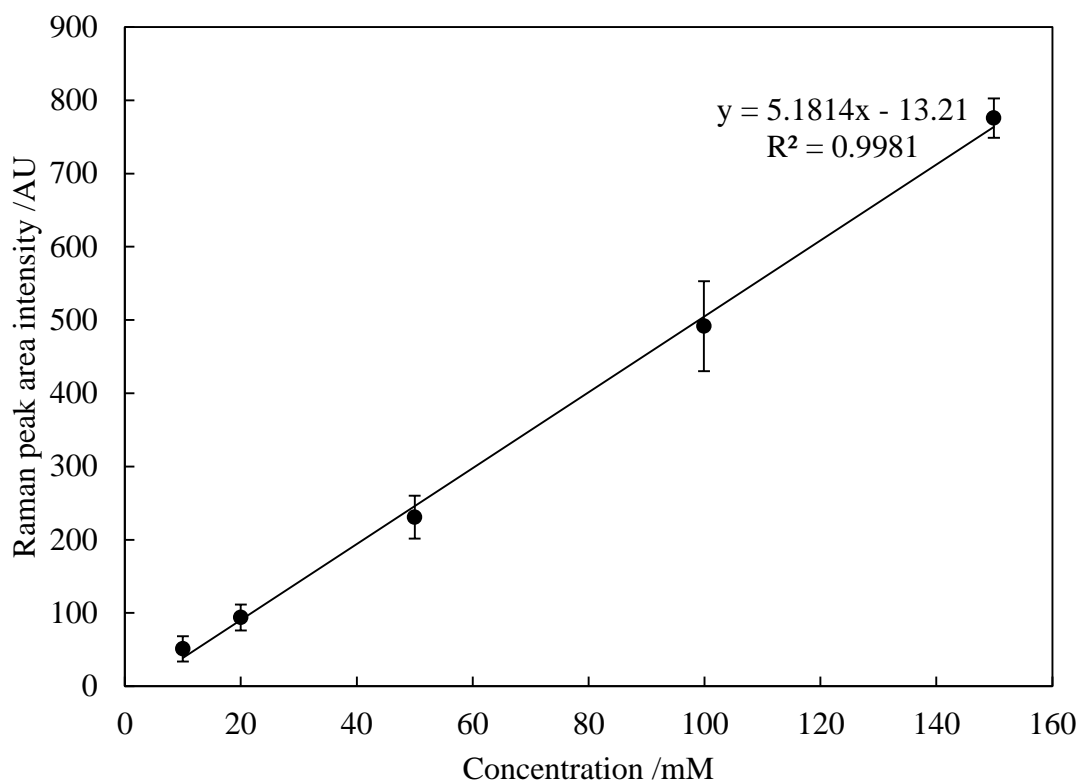
Raman Spectroscopic Monitoring - Results and Discussion

Figure 4.11 Raman spectra calibration of 4-cyanobiphenyl in 66.7% aqueous DMF with a dark spectrum background subtraction of 66.7% aqueous DMF. Concentrations of 0.0100, 0.0200, 0.0500, 0.0999 and 0.1499 M were used for the calibration flowing at $20 \mu\text{L min}^{-1}$ at $20 \text{ }^\circ\text{C}$. An acquisition time of 200 ms was used and averaged from 3 spectra. Laser power was set to 340 mV and in built stray light and electric dark correction was active and set to the default factory settings. The peak area of interest analysed was between Raman shifts $1291.08 - 1300.69 \text{ cm}^{-1}$ with noise subtraction between Raman shifts $1264.02 - 1273.71 \text{ cm}^{-1}$.

Raman Spectroscopic Monitoring - Results and Discussion

Solvent comparison on the Raman peak area was performed using SPSS software (IBM) and a two-tailed t-test performed at the 95% confidence level. The t-test is a comparison of the means of two groups of data taking into account the overlap of variance between the two data groups. In this case the groups of data contain dependent Raman peak area intensity responses to 4-bromobenzonitrile, phenyl boronic acid and 4-cyanobiphenyl. The two independent variables of the two data groups were the 66.7% aqueous dioxane and 66.7% aqueous DMF. Each concentration of the analytes had 16 spectral peak areas associated with it for dioxane and 16 spectral peak areas for DMF. The means of the 16 peak areas were obtained with their standard deviations. The null hypothesis for this comparison was “Varying the solvent does not affect the peak area observed for 4-bromobenzonitrile, phenyl boronic acid and 4-cyanobiphenyl”. The alternative hypothesis was “Varying the solvent does affect the peak area observed for 4-bromobenzonitrile, phenyl boronic acid and 4-cyanobiphenyl”.

The summary group statistics of the data sets is given in Table 4.3, Table 4.4 and Table 4.5. This summary of results was used to determine if there was a significant difference between the Raman peak area responses for 4-bromobenzonitrile, phenyl boronic acid and 4-cyanobiphenyl in the two solvents of 66.7% aqueous dioxane and 66.7% aqueous DMF. Tables 4.6, 4.7 and 4.8 show the results of the t-test for 4-bromobenzonitrile, phenyl boronic acid and 4-cyanobiphenyl respectively. The resulting significance from the t-test demonstrates that for 4-bromobenzonitrile at 50 and 150 mM, and for 4-cyanobiphenyl at 10 mM there is a significant difference between the calibration means. This suggests that the null hypothesis should be rejected and the alternative hypothesis be accepted. The null hypothesis was accepted for the phenyl boronic acid. Nevertheless, the null hypothesis was overall rejected as all

Raman Spectroscopic Monitoring - Results and Discussion

compounds at all concentrations would show no significant difference between Raman peak areas between the two solvents to be accepted. 66.7% aqueous dioxane and 66.7% aqueous DMF have an effect on the Raman peak area signal for the 3 analytes.

4-bromobenzonitrile

Dioxane_or_DMF		N	Mean	Std. Deviation	Std. Error Mean
150 mM	DMF	16	74.80	4.25	1.06
	Dioxane	16	72.83	3.19	0.80
100 mM	DMF	16	34.70	3.58	0.90
	Dioxane	16	46.26	3.03	0.76
70 mM	DMF	16	30.79	2.24	0.56
	Dioxane	16	37.76	3.34	0.83
50 mM	DMF	16	21.95	3.91	0.98
	Dioxane	16	20.64	2.56	0.64
20 mM	DMF	16	6.40	3.30	0.82
	Dioxane	16	14.28	3.11	0.78

Table 4.3 The summary group statistics of 5 calibration standard used in Figure 4.6 and Figure 4.9.

Raman Spectroscopic Monitoring - Results and Discussion

Phenyl boronic acid

Dioxane_or_DMF		N	Mean	Std. Deviation	Std. Error Mean
150 mM	Dioxane	16	49.48	4.30	1.07
	DMF	16	46.35	4.24	1.06
100 mM	Dioxane	16	34.42	5.64	1.41
	DMF	16	25.10	2.87	0.72
70 mM	Dioxane	16	24.01	2.30	0.57
	DMF	16	17.26	4.10	1.02
50 mM	Dioxane	16	15.00	3.54	0.88
	DMF	16	7.84	5.59	1.40
20 mM	Dioxane	16	6.86	2.93	0.73
	DMF	16	2.04	3.52	0.88

Table 4.4 The summary group statistics of 5 calibration standard used in Figure 4.7 and Figure 4.10.

Raman Spectroscopic Monitoring - Results and Discussion

4-cyanobiphenyl

Dioxane_or_DMF		N	Mean	Std. Deviation	Std. Error Mean
150 mM	Dioxane	16	699.37	13.74	3.43
	DMF	16	777.40	9.97	2.49
100 mM	Dioxane	16	457.06	5.78	1.45
	DMF	16	490.12	4.91	1.23
50 mM	Dioxane	16	244.96	8.18	2.04
	DMF	16	225.91	5.53	1.38
20 mM	Dioxane	16	103.22	5.47	1.37
	DMF	16	94.42	5.77	1.44
10 mM	Dioxane	16	48.95	5.02	1.25
	DMF	16	48.52	6.30	1.58

Table 4.5 The summary group statistics of 5 calibration standard used in Figure 4.8 and Figure 4.11.

Monitoring - Results and Discussion

		150 mM		100 mM		70 mM		50 mM		20 mM		
		Equal variances assumed	Equal variances not assumed	Equal variances assumed	Equal variances not assumed	Equal variances assumed	Equal variances not assumed	Equal variances assumed	Equal variances not assumed	Equal variances assumed	Equal variances not assumed	
t-test for Equality of Means	t	1.482	1.482	-9.858	-9.858	-6.93	-6.93	1.122	1.122	-6.955	-6.955	
	df	30	27.841	30	29.179	30	26.266	30	25.863	30	29.892	
	Sig. (2-tailed)	0.149	0.15	0	0	0	0	0.271	0.272	0	0	
	Mean Difference	1.969	1.969	-11.561	-11.561	-6.967	-6.967	1.31	1.31	-7.879	-7.879	
	Std. Error Difference	1.329	1.329	1.173	1.173	1.005	1.005	1.168	1.168	1.133	1.133	
	95% Confidence Interval of the Difference	Lower	-0.745	-0.754	-13.956	-13.959	-9.02	-9.032	-1.075	-1.091	-10.193	-10.193
		Upper	4.684	4.693	-9.166	-9.163	-4.914	-4.901	3.695	3.711	-5.566	-5.565

Table 4.6 the t-test results for the difference between Raman peak areas of 4-bromobenzonitrile in 66.7% aqueous dioxane and 66.7% aqueous DMF.

Spectra were recorded at $20 \mu\text{L min}^{-1}$ at $20 \text{ }^\circ\text{C}$. An acquisition time of 200 ms was used and averaged from 3 spectra. Laser power was set to 340 mV and in built stray light and electric dark correction was active and set to the default factory settings. The peak area of interest analysed was between Raman shifts $778.23 - 780.47 \text{ cm}^{-1}$ with noise subtraction between Raman shifts $749.04 - 751.29 \text{ cm}^{-1}$.

Monitoring - Results and Discussion

		150 mM		100 mM		70 mM		50 mM		20 mM		
		Equal variances assumed	Equal variances not assumed	Equal variances assumed	Equal variances not assumed	Equal variances assumed	Equal variances not assumed	Equal variances assumed	Equal variances not assumed	Equal variances assumed	Equal variances not assumed	
t-test for Equality of Means	t	2.076	2.076	5.892	5.892	5.751	5.751	4.33	4.33	4.207	4.207	
	df	30	29.995	30	22.258	30	23.599	30	25.348	30	29.04	
	Sig. (2-tailed)	0.047	0.047	0	0	0	0	0	0	0	0	
	Mean Difference	3.133	3.133	9.322	9.322	6.752	6.752	7.163	7.163	4.816	4.816	
	Std. Error Difference	1.509	1.509	1.582	1.582	1.174	1.174	1.654	1.654	1.145	1.145	
	95% Confidence Interval of the Difference	Lower	0.051	0.051	6.091	6.043	4.354	4.327	3.784	3.758	2.478	2.475
		Upper	6.216	6.216	12.553	12.601	9.15	9.177	10.541	10.567	7.154	7.158

Table 4.7 the t-test results for the difference between Raman peak areas of phenyl boronic acid in 66.7% aqueous dioxane and 66.7% aqueous DMF.

Spectra were recorded at 20 $\mu\text{L min}^{-1}$ at 20 $^{\circ}\text{C}$. An acquisition time of 200 ms was used and averaged from 3 spectra. Laser power was set to 340 mV and in built stray light and electric dark correction was active and set to the default factory settings. The peak area of interest analysed was between Raman shifts 730.95 - 733.22 cm^{-1} with noise subtraction between Raman shifts 749.04 - 751.29 cm^{-1} .

Monitoring - Results and Discussion

		150 mM		100 mM		50 mM		20 mM		10 mM		
		Equal variances assumed	Equal variances not assumed	Equal variances assumed	Equal variances not assumed	Equal variances assumed	Equal variances not assumed	Equal variances assumed	Equal variances not assumed	Equal variances assumed	Equal variances not assumed	
t-test for Equality of Means	t	-18.4	-18.387	-17.43	-17.43	7.719	7.719	4.425	4.425	0.214	0.214	
	df	30	27.372	30	29.228	30	26.355	30	29.916	30	28.568	
	Sig. (2-tailed)	0	0	0	0	0	0	0	0	0.832	0.832	
	Mean Difference	-78	-78.026	-33.061	-33.061	19.054	19.054	8.798	8.798	0.43	0.43	
	Std. Error Difference	4.244	4.244	1.897	1.897	2.468	2.468	1.988	1.988	2.014	2.014	
	95% Confidence Interval of the Difference	Lower	-86.7	-86.728	-36.934	-36.939	14.013	13.983	4.737	4.737	-3.683	-3.692
		Upper	-69.4	-69.325	-29.187	-29.183	24.095	24.124	12.859	12.86	4.543	4.552

Table 4.8 The t-test results for the difference between Raman peak areas of 4-cyanobiphenyl in 66.7% aqueous dioxane and 66.7% aqueous DMF.

Spectra were recorded at 20 $\mu\text{L min}^{-1}$ at 20 $^{\circ}\text{C}$. An acquisition time of 200 ms was used and averaged from 3 spectra. Laser power was set to 340 mV and in built stray light and electric dark correction was active and set to the default factory settings. The peak area of interest analysed was between Raman shifts 1291.08 - 1300.69 cm^{-1} with noise subtraction between Raman shifts 1264.02 - 1273.71 cm^{-1} .

Raman Spectroscopic Monitoring - Results and Discussion*4.29 Raman flow cell flow and pressure testing*

The Raman flow cell was tested to pressures up to 606.74 kPa whilst monitoring the 66.7% aqueous DMF between Raman shifts 870.98 - 873.16 cm^{-1} . Background noise was subtracted between Raman shifts 899.21 - 901.37 cm^{-1} in a similar fashion to *Raman calibration 4.16* and *Raman calibration 4.17* (described in 4.14). An adjustable back pressure regulator valve was placed in flow after the Raman flow cell and was adjusted to monitor the effect of pressure changes on the Raman signal. Figure 4.12 shows these changes and within 1 standard deviation of variation the peak areas generally overlap one another showing no significant relationship between pressure and Raman peak area.

After considering pressure from the flow system could affect the Raman spectrum, it was proven that it has so significant effect on Raman signal intensity. A factor to consider however was flow rate. Accordingly 0.1004 M 4-cyanobiphenyl in 66.7% aqueous dioxane was flowed at different flow rates (see section *Raman flow testing 4.15*) through the Raman flow cell. The peak monitored for the experiment was between Raman shifts 1291.08 - 1300.69 cm^{-1} with noise subtraction between Raman shifts 1264.02 - 1273.71 cm^{-1} . Figure 4.13 demonstrates the effect of flow rate on Raman peak area intensity. Each individual point overlaps with others within 1 standard deviation of variance in the peak areas and shows there is no trend of relationship between flow rate and Raman peak area intensity between 0 – 120 $\mu\text{L min}^{-1}$.

From these simple experiments, it can be determined that the pressure and flow rate of the liquid in the Raman flow cell have no significant effect on the Raman signal

Raman Spectroscopic Monitoring - Results and Discussion

intensity. This is because in the system designed here, the only possible effects on Raman signal intensity would be derived from solution concentration, temperature, opacity, homogeneity, laser power and sample position.

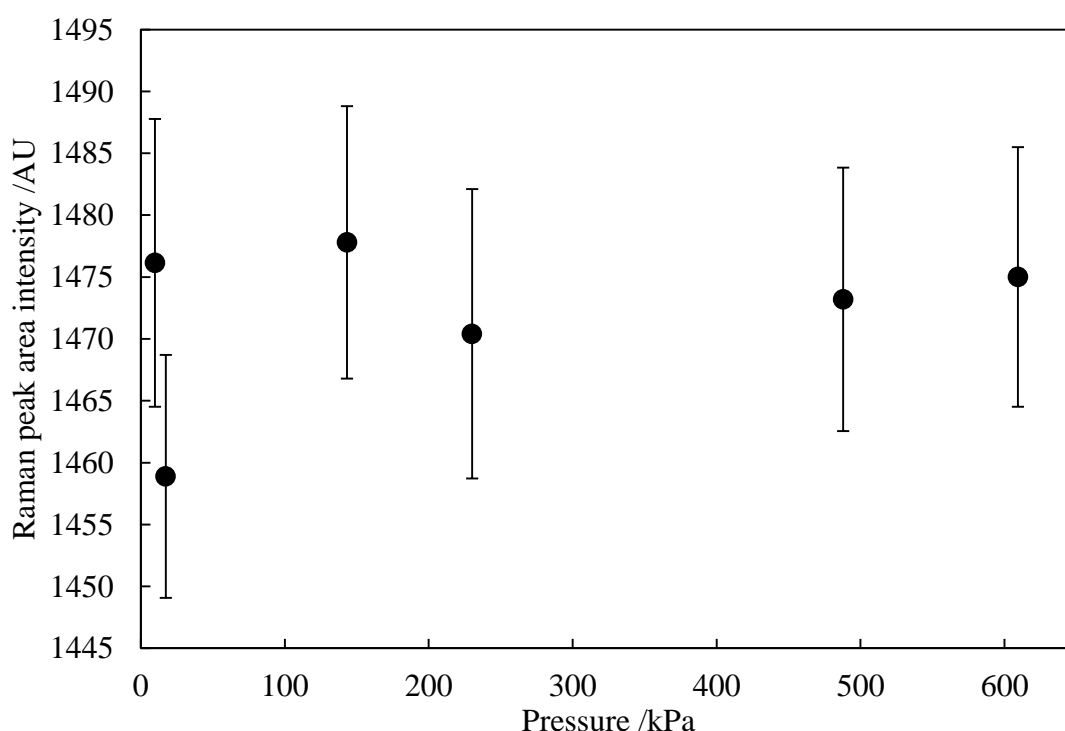


Figure 4.12 Pressure effects on Raman peak area of 66.7% aqueous DMF at $20 \mu\text{L min}^{-1}$. The temperature of the solution recorded was at $20 \text{ }^\circ\text{C}$. The Raman peak observed was between Raman shifts $870.98 - 873.16 \text{ cm}^{-1}$ with noise subtraction between Raman shifts $899.21 - 901.37 \text{ cm}^{-1}$. The spectral conditions used to obtain the data were a 200 ms integration time averaged 3 times with electrical and stray light correction default from the software. The laser used was a 785 nm laser with a power of 340 mW.

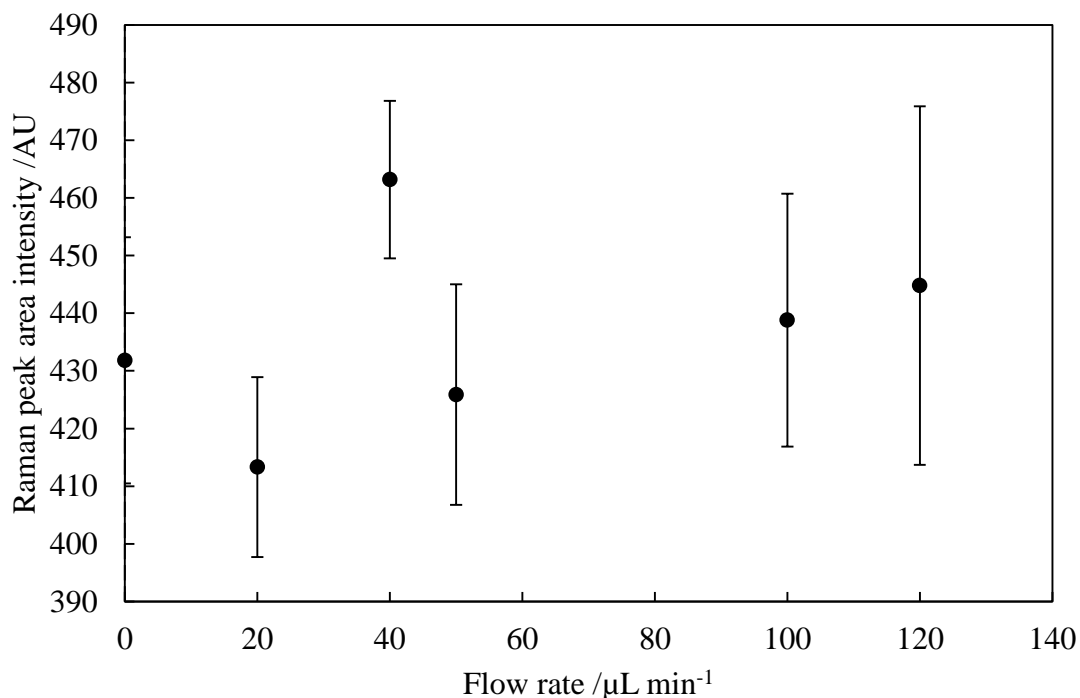
Raman Spectroscopic Monitoring - Results and Discussion

Figure 4.13 Flow effect on Raman peak area intensity of 0.1004 M 4-cyanobiphenyl in 66.7% aqueous dioxane. The Raman peak observed was between Raman shifts 870.98 - 873.16 cm^{-1} with noise subtraction between Raman shifts 899.21 - 901.37 cm^{-1} . The spectral conditions used to obtain the data were a 200 ms integration time averaged 3 times with electrical and stray light correction default from the software. The laser used was a 785 nm laser with a power of 340 mV. A 66.7% aqueous dioxane spectrum was used as a dark spectrum and subtracted from the original spectra.

Raman Spectroscopic Monitoring - Results and Discussion*4.30 Flow reaction monitoring*

A Raman flow cell (volume of approximately 150 μL from flow entrance to exit) was added to the flow Suzuki reaction system previously described in *flow design 3.6*. A CMR made from *monolith 2.5* with *palladium loading 2.14* was used for the reaction. The methodology is detailed in *Flow Suzuki reaction 4.10*. A flow rate of 20 μLmin^{-1} allowed a 12 minute catalyst contact reaction time. The reactions were subjected to 20 W of microwave energy; however the temperatures of the reactions were significantly different. The temperature of the 66.7% aqueous dioxane reaction mixture only reached 59 $^{\circ}\text{C}$ whereas the 66.7% aqueous DMF reached 80 $^{\circ}\text{C}$. This change in heating temperature confirms what was previously suggested that DMF heats more readily when subjected to microwave energy because of its higher dielectric constant.

The reactions were analysed by Raman calibrations from *Raman calibration 4.16* and *Raman calibration 4.17*, as well as analysed by GC-MS (see section *GC-MS analysis 4.2*). The Raman spectra for the two reactions are shown in Figure 4.14. These spectra of the two reaction mixture solvents post-reaction demonstrate a rise in background for the DMF solvent.

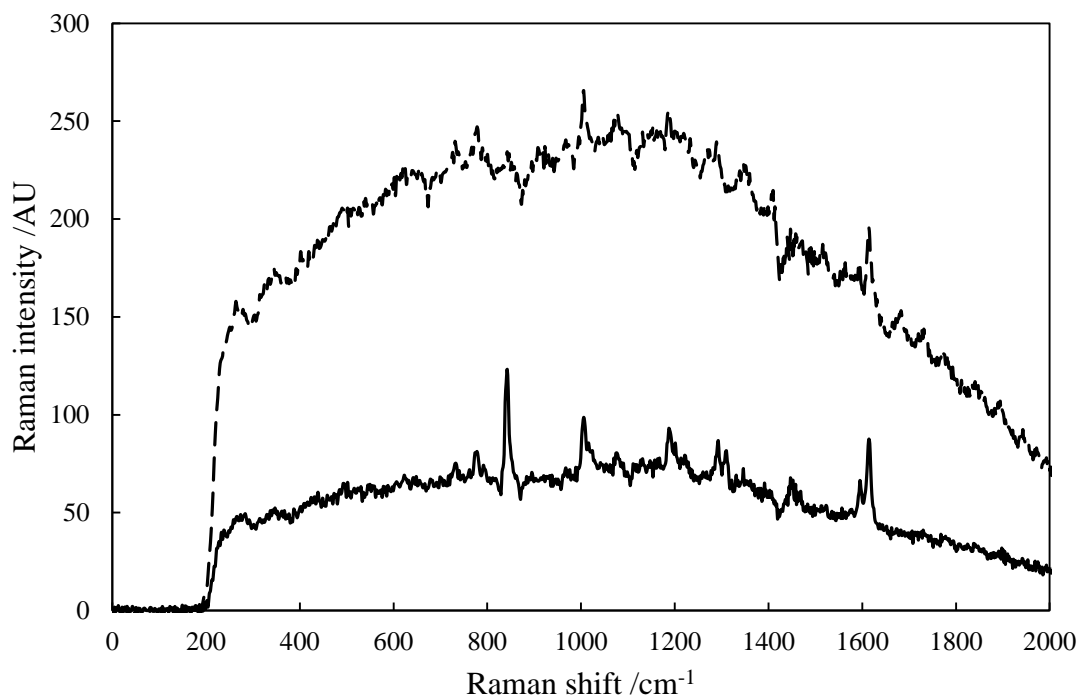
Raman Spectroscopic Monitoring - Results and Discussion

Figure 4.14 The Raman spectra of the reaction mixtures of 0.10 M 4-bromobenzonitrile, 0.12 M phenyl boronic acid and 0.24 M potassium carbonate. The reaction mixtures were passed through a CMR manufactured from *monolith 2.5* and *palladium loading 2.14* with a void pore volume of 240 μL . The flow system used was previously described in *flow design 3.6*. The reaction proceeded at 20 W of microwave power with two different solvents; 66.7% aqueous dioxane as the solid line and 66.7% aqueous DMF as the dashed line. Reaction temperatures were 59 and 80 $^{\circ}\text{C}$ respectively.

When attempting to determine the predicted conversion for the reaction, it was found that the Raman calibration from *Raman calibration 4.17* could not determine the conversion (predicted negative concentrations of 4-cyanobiphenyl of -7 ± 2.5 mM). GC-

Raman Spectroscopic Monitoring - Results and Discussion

MS prediction of the DMF solvent reaction predicted a 28% conversion (see Appendix 17 for chromatograph). This suggests that either the DMF is masking the Raman spectra once it is irradiated or once it comes into contact with the catalyst. The dioxane prediction was however quite accurate. The Raman calibration from *Raman calibration 4.16* had predicted a $24\pm 2\%$ conversion and GC-MS predicted a 24% conversion (Appendix 18). Having observed the success of the Raman predictability for the dioxane solvent calibration, this was re-assessed by more flow reactions (as described in *Flow Suzuki reaction 4.10*). Table 4.9 summarises the reaction conditions for the flow over the same catalyst (see Appendix 19 for chromatograms). Over 300 Raman spectral areas were recorded and averages used to construct Table 4.9. A reaction time of 15 minutes corresponded to a flow rate of $20 \mu\text{Lmin}^{-1}$ and a reaction time of 30 minutes resulted from a flow rate of $10 \mu\text{Lmin}^{-1}$. Some of the Raman and GC-MS conversions were within ± 10 of one another. However the higher conversion saw a much greater difference between the two predictions (GC-MS predictions of 96% and 62%). Another feature seen between the two predictions was the trend of GC-MS predicting higher conversions in all reactions compared to the Raman. A final observation was that the Raman predicted a -2% conversion which was not possible, nevertheless after viewing the variance in the Raman spectra used to observe this value, 0% conversions lay within 1 standard deviation of the data. On attempting to perform more reactions on the same CMR however, the CMR broke down and a dark brown/black residue was visibly observed to be leaching from the monolith. It was postulated that the intense heating from the microwave power was creating small gas pockets which were rupturing the

Raman Spectroscopic Monitoring - Results and Discussion

monolith structural integrity, or that the intense heating was causing rapid dissolution of palladium from the surface of the silica.

Regardless of why the catalyst was breaking down, the Raman spectral calibrations were not predicting correctly all the time and different calibration methods were used in order to define the calibration model used for the Raman system.

Flow rate / $\mu\text{L min}^{-1}$	Microwave power /W	Conversion /%	
		GC-MS	Raman
10	10	42	34
10	20	96	59
20	10	17	15
20	20	62	41
40	10	3	-2
40	20	30	29

Table 4.9 The Suzuki reaction predictions of 0.10 M 4-bromobenzonitrile, 0.12 phenyl boronic acid and 0.24 M potassium carbonate in 66.7% aqueous dioxane. The catalyst used for the reaction was produced from *monolith 2.5* and *palladium loading 2.14* with a void pore volume of 300 μL . The predictions of the Raman were calculated from *Raman calibration 4.16*.

Raman Spectroscopic Monitoring - Results and Discussion*4.31 Microwave power vs Reaction conversion*

To observe the effects of microwave heating on the reaction conversion, the Raman flow cell was removed from the flow system leaving the flow system described in *flow design 3.5*. A CMR was prepared from *monolith 2.5* with *palladium loading 2.14* was used for the reaction. The reaction mixture concentrations were outlined in *Flow Suzuki reaction 4.10*. 66.7% aqueous dioxane was the chosen solvent. A flow rate of $20 \mu\text{L min}^{-1}$ was set and maximum power varied from 10, 20, 25, 30, 35, 40 and 45 W. The products of the reactions were analysed using GC-MS from *GC-MS analysis 4.2*. The results demonstrate that the increase in conversion is observed up to 20 W, after which a decline in conversion is observed (Figure 4.15). Appendix 20 contains all the GC-MS chromatograms used to construct Figure 4.15. After the applied power the CMR was observed to shrink away from the heat shrink tubing walls permitting flow to pass around the monolith rather than through its pores. This could have been due to the increase in surface temperature of the catalyst causing expansion of the silica and thus expanding the tubing and then shrinking once cooled. A different theory was that the monolith was breaking down under these intense microwave conditions and over exposure of the microwaves on the silica was causing a breakdown (see section 4.30).

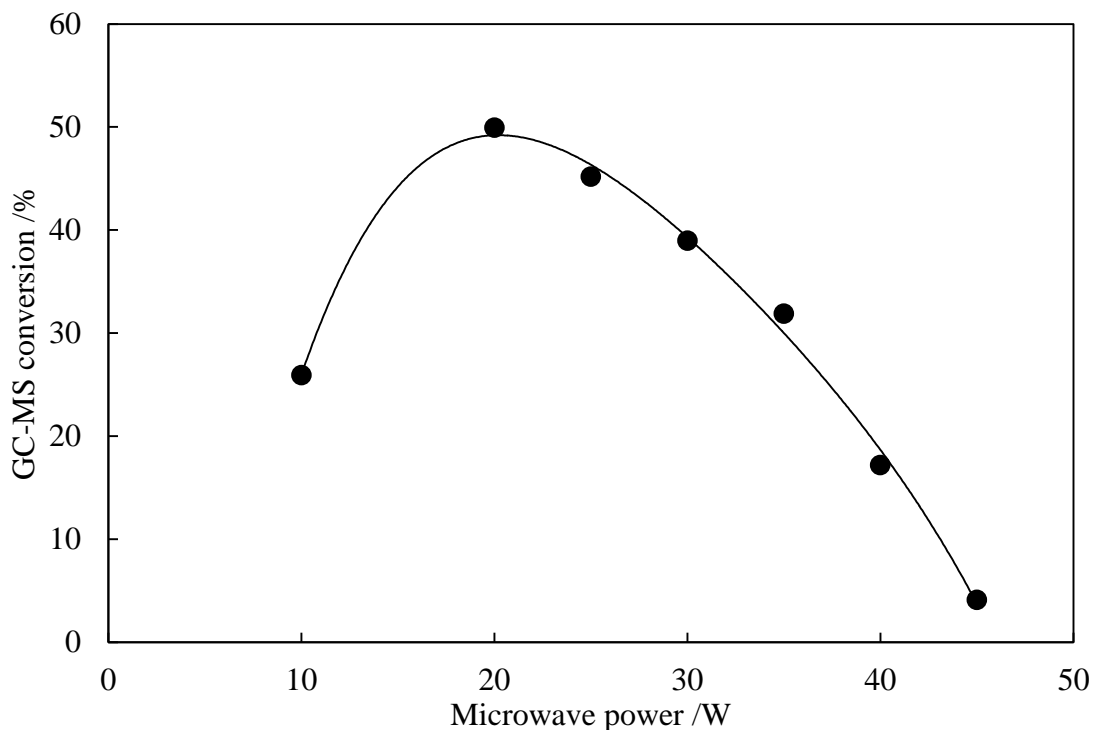
Raman Spectroscopic Monitoring - Results and Discussion

Figure 4.15 The effect of microwave power on Suzuki reaction conversion. The reaction mixture was 0.10 M 4-bromobenzonitrile, 0.12 M phenyl boronic acid and 0.24 M potassium carbonate. The reaction mixtures were passed through a CMR manufactured from *monolith 2.3* with *palladium loading 2.12* with a void pore volume of 240 μL . The flow system used was previously described in *flow design 3.5*. The wattages were varied and flow rate kept constant at 20 $\mu\text{L min}^{-1}$. GC-MS analysis was performed using *GC-MS analysis 4.2*.

Raman Spectroscopic Monitoring - Results and Discussion*4.32 Raman spectral calibration C – results*

The previous calibrations of the Raman spectra for varying concentrations of 4-bromobenzonitrile, phenyl boronic acid and 4-cyanobiphenyl proved unsuccessful. A contributing factor to this was the interaction between the compounds was not being taken into consideration. Each of the calibration solutions previously contained only one variable concentration and one analyte. This approach did not take account of the molecular interaction in reaction solution. For example, observing the spectra for calibrations used for 4-cyanobiphenyl saw an increase in spectral background. This rise altered the peak intensities and masking the 4-bromobenzonitrile peaks and phenyl boronic acid peaks. Subsequently the presence of the reagents could slightly quench any fluorescence signal arising from the 4-cyanobiphenyl background (Figure 4.16). Either way the Raman concentration prediction was false. To account for intermolecular effects and electron distortions from outer molecular influences, all Raman experiments were subsequently moved to a dark room and kept at 20 °C. The intermolecular effects between the components of the reaction were accounted for by standard reaction conversion solutions. Varying different concentrations of 4-bromobenzonitrile, phenyl boronic acid and 4-cyanobiphenyl allowed a true insight into the Raman spectra of the reaction including background interferences. Standard solutions were made to mimic 0, 20, 40, 60, 80 and 100% concentrations (Table 4.1).

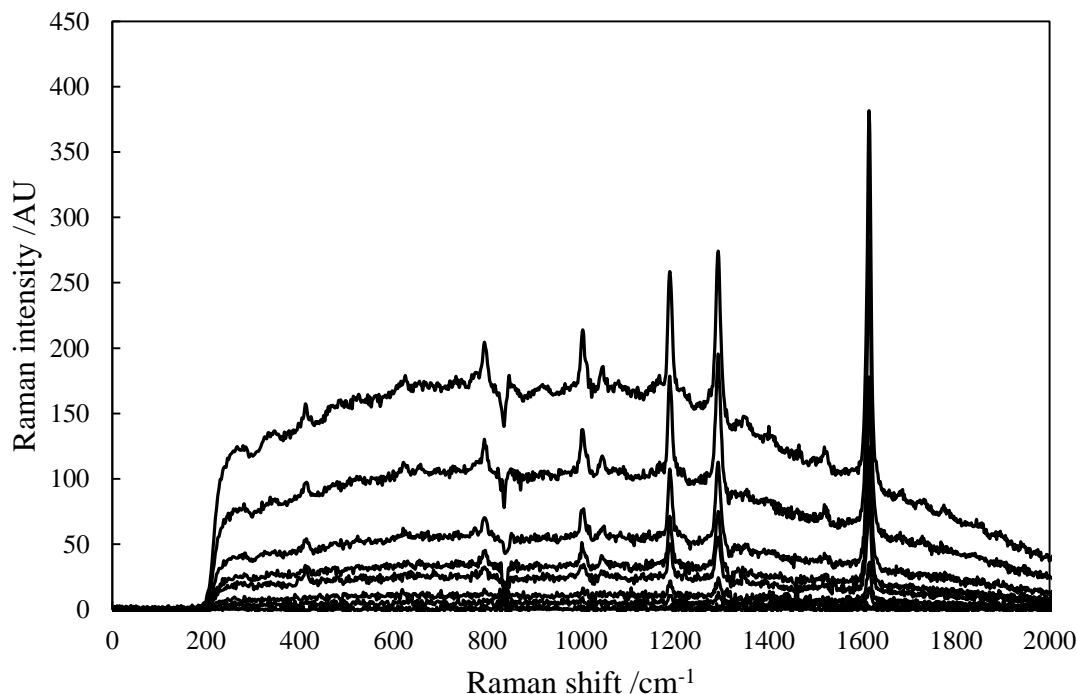
Raman Spectroscopic Monitoring - Results and Discussion

Figure 4.16 The Raman spectra of increasing concentrations of 4-cyanobiphenyl in 66.7% aqueous dioxane. Concentrations of 4-cyanobiphenyl were 0.0020, 0.0100, 0.0199, 0.0498, 0.0697, 0.0996, 0.1494 and 0.1992 M. The spectra were used to construct the calibration graph shown in Figure 4.17. The spectral conditions used to obtain the data were a 1 s integration time averaged 3 times with electrical and stray light correction default from the software. Laser power was set to 340 mV.

Raman Spectroscopic Monitoring - Results and Discussion

The calibration spectra produced an elevation in the background but this did occur for all the constituents that would otherwise be present in the reaction. Figure 4.17 expresses the calibration produced by *Raman calibration 4.18*. Only two compounds were calibrated, the limiting reactant and the product (4-bromobenzonitrile and 4-cyanobiphenyl respectively). As previously, the background noise of a non-specific Raman shift area was subtracted from the 4-bromobenzonitrile and 4-cyanobiphenyl peak. The noise used was between Raman shifts $1570.78 - 1576.05 \text{ cm}^{-1}$. Peaks used for the calibration were between Raman shifts $1591.81 - 1597.04 \text{ cm}^{-1}$ and $1616.15 - 1621.34 \text{ cm}^{-1}$ for 4-bromobenzonitrile and 4-cyanobiphenyl respectively. The calibration graphs prove to be highly linear with an exception of the solution standard 100% conversion. However there are several features observed in the calibration graph shown in Figure 4.17 that was significant. Even though there is a substantial response difference between the two compounds, they can be distinguished from one another. In addition the concentration of 4-bromobenzonitrile at 0 M still gives a relatively high signal. The standard deviation doesn't pass through 0 and suggests there is a contributing influence from something else in the simulated reaction mixture. Examination of the spectra of the calibration (Figure 4.18) for region of interest shows that the increase of the peak for 4-bromobenzonitrile at 100% conversion (0 M 4-bromobenzonitrile) consists of the tail of the 4-cyanobiphenyl peak. An interesting detail was that the spectra were still rising as the concentration of 4-cyanobiphenyl rises.

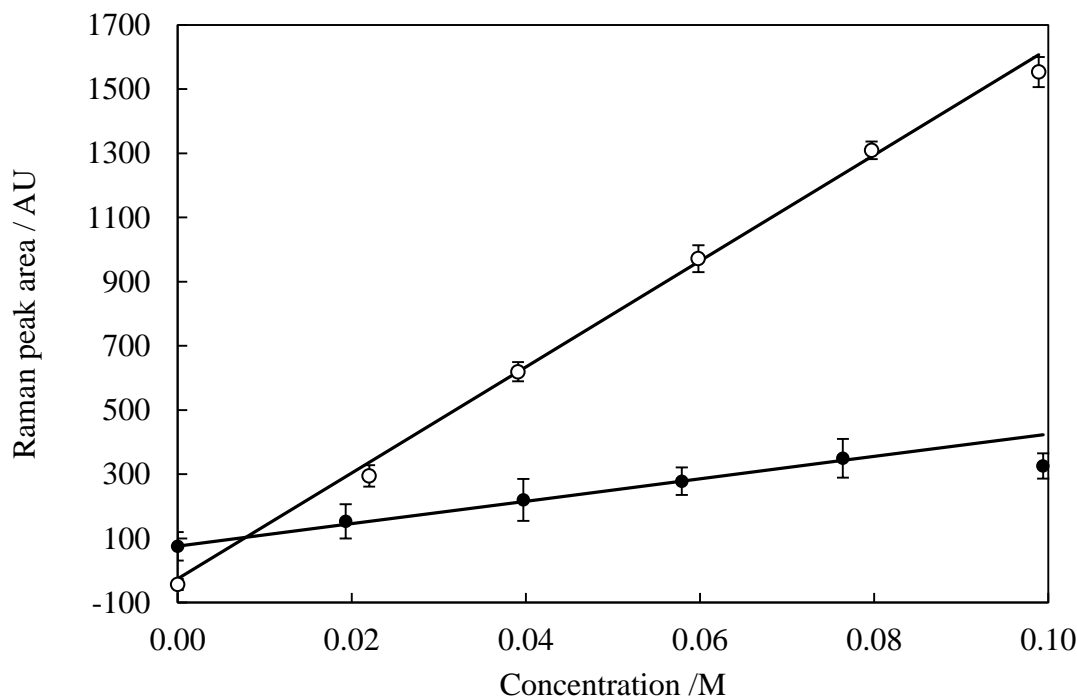
Raman Spectroscopic Monitoring - Results and Discussion

Figure 4.17 The Raman calibration of 4-bromobenzonitrile (●) and 4-cyanobiphenyl (○). The standard solutions used for calibration were described previously in Table 4.1. Peak areas observed between Raman shifts 1591.81 - 1597.04 cm^{-1} and 1616.15 - 1621.34 cm^{-1} respectively. Noise area subtraction for both peaks was between Raman shifts 1570.78 - 1576.05 cm^{-1} . Each calibration solution was flowed at 80 $\mu\text{L min}^{-1}$. The spectral conditions used to obtain the data were a 1 s integration time averaged 3 times with electrical and stray light correction default from the software. Laser power was set to 340 mV.

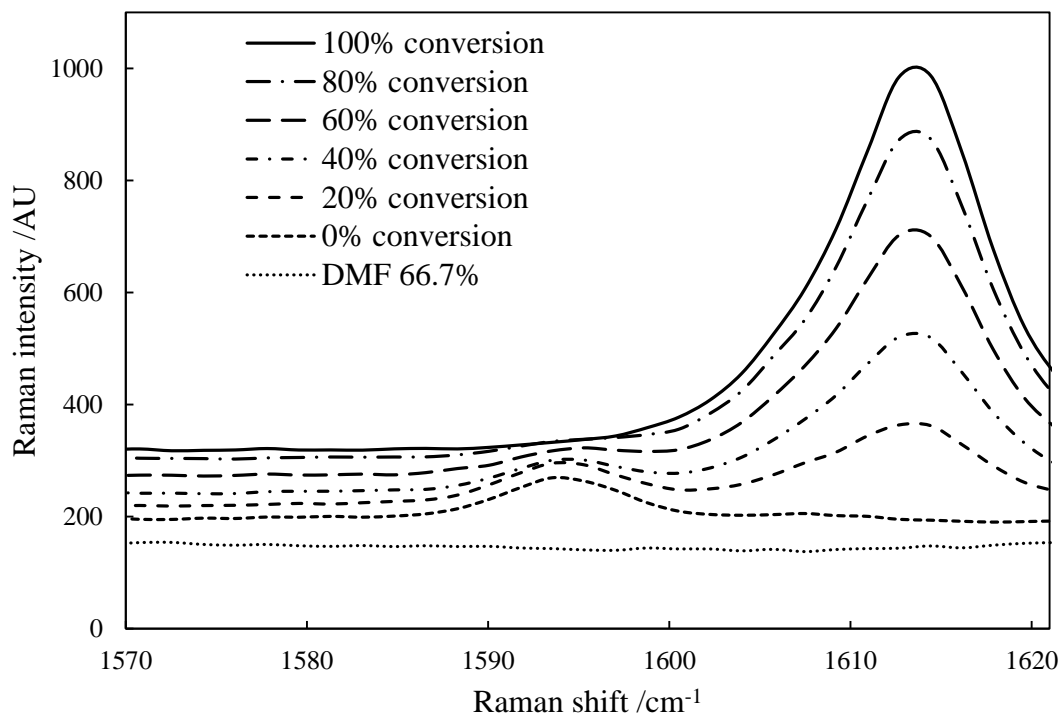
Raman Spectroscopic Monitoring - Results and Discussion

Figure 4.18 Raman spectra of the standard solutions used for the calibration of 4-bromobenzonitrile and 4-cyanobiphenyl in Figure 4.17. The standard solutions used for the spectra were described previously in Table 4.1. Each calibration solution was flowed at $80 \mu\text{L min}^{-1}$. The spectral conditions used to obtain the data were a 1 s integration time averaged 3 times with electrical and stray light correction default from the software. Laser power was set to 340 mV.

Raman Spectroscopic Monitoring - Results and Discussion*4.33 GC-MS analysis calibration*

The standard reaction solutions were also passed through the GC-MS using *GC-MS analysis 4.3*. A calibration involving an internal standard (decane) was used for a more accurate determination of analyte concentration and reaction conversion. Appendix 21 shows the chromatograms used to produce the calibration graph shown in Figure 4.19. The basis of this calibration was on the stability of response of the internal standard. This gave relative peak intensity in the chromatograph that permitted the quantification of 4-bromobenzonitrile and 4-cyanobiphenyl. The areas of the peaks were determined and the percentage peak area intensity between the analyte peak and the internal standard peak was calculated and plotted with the concentration of the analyte. Unlike the Raman detection, the mass spectrometry shows no difference between these organic compounds. The linear relationship between 4-bromobenzonitrile and 4-cyanobiphenyl concentration were both similar. The trend line for calibration appears to be indistinguishable from one another. This method of comparative analysis appeared to be preferable for determining the predictions of the Raman calibration compatibility.

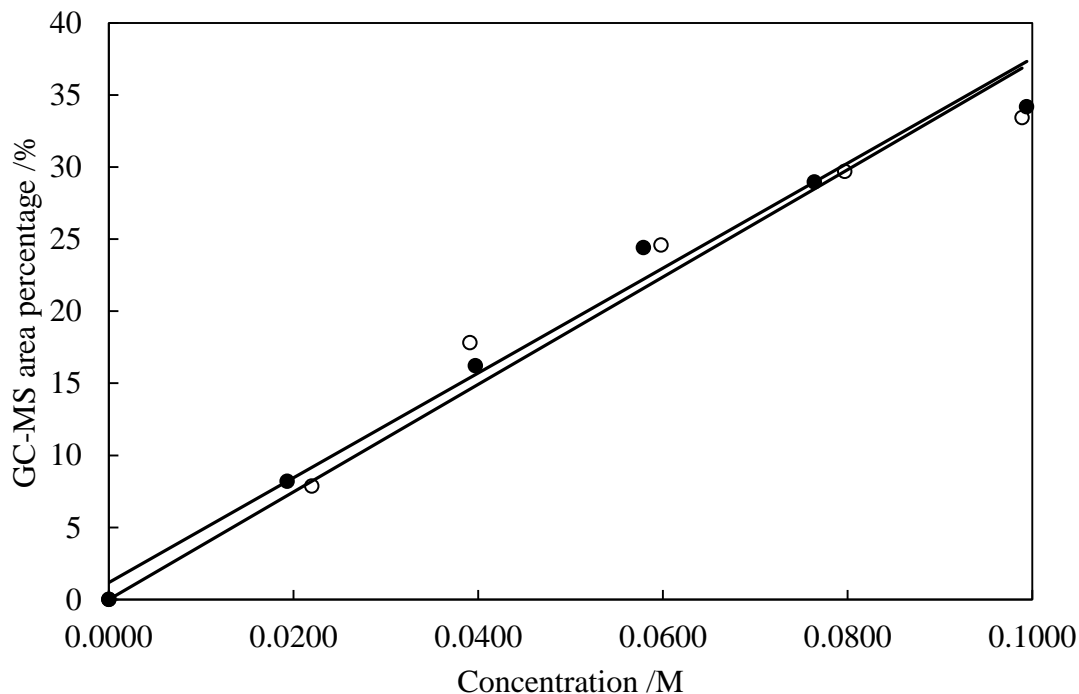
Raman Spectroscopic Monitoring - Results and Discussion

Figure 4.19 GC-MS calibration of 4-bromobenzonitrile (•) and 4-cyanobiphenyl (○) with decane as an internal standard. The chromatographic peaks of interest were 6.42, 11.13 and 15.29 minutes for decane, 4-bromobenzonitrile and 4-cyanobiphenyl respectively. The method for obtaining the data used for the calibration was described in *GC-MS analysis 4.3*.

Raman Spectroscopic Monitoring - Results and Discussion*4.34 Raman spectral calibration C validation*

As in previous work, the Raman calibration was tested using Suzuki flow reactions. The first Suzuki reaction used to test the model was described in *Flow Suzuki reaction 4.10* with 66.7% aqueous DMF at 2 W microwave power. The CMR used was made from *monolith 2.5* with *palladium loading 2.14* with a void volume of 560 μL . At $80 \mu\text{Lmin}^{-1}$ the residence time (catalyst contact) was set at 7 minutes. The reaction temperature was found to be 100 °C. This seemed to be a high temperature for such a low power and was thought to result from increasing the CMR diameter and permitting more of the reactant solvent to interact with the microwave energy. The GC-MS concentrations for the product of the reaction were found to be 0.0722 and 0.0324 M for 4-bromobenzonitrile and 4-cyanobiphenyl respectively. This compared to Raman concentration predictions of 0.0804 and 0.0227 M for 4-bromobenzonitrile and 4-cyanobiphenyl respectively. This relates to a prediction of 28 and 20% conversion for GC-MS and Raman prediction respectively to 4-bromobenzonitrile. This also represents 32 and 23% conversion for GC-MS and Raman prediction respectively for 4-cyanobiphenyl (GC-MS chromatograph shown in Appendix 22). All these conditions showed a $\pm 10\%$ relationship to one another showing some promise for this method of calibration.

An increasing issue with the reaction mixture leaking had occurred during reactions to confirm the Raman calibrations. This was observed previously after repositioning the CMR to a horizontal position in the microwave cavity. Once the CMR was placed horizontally, the only way possible to increase reactor size was to increase its diameter. This presented difficulty when joining the palladium embedded monolith

Raman Spectroscopic Monitoring - Results and Discussion

to the glass connectors. The glass connectors were turned near the end to attach to the monolith and thinned out to allow a PTFE connection to the PEEK tubing. Because the heat shrink tubing used to connect the monolith to the glass is based on friction (between the tubing and the glass) an increase in pressure could overcome the friction forces and sever the connection between the glass and the heat shrink tubing. The increase in monolith diameter was thought to increase the localised pressure relative the glass capillary. This dilemma presented not only difficulties in controlling the flow system but also safety concerns as the liquid from the flow system were leaking into the microwave cavity. In an attempt to control the safety aspect of the system and to obtain a more uniform heating control, the microwave was replaced with a water bath and the glass connectors clamped to the heat shrink tubing. This resulted in a more successful approach, nevertheless after prolonged periods the connectors leaked once again due to the increase in pressure. A further disadvantage was that now the highly controllable aspects of microwave heating were eliminated. However by removing the microwave, the breakdown of the CMRs structure was not observed; confirming that the intensity of microwave energy on the reaction solution was destroying the CMR.

Validating the Raman calibration for *Raman calibration 4.18* was performed using the modified GC-MS calibration (Figure 4.19). By comparing the results of the Raman spectra with the average GC-MS chromatograms for 5 reaction solutions (All chromatograms are in Appendix 23), it was possible to determine the viability of the Raman calibration. Table 4.10 summarises the reaction conditions used from the 5 reactions. Reactions A and B used different size CMRs for reactions whilst C, D and E used a much larger catalyst void volume, permitting an increased flow rate for a lower

Raman Spectroscopic Monitoring - Results and Discussion

residence time in the tubing of the flow system. This meant that the Raman spectral data was achieved faster as well as having possibilities of a higher turnover of 4-cyanobiphenyl production.

Reaction	CMR void volume /mL	Flow rate /mL min ⁻¹	CMR residence time /min	Reaction temperature / °C
A	0.56	0.08	7.0	78
B	0.56	0.04	14.0	93
C	2.70	0.10	27.0	90
D	2.70	0.05	54.0	90
E	2.70	0.05	54.0	90

Table 4.10 Reaction conditions of the Suzuki reaction between 0.10 M 4-bromobenzonitrile, 0.12 M phenyl boronic acid and 0.24 M potassium carbonate in 66.7% aqueous DMF. The reaction was heated by a water bath and the catalyst used was previously described in *monolith 2.5* with *palladium loading 2.14*.

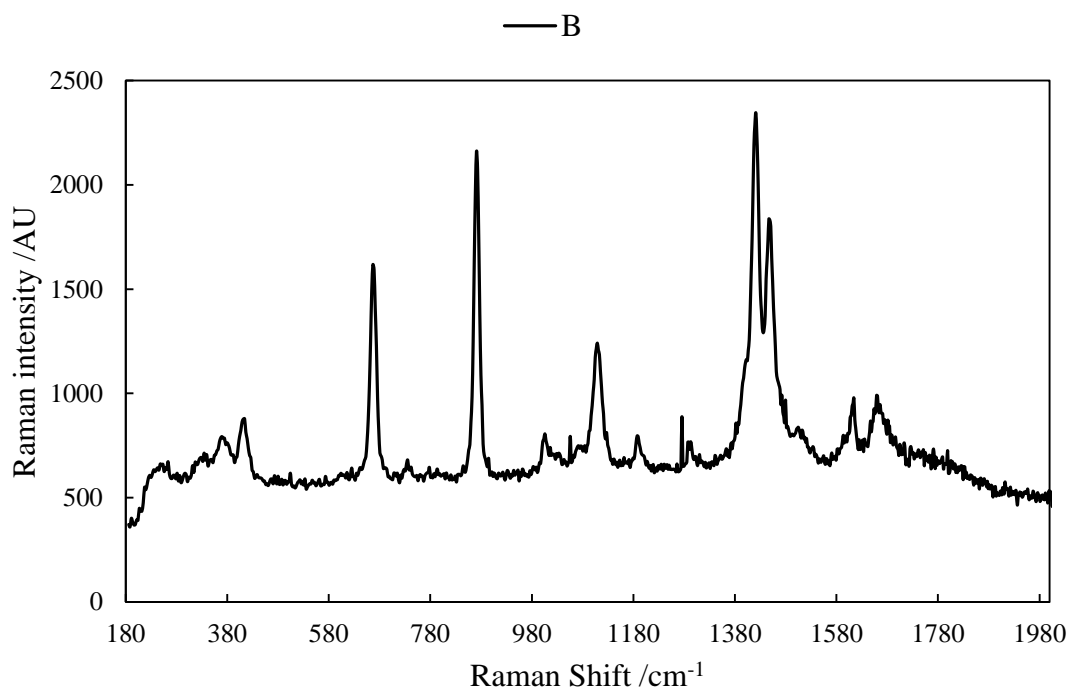
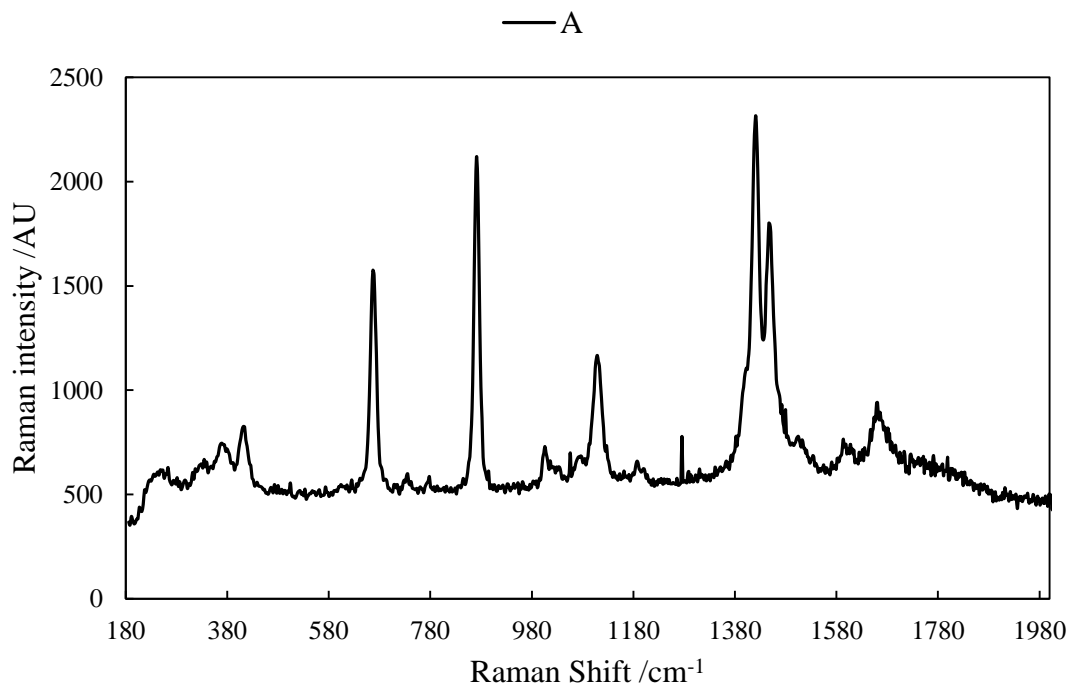
Raman Spectroscopic Monitoring - Results and Discussion

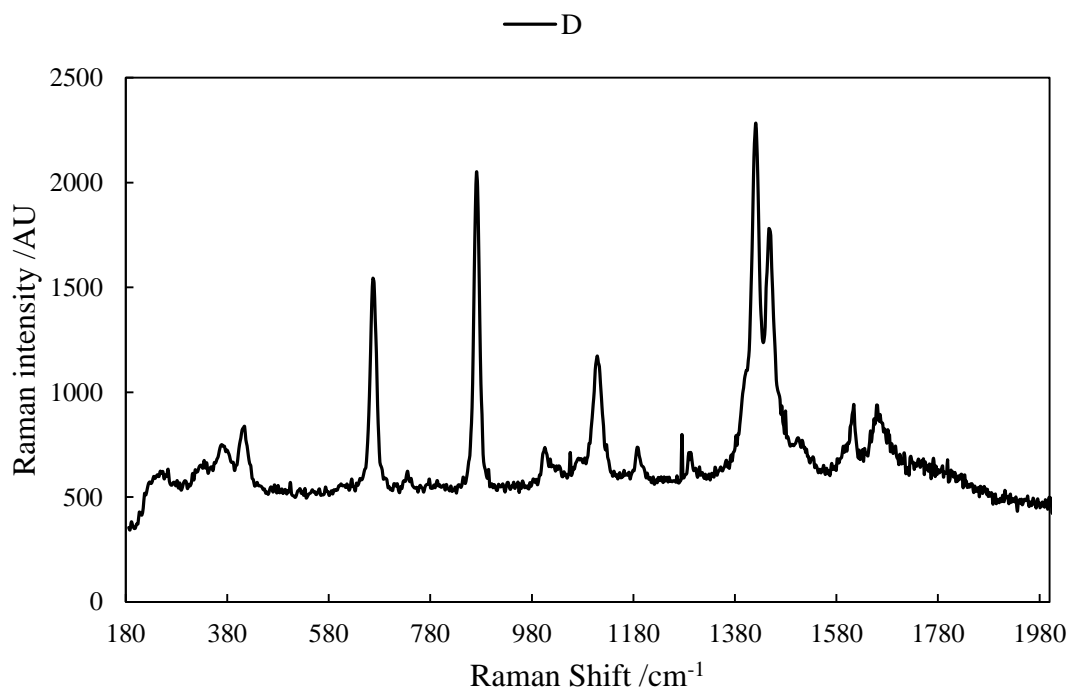
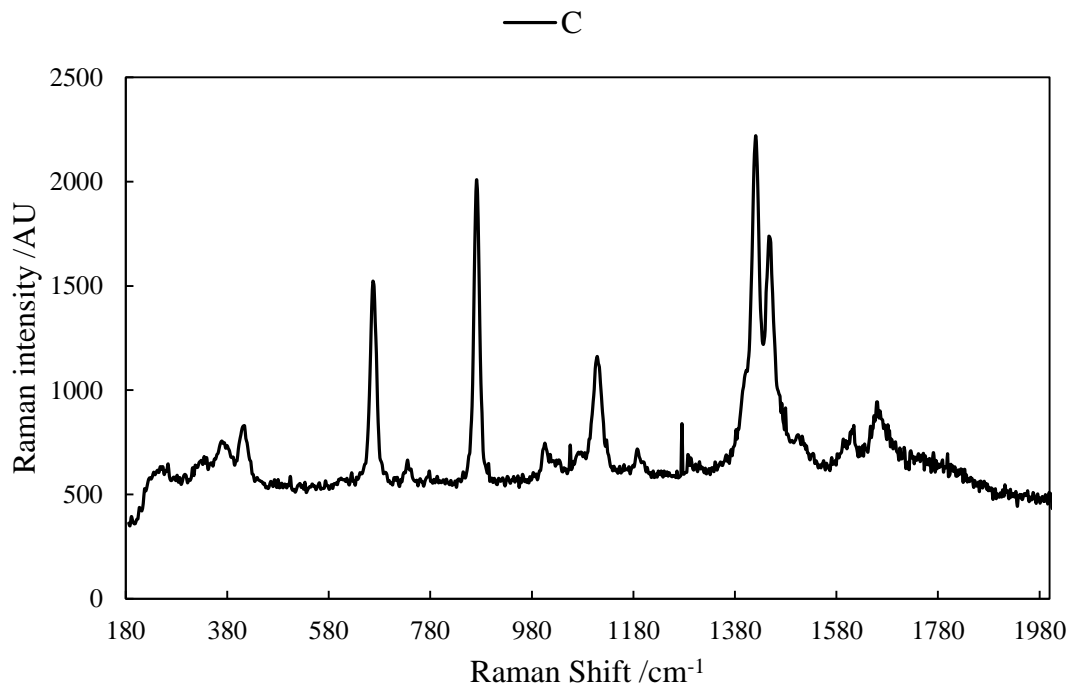
The Raman data obtained for the reactions A to E was compared with GC-MS data. The results show a clear difference for predicting the reaction conversion. Table 4.11 shows the Raman and GC-MS predictions according to the concentrations of 4-bromobenzonitrile and 4-cyanobiphenyl. It can clearly be seen that all the 4-bromobenzonitrile predictions for the reactions are beyond $\pm 10\%$ difference however most of the 4-cyanobiphenyl predictions are within this boundary. Exceptions being reactions D and E were outside the limit. The reason why these predictions were so skewed and arguably greater than previous calibrations was that the Raman spectra contained a much larger amount of noise than previous spectra (Figure 4.20). The increase in spiking noise severely affected the predictability of the 4-bromobenzonitrile concentration. The 4-bromobenzonitrile peak was more susceptible to the influence of the jagged background as it had a weaker signal compared to the 4-cyanobiphenyl. It also affected the background noise region that was subtracted from the peak. This effect on the subtracted background could account for the observed difference in 4-cyanobiphenyl predictions. A further observation in the spectral data was a rise in the background; the baseline was no longer at a Raman intensity of 0 but at approximately 300. This meant that a different factor was affecting the Raman signal that was not accounted for during the calibrations. It was later observed that this affect was due to the Raman spectrometer software.

Raman Spectroscopic Monitoring - Results and Discussion

Reaction	Conversion /%			
	GC-MS prediction		Raman prediction	
	4-bromobenzonitrile	4-cyanobiphenyl	4-bromobenzonitrile	4-cyanobiphenyl
A	14	0	-32	8
B	38	29	2	37
C	34	12	-6	22
D	48	30	2	41
E	67	47	23	63

Table 4.11 Suzuki reaction results for Raman predictions by *Raman calibration 4.18* and *GC-MS analysis 4.3*. The reaction conditions are shown in Table 4.10. All conversion predictions were constructed from the predicted concentrations of 4-bromobenzonitrile and 4-cyanobiphenyl.

Raman Spectroscopic Monitoring - Results and Discussion

Raman Spectroscopic Monitoring - Results and Discussion

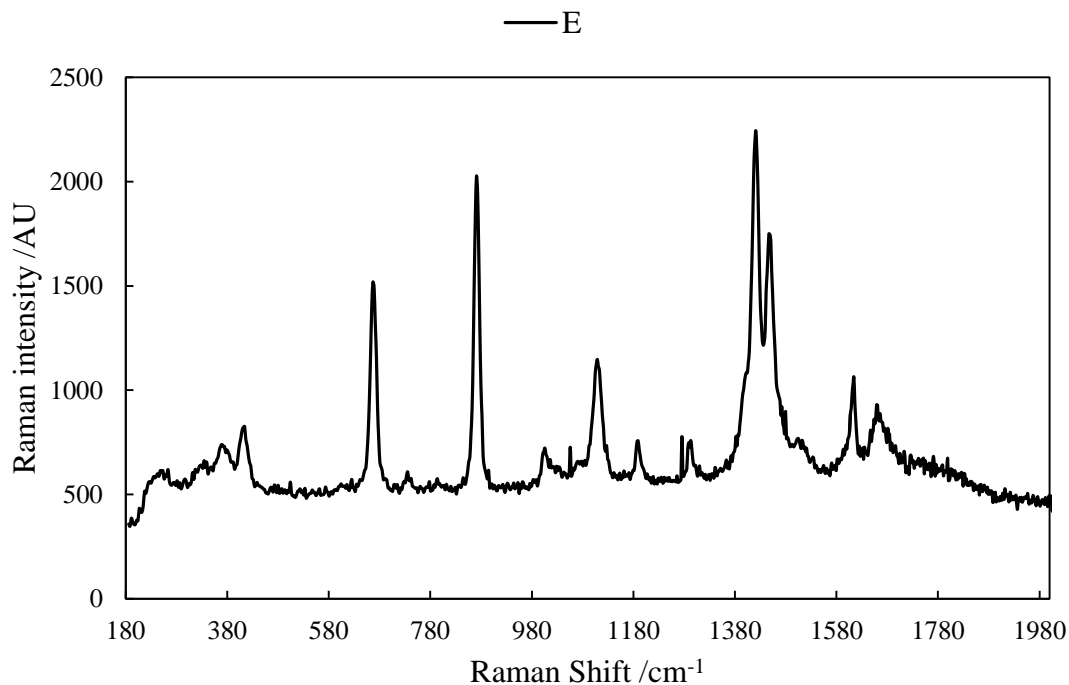
Raman Spectroscopic Monitoring - Results and Discussion

Figure 4.20 The Raman spectra of the Suzuki reactions shown Table 4.10 and Table 4.11. The spectral conditions used to obtain the data were a 1 s integration time averaged 3 times with electrical and stray light correction default from the software. Laser power was set to 340 mV.

Raman Spectroscopic Monitoring - Results and Discussion*4.35 Raman spectral calibration D – results*

Following the inaccurate calibration of *Raman calibration 4.18*, an alternative calibration was carried out. The influence of the signal spiking in the background noise affected the peak area of the 4-bromobenzonitrile and the 4-cyanobiphenyl. Instead of selecting an area close to the peaks to subtract, the actual area under the peak was obtained by postulating a theoretical trapezoid using the maximum and minimum Raman shifts and their intensities as the vectors. By manually deducing each peak area it was possible to construct a calibration graph for 4-bromobenzonitrile and 4-cyanobiphenyl (Figure 4.21). The calibration graph produced was highly linear and once again for these peaks confirms that the 4-cyanobiphenyl peak response is much greater than that of the 4-bromobenzonitrile. Unlike the calibration from *Raman calibration 4.18*, this calibration graph demonstrates that both analytes pass through the origin within 1 standard deviation of the spectra. This is because there is no influence of the background and no influence from each other on the peaks of interest. This calibration approach was however time consuming and required human intervention to produce calibration. One problem observed with the previous calibration was that the 4-bromobenzonitrile peak and 4-cyanobiphenyl peak overlapped very slightly at higher concentration of 4-cyanobiphenyl (see Figure 4.18). Two peaks were independent from one another and were used for this calibration. The trend of both analytes demonstrated a proportional increase to Raman peak area intensity when the concentration of 4-bromobenzonitrile or 4-cyanobiphenyl is increased. Figure 4.22 demonstrates how the calibrations were performed for each individual peak for the 4-cyanobiphenyl calibration.

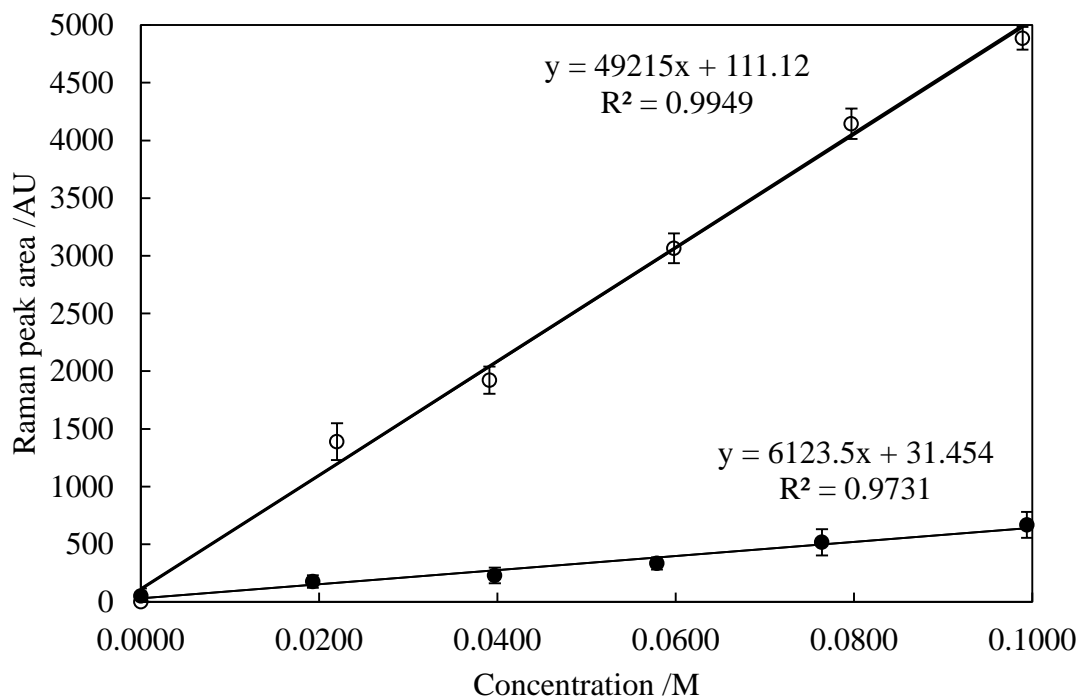
Raman Spectroscopic Monitoring - Results and Discussion

Figure 4.21 The Raman calibration of 4-bromobenzonitrile (•) and 4-cyanobiphenyl (○). The solutions used for calibration were described previously in Table 4.1. Peak areas observed between Raman shifts $760.29 - 793.86 \text{ cm}^{-1}$ and $1250.40 - 1321.73 \text{ cm}^{-1}$ respectively. Noise area subtraction for was performed by using the maximum and minimum Raman shifts and their intensity for each peak as trapezoid vectors. Each calibration standard solution was flowed at $80 \mu\text{L min}^{-1}$. The spectral conditions used to obtain the data were a 1 s integration time averaged 3 times with electrical and stray light correction default from the software. Laser power was set to 340 mV.

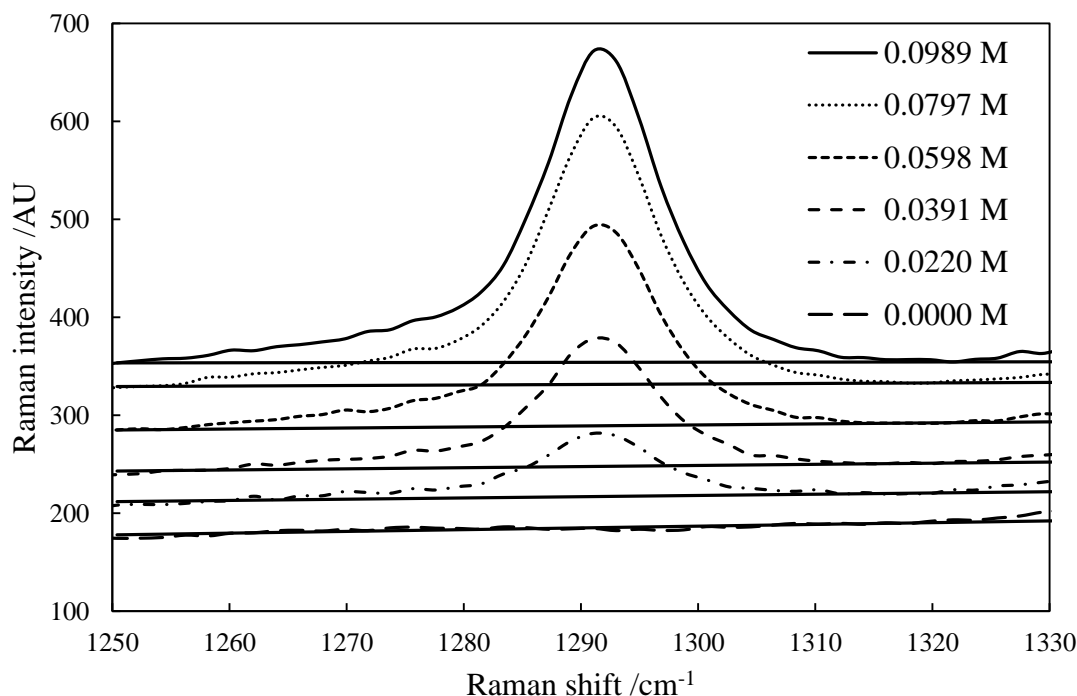
Raman Spectroscopic Monitoring - Results and Discussion

Figure 4.22 Raman spectra of 4-cyanobiphenyl between Raman shifts 1250 – 1330 cm⁻¹. Each spectrum showed an artificial baseline used for the peak area calculation. The solutions used for the spectra were described previously Table 4.1. Each solution was flowed at 80 μL min⁻¹. The spectral conditions used to obtain the data were a 1 s integration time averaged 3 times with electrical and stray light correction default from the software. Laser power was set to 340 mV. Each spectrum had a straight line plotted to determine the baseline of each peak. The calibration of these spectra can be seen in Figure 4.21.

Raman Spectroscopic Monitoring - Results and Discussion

Validating the calibration was done by subjecting reaction data from earlier (Table 4.10 and Table 4.11) to the same data pre-treatment used for *Raman calibration 4.19* and comparing the conversion predictions with the GC-MS predictions in Table 4.11. The reaction conversion predictions are shown in Table 4.12. The 4-cyanobiphenyl predictions were all found to be within $\pm 10\%$ conversion of one another, demonstrating that this methodology of analysis had the potential to be the calibration used for all Suzuki reaction work. However for the 4-bromobenzonitrile the predictive conversions were greatly varied in precision and accuracy. Even when comparing the 4-bromobenzonitrile conversion from the Raman with any of the GC-MS predictions, they were still significantly different (except reactions B and C). Figure 4.23 demonstrates the Raman spectral region used to determine the 4-bromobenzonitrile concentration. Once again the effect of the spiky background was influencing the data. As mentioned previously because 4-bromobenzonitrile has a less intense Raman response to the 4-cyanobiphenyl, the spiky background has a greater influence on the peak signal. Despite the 4-bromobenzonitrile predictability, this methodology showed much greater improvement in predictability of the reaction conversion than that of *Raman calibration 4.18* with respect to 4-cyanobiphenyl. An alternative approach was required to determine the conversion for the reaction.

Raman Spectroscopic Monitoring - Results and Discussion

Reaction	Conversion /%			
	GC-MS prediction		Raman prediction	
	4-bromobenzonitrile	4-cyanobiphenyl	4-bromobenzonitrile	4-cyanobiphenyl
A	14	0	46	7
B	38	29	29	26
C	34	12	39	16
D	48	30	18	26
E	67	47	30	40

Table 4.12 Suzuki reaction results for Raman predictions by *Raman calibration 4.19* and *GC-MS analysis 4.3*. The reaction conditions are shown in Table 4.10.

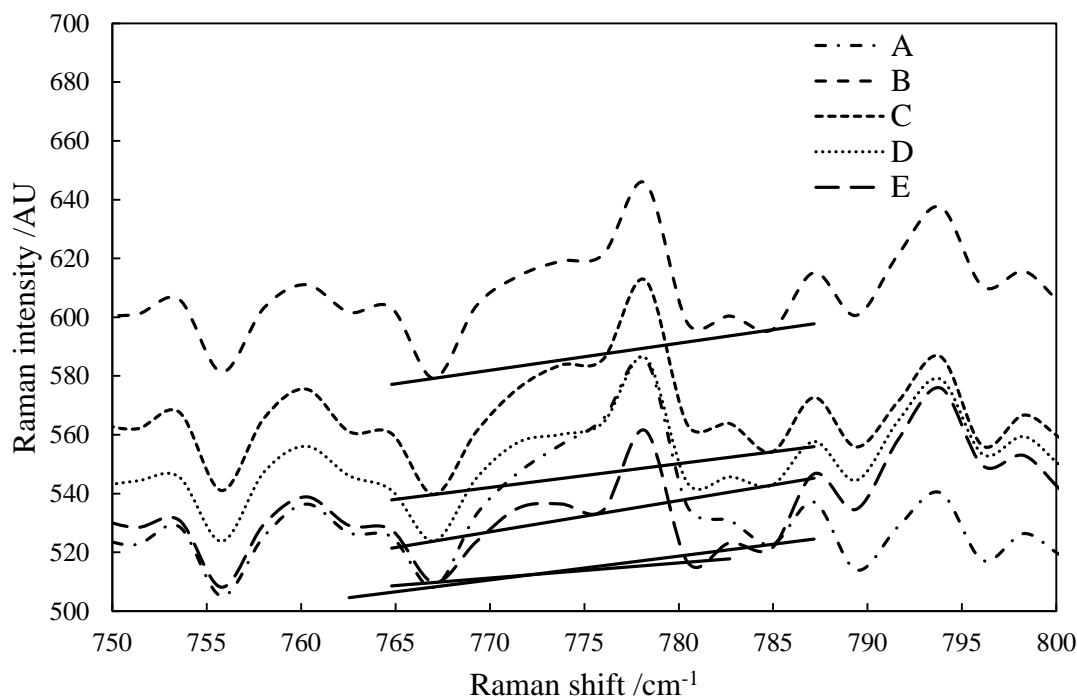
Raman Spectroscopic Monitoring - Results and Discussion

Figure 4.23 Raman spectra of reactions A - E between Raman shifts 750 - 800 cm^{-1} . This was the spectral region used for predicting 4-bromobenzonitrile concentration. The spectral conditions used to obtain the data were a 1 s integration time averaged 3 times with electrical and stray light correction default from the software. Laser power was set to 340 mV. Each spectrum had a straight line plotted to determine the baseline of each peak.

Raman Spectroscopic Monitoring - Results and Discussion*4.36 Raman spectral calibration E – results*

The method used for the revised calibration method was based on an advanced multivariate statistical method called Partial Least Squares Regression (PLSR). It enables not just individual peaks to be calibrated against concentration but permits multivariate analysis i.e. entire or fractions of spectra to be calibrated against concentration. Unlike Principal Component Regression (PCR), PLSR identifies a vector in factor space which is dependent on the variance in each spectrum. This gives stability to the model for calibration as the data permits more flexibility for variance and can permit them to be more accurately predicted.

Most of the contributing Raman spectrum is from the 66.7% aqueous DMF which whilst not influencing the PLSR, was deemed more suitable to use for the spectrum between Raman shifts 1560.22 - 1631.69 cm^{-1} . This region accounted for 4-cyanobiphenyl and 4-bromobenzonitrile responses in the spectrum. The Raman data used for the regression were that obtained for *Raman calibration 4.18*. Instead of selecting an area under the Raman peak and subtracting a background, all the points of Raman intensity were calibrated. Unlike previous calibration attempts, auto scaling, mean centring and a moving average filter were introduced. The auto scaling and row mean centring permitted the spectral data to be comparable by removing magnitude. This brought the data to the same scale and also lowered the effect of variation within each sample. The moving average filter of 5 meant that 5 points of spectral data were averaged to smooth the data and free it from any “roughing” spectral effects; the jagged background previously observed was negated.

Raman Spectroscopic Monitoring - Results and Discussion

Instead of the Raman peak intensity being plotted against concentration, the PLS scores from the data were plotted against the concentration. The scores were constructed by comparing predictor variables to a high correlation with the Raman intensities observed. By using scores as an interval between the Raman intensities and concentration, it produces a correlation that accounts for factors that change the variance in the Raman spectra. Once accounted for, the factors of the PLS were used to establish a linear relationship between concentration and PLS scores, which suggests that because the scores were derived from the spectral values that there was a relationship between Raman intensity and concentration.

The Raman spectral PLS scores were plotted against concentration (Figure 4.24). A highly linear correlation was produced for the concentration of 4-bromobenzonitrile and 4-cyanobiphenyl. On implementing the calibration model with the Raman spectra from reactions A - E (described previously in Table 4.10) it was apparent that the resulting predictions agreed with the GC-MS data. Table 4.13 demonstrates the prediction capability of PLSR method of calibration for the Raman spectroscopic set-up. In addition to the PLSR use on the Raman spectra, it was also used on the GC-MS chromatograms obtained from the calibration in order to compare the two different techniques of area ratio analysis (discussed in 4.33) and PLSR. The PLSR calibration for the GC-MS used the same calibration standards used for the calibration of the Raman spectra. Five factors were accounted for in the GC-MS chromatograms between 5 and 20 minutes with auto scaling, row mean centring and a 5 point moving average smoothing before analysis. The resulting calibration was highly linear for both

Raman Spectroscopic Monitoring - Results and Discussion

4-cyanobiphenyl and 4-bromobenzonitrile although some deviation was apparent; nevertheless the trend was still observed (Appendix 24).

Comparing each of the predicted conversions in Table 4.13 showed that for the PLSR predictions the 4-bromobenzonitrile and 4-cyanobiphenyl predictions to be very similar. This was to be expected as the exact same multivariate data was used to calibrate both calibration sets. However, there were still some discrepancies on the conversion prediction accuracy. For the most part the Raman predictions were within $\pm 10\%$ of their GC-MS counterparts for both GC-MS PLSR and GC-MS area ratio. There were conflicting conversion predictions for both 4-cyanobiphenyl and 4-bromobenzonitrile.

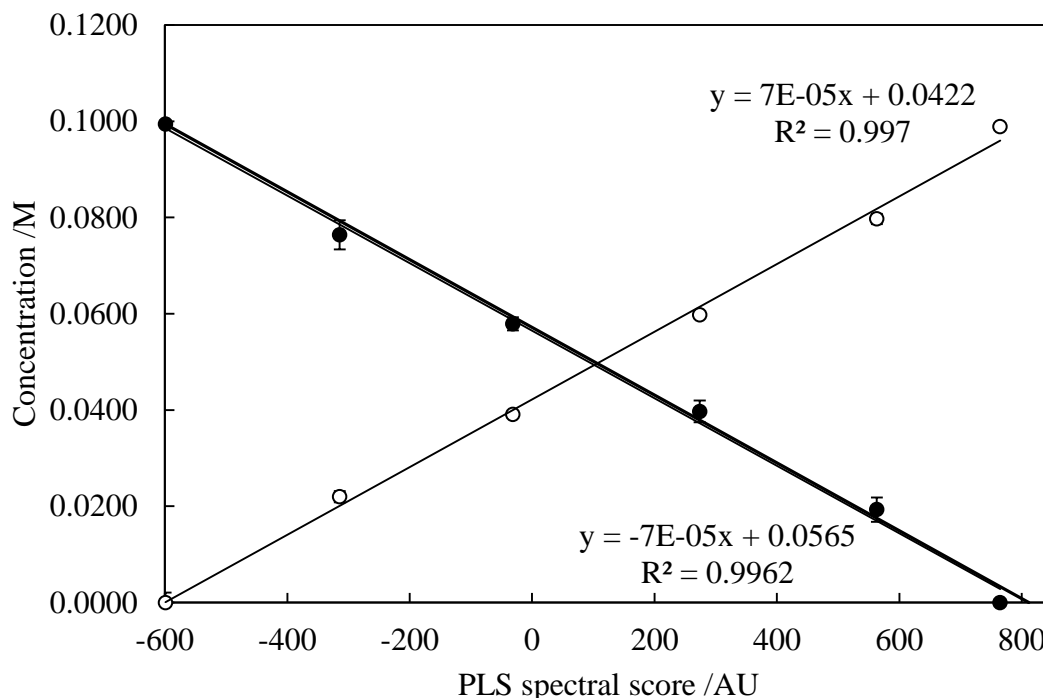
Raman Spectroscopic Monitoring - Results and Discussion

Figure 4.24 The Raman calibration of 4-bromobenzonitrile (•) and 4-cyanobiphenyl (○). The standard solutions used for calibration were described previously in Table 4.1. Peak areas observed between Raman shifts 1560.22 - 1631.69 cm^{-1} . Each calibration solution was flowed at 80 $\mu\text{L min}^{-1}$. The spectral conditions used to obtain the data were a 1 s integration time averaged 3 times with electrical and stray light correction default from the software. Laser power was set to 340 mV. 5 factors were accounted for in the PLSR process.

Raman Spectroscopic Monitoring - Results and Discussion

Reaction	Raman conversion /%		GC-MS conversion /%			
	PLSR		PLSR		Area ratio	
	BBN	CBP	BBN	CBP	BBN	CBP
A	8	7	8	7	14	0
B	38	36	28	26	38	29
C	22	21	6	5	34	12
D	40	38	26	24	48	30
E	60	58	47	44	67	47

Table 4.13 Table of conversions predicted by the Raman PLSR method of calibration, a PLSR GC-MS method, and an area GC-MS method (described in *GC-MS analysis 4.3*). BBN was abbreviated from 4-bromobenzonitrile and CBP was abbreviated from 4-cyanobiphenyl. The reaction conditions are shown in Table 4.10.

Raman Spectroscopic Monitoring - Results and Discussion

To observe the conversion predictions given in Table 4.13, the averages of 4-bromobenzonitrile and 4-cyanobiphenyl predictions were used in order to better reflect the true value of the conversion. Table 4.14 shows the averages of the conversions and indicates that they are all to be within $\pm 10\%$ of one another (with exception to reaction C for PLSR). This demonstrates that the PLSR method of calibration was best suited for the Raman spectra data but was not so suitable for the GC-MS data. Also the averaging suggests that the accuracy of the Raman agrees with all of the GC-MS predictions from the area ratio calibration of 4.33 within $\pm 3\%$; much more optimistic than previously expected.

This final calibration model was used in the optimisation of the Suzuki reaction in the flow system described in *flow design 3.7*.

Raman Spectroscopic Monitoring - Results and Discussion

Reaction	Raman	GCMS	
	Average of BBN and CBP conversion /%	Average of BBN and CBP conversion /%	
	PLSR	PLSR	Area ratio
A	8	7	7
B	37	27	34
C	22	5	23
D	39	25	39
E	59	46	57

Table 4.14 Table of conversions predicted by the Raman PLSR method of calibration, a PLSR GC-MS method, and an area GC-MS method (described in *GC-MS analysis 4.3*). BBN was abbreviated from 4-bromobenzonitrile and CBP was abbreviated from 4-cyanobiphenyl. The averages were calculated from Table 4.13. The reaction conditions are shown in Table 4.10.

Raman Spectroscopic Monitoring - Results and Discussion*4.37 Flow reaction monitoring – Flow system design F*

The use of the microwave proved to have a detrimental effect on the catalyst stability and was affecting the performance of the reaction. The flow system was modified to accommodate a different heating source. A column heater was put in place of the microwave reactor and the 275.79 kPa back pressure valve was removed. This led to the final design of *flow design 3.7*. Utilizing this design meant that the rapid expansion of bubbles from hot spots in the solvent were not occurring so the back pressure valve was not required. In addition not only could the diameter of the catalyst be varied but also the length, enabling much longer catalyst residence time to be achieved. From an industrial point of view, this would be highly advantageous with a higher turnover of product per unit time. This is often the case as the amount of product made per unit time would be more cost effective and more profitable.

The multivariate Raman calibration (see section *Raman calibration 4.20*) was used with the flow data and the concentration of 4-bromobenzonitrile and 4-cyanobiphenyl was determined to establish relative conversion. The flow rates used were 0.027, 0.042, 0.057, 0.080, 0.095, 0.110, 0.140, 0.170, 0.245 and 0.381 mL min⁻¹. These flow rates correspond to residence times of 2461, 1573, 1156, 827, 696, 600, 471, 387, 268 and 173 seconds respectively. The CMR void volume for these series of reactions was 1.0961 mL. Figure 4.26 presents the resulting Raman predictions for 4-cyanobiphenyl production and reaction conversion (original data in Appendix 25). Interestingly the optimum conversion was not the optimum 4-cyanobiphenyl production. This is because the flow rate governs the amount of product produced per unit time, and from an industrial point of view, the optimum flow rate was between 0.25

Raman Spectroscopic Monitoring - Results and Discussion

- 0.38 mL min⁻¹. If the predictive line is correct then the optimum flow rate determined from the derivative of the equation of the line of best fit was at 0.30 mL min⁻¹. At this flow rate the amount of 4-cyanobiphenyl produced by this flow system would have been 53 g h⁻¹. This flow rate conversion was however only 14%. In terms of reaction efficiency the optimum conversion for this reaction was at the lowest flow rate 0.027 mL min⁻¹, even though the production of 4-cyanobiphenyl was 17 g h⁻¹ (Table 4.11).

Raman Spectroscopic Monitoring - Results and Discussion

Flow rate /mL min ⁻¹	Conversion /%	CBP produced /g h ⁻¹
0.0267	61.26	17.02
0.0418	44.45	19.50
0.0569	41.27	24.69
0.0795	33.47	28.22
0.0946	25.43	25.87
0.1096	26.04	30.67
0.1398	23.95	36.14
0.1699	22.64	41.67
0.2453	18.95	50.98
0.3809	10.57	46.83

Table 4.15 Results of the Suzuki cross-coupling reaction between 4-bromobenzonitrile (0.10 M) and phenyl boronic acid (0.12 M) in the presence of potassium carbonate (0.24 M). The CMR used was produced from *monolith 2.5* with *palladium loading 2.14* with a void volume of 1.0961 mL. The reaction temperature was controlled with a column heater set at 80 °C. 4-Cyanobiphenyl concentrations and reaction conversions were determined *Raman calibration 4.20*.

In principle this calibration technique was used to monitor and determine the optimum conversion and production for the reaction. Using the same data a kinetic diagram with respect to 4-bromobenzonitrile and 4-cyanobiphenyl was constructed. The

Raman Spectroscopic Monitoring - Results and Discussion

resulting concentrations of the reactions were recorded relative to the reaction mixtures reaction time with the CMR (Figure 4.27). Examining the concentration differences over different reaction times gave an indication of the reaction kinetics and how the catalyst activity was functioning. A theoretical line of best fit was placed for a second order reaction and adjusted for the lowest residual difference between the theoretical line of best fit and the actual data points predicted for both 4-bromobenzonitrile and 4-cyanobiphenyl. To construct Figure 4.27 the concentration data was fitted to various integrated rate equations that were equivalent to alternative empirical rate laws. The theoretical lines were found to correspond to the 2nd order rate law (Equation 4.5) and subsequently the integrated rate Equation 4.6, suggests that the rate of reaction was possibly be first order with respect to both 4-bromobenzonitrile (*BBN*) and phenyl boronic acid (*PBA*). For the reaction conditions used, the overall 2nd order rate constant k is $4.45 \times 10^{-3} \text{ M}^{-1} \text{ s}^{-1}$. This was calculated by substituting Equation 6 with the initial concentrations of 4-bromobenzonitrile and phenyl boronic acid. The measured amount of 4-bromobenzonitrile over time was previously obtained and this was used to calculate the remaining amount of phenyl boronic acid. By plotting the natural logarithm of this change (multiplied by the initial concentration factor) against time, it was possible to obtain a gradient for a straight line that was equivalent to $k/([BBN]_0 [PBA]_0)$.

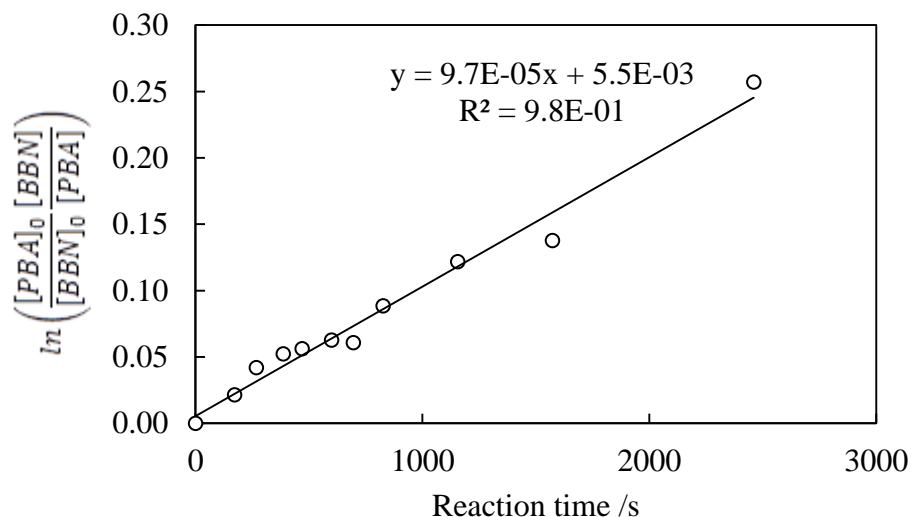
Raman Spectroscopic Monitoring - Results and Discussion

Figure 4.25 Plot to determine the 2nd order rate of reaction based on Equation 4.6. the results obtained were from the Suzuki cross-coupling reaction between 4-bromobenzonitrile (0.10 M) and phenyl boronic acid (0.12 M) in the presence of potassium carbonate (0.24 M). The CMR used was produced from *monolith 2.5* with *palladium loading 2.14* with a void volume of 1.0961 mL. The reaction was performed at volumetric solution flow rates of 0.03 to 0.38 mL min⁻¹ and the temperature in the column heater was set at 80 °C. 4-Cyanobiphenyl concentrations and reaction conversions were determined *Raman calibration 4.20*.

$$\text{Rate of reaction} = k[\text{BBN}][\text{PBA}] \quad \text{Equation 4.5}$$

Rate law for the Suzuki reaction between 4-bromobenzonitrile (BBN) and phenyl boronic acid (PBA)

Raman Spectroscopic Monitoring - Results and Discussion

$$\frac{1}{[PBA]_0[BBN]_0} \cdot \ln \frac{[PBA]_0}{[BBN]_0} \cdot \frac{[BBN]}{[PBA]} = kt \quad \text{Equation 4.6}$$

Reaction kinetic equation for an overall second order reaction with phenyl boronic acid (PBA) and 4-bromobenzonitrile (BBN) being both first order¹⁷⁶.

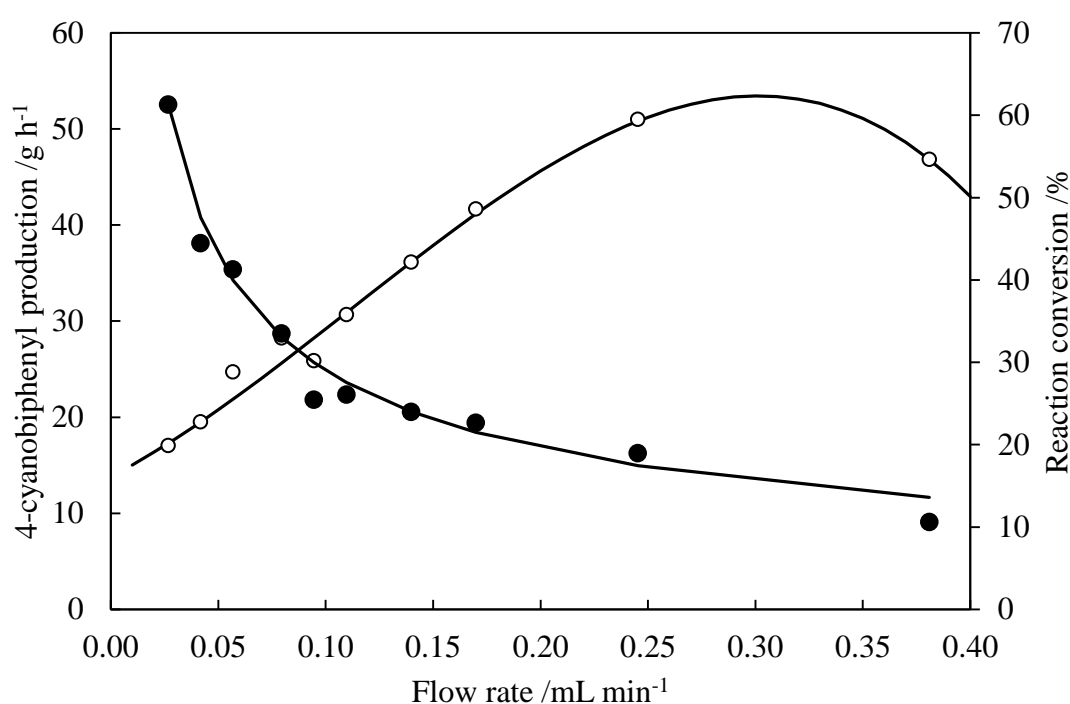


Figure 4.26 The influence of flow rate and reaction time on 4-cyanobiphenyl production (○) and conversion (●) in the Suzuki cross-coupling reaction between 4-bromobenzonitrile (0.10 M) and phenyl boronic acid (0.12 M) in the presence of potassium carbonate (0.24 M). The CMR used was produced from *monolith 2.5* with *palladium loading 2.14* with a void volume of 1.0961 mL. The reaction was performed at volumetric solution flow rates of 0.03 to 0.38 mL min⁻¹ and the temperature in the column heater was set at 80 °C. 4-Cyanobiphenyl concentrations and reaction

Raman Spectroscopic Monitoring - Results and Discussion

conversions were determined *Raman calibration 4.20*. For original data see Appendix 25.

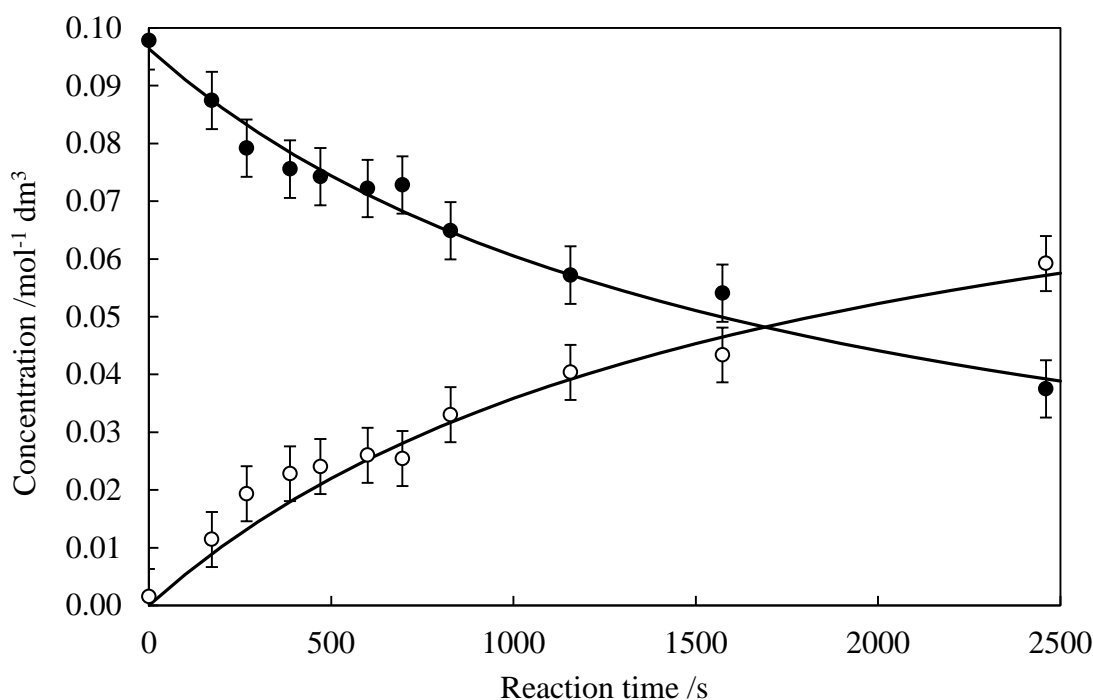


Figure 4.27 Plots of the concentrations of 4-bromobenzonitrile (●) and 4-cyanobiphenyl (○) determined by *Raman calibration 4.20* as a function of the CMR residence time. The CMR used was produced from *monolith 2.5* with *palladium loading 2.14* with a void volume of 1.0961 mL. The reaction was performed at volumetric solution flow rates of 0.03 to 0.38 mL min⁻¹ and the temperature in the column heater was set at 80 °C. The solid line lines show the best fit to the 2nd order integrated rate Equation 4.6 with $k = 4.45 \times 10^{-3} \text{ M}^{-1} \text{ s}^{-1}$. For original data see Appendix 25.

Raman Spectroscopic Monitoring - Results and Discussion

The heterogeneous Suzuki reaction that was occurring between 4-bromobenzonitrile and phenyl boronic acid in the presence of potassium carbonate over catalysed palladium can be described by adopting either a Langmuir-Hinshelwood or an Eley-Rideal mechanism. These mechanisms describe bimolecular kinetics on a heterogeneous surface. The Langmuir-Hinshelwood mechanism assumes that both reactants react on the surface of the catalyst, and that both must be adsorbed on the surface for this to occur (Figure 4.28a). The Eley-Rideal mechanism assumes that only one reactant need adsorb on the catalyst for the reaction to occur and the other reactant is in the vicinity of the adsorbed reactant (Figure 4.28b). The reaction mechanism for the Suzuki reaction of a homogeneous solution describes that the organo halide and organo boronic acid bind with the palladium separately. Elimination of both the halide and boronic acid functional groups occur and the organic substituent's react together on the catalyst and join through reductive elimination¹⁷⁷. The homogeneous mechanism appears to be closer related to the Langmuir-Hinshelwood mechanism than the Eley-Rideal mechanism as both reactants must be bound or adsorbed to the catalyst for the reaction to occur. The Eley-Rideal mechanism requires one of the reactants to be bound or adsorbed.

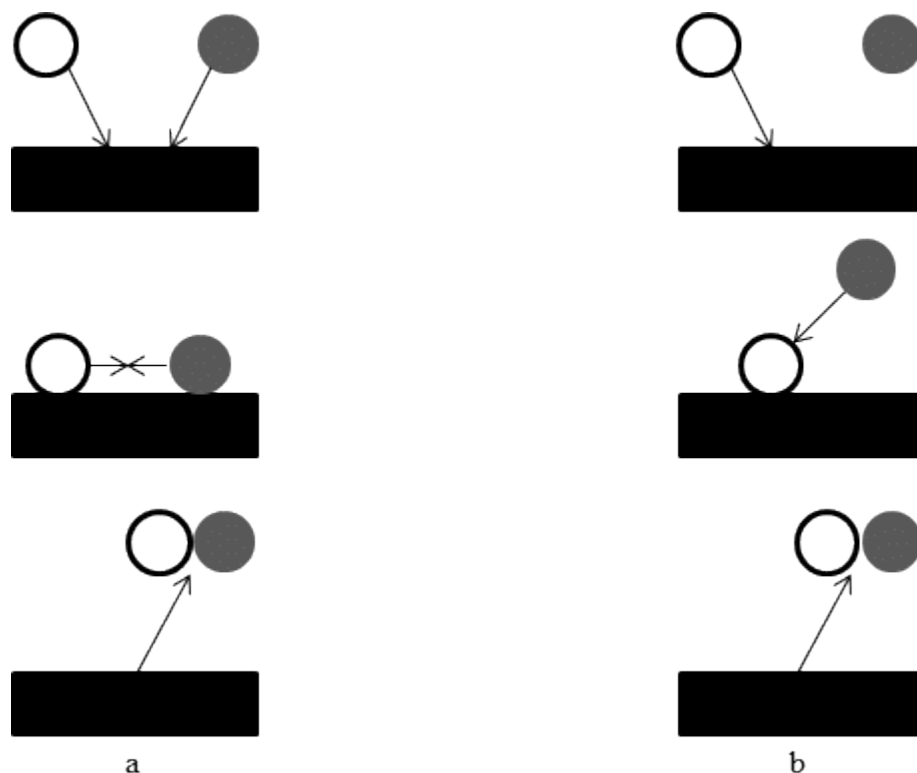
Raman Spectroscopic Monitoring - Results and Discussion

Figure 4.28 Heterogeneous catalyst reaction mechanisms of a) the Langmuir-Hinshelwood and b) the Eley-Rideal mechanism for reactant to catalyst binding.

Adsorption of the reactant greatly affects the order of the reaction species and since the reaction was determined to be second order with respect to 4-bromobenzonitrile. In reality the order of the individual reactants could have been between 0 and 1 for 4-bromobenzonitrile or phenyl boronic acid, dependant if the reactant was strong or weakly adsorbed. If the reactant was strongly adsorbed to the surface then it would easily saturate the surface of the catalyst, and increasing the concentration of the bulk solution would have little or no effect on the reaction rate and its reaction order would have been closer to 0. A weakly adsorbing reactant would have a proportional relationship between the adsorbed reactant and the bulk solution

Raman Spectroscopic Monitoring - Results and Discussion

concentration¹⁷⁸. Despite the adsorption relationship, the resulting concentration relationships with reaction time from Figure 4.27 cannot determine whether the reaction takes a Langmuir-Hinshelwood mechanism or an Eley-Rideal mechanism. The way to determine this could be achieved through repeating the reaction whilst only varying either 4-bromobenzonitrile or phenyl boronic acid concentration. The response on the formation of 4-cyanobiphenyl would help determine which mechanism is occurring.

4.38 Summary

Many different flow reaction systems were assessed for their capability to handle the flow pressures, heating mechanisms and to integrate the Suzuki reaction between 4-bromobenzonitrile and phenyl boronic acid. Conventional Suzuki reaction chemistry showed the reaction was performed using the same conditions as for the flow reaction chemistry (with respect to catalyst, reaction time, reactant concentration and reaction temperature). Three Suzuki flow reaction methods were used for comparison using different flow designs (see section *Flow Suzuki reaction 4.9*, *Flow Suzuki reaction 4.10* and *Flow Suzuki reaction 4.11*) each with their own draw backs and advantages. However, the fundamental conclusion for the reaction was that the CMRs could not sustain the constant heating from microwaves. This led to the use of a column heater heating the flow reaction (see section 4.37). Further improvements led to Raman spectroscopic monitoring of the flow system post reaction. This gave qualitative and quantitative details of the composition of the reaction mixture. Five Raman techniques of calibration were used to determine the concentration of reactants and product. Only one method of calibration agreed with GC-MS concentration predictions. The

Raman Spectroscopic Monitoring - Results and Discussion

calibration was based on the PLSR method described in 4.36. The PLSR calibration method lead to fast optimisation of the flow rate and showed basic kinetic information of the Suzuki reaction in flow.

Following the success of the Suzuki reaction in batch, Suzuki reaction in flow, Raman concentration calibration, flow reaction optimisation and basic kinetic information, the reaction set-up could be adapted to accommodate other organic synthesis reactions.

Raman Spectroscopic Monitoring - Results and Discussion

5.0 Acetylation reactions with Raman spectroscopic monitoring

Acetylation reaction chemistry is an area of organic synthesis that has many uses including the production of aspirin and bio fuels making it an essential stage in industrial use³⁶. Compared to the Suzuki reaction, the acetylation reaction involving acetic anhydride and an alcohol group is relatively simple. There are two key differences between the Suzuki and acetylation flow reactions; the reagent mixture and the catalyst. The monoliths present in both were the same but the acid catalysed acetylation reaction required an acid strong enough to activate the acetic anhydride to react. The speed of this reaction makes it a good example of the use of high throughput flow reaction chemistry.

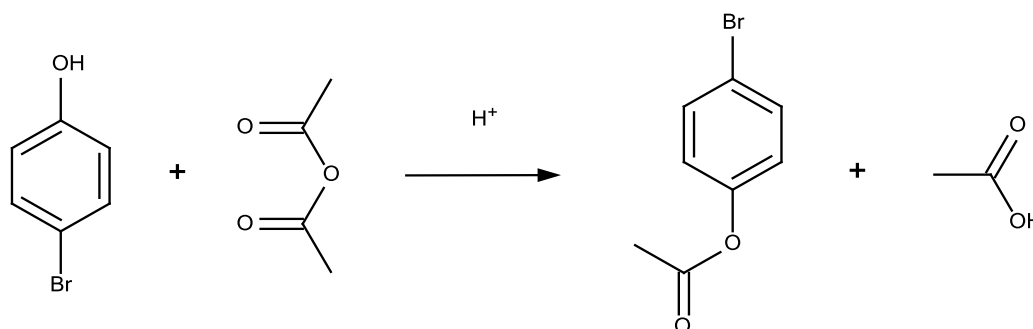
Each of the components of the reaction mixture (see section 5.1) is Raman active. The objectives for using the acetylation reaction in flow reaction chemistry is to demonstrate that the Suzuki reaction previously used in chapter 4 could be altered to accommodate different reactions. For this to occur, a new catalyst was required and needed to be characterised, a batch reaction had to be performed, the batch reaction had to be transferred to flow reaction chemistry, and reagent/product concentrations had to be obtained by a rapid responsive analysis (Raman spectroscopy).

Experimental*5.1 Acetylation reaction chemistry*

The acetylation reaction performed is described in Reaction Scheme 5.1. The reaction describes how 4-bromophenol (99% Sigma Aldrich) reacts with excess acetic

Raman Spectroscopic Monitoring - Results and Discussion

anhydride ($\geq 99\%$ Sigma Aldrich) to produce 4-bromophenyl acetate ($\geq 99\%$ Apollo Scientific) and acetic acid in the presence of an acid catalyst.



Reaction Scheme 5.1 The reaction between 0.3 M 4-bromophenol and excess acetic anhydride to form 4-bromophenyl acetate and acetic acid in the presence of an acid catalyst. The solvent for the reaction was acetic anhydride acting both as reactant and solvent. The catalyst for the reaction was the tungstosilicic acid immobilized on a silica monolith.

5.2 Catalyst preparation - HPA

The catalyst for the reaction was an inorganic heteropoly acid (HPA) embedded on a silica monolith. The monolith was generated from *monolith 2.5*. HPA was immobilized through a 40 wt% solution of tungstosilic acid ($\text{H}_4\text{SiW}_{12}\text{O}_{40}$) ($\geq 99.9\%$ Sigma Aldrich) relative the exact void volume of the silica monolith. Here it was dried at 90 °C and then calcinated at 200 °C (Microwave Furnace, CEM MAS7000) for 2 hours (ramp at 1 °C min⁻¹) in air. Here the HPA monolith was trapped in Teflon heat shrink tubing (Adtech) at 360 °C for 15 minutes and sealed with two glass rods either side.

Raman Spectroscopic Monitoring - Results and Discussion*5.3 Catalyst characterisation*

The immobilized HPA was characterised by SEM - EDX analysis (EVO 60 Carl Zeiss, INCA System 350 Oxford Instruments). Monolith-HPA samples were dried, cut and attached to aluminium SEM mounts with super glue. No sputtering was required (due to the conductive nature of tungsten coating) and placed in the scanning electron microscope for imaging and analysis.

5.4 Raman analysis conditions

The spectral conditions used to obtain the data were a 1 s integration time averaged 3 times with electrical and stray light correction default from the software (SpectraSuite Ocean Optics). Laser (785 nm at 350 mV Ocean Optics) power was set to 340 mV. Each solution was recorded using the Raman flow cell fitted with a Raman probe (RIP-RPB-785-SS Ocean Optics) previously shown in Figure 4.1 under static conditions. Raman spectra were obtained from a Raman spectrometer (QE65000 Ocean Optics) for 0.3 M 4-bromophenol (99% Sigma Aldrich) and 0.3 M 4-bromophenyl acetate ($\geq 99\%$ Apollo Scientific) in acetic anhydride, and for acetic anhydride ($\geq 99\%$ Sigma Aldrich).

5.5 Batch acetylation reaction

A 0.3 M solution of 4-bromophenol (99% Sigma Aldrich) in 100 mL acetic anhydride ($\geq 99\%$ Sigma Aldrich) was placed in a round bottom flask at room temperature. One spatula full of tungstosilicic acid (approximately 0.02 g, $\geq 99.9\%$ Sigma Aldrich) was added to the reaction mixture and was left stirring for 5 minutes at

Raman Spectroscopic Monitoring - Results and Discussion

120 rpm. The resulting solution was tested for purity using GC-MS analysis from *GC-MS analysis 4.3* without the decane addition.

5.6 Flow acetylation reaction

The acetylation reactions were all performed using 0.3 M 4-bromophenol (99% Sigma Aldrich) in acetic anhydride at 20 °C ($\geq 99\%$ Sigma Aldrich). The catalyst used for every reaction was immobilized tungstosilicic acid ($\geq 99.9\%$ Sigma Aldrich) as described in *catalyst preparation 5.2* with CMR volumes of approximately 0.24 mL. CMR volumes were determined by the difference between a dry and wet monolith. The flow system used was very similar to *flow design 3.7* except no column heater was necessary. Flow rates were varied to alter catalyst residence time.

5.7 Acetylation Raman spectral calibration – A

Raman spectra were calibrated by monitoring 4-bromophenol (99% Sigma Aldrich) and 4-bromophenyl acetate ($\geq 99\%$ Apollo Scientific). Two peaks were observed between Raman shifts 237.81 – 278.83 cm^{-1} , and 281.37 – 309.31 cm^{-1} for 4-bromophenyl acetate and 4-bromophenol respectively. These peaks had their baseline subtracted from beneath them using the same method as *Raman calibration 4.19*.

5.8 Acetylation Raman spectral calibration – B

Raman spectra were calibrated between Raman shifts 230.07 – 321.95 cm^{-1} . The pre-spectral treatment and PLSR calibration used was the same as described in *Raman calibration 4.20*. Five factors were also used which accounted for over 99% of the data

Raman Spectroscopic Monitoring - Results and Discussion

variance. The training spectra used were spectra simulating reaction conversions 20 - 100% with the validation spectrum from the simulated 0% conversion.

5.9 HPA influence on Raman spectra

Tungstosilicic acid ($\geq 99.9\%$ Sigma Aldrich) concentrations were varied in batch reactions of 0.3 M 4-bromophenol (99% Sigma Aldrich) in acetic anhydride ($\geq 99\%$ Sigma Aldrich). Each reaction was carried out for 1 hour at 20 °C stirring at 120 rpm. The terminated reaction mixtures were passed through the Raman flow cell. The spectral conditions of analysis were described previously in *Raman analysis 5.4*. The 4-bromophenyl acetate peak was monitored between Raman shifts 235.23 – 286.47 cm^{-1} . Manual baseline subtraction occurred as described in *Raman calibration 4.19* and plotted.

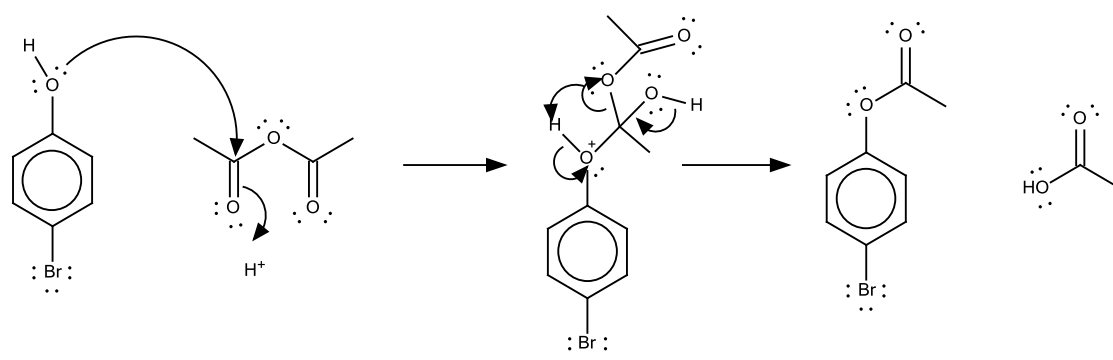
Raman Spectroscopic Monitoring - Results and DiscussionResults*5.10 Acetylation reaction*

The acetylation reaction was performed by reacting 4-bromophenol with acetic anhydride with the further prospect of generating a multi-flow system with the Suzuki reaction. In the Suzuki reaction, electron withdrawing groups in the para position favour the oxidative addition to the palladium by generating a higher δ^+ charge on the carbon bound with the halide. An electron withdrawing group in the para position disfavours the oxidative addition to the palladium by increasing the δ^- charge on the alpha carbon with the halide. Contemplating this, the alcohol group on 4-bromophenol would be a much weaker reactant for the Suzuki reaction than that of the acetylation product of 4-bromophenyl acetate due to the electron donating and electron withdrawing properties of the para position functional groups. For this reason, 4-bromophenol was chosen as the reactant. Acetic anhydride was also used instead of acetic acid as it is a more powerful acetylation agent due to its stability making two δ^+ carbons prone to nucleophilic attack. This draw of electrons from the two carbons increased their δ^+ charge making it more effective than acetic acid. Acetic acid draws electron density from the acidic proton resulting in drawing less electron density from the O=C-O carbon.

Catalysis for this reaction uses an acid to activate the acetic anhydride even further making a δ^+ carbon prone to attack. The mechanism for the reaction is described in Reaction Scheme 5.2. The source of the acidic protons was from the heteropoly acid tungstosilicic acid. Tungstosilicic acid is a strong inorganic acid with a very high Brønsted acid strength ($\text{pK}_a = -3.0$)¹⁷⁹. Its structure is based on the Keggin mould. The

Raman Spectroscopic Monitoring - Results and Discussion

elemental composition of tungstosilicic acid is $H_4[Si(W_3O_{10})_4]$, which has such a high stability that it permits the metals in the anion to be reduced considerably resulting in highly acidic protons. This capability has been utilized in the acetylation reaction as this inorganic structure was applied to immobilization chemistry allowing acid separation from the reaction mixture physically.



Reaction Scheme 5.2 The acetylation reaction mechanism between 4-bromophenol and acetic anhydride in the presence of an acid.

5.11 Tungstosilicic acid immobilization

The CMR was prepared by the method described in *catalyst preparation 5.2*. The approach was brought about in the same fashion as the palladium immobilization; physical entrapment within the nano-pores of the silica monolith. The tungstosilicic acid was heated at 90 °C to dry the tungstosilicic acid to the surface of the silica, from here, the calcinations at 200 °C shrank the monolith anchoring the tungstosilicic acid to the surface.

The CMR once produced was characterised by SEM analysis to confirm the presence of the tungstosilicic acid. The resulting SEM EDX images provided

Raman Spectroscopic Monitoring - Results and Discussion

information on the monolithic structure, showing that the presence of tungsten on the surface permitted a high conductance (Figure 5.1). The high resolution demonstrated total coverage of the surface of the silica with tungsten. The EDX image of Figure 5.1 shows white clusters around the micro-pores of the solid structure suggesting that these clusters were being formed containing the heavier metal tungsten. EDX analysis of a non-clustered area of the support structure showed the presence of tungsten, and thus the presence of the tungstosilicic acid (Figure 5.2). This complete coverage of the surface of the silica with tungstosilicic acid meant that the contact of the HPA with any flowing solution would be maximised for effective and efficient acetylation reactions.

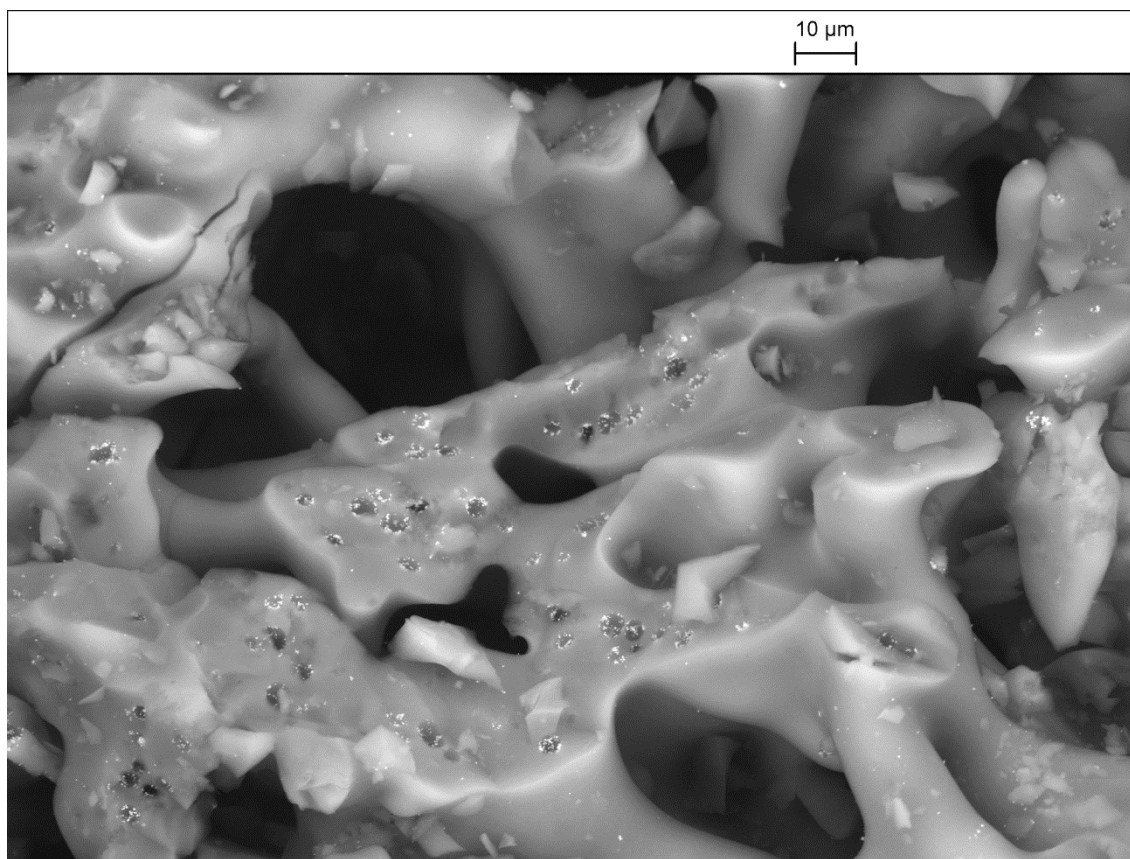
Raman Spectroscopic Monitoring - Results and Discussion

Figure 5.1 SEM-EDX image of a CMR produced from *catalyst preparation 5.2*. No sputtering was performed. White spots of heavier elements can be seen around the smaller micro-pores within the silica.

Raman Spectroscopic Monitoring - Results and Discussion

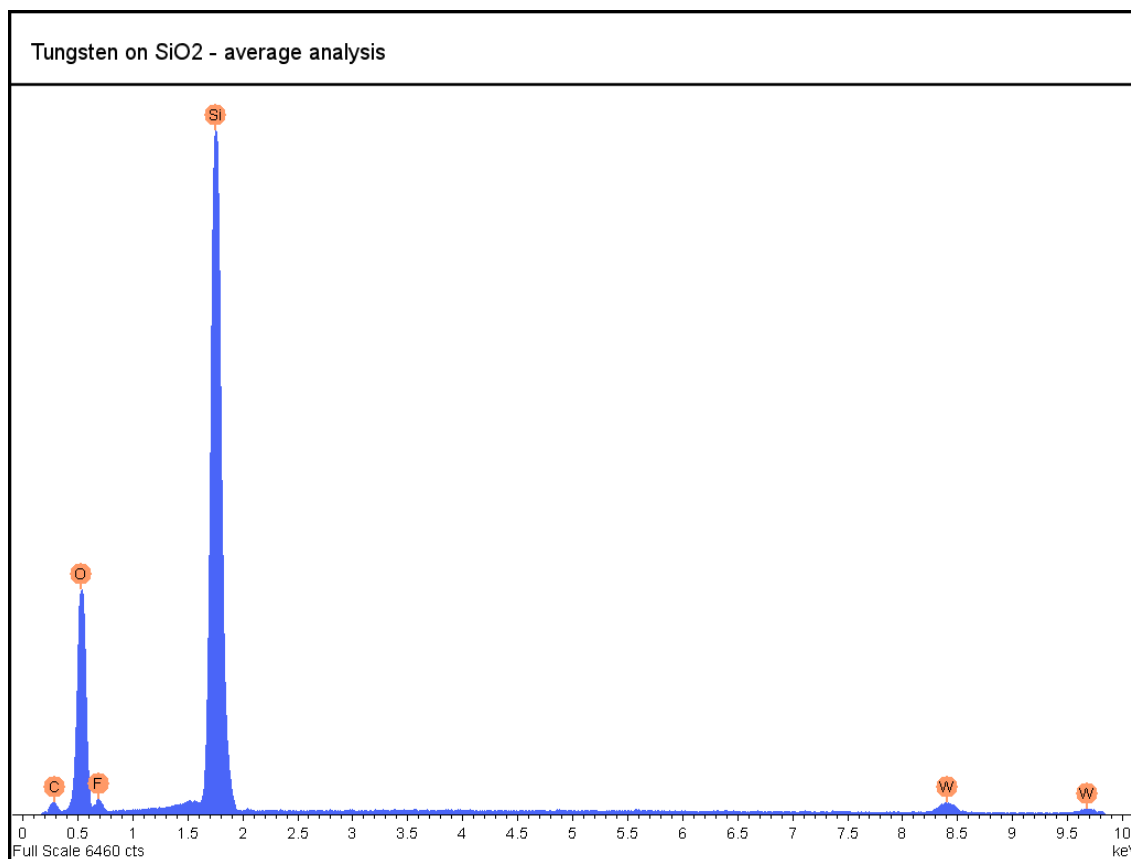


Figure 5.2 EDX area analysis of a non-cluster surface of the monolith from Figure 5.1.

Raman Spectroscopic Monitoring - Results and Discussion*5.12 Batch acetylation reaction - results*

The acetylation reaction described in 5.5 was performed with tungstosilicic acid as the catalyst. This was done because 4-bromophenyl acetate was difficult to purchase pure. The resulting solution was purified by liquid-liquid extraction in DCM (50 mL) and 3 x 100 mL washes of water. The resulting DCM layer was dried under magnesium sulphate and tested for purity of 4-bromophenyl acetate under GC-MS conditions described in *GC-MS analysis 4.3* (without decane addition). The resulting chromatograph can be found in Appendix 26. No 4-bromophenol or the by-product acetic acid remained with pure 4-bromophenyl acetate. The yield of the reaction was not calculated as only the pure 4-bromophenyl acetate was required.

The 4-bromophenyl acetate was synthesised and purified for the purposes of Raman calibration standard solutions.

5.13 Acetylation reaction Raman spectra

Each component of the reaction was analysed by Raman spectroscopy. Individual identifiable peaks were observed for 4-bromophenol, acetic anhydride and 4-bromophenyl acetate. Figure 5.3 shows the overlay of each spectrum. For calibration the acetic anhydride peaks were not monitored due to being in significant excess; it was not likely to be affected by 0.3 M difference as the amount of moles in pure acetic anhydride is 10.58 M (determined by density/molecular mass).

Strong individual peaks for 4-bromophenol were observed at Raman shifts 252.80 and 715.05 cm^{-1} . Strong individual peaks for 4-bromophenyl acetate were observed at Raman shifts 296.64 and 1275.65 cm^{-1} . Most other peaks overlapped with

Raman Spectroscopic Monitoring - Results and Discussion

one another which were to be expected as 4-bromophenol and 4-bromophenyl acetate are similar in structure.

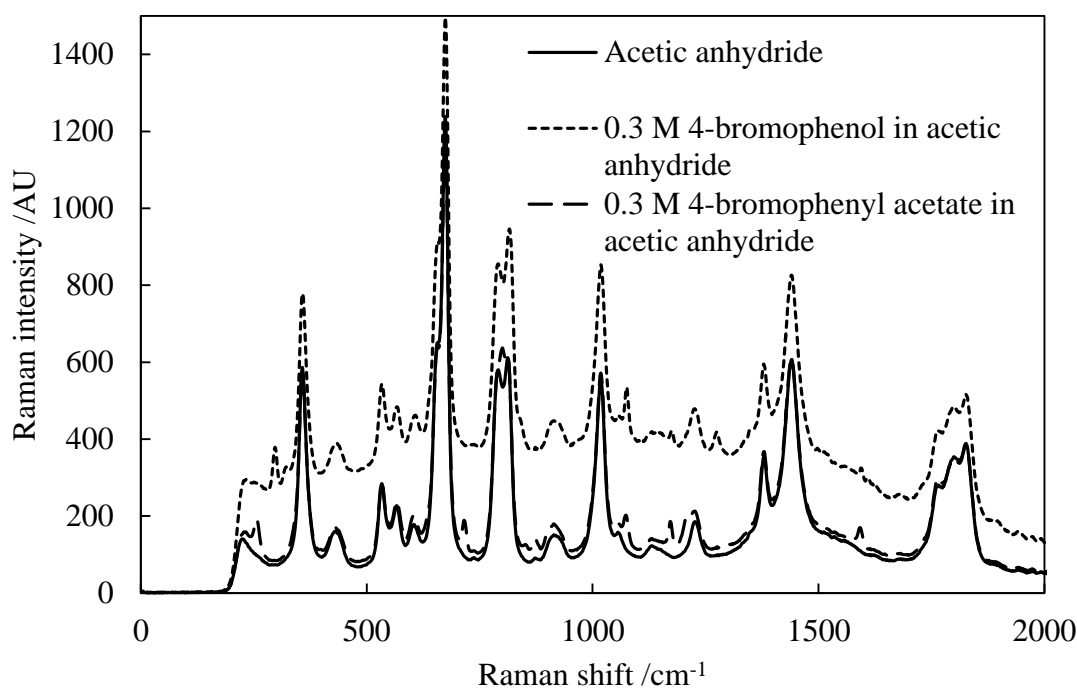


Figure 5.3 The Raman spectra of acetic anhydride, 0.3 M 4-bromophenol and 0.3 M 4-bromophenyl acetate. The spectral conditions used to obtain the data were a 1 s integration time averaged 3 times with electrical and stray light correction default from the software. Laser power was set to 340 mV. Each Raman measurement was performed under static conditions.

Raman Spectroscopic Monitoring - Results and Discussion*5.14 Acetylation Raman spectral calibration – A results*

Initial calibrations for this reaction were performed during the same time span as the *Raman calibration 4.19* for the Suzuki reactions. Because of this the same calibration approach was performed monitoring two peaks and subtracting their assumed baseline. The two peaks monitored were observed between Raman shifts $237.81 - 278.83 \text{ cm}^{-1}$, and $281.37 - 309.31 \text{ cm}^{-1}$ for 4-bromophenyl acetate and 4-bromophenol respectively. By subtracting an assumed baseline below the peak of interest, a final actual peak area was determined for each analyte.

Initial calibrations used standard reaction solutions by varying the concentrations of 4-bromophenol, 4-bromophenyl acetate and acetic acid in acetic anhydride. Reaction solutions simulated were 0, 20, 40, 60, 80 and 100% conversions for 0.3 M 4-bromophenol starting material. Table 5.1 shows the concentrations used for the calibration. The calibration model is shown in Figure 5.4. The resulting peak areas observed using this methodology appeared to be linear for both 4-bromophenol and 4-bromophenyl acetate. The origin however at first appears to be well above 0 for 4-bromophenyl acetate. The addition of 1 standard deviation of error shows that the origin is still outside the limit of the origin, this suggests the baseline correction may not be correct.

On attempting flow reaction chemistry in order to measure the Raman responses, it was apparent that the reaction solutions were finishing a different colour to that of the batch reaction product. On investigation the colour of 4-bromophenyl acetate was yellow on the batch reaction, and clear on flow reaction. It was assumed that an extra component was responsible for the colour change in batch as opposed to the flow reaction. Because the 4-bromophenyl acetate used for the calibrations was from the

Raman Spectroscopic Monitoring - Results and Discussion

batch reaction, this would have affected the observed reaction mixture predictions. On examining the Raman spectra further for the two reactions (described in *Flow acetylation reaction 5.6*), the spectra baseline was below the unreacted spectra (Figure 5.5). This extra factor was not only affecting the colour of the reaction solution but also the Raman spectra for the calibration. Suspected components of the batch reaction mixture responsible for this colour change lay with the tungstosilicic acid. Corrected calibration spectra were required which could have been achieved by further purification of 4-bromophenyl acetate or it importing from an outside source.

Conversion /%	Concentration /M		
	4-bromophenol	acetic acid	4-bromophenyl acetate
0	0.2999	0.0000	0.0000
20	0.2398	0.0601	0.0600
40	0.1799	0.1197	0.1200
60	0.1197	0.1810	0.1800
80	0.0601	0.2398	0.2400
100	0.0000	0.3002	0.3000

Table 5.1 The concentration of 4-bromophenol, acetic acid and 4-bromophenyl acetate used for Raman spectroscopic calibration in relation to simulated conversions. 4-bromophenyl acetate was produced in-house.

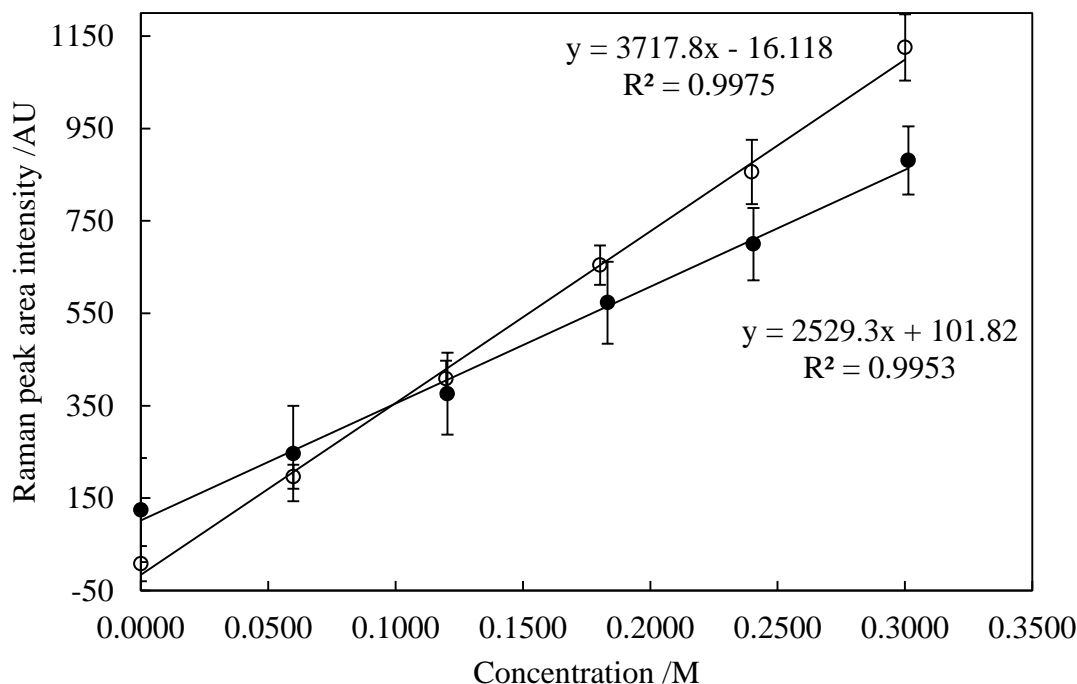
Raman Spectroscopic Monitoring - Results and Discussion

Figure 5.4 The Raman calibration of 4-bromophenyl acetate (•) and 4-bromophenol (○).

The solutions used for calibration were described previously in Table 5.1. Peak areas observed between Raman shifts $237.81 - 278.83 \text{ cm}^{-1}$, and $281.37 - 309.31 \text{ cm}^{-1}$ respectively. Noise area subtraction for was performed by using the maximum and minimum Raman shifts and their intensity for each peak as trapezoid vectors. Each calibration solution was static for acquisition recording. The spectral conditions used to obtain the data were a 1 s integration time averaged 3 times with electrical and stray light correction default from the software. Laser power was set to 340 mV.

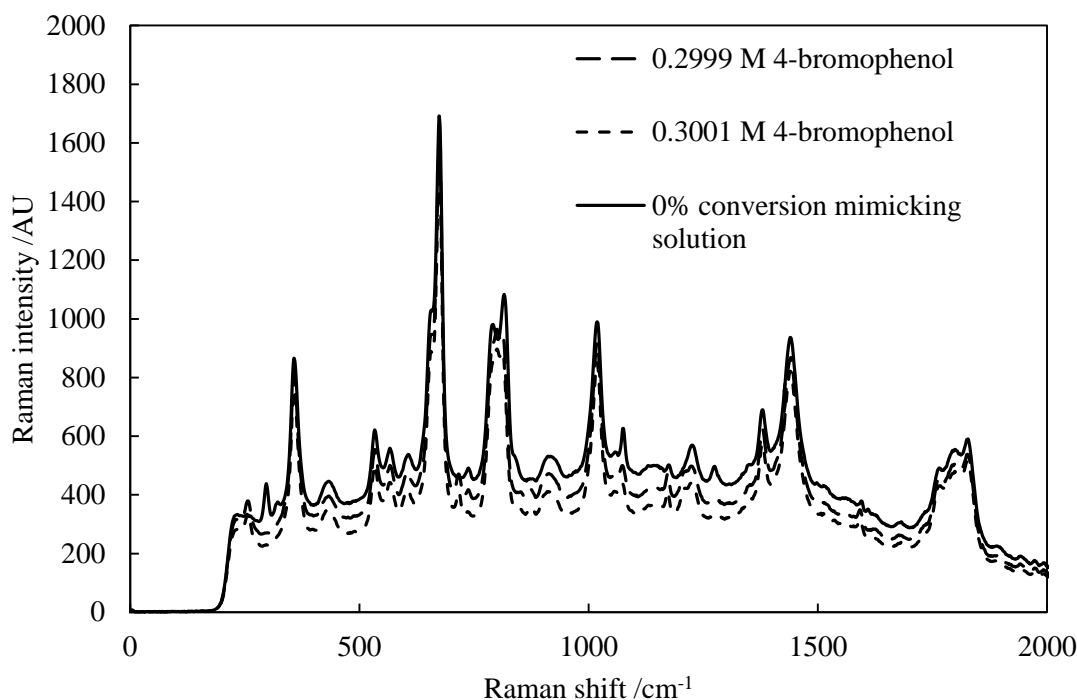
Raman Spectroscopic Monitoring - Results and Discussion

Figure 5.5 The Raman spectra of 2 flow reactions and the 0% standard conversion from Table 5.1. The reactions had the same CMR void volume and flow rate of 0.2420 mL and 0.08 mL min⁻¹. Initial starting concentrations of the different solutions were 0.2999 M and 0.3001 M 4-bromophenol. Reaction temperature was at 20 °C. The spectral conditions used to obtain the data were a 1 s integration time averaged 3 times with electrical and stray light correction default from the software. Laser power was set to 340 mV. Raman measurements were flowing for the reactions and static for the standard solution.

Raman Spectroscopic Monitoring - Results and Discussion

A new sample of 4-bromophenyl acetate was purchased from Apollo Scientific and colour was observed to be clear. Calibration standard solutions were remade and their concentrations are shown in Table 5.2. The Raman spectra of these solutions differed greatly to the Raman spectra of the in-house produced 4-bromophenyl acetate. Figure 5.6 and Figure 5.7 show the two sets of Raman spectra for both the in-house and purchased 4-bromophenyl acetate respectively. It can be seen that the artefact in the initial calibration solution from the in-house 4-bromophenyl acetate increased the background across the spectrum raising the peak height and intensities. Another trend in the initial data set in comparison to the purchased 4-bromophenyl acetate was the direction of the trend. At 0% conversion, the spectral background increased with increasing concentration of 4-bromophenyl acetate for the in-house, but spectral background decreased in the purchased reagent.

The calibration using the purchased product seemed to be more appropriate and showed greater promise for Raman predictive purposes as it was certifiably pure. Examination of the reaction solutions used previously for Figure 5.5 showed the spectral peaks for 4-bromophenyl acetate had a rise in background that could not be accounted for by either calibration. The background was within the limits of the purchased 4-bromophenyl acetate spectra but it could not account for the rise in spectral peak. An alternative predictive approach was needed in order to account for this extra factor change. PLSR previously used for the Suzuki reaction was used.

Raman Spectroscopic Monitoring - Results and Discussion

Conversion /%	Concentration /M		
	4-bromophenol	acetic acid	4-bromophenyl acetate
0	0.3000	0.0000	0.0000
20	0.2399	0.0603	0.0598
40	0.1803	0.1194	0.1203
60	0.1198	0.1835	0.1833
80	0.0599	0.2403	0.2405
100	0.0000	0.3037	0.3013

Table 5.2 The concentration of 4-bromophenol, acetic acid and 4-bromophenyl acetate used for Raman spectroscopic calibration in relation to simulated conversions. 4-bromophenyl acetate was purchased.

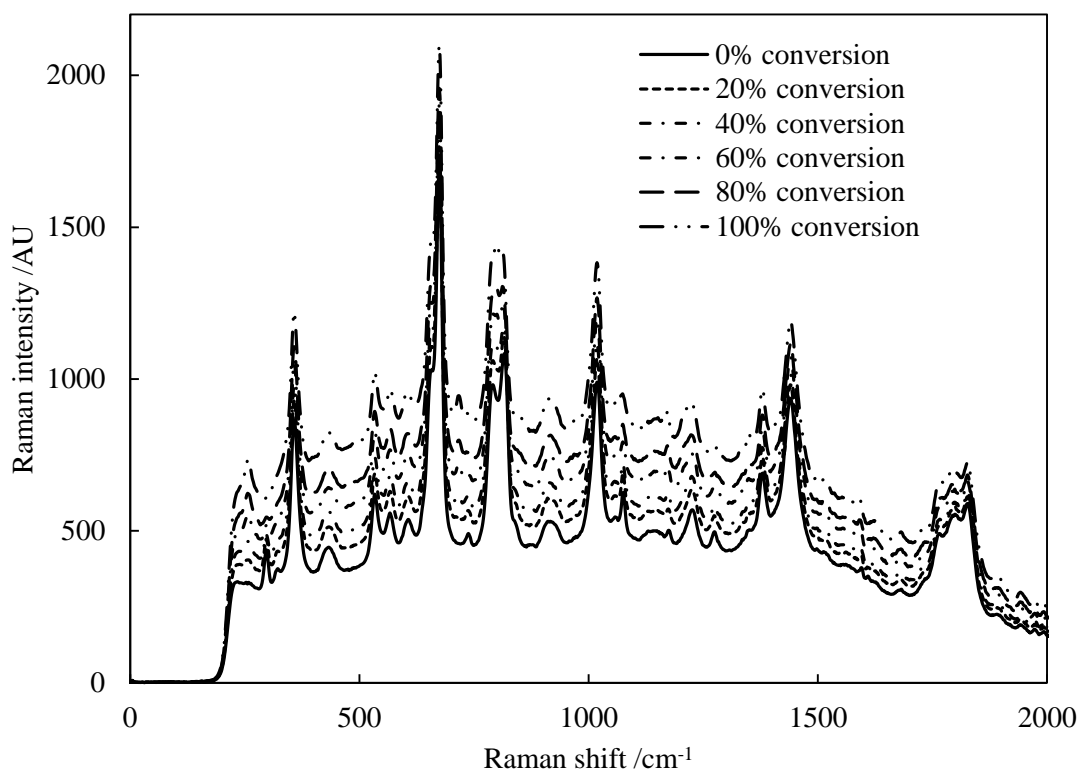
Raman Spectroscopic Monitoring - Results and Discussion

Figure 5.6 Raman spectra of the standard reaction solutions presented in Table 5.1. Each solution was static during acquisition. The spectral conditions used to obtain the data were a 1 s integration time averaged 3 times with electrical and stray light correction default from the software. Laser power was set to 340 mV.

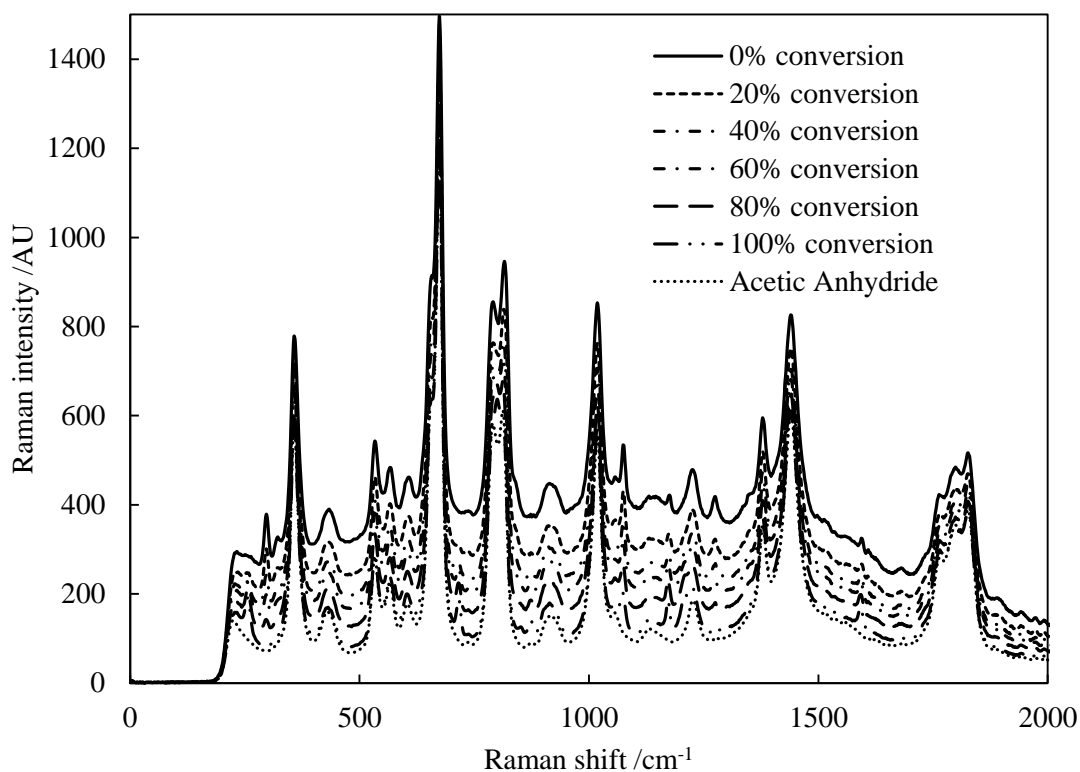
Raman Spectroscopic Monitoring - Results and Discussion

Figure 5.7 Raman spectra of the standard reaction solutions presented in Table 5.2. Each solution was static during acquisition. The spectral conditions used to obtain the data were a 1 s integration time averaged 3 times with electrical and stray light correction default from the software. Laser power was set to 340 mV.

Raman Spectroscopic Monitoring - Results and Discussion*5.15 Acetylation Raman spectral calibration – B results*

Previous calibrations led to results being non-precise and inaccurate due to the modelling calibration being ill equipped to predict the Raman spectra of reaction solutions. The use of PLSR in Raman spectra meant that a large number of spectral factors contribute to the Raman signals. Pre-spectral processing techniques such as auto-centring, row mean square centring, and smoothing (by an averaging filter of 5 points) permitted the successful calibration. Figure 5.8 describes the calibration between the PLS scores and the concentration of both 4-bromophenol and 4-bromophenyl acetate. As previously reported for the Suzuki calibration using PLSR, the calibration model fits a highly linear trend that passes through the origin. The data used for the calibration was taken from the Raman spectra observed Figure 5.7.

One problem with this calibration was that even though PLSR will account for the different artefacts influencing the spectra, it is still based on the solutions that did not account for the presence of an extra artefact affecting the reactions. Nevertheless the calibration model was still tested with the intent of optimising the reaction flow rates.

Flow rates of 0.5, 1.0, 1.5, 2.0, 2.5, 3.0, 3.5 and 4.0 mL min⁻¹ were used to try and optimise the amount of 4-bromophenyl acetate produced. The conversion and amount of 4-bromophenyl acetate produced per hour was plotted with the flow rate for a CMR void volume of 0.4467 mL. The residence time had no effect on the production of 4-bromophenyl acetate at higher flow rates above 2.5 mL min⁻¹ (Figure 5.9). At the flow rates increase the production equilibrates and the conversion at these flow rates reduces almost linearly. Two points at 1.0 and 1.5 mL min⁻¹ do not appear to fit the straight line of conversion trend with increased flow rates. One of the reasons for this could be that the same solution was used and flow rate increased making the first reactions leach the

Raman Spectroscopic Monitoring - Results and Discussion

largest amount of tungstosilicic acid. Tungstosilicic acid would have been leaching the highest on the first reactions of the flow system. This may also account for the lack of increased production or optimal pinnacle in 4-bromophenyl acetate production as continued leaching of the acid was distorting the flow system measurements and this would mean any measurements were unrepeatably.

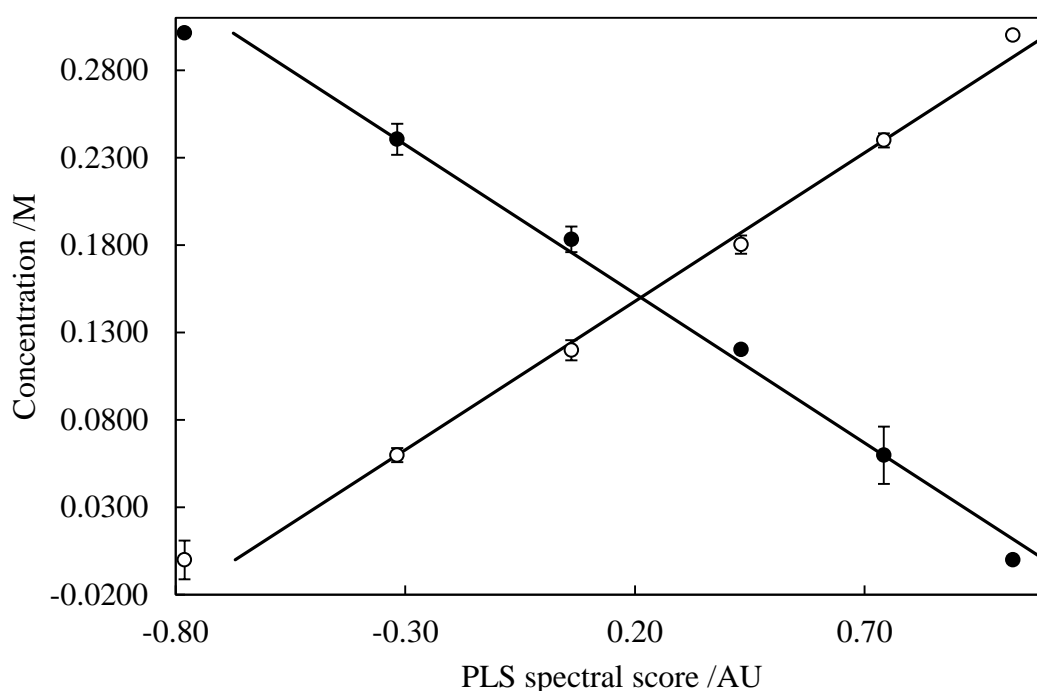


Figure 5.8 The Raman calibration of 4-bromophenol (•) and 4-bromophenyl acetate (○). The solutions used for calibration were described previously in Table 5.2. Peak areas were observed between Raman shifts $230.09 - 321.95 \text{ cm}^{-1}$. Each calibration solution was static during acquisition. The spectral conditions used to obtain the data were a 1 s integration time averaged 3 times with electrical and stray light correction default from the software. Laser power was set to 340 mV. Five factors were accounted for in the PLSR process.

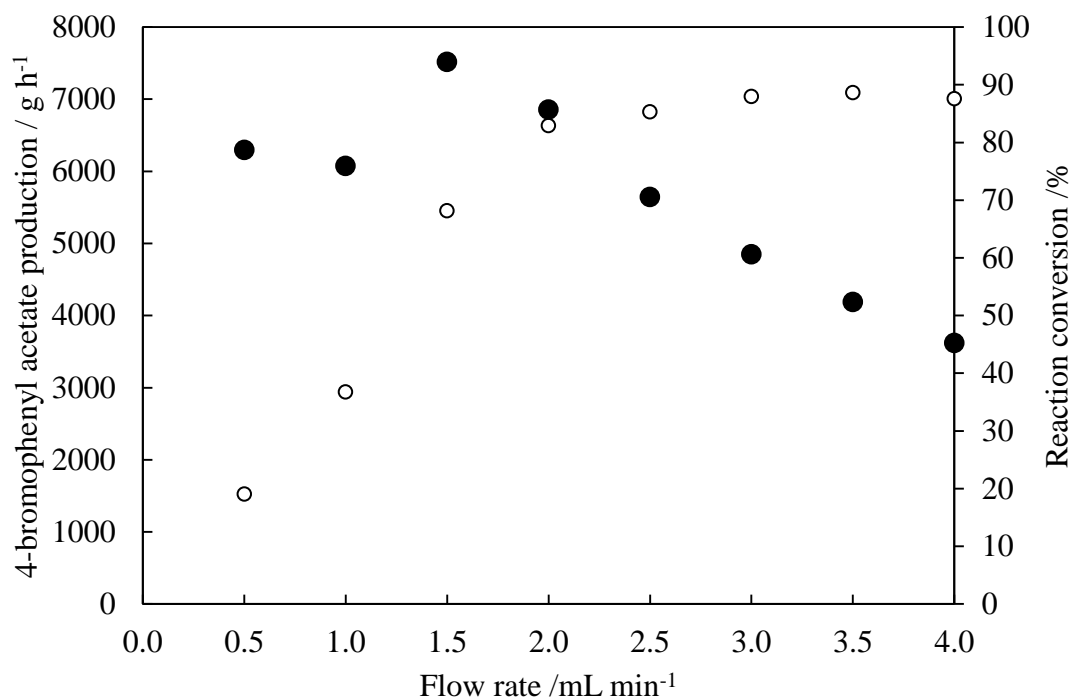
Raman Spectroscopic Monitoring - Results and Discussion

Figure 5.9 The influence of flow rate on 4-bromophenyl acetate production (○) and conversion (●) in the acetylation reaction between 0.2948 M 4-bromophenol and excess acetic anhydride. The CMR used was produced from *catalyst preparation 5.2* with a void volume of 0.4467 mL. The reaction was performed at volumetric solution flow rates of 0.5 to 4.0 mL min⁻¹ and the temperature in the column heater was set at 20 °C. 4-bromophenyl acetate production and conversion was determined by 5.8.

Raman Spectroscopic Monitoring - Results and Discussion*5.16 HPA influences on Raman spectra – results*

Based on the theory that tungstosilicic acid is influencing the spectra, batch reactions of 0.3000 M 4-bromophenol in acetic anhydride with varying concentrations of tungstosilicic acid were carried out. Once complete the reaction mixtures were passed through the Raman flow cell and measured statically. Figure 5.10 shows the Raman spectra obtained for the batch solutions. It indicates that the tungstosilicic acid concentration changed the spectral background for what is essentially the same concentration solution of 4-bromophenyl acetate. During the reactions, a colour change was also observed and was denser in colour as the increase in catalyst concentration was performed. This suggests that the first calibration of 5.7 using the in-house produced 4-bromophenyl acetate was contaminated. GC-MS only detected the volatiles of the solution which did not include tungstosilicic acid; consequently the solution was pure in terms of organics, but not for inorganics.

The spectra were overlapped for each concentration of tungstosilicic acid (Figure 5.10). Baseline subtraction from the 4-bromophenyl acetate peak (described previously in 5.7) demonstrated that the HPA was increasing the 4-bromophenyl acetate peak area. Another observation in the data led to the decrease in peak area response above 0.0007 M tungstosilicic acid. This was due to the solubility of the tungstosilicic acid reaching saturation point at 0.0007 M. The Raman response from the higher concentrations revealed less signal response from not only the 4-bromophenyl acetate but also the acetic anhydride. Previously it was considered that the cause of the reaction distortion in Raman spectra was due to an extra factor not accounted for in the calibration. The factor that it was not accounting for was the leaching of the tungstosilicic acid from the CMR.

Raman Spectroscopic Monitoring - Results and Discussion

The calibration described from 5.8 was also put into place for predicting the concentrations of 4-bromophenyl acetate at the varying concentrations of tungstosilicic acid. The data from the PLSR calibration integrated into the data from Figure 5.10 showed that as the concentration of tungstosilicic acid increased, the concentration of 4-bromophenyl acetate decreased (Figure 5.12). However this could not be possible as all reactions were taken to completion so the concentration of 4-bromophenyl acetate should be at approximately 0.3 M if the tungstosilicic acid was not affecting the Raman spectra. The reason for this low predictability arose from the original calibration. PLSR is a multivariate technique that utilizes variation in a range of Raman shifts in order to calibrate the concentration. This range covered non-peak backgrounds that were altered by the varying tungstosilicic acid concentration. Because of this the measured response of the reaction spectra measured the variance of all the background too, which distorted the predictability of the data.

Unfortunately calibration by this methodology was not possible for this reaction. The extra factor of the tungstosilicic acid leaching into the flow system meant that in order to predict effectively this had to be accounted for in the calibration standard reaction solutions. The HPA had a co-linear effect on the spectra distorting any previous calibrations that could not accommodate this. Any calibrations with the tungstosilicic acid could not be done as the reaction proceeds at room temperature and the addition of the tungstosilicic acid would initiate the reaction in a faster time than it would take to pass the calibration solution through the Raman flow cell. Nevertheless, although this methodology could not predict the accurate concentrations of 4-bromophenol and 4-bromophenyl acetate, it could still be used to monitor the reaction manually.

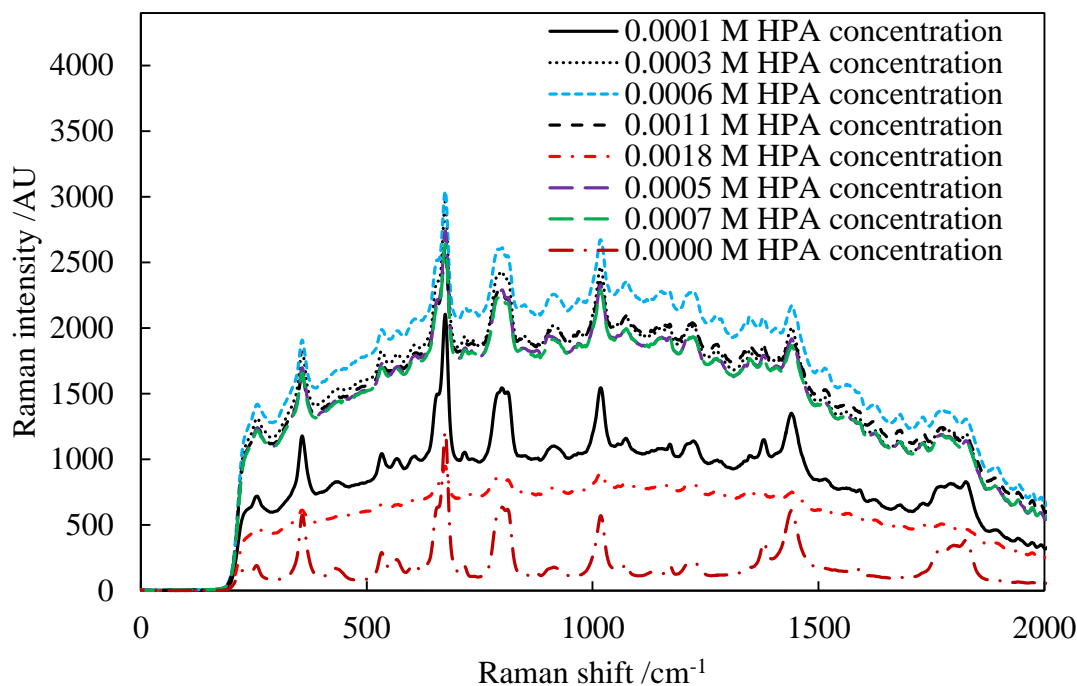
Raman Spectroscopic Monitoring - Results and Discussion

Figure 5.10 Raman spectra of completed batch reactions producing 0.3 M 4-bromophenyl acetate in acetic anhydride. Concentrations of tungstosilicic acid were varied at 0.0000, 0.0001, 0.0003, 0.0005, 0.0006, 0.0007, 0.0011 and 0.0018 M. Reaction temperatures were at 20 °C. Each solution was static during Raman acquisition. The spectral conditions used to obtain the data were a 1 s integration time averaged 3 times with electrical and stray light correction default from the software. Laser power was set to 340 mV.

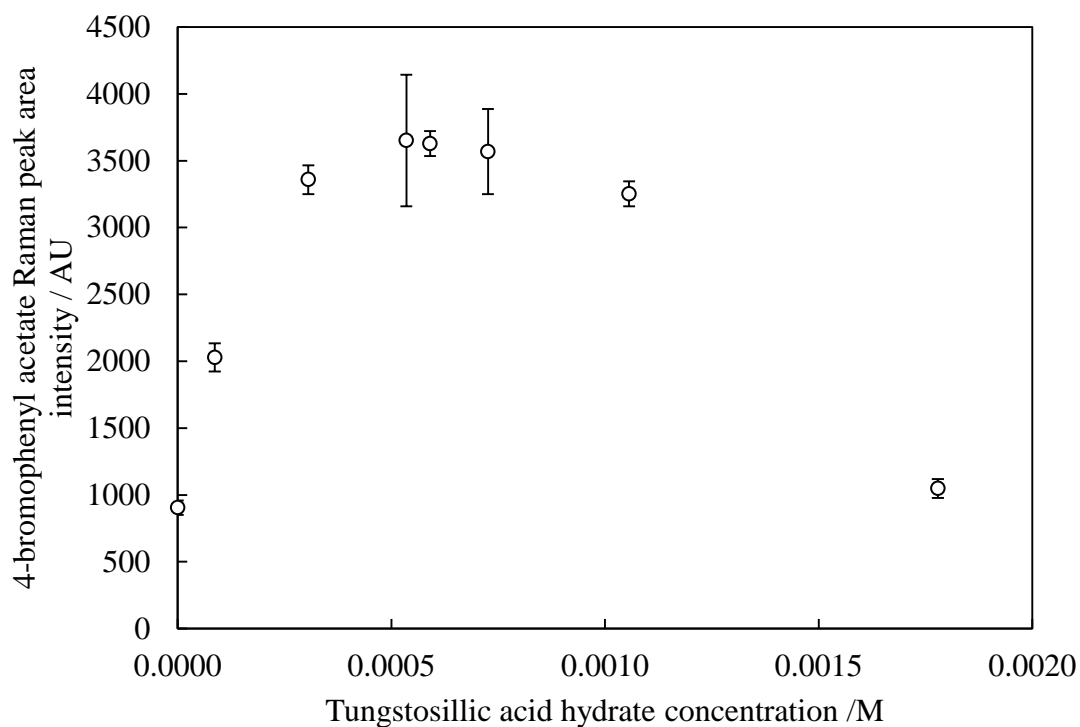
Raman Spectroscopic Monitoring - Results and Discussion

Figure 5.11 The influence of increased HPA concentration on the Raman peak area signal of 4-bromophenyl acetate. The peak monitored was between Raman shifts $235.23 - 286.47 \text{ cm}^{-1}$ from the Raman spectra shown in Figure 5.10. The calibration method for peak analysis was described in 5.7. Each solution was static during Raman acquisition. The spectral conditions used to obtain the data were a 1 s integration time averaged 3 times with electrical and stray light correction default from the software. Laser power was set to 340 mV.

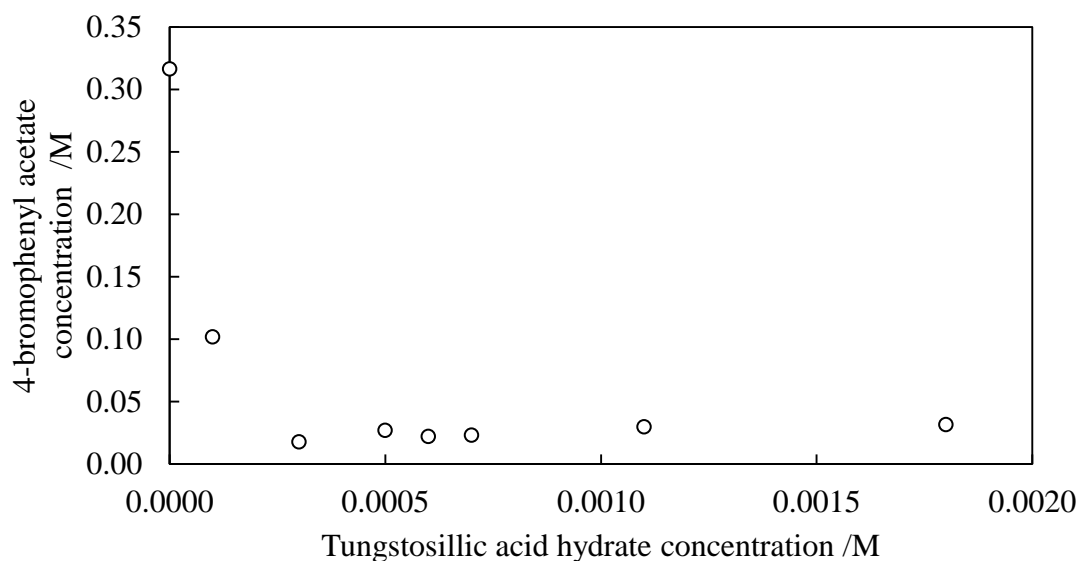
Raman Spectroscopic Monitoring - Results and Discussion

Figure 5.12 The influence of increased HPA concentration on the concentration of 4-bromophenyl acetate. The calibration described in 5.8 was applied to the Raman spectra shown in Figure 5.10. The spectral region of interest was between Raman shifts $230.09 - 321.95 \text{ cm}^{-1}$. Each solution was static during Raman acquisition. The spectral conditions used to obtain the data were a 1 s integration time averaged 3 times with electrical and stray light correction default from the software. Laser power was set to 340 mV.

Raman Spectroscopic Monitoring - Results and Discussion*5.17 Summary*

The acetylation reaction between 4-bromophenol and acetic anhydride was successfully implemented into the flow reaction system. An adaptation of the monoliths used previously (see section *monolith 2.5*) lead to a CMR being produced that contained a complete coverage of tungstosilicic acid. This inorganic heteropoly acid catalyst provided a fast reaction with comparison to the Suzuki reactions previously performed. Despite the success in integrating this new catalyst for a different reaction there was a problem with reaction monitoring.

Raman spectroscopic monitoring calibrations were unable to determine reagent and product concentrations. Unfortunately the heterogeneous catalyst was leaching into the flow of reagents and distorting the Raman spectra generating a co linear effect; as the concentration of tungstosilicic acid increases signal, there is a decrease in 4-bromophenol and 4-bromophenyl acetate signal. Raman spectroscopy could not be used to monitor this reaction unless a purification stage pre-Raman flow cell was in place or a different immobilised catalyst was used. Further studies for this reaction and that would possibly be beneficial for any heterogeneous catalysis within this flow system would be a catalyst capture technique to pluck any leaching catalyst from the reaction solution.

6.0 Conclusion

A fully integrated continuous flow reaction system was made successfully incorporating a heterogeneous catalyst, heating mechanism and in-line detection system. The initial development started with the heterogeneous catalyst. Silica monoliths were chosen as an immobilisation medium due to their high surface area, lack of swelling in organic solvents, rigid structure, chemical tolerance, temperature tolerance and porous nature. These monolithic structures were characterised to identify the best solid support that could progress the project further. These types of monoliths produced concurred with literature values with respect to porosity, microstructure and surface area^{152, 180}. However silica monoliths produced by *monolith 2.3* did not agree with literature values for nano pore sizes which were determined between 50 – 250 nm whereas observed values showed no distinct nano pores present¹⁸¹. By selecting the silica monolith produced from *monolith 2.5* it was possible to scale-up the CMR to incorporate larger flow volumes increasing catalyst residence time and productivity. Once scale-up was successfully determined, the monoliths were then subjected to various method of palladium immobilisation. This would later function as the solid supported catalyst for the Suzuki reaction. The palladium immobilisation had challenges as the palladium clusters were either too large or leaching into the flow system. This was unacceptable as the larger clusters would reduce residence time due to a smaller surface area and the leaching demonstrated a high lack of control which defeats the purpose of immobilisation. This was then remedied with a method of immobilisation where palladium was anchored to the silica in the nano pores. This showed minimal leaching and promoted a larger surface area for the palladium to act as a catalyst. Another factor was the spread of catalyst on the monolithic surface. The final chosen method for palladium immobilisation (described in *palladium loading 2.14*) demonstrated these

characteristics as well as having high surface areas, high porosity and high reproducibility with the silica monoliths described in *monolith 2.5*. This same methodology was used by He et al. and showed successful Suzuki reaction flow chemistry¹⁰¹.

Integrating the heterogeneous catalyst into the flow system was the greatest challenge with respect to engineering the flow system. The microwave heating chamber was not designed to accommodate the size of catalysts that were being produced. Placing the CMR in flow was simple, but maintaining it was the difficulty as prolonged pumping and pressures especially whilst being heated in the microwave chamber. This produced fractures in the links between the glass connectors and the heat shrink tubing. The leaking of the reactants out of the flow stream meant any flow leaving the microwave chamber as intended for analysis was not representative of the reaction conditions. After exhausting possibilities in integrating the microwave heating into the flow system, it was abandoned and a column heater was introduced. This gave an option of elongating the catalyst to increase catalyst residence time with the reactants, and improved the glass-tubing connectivity holding the CMR in place. Assimilating the column heater to control reaction temperature constructed a fully integrated flow reaction system resulting in the effective application of the Suzuki reaction between 4-bromobenzonitrile and phenyl boronic acid. It is possible to use microwave heating in this system as proven from previous research¹⁸². However the design of the microwave used in this project was designed for batch round bottom flasks as reactors rather than flow reactors. For microwaves to be more effective in this larger reaction system a different microwave heating design would be required.

The newly developed flow system was initially being analysed using GC-MS. However this was time consuming and lacks immediate reaction monitoring. A spectroscopic in-line analysis window was installed. This opened an opportunity to

replace the GC-MS with Raman spectroscopic analysis. The analysis required calibration and several calibration attempts were carried out, however for quantification a PLSR model was the best choice. The model concurred with GC-MS results. The Raman spectral monitoring permitted optimisation of flow reaction conditions as well as providing some reaction kinetic information. Other research groups such as Mozharov et al. have performed reaction quantification using Raman spectroscopy in flow reaction chemistry without PLSR, although the reaction quantified with their system was not as complex as the heterogeneous Suzuki reaction¹³⁶. Additional information such as impurity identification is also possible with this methodology making this flow system highly favourable for a range of reactions.

The operational and fully analysed flow system was used for a secondary reaction involving a different catalyst. A heteropoly acid was embedded on the surface of the same monoliths produced from 2.5. This provided a heterogeneous source of protons to catalyse the acetylation reaction between 4-bromophenol and acetic anhydride. The immobilisation of the HPA was successful and was clearly characterised. As a batch acetylation reaction the HPA catalyst caused swift reaction completion at room temperature as reported from Hevani et al.¹⁸³. On replacing the palladium CMR with HPA-CMR there were difficulties. It was discovered that the HPA was leaching off the CMR and causing great disruption to the Raman spectra. The leaching of HPA has been observed in other research¹⁸⁴⁻¹⁸⁶. This made quantification and reaction monitoring incredibly difficult. Despite the lack of in-line monitoring the reaction was still successfully integrated into the flow system.

In summary, the flow system design was an impressive tool that if continued could be valuable in contributing to future flow organic reaction analysis. The Suzuki and acetylation reactions were achieved in flow with potential of many more reactions within this flow system design. Most of which could be monitored by Raman

spectroscopy to optimise and determine reaction kinetics; as proven with the Suzuki reactions. In addition to reaction monitoring, different heating regimes can be explored and exploited including adaptable designs to microwave heating.

7.0 Further Work

Further work with this project would be beneficial to a host of areas in organic flow synthetic chemistry including automation, chemical library database development, reaction optimisation, reaction kinetic studies, and reaction condition adaptation. In particular the project should develop to replace other heating regimes into the flow system including IR heating and an adapted microwave system. This would demonstrate effective use and reaction control utilising the advantages of both IR and microwave heating to increase reaction rates and efficiencies.

Another keen area of interest with this project is automation especially automated optimisation. This system is capable of full automotive control and by relaying results from the Raman spectra, it is possible to generate a feedback loop that can increase and decrease the flow rate in accordance with the intensity of particular peaks. This would provide an insightful and valuable tool for reaction control with minimal human interference. Another subject on automation is automotive reactant introduction. Controlling a system to provide this type of data would be valuable in developing a library of compounds for Raman detection that can positively identify a molecule in the same fashion as mass spectrometry in GC-MS. The fingerprint spectrum of compounds can be relayed back into computer memory and recorded for future routine laboratory analysis.

A final future objective is using this flow system design to assess the stability and turnover rate of different heterogeneous catalysts for the same reaction. This would be comparative work demonstrating the capability of different catalysts on the same reaction mixture with only having to replace the CMR. For example, there are many different types of palladium catalysts that have been developed for the Suzuki reaction and the heterogeneous immobilisation techniques can be applied to the same monolithic

material and placed within the flow system. Other reactions such as Heck and Sonogashira reactions which both use palladium catalysis can also be incorporated into the reaction flow system just by changing the reactants and solvents. Not only can palladium be used but the potential for alternative proton donating heterogeneous catalyst too. The acetylation study can be modified as the catalyst leaching was significantly affecting the Raman spectrum. So by altering or changing the catalyst it is still possible to perform reaction optimisation and kinetic studies of acetylation reactions.

Overall the further development with this project aims to improve the flow systems original design without changing the fundamentals of a continuous flow pump, heating system, heterogeneous catalyst and Raman reaction monitoring.

Chaplain, G., Haswell, S. J., Fletcher, P. D. I., Kelly, S. M. & Mansfield, A. Development and Evaluation of a Raman Flow Cell for Monitoring Continuous Flow Reactions. *Australian Journal of Chemistry* **66**, 208-212, doi: 10.1071/CH12379 (2013)

Chaplain, G., Haswell, S. J., Fletcher, P. D. I., Kelly, S. M. & Mansfield, A. Reaction Monitoring using Raman spectroscopy in a flow micro reactor system, *Analytical Research Forum*, Loughborough 2010

1. Ahmed-Omer, B.; Brandt, J. C.; Wirth, T., Advanced organic synthesis using microreactor technology. *Organic & Biomolecular Chemistry* **2007**, 5, (5), 733-740.
2. Baumann, M.; Baxendale, I. R.; Ley, S. V.; Smith, C. D.; Tranmer, G. K., Fully Automated Continuous Flow Synthesis of 4,5-Disubstituted Oxazoles. *Organic Letters* **2006**, 8, (23), 5231-5234.
3. Fortt, R.; Wootton, R. C. R.; de Mello, A. J., Continuous-Flow Generation of Anhydrous Diazonium Species: Monolithic Microfluidic Reactors for the Chemistry of Unstable Intermediates. *Organic Process Research & Development* **2003**, 7, (5), 762-768.
4. Banister, J. A.; Lee, P. D.; Poliakoff, M., Flow Reactors for Preparative Chemistry in Supercritical Fluid Solution: "Solvent-Free" Synthesis and Isolation of Cr(CO)₅(C₂H₄) and (η⁵-C₅H₅)Mn(CO)₂(η²-H₂). *Organometallics* **1995**, 14, (8), 3876-3885.
5. Moorthy, J.; Khoury, C.; Moore, J. S.; Beebe, D. J., Active control of electroosmotic flow in microchannels using light. *Sensors and Actuators B: Chemical* **2001**, 75, (3), 223-229.
6. Lima, J. L. F. C.; Santos, J. L. M.; Dias, A. C. B.; Ribeiro, M. F. T.; Zagatto, E. A. G., Multi-pumping flow systems: an automation tool. *Talanta* **2004**, 64, (5), 1091-1098.
7. Bolton, K. F.; Canty, A. J.; Deverell, J. A.; Guijt, R. M.; Hilder, E. F.; Rodemann, T.; Smith, J. A., Macroporous monolith supports for continuous flow capillary microreactors. *Tetrahedron Letters* **2006**, 47, (52), 9321-9324.
8. Brivio, M.; Verboom, W.; Reinhoudt, D. N., Miniaturized continuous flow reaction vessels: influence on chemical reactions. *Lab on a Chip* **2006**, 6, (3), 329-344.
9. Shaw, K. J.; Docker, P. T.; Yelland, J. V.; Dyer, C. E.; Greenman, J.; Greenway, G. M.; Haswell, S. J., Rapid PCR amplification using a microfluidic device with integrated microwave heating and air impingement cooling. *Lab on a Chip* **2010**, 10, (13), 1725-1728.
10. Petersen, T. P.; Ritzén, A.; Ulven, T., A Multistep Continuous-Flow System for Rapid On-Demand Synthesis of Receptor Ligands. *Organic Letters* **2009**, 11, (22), 5134-5137.
11. Phan, N. T. S.; Khan, J.; Styring, P., Polymer-supported palladium catalysed Suzuki–Miyaura reactions in batch and a mini-continuous flow reactor system. *Tetrahedron* **2005**, 61, (51), 12065-12073.
12. Wiles, C.; Watts, P., Continuous Flow Reactors, a Tool for the Modern Synthetic Chemist. *European Journal of Organic Chemistry* **2008**, 2008, (10), 1655-1671.
13. Sacks, M. E.; Lee, S.-I.; Biesenberger, J. A., Effect of temperature variations on molecular weight distributions: batch, chain addition polymerizations. *Chemical Engineering Science* **1973**, 28, (1), 241-257.
14. Greenway, G. M.; Haswell, S. J.; Morgan, D. O.; Skelton, V.; Styring, P., The use of a novel microreactor for high throughput continuous flow organic synthesis. *Sensors and Actuators B: Chemical* **2000**, 63, (3), 153-158.
15. Rott, N., Note on the History of the Reynolds Number. *Annual Review of Fluid Mechanics* **1990**, 22, (1), 1-12.
16. Holman, J. P., *Heat transfer*. McGraw-Hill: 2002.
17. Adams, J. D.; Soh, H. T., Perspectives on Utilizing Unique Features of Microfluidics Technology for Particle and Cell Sorting. *Journal of the Association for Laboratory Automation* **2009**, 14, (6), 331-340.

18. Smith, F. T., On the High Reynolds Number Theory of Laminar Flows. *IMA Journal of Applied Mathematics* **1982**, 28, (3), 207-281.
19. Dimotakis, P. E., The mixing transition in turbulent flows. *Journal of Fluid Mechanics* **2000**, 409, 69-98.
20. Einstein, A., Investigation on the theory of Brownian movement. *Ann. der Physik* **1905**.
21. Kamholz, A. E.; Yager, P., Theoretical Analysis of Molecular Diffusion in Pressure-Driven Laminar Flow in Microfluidic Channels. *Biophysical Journal* **2001**, 80, (1), 155-160.
22. Peyman, S. A.; Iles, A.; Pamme, N., Rapid on-chip multi-step (bio)chemical procedures in continuous flow - manoeuvring particles through co-laminar reagent streams. *Chemical Communications* **2008**, 0, (10), 1220-1222.
23. Vojtišek, M.; Iles, A.; Pamme, N., Rapid, multistep on-chip DNA hybridisation in continuous flow on magnetic particles. *Biosensors and Bioelectronics* **2010**, 25, (9), 2172-2176.
24. Liu, R. H.; Stremler, M. A.; Sharp, K. V.; Olsen, M. G.; Santiago, J. G.; Adrian, R. J.; Aref, H.; Beebe, D. J., Passive mixing in a three-dimensional serpentine microchannel. *Microelectromechanical Systems, Journal of* **2000**, 9, (2), 190-197.
25. Kim, D. S.; Lee, S. H.; Kwon, T. H.; Ahn, C. H., A serpentine laminating micromixer combining splitting/recombination and advection. *Lab on a Chip* **2005**, 5, (7), 739-747.
26. Rathore, A. S., Theory of electroosmotic flow, retention and separation efficiency in capillary electrochromatography. *Electrophoresis* **2002**, 23, (22-23), 3827-3846.
27. Baker, D. R., *Capillary electrophoresis*. John Wiley & Sons: 1995.
28. Sniady, A.; Bedore, M. W.; Jamison, T. F., One-Flow, Multistep Synthesis of Nucleosides by Brønsted Acid-Catalyzed Glycosylation. *Angewandte Chemie* **2011**, 123, (9), 2203-2206.
29. Noel, T.; Naber, J. R.; Hartman, R. L.; McMullen, J. P.; Jensen, K. F.; Buchwald, S. L., Palladium-catalyzed amination reactions in flow: overcoming the challenges of clogging via acoustic irradiation. *Chemical Science* **2011**, 2, (2), 287-290.
30. Baxendale, I. R.; Ley, S. V.; Mansfield, A. C.; Smith, C. D., Multistep Synthesis Using Modular Flow Reactors: Bestmann–Ohira Reagent for the Formation of Alkynes and Triazoles. *Angewandte Chemie International Edition* **2009**, 48, (22), 4017-4021.
31. Tanaka, Y.; Slyadnev, M. N.; Hibara, A.; Tokeshi, M.; Kitamori, T., Non-contact photothermal control of enzyme reactions on a microchip by using a compact diode laser. *Journal of Chromatography A* **2000**, 894, (1-2), 45-51.
32. Poe, S. L.; Cummings, M. A.; Haaf, M. P.; McQuade, D. T., Solving the Clogging Problem: Precipitate-Forming Reactions in Flow. *Angewandte Chemie International Edition* **2006**, 45, (10), 1544-1548.
33. He, P.; Haswell, S. J.; Fletcher, P. D. I., Microwave-assisted Suzuki reactions in a continuous flow capillary reactor. *Applied Catalysis A: General* **2004**, 274, (1-2), 111-114.
34. Abahmane, L.; Knauer, A.; Köhler, J. M.; Groß, G. A., Synthesis of polypyridine derivatives using alumina supported gold nanoparticles under micro continuous flow conditions. *Chemical Engineering Journal* **2011**, 167, (2-3), 519-526.

35. He, P.; Watts, P.; Marken, F.; Haswell, S. J., Electrosynthesis of phenyl-2-propanone derivatives from benzyl bromides and acetic anhydride in an unsupported micro-flow cell electrolysis process. *Green Chemistry* **2007**, *9*, (1), 20-22.
36. He, P.; Haswell, S.; Fletcher, P.; Kelly, S.; Mansfield, A., Acetylation of Alcohols and Phenols Using Continuous-Flow, Tungstosilicic Acid-Supported, Monolith Microreactors With Scale-Up Capability. *Journal of Flow Chemistry* **2012**, *2*, (2), 47-51.
37. Bula, W. P.; Verboom, W.; Reinhoudt, D. N.; Gardeniers, H. J. G. E., Multichannel quench-flow microreactor chip for parallel reaction monitoring. *Lab on a Chip* **2007**, *7*, (12), 1717-1722.
38. Haswell, S. J.; O'Sullivan, B.; Styring, P., Kumada-Corriu reactions in a pressure-driven microflow reactor. *Lab on a Chip* **2001**, *1*, (2), 164-166.
39. Kikutani, Y.; Kitamori, T., Micro-Flow Reaction Systems for Combinatorial Syntheses. *Macromolecular Rapid Communications* **2004**, *25*, (1), 158-168.
40. Liu, S.; Fukuyama, T.; Sato, M.; Ryu, I., Continuous Microflow Synthesis of Butyl Cinnamate by a Mizoroki-Heck Reaction Using a Low-Viscosity Ionic Liquid as the Recycling Reaction Medium. *Organic Process Research & Development* **2004**, *8*, (3), 477-481.
41. Sugimoto, A.; Fukuyama, T.; Rahman, M. T.; Ryu, I., An automated-flow microreactor system for quick optimization and production: application of 10- and 100-gram order productions of a matrix metalloproteinase inhibitor using a Sonogashira coupling reaction. *Tetrahedron Letters* **2009**, *50*, (46), 6364-6367.
42. Nagaki, A.; Kenmoku, A.; Moriwaki, Y.; Hayashi, A.; Yoshida, J.-i., Cross-Coupling in a Flow Microreactor: Space Integration of Lithiation and Murahashi Coupling. *Angewandte Chemie* **2010**, *122*, (41), 7705-7709.
43. Martin, R.; Buchwald, S. L., Palladium-Catalyzed Suzuki-Miyaura Cross-Coupling Reactions Employing Dialkylbiaryl Phosphine Ligands. *Accounts of Chemical Research* **2008**, *41*, (11), 1461-1473.
44. Sahoo, H. R.; Kralj, J. G.; Jensen, K. F., Multistep Continuous-Flow Microchemical Synthesis Involving Multiple Reactions and Separations. *Angewandte Chemie* **2007**, *119*, (30), 5806-5810.
45. Bou-Hamdan, F. R.; Lévesque, F.; O'Brien, A. G.; Seeberger, P. H., Continuous flow photolysis of aryl azides: Preparation of 3H-azepinones. *Beilstein Journal of Organic Chemistry* **2011**, *7*, 1124-1129.
46. Miyaura, N.; Yamada, K.; Suzuki, A., A new stereospecific cross-coupling by the palladium-catalyzed reaction of 1-alkenylboranes with 1-alkenyl or 1-alkynyl halides. *Tetrahedron Letters* **1979**, *20*, (36), 3437-3440.
47. Kotha, S.; Lahiri, K.; Kashinath, D., Recent applications of the Suzuki-Miyaura cross-coupling reaction in organic synthesis. *Tetrahedron* **2002**, *58*, (48), 9633-9695.
48. Hegedus, L. S., *Organometallics in Synthesis*. John Wiley and Sons: 2002.
49. Guram, A. S.; King, A. O.; Allen, J. G.; Wang, X.; Schenkel, L. B.; Chan, J.; Bunel, E. E.; Faul, M. M.; Larsen, R. D.; Martinelli, M. J.; Reider, P. J., New Air-Stable Catalysts for General and Efficient Suzuki-Miyaura Cross-Coupling Reactions of Heteroaryl Chlorides. *Organic Letters* **2006**, *8*, (9), 1787-1789.
50. Na, Y.; Park, S.; Han, S. B.; Han, H.; Ko, S.; Chang, S., Ruthenium-Catalyzed Heck-Type Olefination and Suzuki Coupling Reactions: Studies on the Nature of Catalytic Species. *Journal of the American Chemical Society* **2003**, *126*, (1), 250-258.

51. Thathagar, M. B.; Beckers, J.; Rothenberg, G., Copper-Catalyzed Suzuki Cross-Coupling Using Mixed Nanocluster Catalysts. *Journal of the American Chemical Society* **2002**, 124, (40), 11858-11859.
52. Tobisu, M.; Xu, T.; Shimasaki, T.; Chatani, N., Nickel-Catalyzed Suzuki–Miyaura Reaction of Aryl Fluorides. *Journal of the American Chemical Society* **2011**, 133, (48), 19505-19511.
53. Bedford, R. B.; Hazelwood, S. L.; Albisson, D. A., Platinum Catalysts for Suzuki Biaryl Coupling Reactions. *Organometallics* **2002**, 21, (13), 2599-2600.
54. Leadbeater, N. E.; Marco, M., Transition-Metal-Free Suzuki-Type Coupling Reactions. *Angewandte Chemie International Edition* **2003**, 42, (12), 1407-1409.
55. Arvela, R. K.; Leadbeater, N. E.; Sangi, M. S.; Williams, V. A.; Granados, P.; Singer, R. D., A Reassessment of the Transition-Metal Free Suzuki-Type Coupling Methodology. *The Journal of Organic Chemistry* **2004**, 70, (1), 161-168.
56. Noël, T.; Kuhn, S.; Musacchio, A. J.; Jensen, K. F.; Buchwald, S. L., Suzuki–Miyaura Cross-Coupling Reactions in Flow: Multistep Synthesis Enabled by a Microfluidic Extraction. *Angewandte Chemie* **2011**, 123, (26), 6065-6068.
57. Baraznenok, I. L.; Nenajdenko, V. G.; Balenkova, E. S., Chemical Transformations Induced by Triflic Anhydride. *Tetrahedron* **2000**, 56, (20), 3077-3119.
58. Mennecke, K.; Kirschning, A., Polyionic polymers – heterogeneous media for metal nanoparticles as catalyst in Suzuki–Miyaura and Heck–Mizoroki reactions under flow conditions. *Beilstein Journal of Organic Chemistry* **2009**, 5, 21.
59. Lee, C. K. Y.; Holmes, A. B.; Ley, S. V.; McConvey, I. F.; Al-Duri, B.; Leeke, G. A.; Santos, R. C. D.; Seville, J. P. K., Efficient batch and continuous flow Suzuki cross-coupling reactions under mild conditions, catalysed by polyurea-encapsulated palladium (ii) acetate and tetra-n-butylammonium salts. *Chemical Communications* **2005**, 0, (16), 2175-2177.
60. Zhu, L.; Gamez, G.; Chen, H. W.; Huang, H. X.; Chingin, K.; Zenobi, R., Real-time, on-line monitoring of organic chemical reactions using extractive electrospray ionization tandem mass spectrometry. *Rapid Communications in Mass Spectrometry* **2008**, 22, (19), 2993-2998.
61. Balaraju, M.; Nikhitha, P.; Jagadeeswaraiyah, K.; Srilatha, K.; Sai Prasad, P. S.; Lingaiah, N., Acetylation of glycerol to synthesize bioadditives over niobic acid supported tungstophosphoric acid catalysts. *Fuel Processing Technology* **2010**, 91, (2), 249-253.
62. Melero, J. A.; van Grieken, R.; Morales, G.; Paniagua, M., Acidic Mesoporous Silica for the Acetylation of Glycerol: Synthesis of Bioadditives to Petrol Fuel. *Energy & Fuels* **2007**, 21, (3), 1782-1791.
63. Silva, L. N.; Gonçalves, V. L. C.; Mota, C. J. A., Catalytic acetylation of glycerol with acetic anhydride. *Catalysis Communications* **2010**, 11, (12), 1036-1039.
64. Smith, K.; El-Hiti, G. A.; Jayne, A. J.; Butters, M., Acetylation of aromatic ethers using acetic anhydride over solid acid catalysts in a solvent-free system. Scope of the reaction for substituted ethers. *Organic & Biomolecular Chemistry* **2003**, 1, (9), 1560-1564.
65. Burke, M. D.; Berger, E. M.; Schreiber, S. L., Generating Diverse Skeletons of Small Molecules Combinatorially. *Science* **2003**, 302, (5645), 613-618.
66. Chakraborti, A. K.; Gulhane, R., Indium(III) chloride as a new, highly efficient, and versatile catalyst for acylation of phenols, thiols, alcohols, and amines. *Tetrahedron Letters* **2003**, 44, (35), 6749-6753.

67. Ghosh, R.; Maiti, S.; Chakraborty, A., Facile catalyzed acylation of heteroatoms using BiCl₃ generated in situ from the procatalyst BiOCl and acetyl chloride. *Tetrahedron Letters* **2004**, 45, (36), 6775-6778.
68. Ahluwalia, V. K.; Agarwal, R., *Comprehensive Practical Organic Chemistry: Preparation and Quantitative Analysis*. Hyderabad: Universities Press, India, 2000.
69. Wu, J.; Zhang, J.; Zhang, H.; He, J.; Ren, Q.; Guo, M., Homogeneous Acetylation of Cellulose in a New Ionic Liquid. *Biomacromolecules* **2004**, 5, (2), 266-268.
70. Yoshida, A.; Hao, X.; Yamazaki, O.; Nishikido, J., Development of Fluorous Lewis Acid-Catalyzed Reactions. *Molecules* **2006**, 11, (8), 627-640.
71. Ishihara, K.; Hasegawa, A.; Yamamoto, H., Single-pass reaction column system with super Bronsted acid-loaded resin. *Synlett* **2002**, (8), 1296-1298.
72. Wild, G. P.; Wiles, C.; Watts, P.; Haswell, S. J., The use of immobilized crown ethers as in-situ N-protecting groups in organic synthesis and their application under continuous flow. *Tetrahedron* **2009**, 65, (8), 1618-1629.
73. Tsutsui, M.; Zeiss, H., π -Complexes of the transition metals. XII. Synthesis with allyl chromium and nickel compounds. *Journal of the American Chemical Society* **1959**, 81, (22), 6090-6091.
74. Pozar, D. M., *Microwave Engineering*. Addison-Wesley Publishing Co: 1993.
75. Harsany, S. C., *Principles of microwave technology*. Upper Saddle River, N.J. : Prentice Hall: 1997.
76. Stuerge, D., Microwave-Material Interactions and Dielectric Properties, Key Ingredients for Mastery of Chemical Microwave Processes. In *Microwaves in Organic Synthesis*, Wiley-VCH Verlag GmbH: 2008; pp 1-61.
77. Kappe, C. O.; Stadler, A., Microwave Theory. In *Microwaves in Organic and Medicinal Chemistry*, Wiley-VCH Verlag GmbH & Co. KGaA: 2006; pp 9-28.
78. Nicula, R.; Stir, M.; Ishizaki, K.; Català-Civera, J. M.; Vaucher, S., Rapid nanocrystallization of soft-magnetic amorphous alloys using microwave induction heating. *Scripta Materialia* **2009**, 60, (2), 120-123.
79. Zhang, X.; O. Hayward, D.; Michael P. Mingos, D., Apparent equilibrium shifts and hot-spot formation for catalytic reactions induced by microwave dielectric heating. *Chemical Communications* **1999**, (11), 975-976.
80. de la Hoz, A.; Diaz-Ortiz, A.; Moreno, A., Microwaves in organic synthesis. Thermal and non-thermal microwave effects. *Chemical Society Reviews* **2005**, 34, (2), 164-178.
81. Kappe, O. C., Microwave dielectric heating in synthetic organic chemistry. *Chemical Society Reviews* **2008**, 37, (6), 1127-1139.
82. Baxendale, I. R.; Griffiths-Jones, C. M.; Ley, S. V.; Tranmer, G. K., Microwave-Assisted Suzuki Coupling Reactions with an Encapsulated Palladium Catalyst for Batch and Continuous-Flow Transformations. *Chemistry – A European Journal* **2006**, 12, (16), 4407-4416.
83. Arvela, R. K.; Leadbeater, N. E.; Collins Jr, M. J., Automated batch scale-up of microwave-promoted Suzuki and Heck coupling reactions in water using ultra-low metal catalyst concentrations. *Tetrahedron* **2005**, 61, (39), 9349-9355.
84. Chanthavong, F.; Leadbeater, N. E., The application of organic bases in microwave-promoted Suzuki coupling reactions in water. *Tetrahedron Letters* **2006**, 47, (12), 1909-1912.
85. Wong, H.; Pink, C. J.; Ferreira, F. C.; Livingston, A. G., Recovery and reuse of ionic liquids and palladium catalyst for Suzuki reactions using organic solvent nanofiltration. *Green Chemistry* **2006**, 8, (4), 373-379.

86. Pechtl, M. H. G.; Scholten, J. D.; Dupont, J., Carbon-Carbon Cross Coupling Reactions in Ionic Liquids Catalysed by Palladium Metal Nanoparticles. *Molecules* **2010**, 15, (5), 3441-3461.
87. Bedford, R. B.; Draper, S. M.; Noelle Scully, P.; Welch, S. L., Palladium bis(phosphinite) 'PCP'-pincer complexes and their application as catalysts in the Suzuki reaction. *New Journal of Chemistry* **2000**, 24, (10), 745-747.
88. Wolfe, J. P.; Singer, R. A.; Yang, B. H.; Buchwald, S. L., Highly Active Palladium Catalysts for Suzuki Coupling Reactions. *Journal of the American Chemical Society* **1999**, 121, (41), 9550-9561.
89. Hanefeld, U.; Gardossi, L.; Magner, E., Understanding enzyme immobilisation. *Chemical Society Reviews* **2009**, 38, (2), 453-468.
90. Phan, N. T. S.; Brown, D. H.; Styring, P., A facile method for catalyst immobilisation on silica: nickel-catalysed Kumada reactions in mini-continuous flow and batch reactors. *Green Chemistry* **2004**, 6, (10), 526-532.
91. Djakovitch, L.; Koehler, K., Heterogeneously catalysed Heck reaction using palladium modified zeolites. *Journal of Molecular Catalysis A: Chemical* **1999**, 142, (2), 275-284.
92. Solodenko, W.; Wen, H.; Leue, S.; Stuhlmann, F.; Sourkouni-Argirusi, G.; Jas, G.; Schönfeld, H.; Kunz, U.; Kirschning, A., Development of a Continuous-Flow System for Catalysis with Palladium(0) Particles. *European Journal of Organic Chemistry* **2004**, 2004, (17), 3601-3610.
93. Seen, A. J.; Townsend, A. T.; Bellis, J. C.; Cavell, K. J., Increased catalytic activity of cationic palladium(II) complexes on immobilisation in Nafion-H+. *Journal of Molecular Catalysis A: Chemical* **1999**, 149, (1-2), 233-242.
94. Dimitratos, N.; Lopez-Sanchez, J. A.; Anthonykutty, J. M.; Brett, G.; Carley, A. F.; Tiruvalam, R. C.; Herzing, A. A.; Kiely, C. J.; Knight, D. W.; Hutchings, G. J., Oxidation of glycerol using gold-palladium alloy-supported nanocrystals. *Physical Chemistry Chemical Physics* **2009**, 11, (25), 4952-4961.
95. Freeman, J. H.; Wagner, E. C., 1,2,4-Benzothiadiazine dioxides and 3,4-dihydro-1,2,4- Benzothiadiazine dioxides 1, 2. *The Journal of Organic Chemistry* **1951**, 16, (6), 815-837.
96. Karimi, B.; Zamani, A.; Abedi, S.; Clark, J. H., Aerobic oxidation of alcohols using various types of immobilized palladium catalyst: the synergistic role of functionalized ligands, morphology of support, and solvent in generating and stabilizing nanoparticles. *Green Chemistry* **2009**, 11, (1), 109-119.
97. Sandee, A. J.; Dimitrijevic, D.; van Haaren, R. J.; Reek, J. N. H.; Kamer, P. C. J.; van Leeuwen, P. W. N. M., Silica immobilised palladium phosphine complexes as recyclable, regioselective catalysts for the allylic alkylation. *Journal of Molecular Catalysis A: Chemical* **2002**, 182-183, (0), 309-317.
98. Yu, T.-C.; Shaw, H., The effect of sulfur poisoning on methane oxidation over palladium supported on γ -alumina catalysts. *Applied Catalysis B: Environmental* **1998**, 18, (1-2), 105-114.
99. Richardson, J. M.; Jones, C. W., Strong evidence of solution-phase catalysis associated with palladium leaching from immobilized thiols during Heck and Suzuki coupling of aryl iodides, bromides, and chlorides. *Journal of Catalysis* **2007**, 251, (1), 80-93.
100. Crudden, C. M.; Sateesh, M.; Lewis, R., Mercaptopropyl-Modified Mesoporous Silica: A Remarkable Support for the Preparation of a Reusable, Heterogeneous Palladium Catalyst for Coupling Reactions. *Journal of the American Chemical Society* **2005**, 127, (28), 10045-10050.

101. He, P.; Haswell, S. J.; Fletcher, P. D. I.; Kelly, S. M.; Mansfield, A., Scaling up of continuous-flow, microwave-assisted, organic reactions by varying the size of Pd-functionalized catalytic monoliths. *Beilstein Journal of Organic Chemistry* **2011**, 7, 1150-1157.
102. Das, D. D.; Sayari, A., Applications of pore-expanded mesoporous silica 6. Novel synthesis of monodispersed supported palladium nanoparticles and their catalytic activity for Suzuki reaction. *Journal of Catalysis* **2007**, 246, (1), 60-65.
103. Richter, T.; Shultz-Lockyear, L. L.; Oleschuk, R. D.; Bilitewski, U.; Harrison, D. J., Bi-enzymatic and capillary electrophoretic analysis of non-fluorescent compounds in microfluidic devices: Determination of xanthine. *Sensors and Actuators B: Chemical* **2002**, 81, (2-3), 369-376.
104. Seong, G. H.; Crooks, R. M., Efficient Mixing and Reactions within Microfluidic Channels Using Microbead-Supported Catalysts. *Journal of the American Chemical Society* **2002**, 124, (45), 13360-13361.
105. Srinivasan, A.; Bach, H.; Sherman, D. H.; Dordick, J. S., Bacterial P450-catalyzed polyketide hydroxylation on a microfluidic platform. *Biotechnology and Bioengineering* **2004**, 88, (4), 528-535.
106. Sakai-Kato, K.; Kato, M.; Toyo'oka, T., Creation of an On-Chip Enzyme Reactor by Encapsulating Trypsin in Sol-Gel on a Plastic Microchip. *Analytical Chemistry* **2003**, 75, (3), 388-393.
107. Sakai-Kato, K.; Kato, M.; Ishihara, K.; Toyo'oka, T., An enzyme-immobilization method for integration of biofunctions on a microchip using a water-soluble amphiphilic phospholipid polymer having a reacting group. *Lab on a Chip* **2004**, 4, (1), 4-6.
108. Heule, M.; Rezwani, K.; Cavalli, L.; Gauckler, L. J., A Miniaturized Enzyme Reactor Based on Hierarchically Shaped Porous Ceramic Microstruts. *Advanced Materials* **2003**, 15, (14), 1191-1194.
109. Nomura, A.; Shin, S.; Mehdi, O. O.; Kauffmann, J.-M., Preparation, Characterization, and Application of an Enzyme-Immobilized Magnetic Microreactor for Flow Injection Analysis. *Analytical Chemistry* **2004**, 76, (18), 5498-5502.
110. Abbott, R. W.; Townshend, A.; Gill, R., Determination of morphine by flow injection analysis with chemiluminescence detection. *Analyst* **1986**, 111, (6), 635-640.
111. Lee, D.; Lee, S.; Seong, G. H.; Choo, J.; Lee, E. K.; Gweon, D.-G.; Lee, S., Quantitative Analysis of Methyl Parathion Pesticides in a Polydimethylsiloxane Microfluidic Channel Using Confocal Surface-Enhanced Raman Spectroscopy. *Appl. Spectrosc.* **2006**, 60, (4), 373-377.
112. Canty, A. J.; Deverell, J. A.; Gömann, A.; Guijt, R. M.; Rodemann, T.; Smith, J. A., Microfluidic Devices for Flow-Through Supported Palladium Catalysis on Porous Organic Monolith. *Australian Journal of Chemistry* **2008**, 61, (8), 630-633.
113. Yermilov, V.; Rubio, J.; Becchi, M.; Friesen, M. D.; Pignatelli, B.; Ohshima, H., Formation of 8-nitroguanine by the reaction of guanine with peroxyxynitrite in vitro. *Carcinogenesis* **1995**, 16, (9), 2045-2050.
114. Miller, P. W.; Long, N. J.; de Mello, A. J.; Vilar, R.; Passchier, J.; Gee, A., Rapid formation of amides via carbonylative coupling reactions using a microfluidic device. *Chemical Communications* **2006**, 0, (5), 546-548.
115. Ratner, D. M.; Murphy, E. R.; Jhunjunwala, M.; Snyder, D. A.; Jensen, K. F.; Seeberger, P. H., Microreactor-based reaction optimization in organic chemistry-glycosylation as a challenge. *Chemical Communications* **2005**, 0, (5), 578-580.

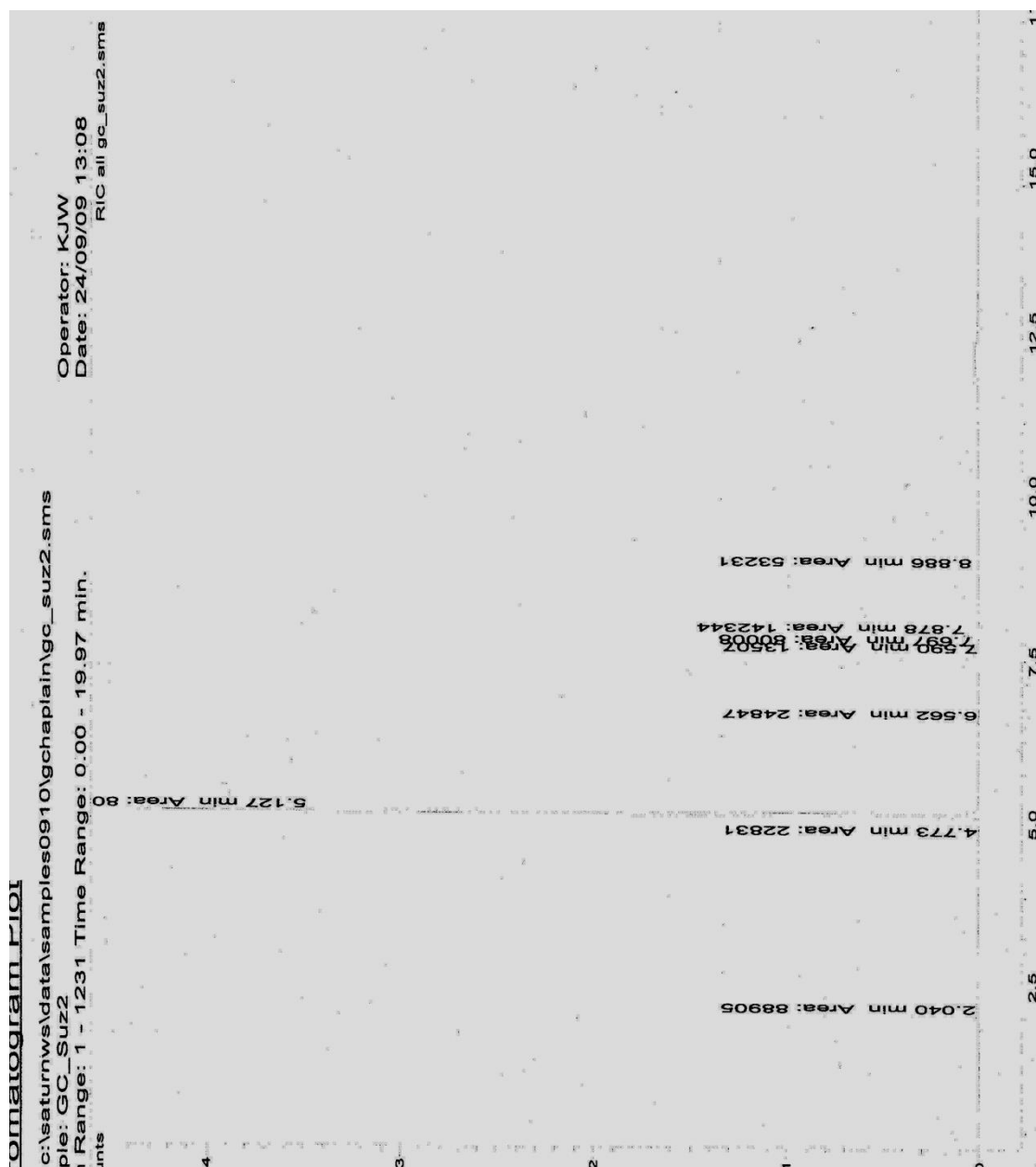
116. Alza, E.; Rodríguez-Escrich, C.; Sayalero, S.; Bastero, A.; Pericàs, M. A., A Solid-Supported Organocatalyst for Highly Stereoselective, Batch, and Continuous-Flow Mannich Reactions. *Chemistry – A European Journal* **2009**, 15, (39), 10167-10172.
117. Hook, B. D. A.; Dohle, W.; Hirst, P. R.; Pickworth, M.; Berry, M. B.; Booker-Milburn, K. I., A Practical Flow Reactor for Continuous Organic Photochemistry. *The Journal of Organic Chemistry* **2005**, 70, (19), 7558-7564.
118. Lee, C.-C.; Sui, G.; Elizarov, A.; Shu, C. J.; Shin, Y.-S.; Dooley, A. N.; Huang, J.; Daridon, A.; Wyatt, P.; Stout, D.; Kolb, H. C.; Witte, O. N.; Satyamurthy, N.; Heath, J. R.; Phelps, M. E.; Quake, S. R.; Tseng, H.-R., Multistep Synthesis of a Radiolabeled Imaging Probe Using Integrated Microfluidics. *Science* **2005**, 310, (5755), 1793-1796.
119. Gömann, A.; Deverell, J. A.; Munting, K. F.; Jones, R. C.; Rodemann, T.; Canty, A. J.; Smith, J. A.; Guijt, R. M., Palladium-mediated organic synthesis using porous polymer monolith formed in situ as a continuous catalyst support structure for application in microfluidic devices. *Tetrahedron* **2009**, 65, (7), 1450-1454.
120. Bart, J. C. J., Separation Techniques. In *Additives in Polymers*, John Wiley & Sons, Ltd: 2005; pp 171-298.
121. Poole, C. F., Chapter 1 - General Concepts in Column Chromatography. In *The Essence of Chromatography*, Elsevier Science: Amsterdam, 2003; pp 1-78.
122. Tang, D.; Wen, L.-S.; Santschi, P. H., Analysis of biogenic thiols in natural water samples by high-performance liquid chromatographic separation and fluorescence detection with ammonium 7-fluorobenzo-2-oxa-1,3-diazole-4-sulfonate (SBD-F). *Analytica Chimica Acta* **2000**, 408, (1-2), 299-307.
123. Liang, Z.; Chiem, N.; Ocvirk, G.; Tang, T.; Fluri, K.; Harrison, D. J., Microfabrication of a Planar Absorbance and Fluorescence Cell for Integrated Capillary Electrophoresis Devices. *Analytical Chemistry* **1996**, 68, (6), 1040-1046.
124. Gardiner, D., Introduction to Raman Scattering. In *Practical Raman Spectroscopy*, Gardiner, D.; Graves, P., Eds. Springer Berlin Heidelberg: 1989; pp 1-12.
125. Langseth, A.; Stoicheff, B. P., High resolution Raman spectroscopy of gases: VI. Rotational spectrum of symmetric benzene-d₃. *Canadian Journal of Physics* **1956**, 34, (4), 350-353.
126. Long, D. A., Classical Theory of Rayleigh and Raman Scattering. In *The Raman Effect*, John Wiley & Sons, Ltd: 2002; pp 31-48.
127. Long, D. A., Polarization of Electromagnetic Radiation. In *The Raman Effect*, John Wiley & Sons, Ltd: 2002; pp 565-578.
128. Pelletier, M. J., *Analytical Applications of Raman Spectroscopy*. Blackwell Science Ltd: 1999.
129. Zhang, X.; Young, M. A.; Lyandres, O.; Van Duyne, R. P., Rapid Detection of an Anthrax Biomarker by Surface-Enhanced Raman Spectroscopy. *Journal of the American Chemical Society* **2005**, 127, (12), 4484-4489.
130. Chase, D. B., Fourier transform Raman spectroscopy. *Journal of the American Chemical Society* **1986**, 108, (24), 7485-7488.
131. Otto, K.; Hubbard, C. P.; Weber, W. H.; Graham, G. W., Raman spectroscopy of palladium oxide on γ -alumina applicable to automotive catalysts: Nondestructive, quantitative analysis; oxidation kinetics; fluorescence quenching. *Applied Catalysis B: Environmental* **1992**, 1, (4), 317-327.

132. J. Ampiah-Bonney, R.; D. Walmsley, A., Monitoring of the acid catalysed esterification of ethanol by acetic acid using Raman spectroscopy. *Analyst* **1999**, 124, (12), 1817-1821.
133. Fletcher, P. D. I.; Haswell, S. J.; Zhang, X., Monitoring of chemical reactions within microreactors using an inverted Raman microscopic spectrometer. *Electrophoresis* **2003**, 24, (18), 3239-3245.
134. Urakawa, A.; Trachsel, F.; von Rohr, P. R.; Baiker, A., On-chip Raman analysis of heterogeneous catalytic reaction in supercritical CO₂: phase behaviour monitoring and activity profiling. *Analyst* **2008**, 133, (10), 1352-1354.
135. Leadbeater, N. E.; Smith, R. J.; Barnard, T. M., Using in situ Raman monitoring as a tool for rapid optimisation and scale-up of microwave-promoted organic synthesis: esterification as an example. *Organic & Biomolecular Chemistry* **2007**, 5, (5), 822-825.
136. Mozharov, S.; Nordon, A.; Littlejohn, D.; Wiles, C.; Watts, P.; Dallin, P.; Girkin, J. M., Improved Method for Kinetic Studies in Microreactors Using Flow Manipulation and Noninvasive Raman Spectrometry. *Journal of the American Chemical Society* **2011**, 133, (10), 3601-3608.
137. Lee, M.; Lee, J.-P.; Rhee, H.; Choo, J.; Gyu Chai, Y.; Kyu Lee, E., Applicability of laser-induced Raman microscopy for in situ monitoring of imine formation in a glass microfluidic chip. *Journal of Raman Spectroscopy* **2003**, 34, (10), 737-742.
138. Rea, D. G., Study of the Experimental Factors Affecting Raman Band Intensities in Liquids. *J. Opt. Soc. Am.* **1959**, 49, (1), 90-100.
139. Xie, S.; Iglesia, E.; Bell, A. T., Effects of Temperature on the Raman Spectra and Dispersed Oxides. *The Journal of Physical Chemistry B* **2001**, 105, (22), 5144-5152.
140. Mabbott, S.; Eckmann, A.; Casiraghi, C.; Goodacre, R., 2p or not 2p: tuppence-based SERS for the detection of illicit materials. *Analyst* **2013**, 138, (1), 118-122.
141. Brereton, R. G., Experimental Design. In *Chemometrics*, John Wiley & Sons, Ltd: 2003; pp 15-117.
142. Chiang, L. H.; Pell, R. J.; Seasholtz, M. B., Exploring process data with the use of robust outlier detection algorithms. *Journal of Process Control* **2003**, 13, (5), 437-449.
143. Hardy, A. J.; MacLaurin, P.; Haswell, S. J.; de Jong, S.; Vandeginste, B. G. M., Double-case diagnostic for outliers identification. *Chemometrics and Intelligent Laboratory Systems* **1996**, 34, (1), 117-129.
144. Barnes, S. E.; Cygan, Z. T.; Yates, J. K.; Beers, K. L.; Amis, E. J., Raman spectroscopic monitoring of droplet polymerization in a microfluidic device. *Analyst* **2006**, 131, (9), 1027-1033.
145. Trosvik, P.; Skånseng, B.; Jakobsen, K. S.; Stenseth, N. C.; Næs, T.; Rudi, K., Multivariate Analysis of Complex DNA Sequence Electropherograms for High-Throughput Quantitative Analysis of Mixed Microbial Populations. *Applied and Environmental Microbiology* **2007**, 73, (15), 4975-4983.
146. Guiteras, J.; Beltrán, J. L.; Ferrer, R., Quantitative multicomponent analysis of polycyclic aromatic hydrocarbons in water samples. *Analytica Chimica Acta* **1998**, 361, (3), 233-240.
147. Rohleder, D.; Kiefer, W.; Petrich, W., Quantitative analysis of serum and serum ultrafiltrate by means of Raman spectroscopy. *Analyst* **2004**, 129, (10), 906-911.

148. Cozzolino, D.; Morón, A., Potential of near-infrared reflectance spectroscopy and chemometrics to predict soil organic carbon fractions. *Soil and Tillage Research* **2006**, 85, (1–2), 78-85.
149. Shore, G.; Morin, S.; Organ, M. G., Catalysis in Capillaries by Pd Thin Films Using Microwave-Assisted Continuous-Flow Organic Synthesis (MACOS). *Angewandte Chemie* **2006**, 118, (17), 2827-2832.
150. Cheng, F.; Kelly, S. M.; Young, N. A.; Hope, C. N.; Beverley, K.; Francesconi, M. G.; Clark, S.; Bradley, J. S.; Lefebvre, F., Preparation of Mesoporous Pd/Si₃N₄ Nanocomposites as Heterogeneous Catalysts via Three Different Chemical Routes. *Chemistry of Materials* **2006**, 18, (25), 5996-6005.
151. Qu, Q.-s.; He, Y.-z.; Gan, W.-e.; Deng, N.; Lin, X.-q., Electrochromatography with a 2.7 mm inner diameter monolithic column. *Journal of Chromatography A* **2003**, 983, (1–2), 255-262.
152. Fletcher, P.; Haswell, S.; He, P.; Kelly, S.; Mansfield, A., Permeability of silica monoliths containing micro- and nano-pores. *Journal of Porous Materials* **2011**, 18, (4), 501-508.
153. Clavier, C. W.; Rodman, D. L.; Sinski, J. F.; Allain, L. R.; Im, H.-J.; Yang, Y.; Clark, J. C.; Xue, Z.-L., A method for the preparation of transparent mesoporous silica sol-gel monoliths containing grafted organic functional groups. *Journal of Materials Chemistry* **2005**, 15, (24), 2356-2361.
154. Mohammad, A.; Julian, R. J.; Larry, L. H., Fabricating sol-gel glass monoliths with controlled nanoporosity. *Biomedical Materials* **2007**, 2, (1), 6.
155. Grimm, S.; Lange, A.; Enke, D.; Steinhart, M., Imprinting macropore arrays into mesoporous silica monoliths. *Journal of Materials Chemistry* **2012**, 22, (19), 9490-9493.
156. Li, Y.; Xu, R.; Couderc, S.; Bloor, D. M.; Holzwarth, J. F.; Wyn-Jones, E., Binding of Tetradecyltrimethylammonium Bromide to the ABA Block Copolymer Pluronic F127 (EO97 PO69 EO97): Electromotive Force, Microcalorimetry, and Light Scattering Studies. *Langmuir* **2001**, 17, (19), 5742-5747.
157. Siouffi, A. M., Silica gel-based monoliths prepared by the sol-gel method: facts and figures. *Journal of Chromatography A* **2003**, 1000, (1–2), 801-818.
158. CEM, Private communication. In Private communication from CEM inc. ed.
159. Leadbeater, N. E.; Marco, M., Ligand-Free Palladium Catalysis of the Suzuki Reaction in Water Using Microwave Heating. *Organic Letters* **2002**, 4, (17), 2973-2976.
160. Leadbeater, N. E.; Smith, R. J., Real-Time Monitoring of Microwave-Promoted Suzuki Coupling Reactions Using in Situ Raman Spectroscopy. *Organic Letters* **2006**, 8, (20), 4589-4591.
161. Leadbeater, N. E.; Williams, V. A.; Barnard, T. M.; Collins, M. J., Open-Vessel Microwave-Promoted Suzuki Reactions Using Low Levels of Palladium Catalyst: Optimization and Scale-Up. *Organic Process Research & Development* **2006**, 10, (4), 833-837.
162. Hedrick, J. L.; Labadie, J. W., *Step-growth polymers for high-performance materials: new synthetic methods*. American Chemical Society. Division of Polymer Chemistry: 1996.
163. Artok, L.; Bulut, H., Heterogeneous Suzuki reactions catalyzed by Pd(0)-Y zeolite. *Tetrahedron Letters* **2004**, 45, (20), 3881-3884.
164. Baleizão, C.; Corma, A.; García, H.; Leyva, A., Oxime Carbapalladacycle Covalently Anchored to High Surface Area Inorganic Supports or Polymers as

- Heterogeneous Green Catalysts for the Suzuki Reaction in Water. *The Journal of Organic Chemistry* **2003**, 69, (2), 439-446.
165. Broutin, P.-E.; Čerňa, I.; Campaniello, M.; Leroux, F.; Colobert, F., Palladium-Catalyzed Borylation of Phenyl Bromides and Application in One-Pot Suzuki–Miyaura Biphenyl Synthesis. *Organic Letters* **2004**, 6, (24), 4419-4422.
166. Doucet, H., Suzuki–Miyaura Cross-Coupling Reactions of Alkylboronic Acid Derivatives or Alkyltrifluoroborates with Aryl, Alkenyl or Alkyl Halides and Triflates. *European Journal of Organic Chemistry* **2008**, 2008, (12), 2013-2030.
167. Kostas, I. D.; Andreadaki, F. J.; Kovala-Demertzi, D.; Christos, P.; Demertzis, M. A., Suzuki–Miyaura cross-coupling reaction of aryl bromides and chlorides with phenylboronic acid under aerobic conditions catalyzed by palladium complexes with thiosemicarbazone ligands. *Tetrahedron Letters* **2005**, 46, (12), 1967-1970.
168. Leadbeater, N. E.; Marco, M., Transition-Metal-Free Suzuki-Type Coupling Reactions: Scope and Limitations of the Methodology. *The Journal of Organic Chemistry* **2003**, 68, (14), 5660-5667.
169. Leadbeater, N. E.; Resouly, S. M., Suzuki aryl couplings mediated by phosphine-free nickel complexes. *Tetrahedron* **1999**, 55, (40), 11889-11894.
170. Molander, G. A.; Biolatto, B., Palladium-Catalyzed Suzuki–Miyaura Cross-Coupling Reactions of Potassium Aryl- and Heteroaryltrifluoroborates. *The Journal of Organic Chemistry* **2003**, 68, (11), 4302-4314.
171. Molander, G. A.; Katona, B. W.; Machrouhi, F., Development of the Suzuki–Miyaura Cross-Coupling Reaction: Use of Air-Stable Potassium Alkynyltrifluoroborates in Aryl Alkynylation. *The Journal of Organic Chemistry* **2002**, 67, (24), 8416-8423.
172. Ohe, T.; Miyaura, N.; Suzuki, A., Palladium-catalyzed cross-coupling reaction of organoboron compounds with organic triflates. *The Journal of Organic Chemistry* **1993**, 58, (8), 2201-2208.
173. Tao, B.; Boykin, D. W., Simple Amine/Pd(OAc)₂-Catalyzed Suzuki Coupling Reactions of Aryl Bromides under Mild Aerobic Conditions. *The Journal of Organic Chemistry* **2004**, 69, (13), 4330-4335.
174. Wang, Y.; Sauer, D. R., Use of Polymer-Supported Pd Reagents for Rapid and Efficient Suzuki Reactions Using Microwave Heating. *Organic Letters* **2004**, 6, (16), 2793-2796.
175. Zim, D.; Gruber, A. S.; Ebeling, G.; Dupont, J.; Monteiro, A. L., Sulfur-Containing Palladacycles: Efficient Phosphine-Free Catalyst Precursors for the Suzuki Cross-Coupling Reaction at Room Temperature. *Organic Letters* **2000**, 2, (18), 2881-2884.
176. Laidler, K. J.; Meiser, J. H.; Sanctuary, B. C., *Physical Chemistry*. 4th ed.; Houghton Mifflin Boston, 2003.
177. Aliprantis, A. O.; Canary, J. W., Observation of Catalytic Intermediates in the Suzuki Reaction by Electrospray Mass Spectrometry. *Journal of the American Chemical Society* **1994**, 116, (15), 6985-6986.
178. Ammann, M.; Poschl, U.; Rudich, Y., Effects of reversible adsorption and Langmuir-Hinshelwood surface reactions on gas uptake by atmospheric particles. *Physical Chemistry Chemical Physics* **2003**, 5, (2), 351-356.
179. Huang, W.-g.; He, D.-h.; Liu, J.-y.; Zhu, Q.-m., Catalytic condensation of formaldehyde and methyl formate over 12-tungstosilicic compounds. *Applied Catalysis A: General* **2000**, 199, (1), 93-98.
180. He, P.; Davies, J.; Greenway, G.; Haswell, S. J., Measurement of acetylcholinesterase inhibition using bienzymes immobilized monolith micro-

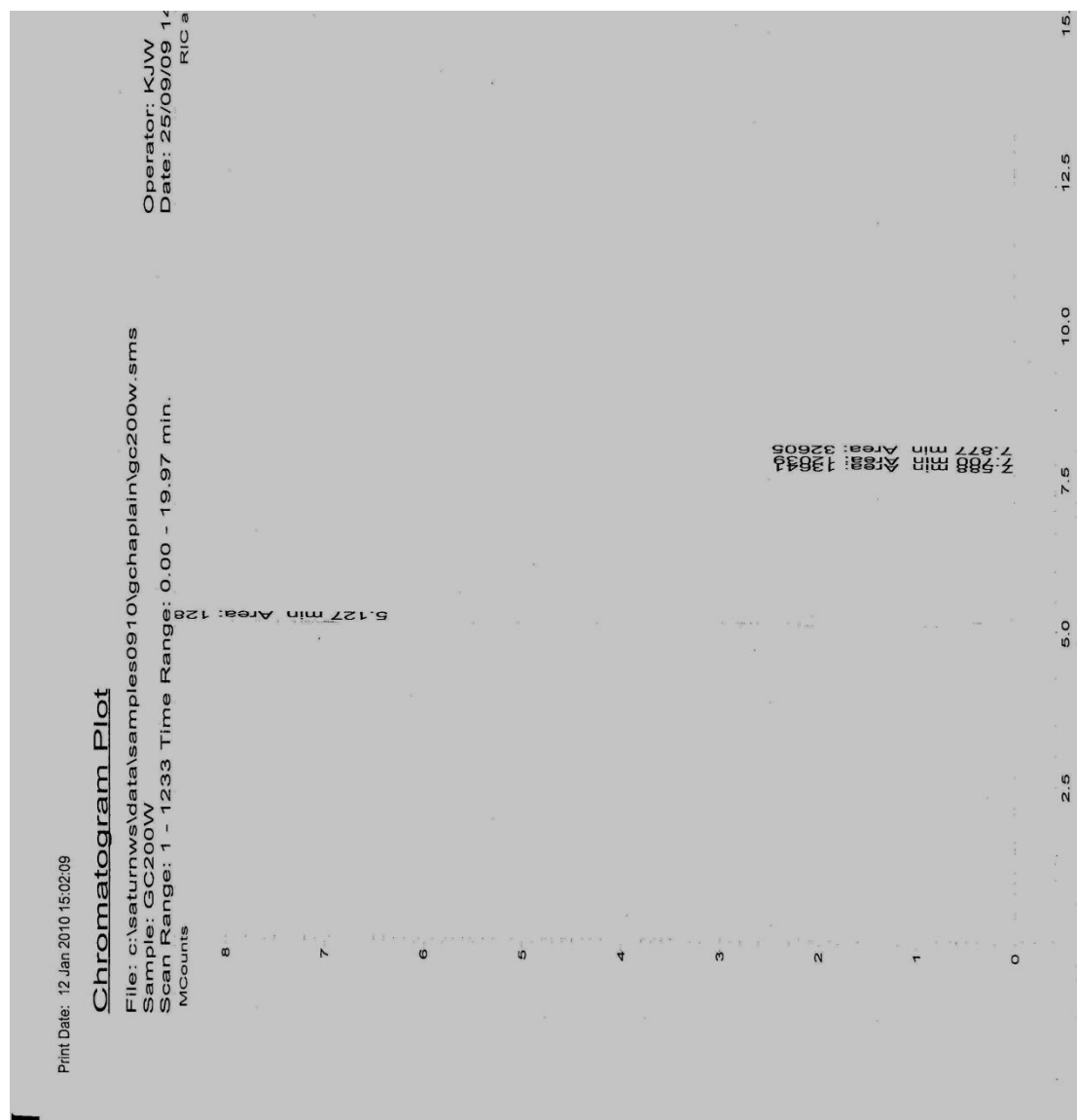
- reactor with integrated electrochemical detection. *Anal Chim Acta* **2010**, 659, (1-2), 9-14.
181. Cao, W.; Gerhardt, R.; Wachtman, J. B., Preparation and Sintering of Colloidal Silica-Potassium Silicate Gels. *Journal of the American Ceramic Society* **1988**, 71, (12), 1108-1113.
182. He, P.; Haswell, S. J.; Fletcher, P. D. I., Microwave heating of heterogeneously catalysed Suzuki reactions in a micro reactor. *Lab on a Chip* **2004**, 4, (1), 38-41.
183. Heravi, M. M.; Behbahani, F. K.; Bamoharram, F. F., H₁₄[NaP₅W₃O₁₁]: A heteropoly acid catalyzed acetylation of alcohols and phenols in acetic anhydride. *Journal of Molecular Catalysis A: Chemical* **2006**, 253, (1-2), 16-19.
184. Javid, A.; Heravi, M. M.; Bamoharram, F. F., One-Pot Synthesis of 1,8-Dioxooctahydroxanthenes Utilizing Silica-Supported Preyssler Nano Particles as Novel and Efficient Reusable Heterogeneous Acidic Catalyst. *E-Journal of Chemistry* **2011**, 8, (2), 910-916.
185. Zhang, F.; Yuan, C.; Wang, J.; Kong, Y.; Zhu, H.; Wang, C., Synthesis of fructose over dealuminated USY supported heteropoly acid and its salt catalysts. *Journal of Molecular Catalysis A: Chemical* **2006**, 247, (1-2), 130-137.
186. Zhu, Z.; Yang, W., Preparation, Characterization and Shape-Selective Catalysis of Supported Heteropolyacid Salts K_{2.5}H_{0.5}PW₁₂O₄₀, NH₄)_{2.5}H_{0.5}PW₁₂O₄₀, and Ce_{0.83}H_{0.5}PW₁₂O₄₀ on MCM-41 Mesoporous Silica. *The Journal of Physical Chemistry C* **2009**, 113, (39), 17025-17031.



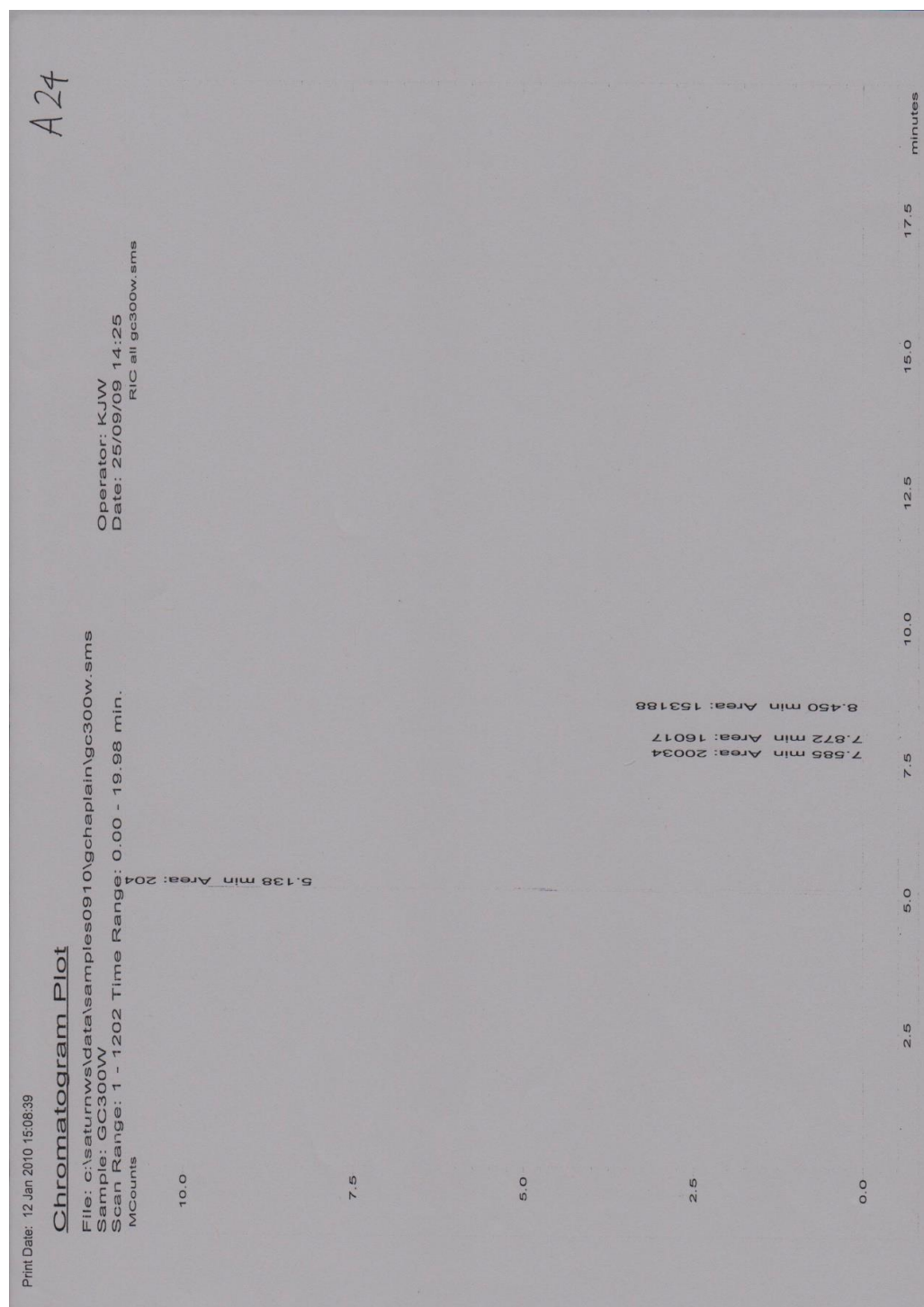
Appendix 1 GC-MS chromatograph of the flow Suzuki reaction of 0.1 M 4-bromobenzonitrile, 0.12 M phenyl boronic acid and 0.25 M potassium carbonate in 66.7% DMF in water. Reactant solution was injected into a 2144.3 μ L injection loop with a carrier solvent of NMF. Reaction conditions were 3.9 minutes at microwave power of 80 W.



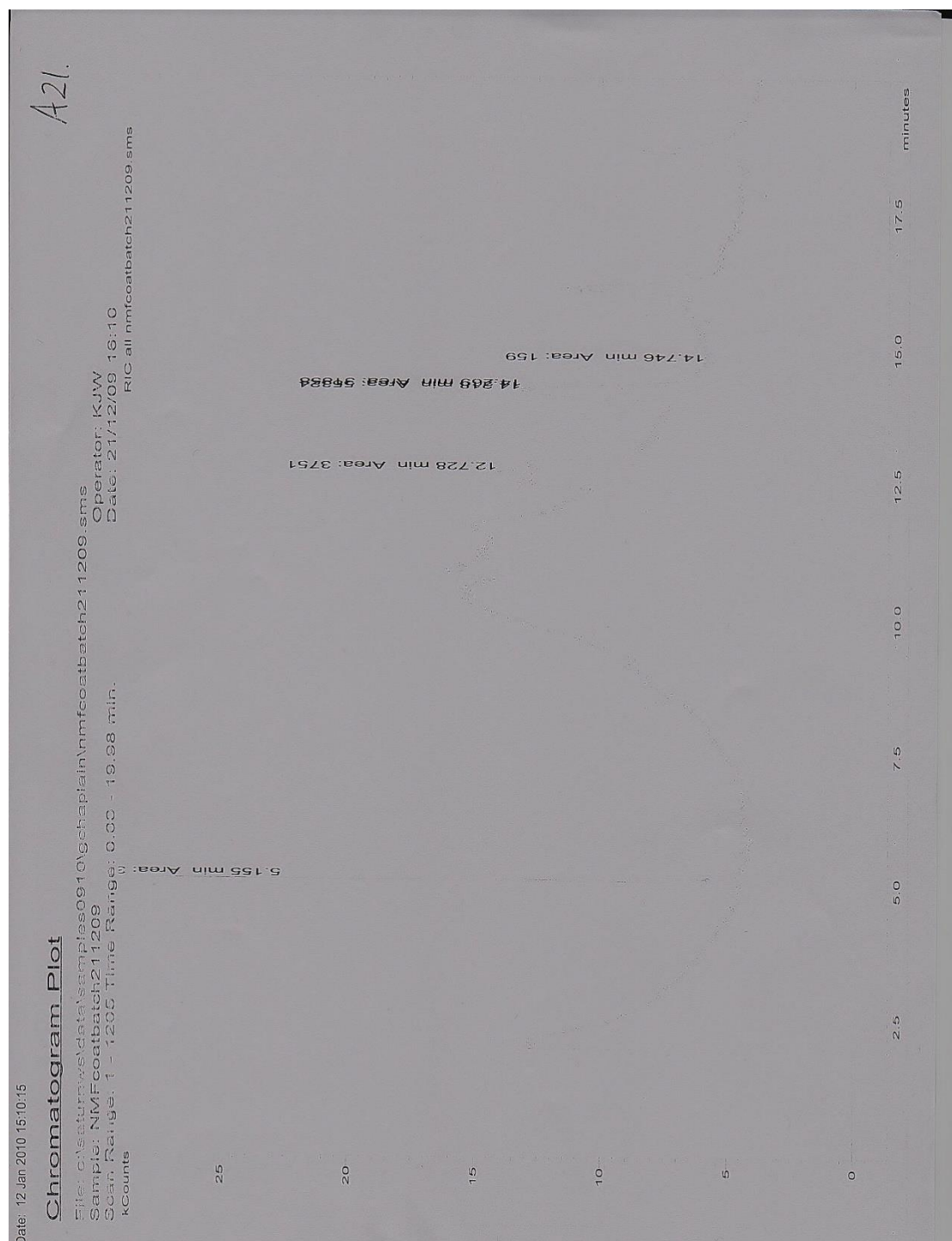
Appendix 2 GC-MS chromatograph of the flow Suzuki reaction of 0.1 M 4-bromobenzonitrile, 0.12 M phenyl boronic acid and 0.25 M potassium carbonate in 66.7% DMF in water. Reactant solution was injected into a 2144.3 μ L injection loop with a carrier solvent of NMF. Reaction conditions were 7.9 minutes at microwave power of 80 W.



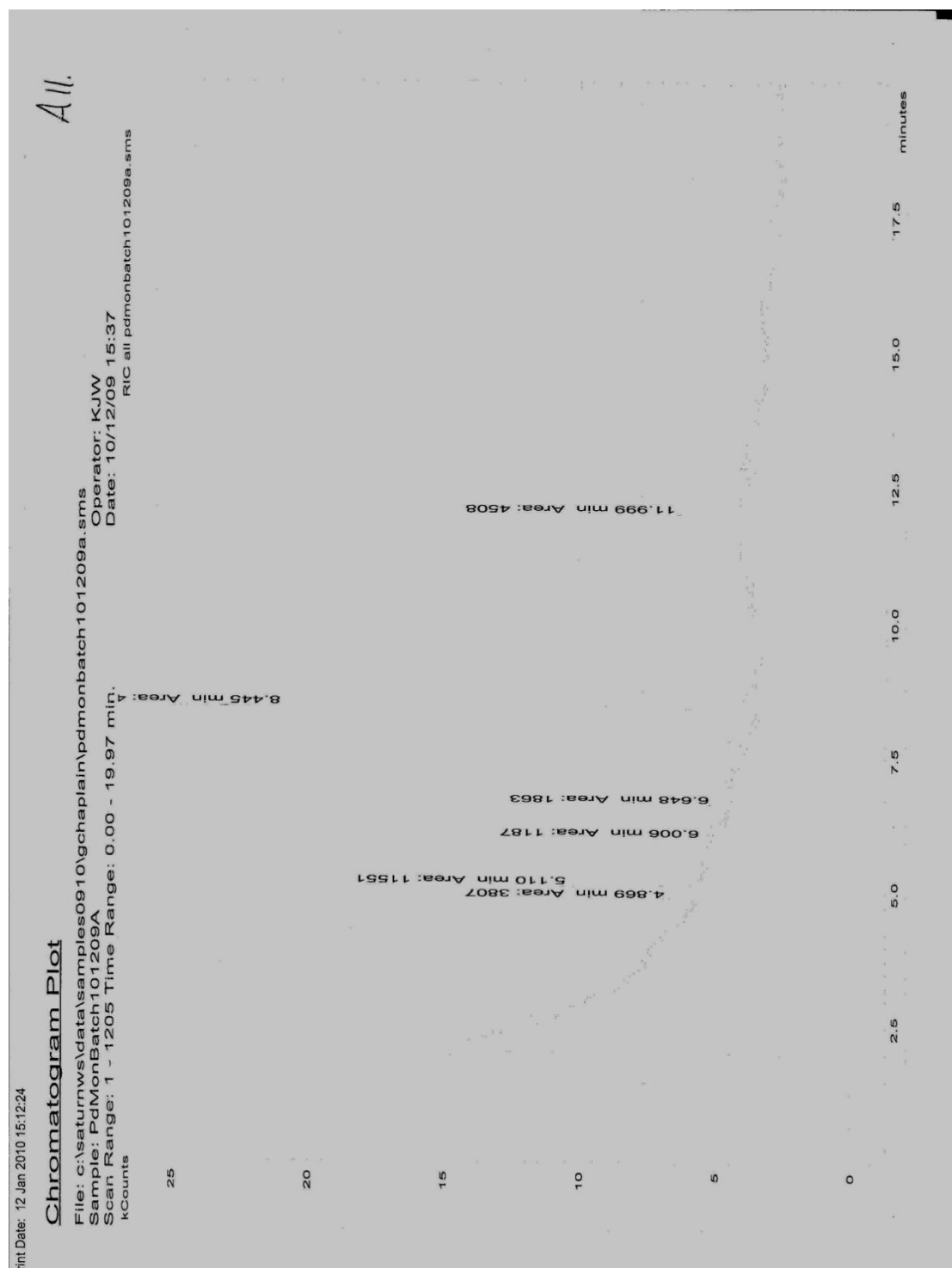
Appendix 3 GC-MS chromatograph of the flow Suzuki reaction of 0.1 M 4-bromobenzonitrile, 0.12 M phenyl boronic acid and 0.25 M potassium carbonate in 66.7% DMF in water. Reactant solution was injected into a 2144.3 μL injection loop with a carrier solvent of NMF. Reaction conditions were 3.9 minutes at microwave power of 200 W.



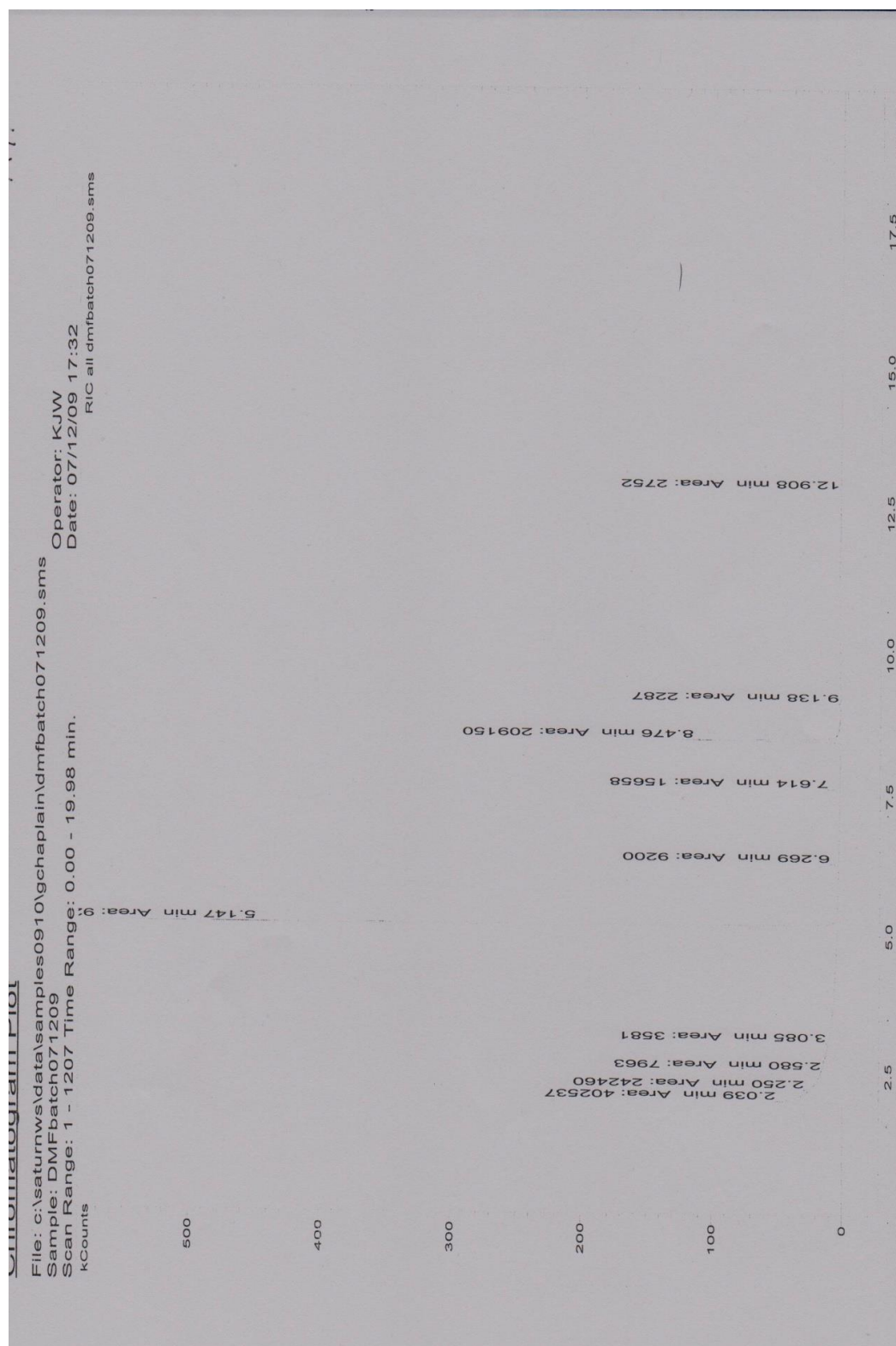
Appendix 4 GC-MS chromatograph of the flow Suzuki reaction of 0.1 M 4-bromobenzonitrile, 0.12 M phenyl boronic acid and 0.25 M potassium carbonate in 66.7% DMF in water. Reactant solution was injected into a 2144.3 μL injection loop with a carrier solvent of NMF. Reaction conditions were 7.9 minutes at microwave power of 300 W.



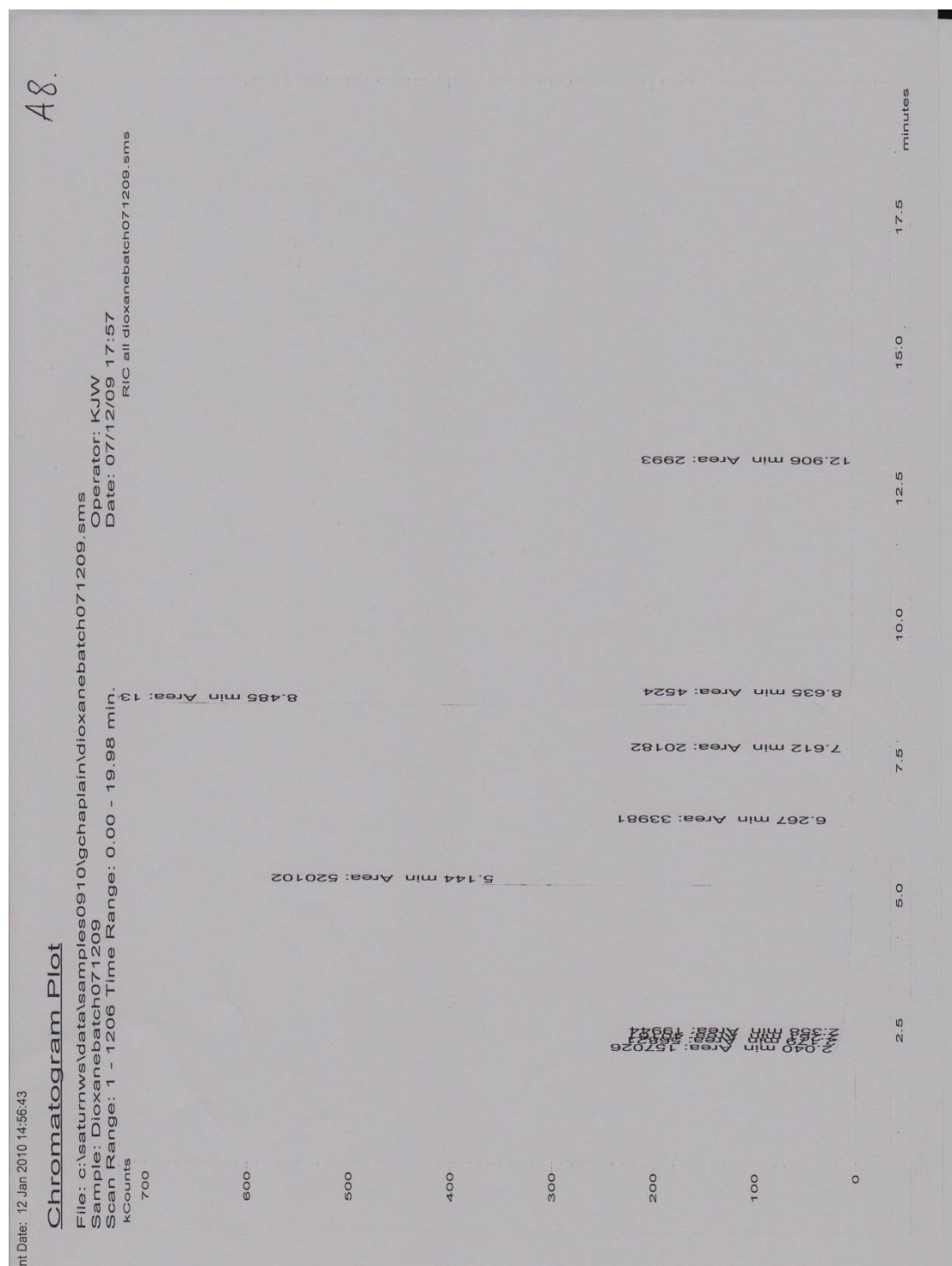
Appendix 5 GC-MS chromatograph of the batch Suzuki reaction of 0.025 M 4-bromobenzonitrile, 0.026 M phenyl boronic acid and 0.121 M potassium carbonate in 66.7% DMF in water. Reaction solution was held in a catalytic monolith after NMF was flowed through the reactor at 80 °C. Reaction time was 120 minutes at 80 °C.



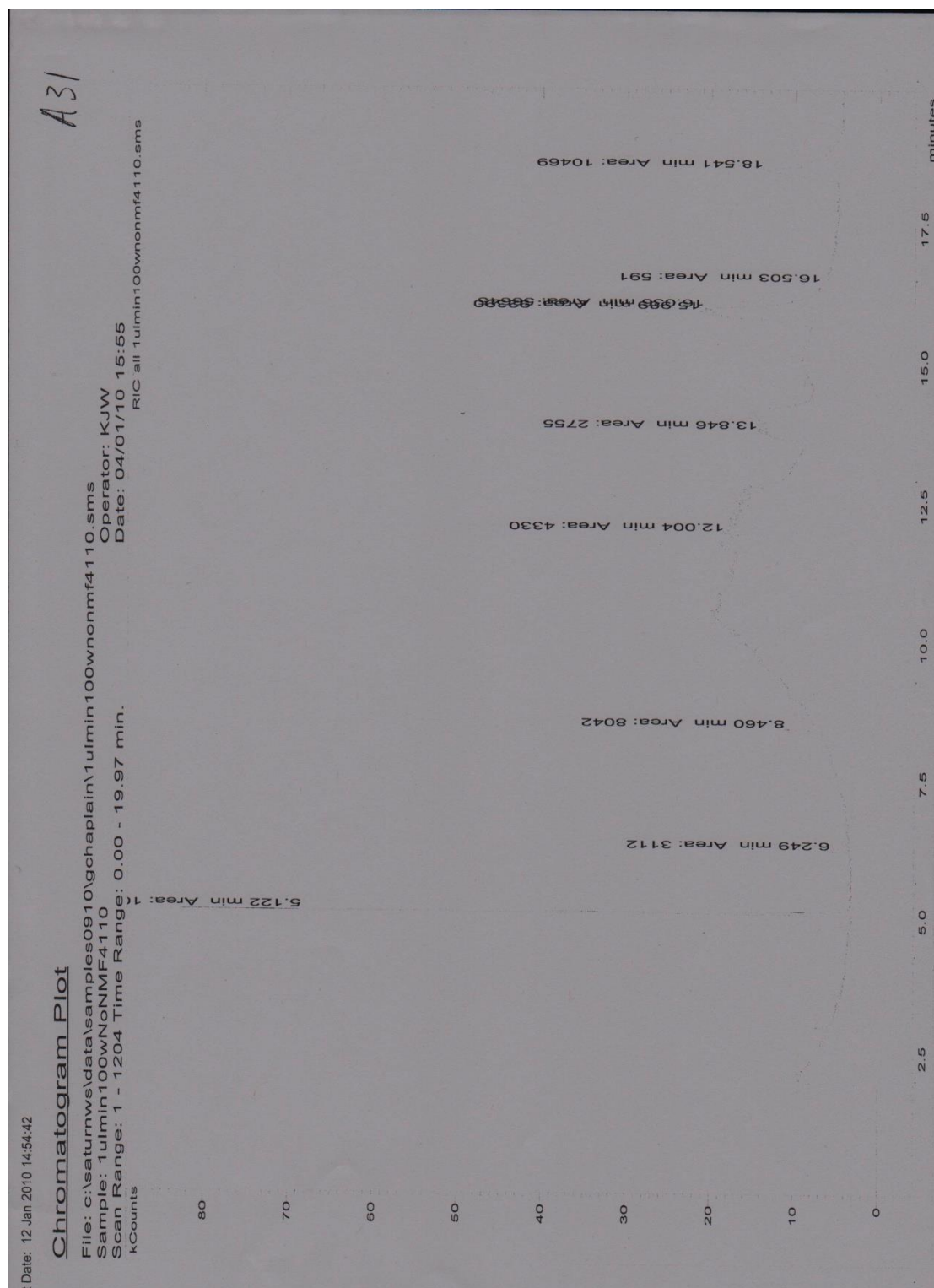
Appendix 6 GC-MS chromatograph of the batch Suzuki reaction of 0.025 M 4-bromobenzonitrile, 0.026 M phenyl boronic acid and 0.121 M potassium carbonate in 66.7% aqueous DMF. The catalyst for the reaction was palladium on a silica monolith. Reaction solution was held for 120 minutes at 80 °C.



Appendix 7 GC-MS chromatograph of the batch Suzuki reaction of 0.025 M 4-bromobenzonitrile, 0.026 M phenyl boronic acid and 0.121 M potassium carbonate in 66.7% aqueous DMF. Catalyst used was palladium on charcoal for 120 minutes at 80 °C.



Appendix 8 GC-MS chromatograph of the batch Suzuki reaction of 0.025 M 4-bromobenzonitrile, 0.026 M phenyl boronic acid and 0.121 M potassium carbonate in 66.7% aqueous dioxane. Catalyst used was palladium on charcoal for 120 minutes at 80 °C.

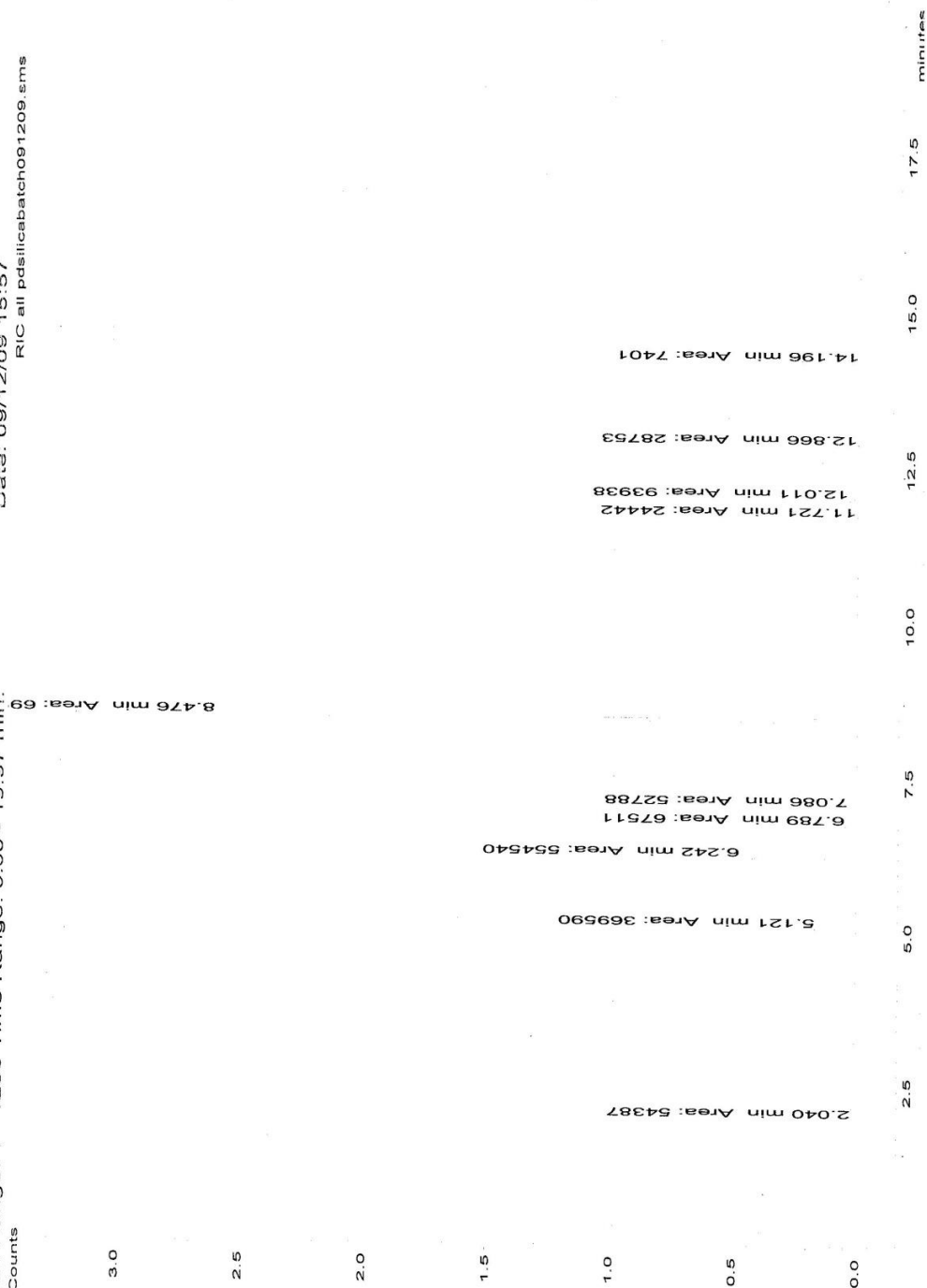


Appendix 9 GC-MS chromatograph of the flow Suzuki reaction of 0.025 M 4-bromobenzonitrile, 0.026 M phenyl boronic acid and 0.121 M potassium carbonate in 66.7% aqueous dioxane

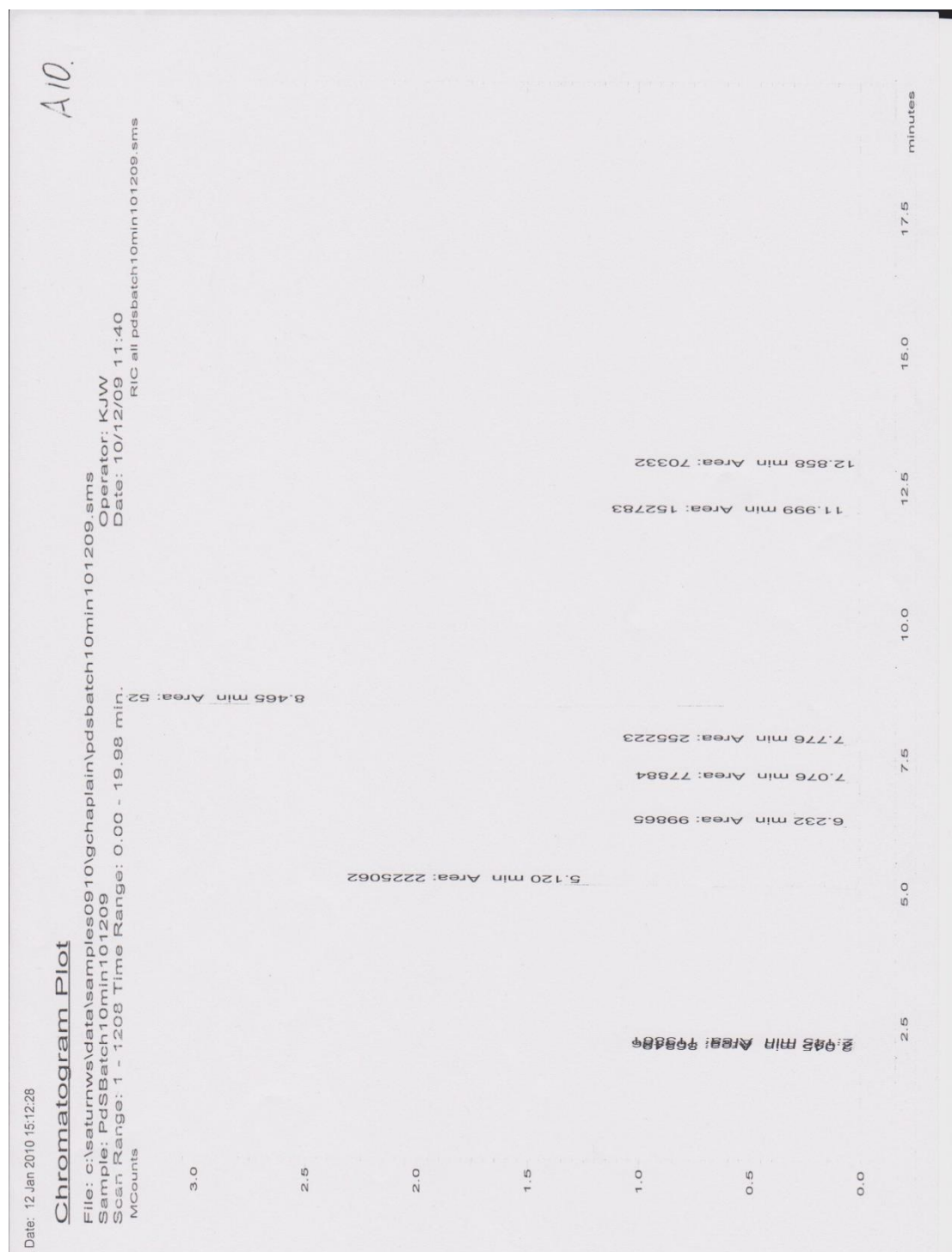
H4

Chromatogram Plot

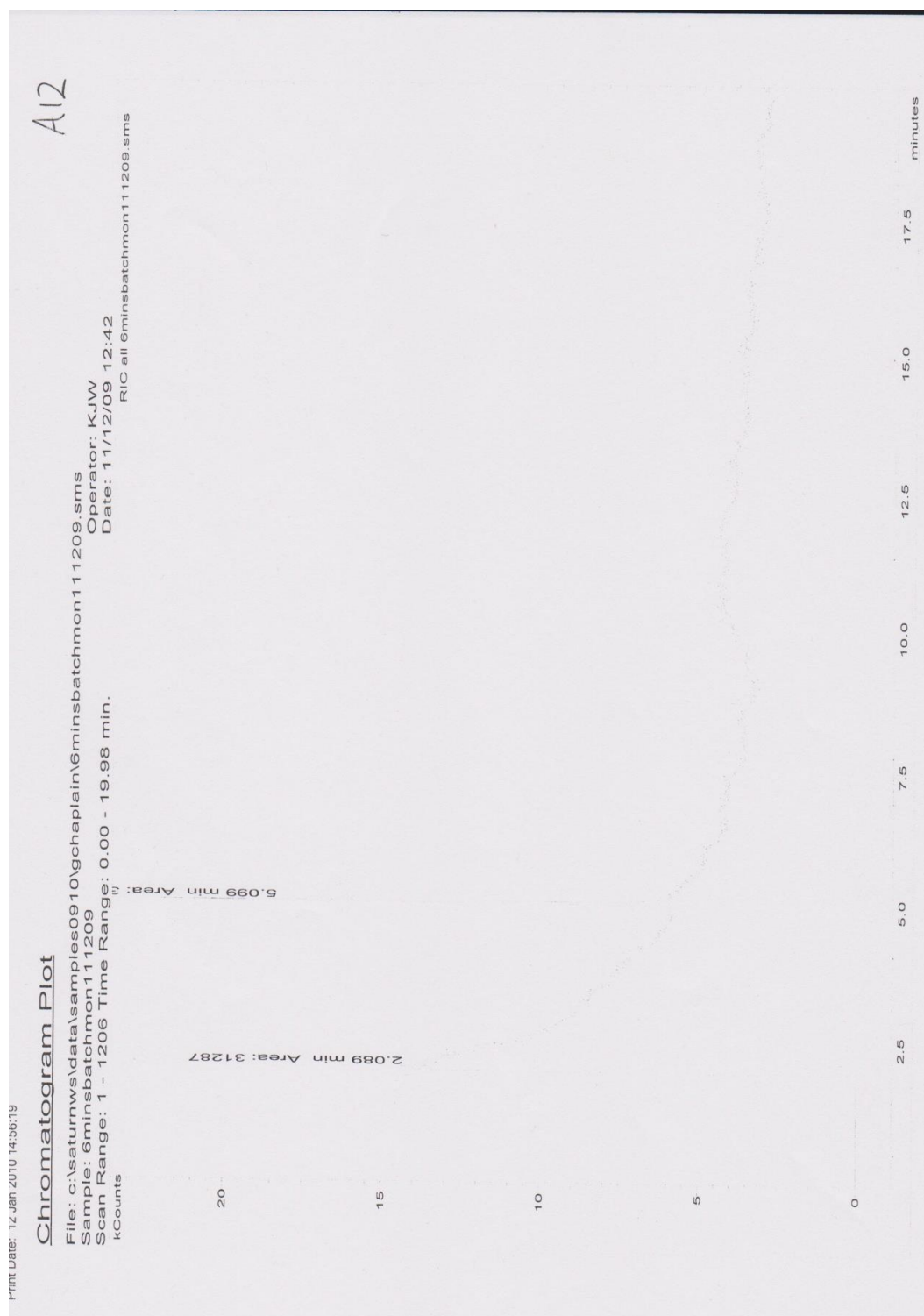
File: c:\saturmws\data\samples0910\gchaplain\pdsilicabatch091209.sms
 Sample: PdSilicaBatch091209
 Scan Range: 1 - 1208 Time Range: 0:00 - 19:97 min.
 MCounts
 Operator: KJW
 Date: 09/12/09 15:57
 RIC all pdsilicabatch091209.sms



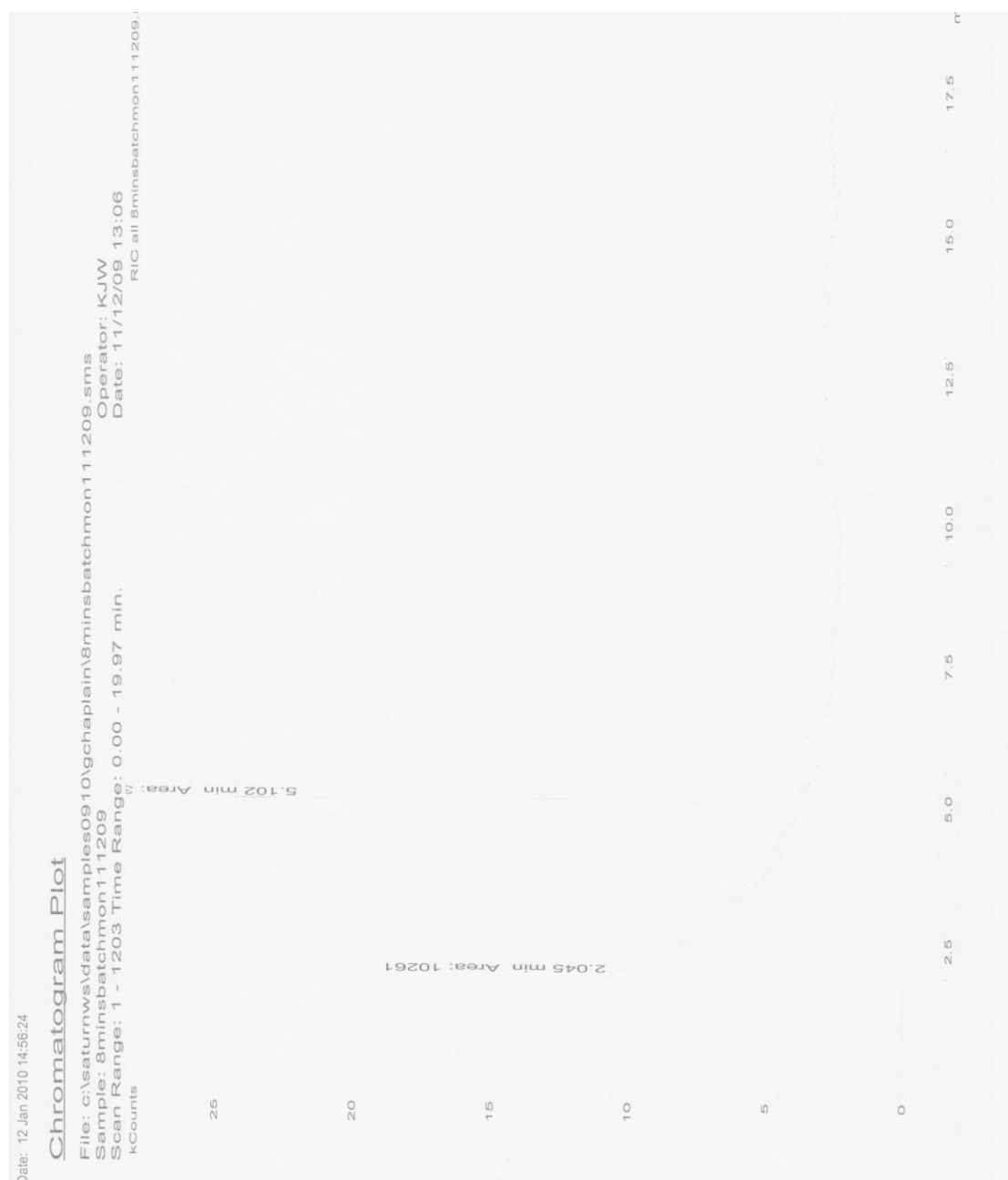
Appendix 10 GC-MS chromatograph of the batch Suzuki reaction of 0.025 M 4-bromobenzonitrile, 0.026 M phenyl boronic acid and 0.121 M potassium carbonate in 66.7% aqueous dioxane. Catalyst used was palladium on silica 60 mesh beads for 120 minutes at 80 °C. Retention times for 4-cyanobiphenyl and 4-bromobenzonitrile were at 8.47 and 5.12 minutes respectively.



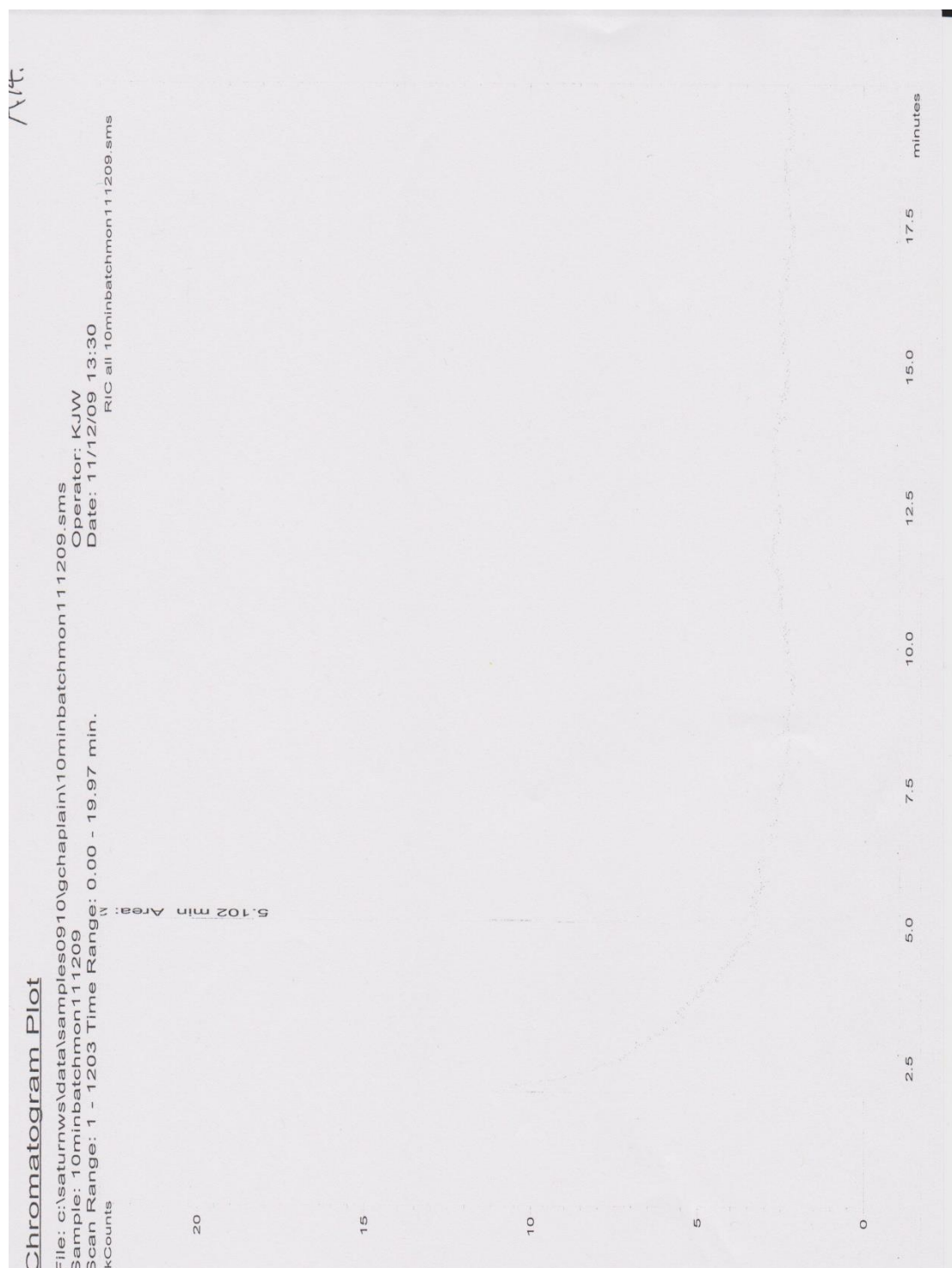
Appendix 11 GC-MS chromatograph of the batch Suzuki reaction of 0.025 M 4-bromobenzonitrile, 0.026 M phenyl boronic acid and 0.121 M potassium carbonate in 66.7% aqueous dioxane. Catalyst used was palladium on silica 60 mesh beads for 10 minutes at 80 °C



Appendix 12 GC-MS chromatograph of the batch Suzuki reaction of 0.025 M 4-bromobenzonitrile, 0.026 M phenyl boronic acid and 0.121 M potassium carbonate in 66.7% aqueous DMF. The catalyst for the reaction was palladium on a silica monolith. Reaction solution was held for 6 minutes at 80 °C.



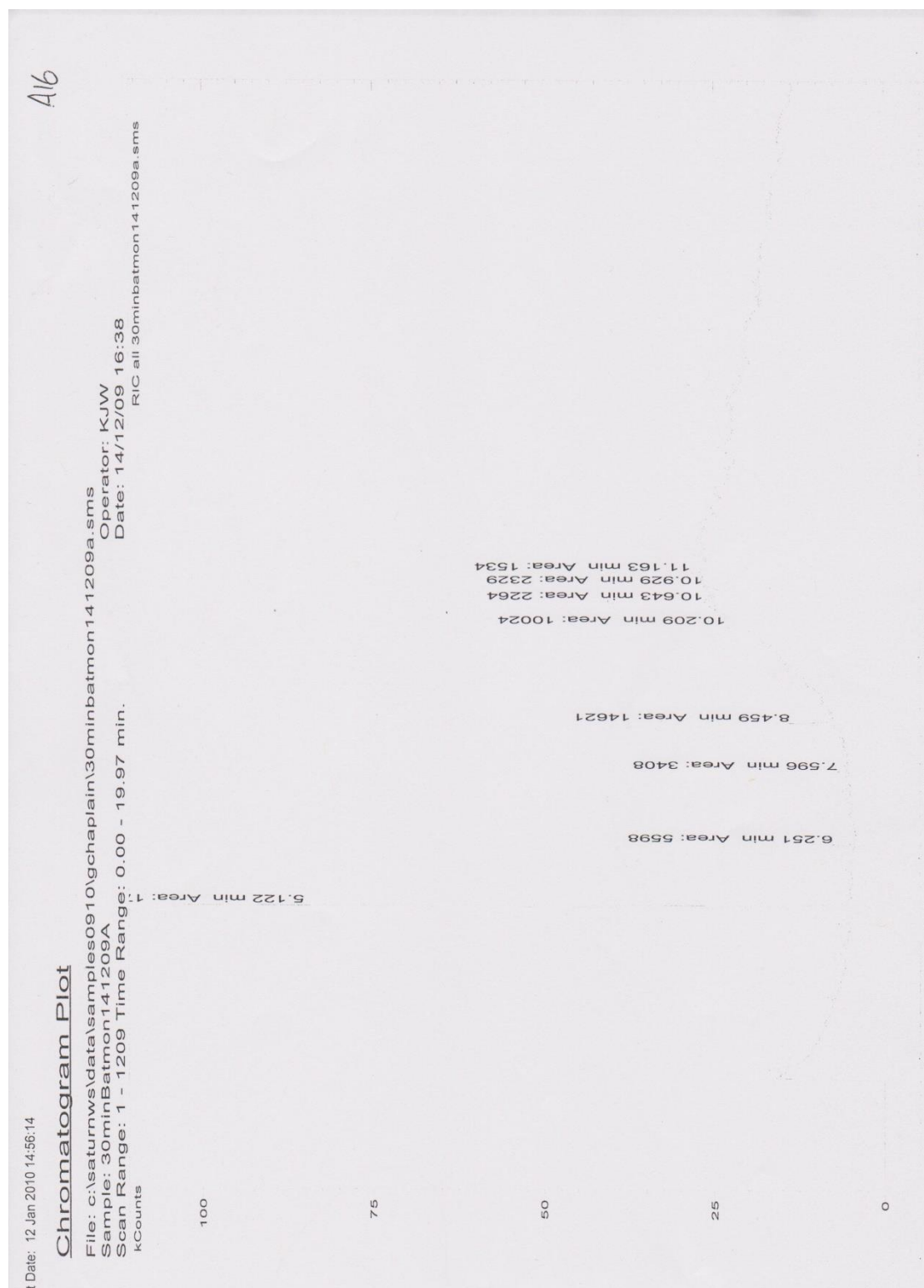
Appendix 13 GC-MS chromatograph of the batch Suzuki reaction of 0.025 M 4-bromobenzonitrile, 0.026 M phenyl boronic acid and 0.121 M potassium carbonate in 66.7% aqueous DMF. The catalyst for the reaction was palladium on a silica monolith. Reaction solution was held for 8 minutes at 80 °C.



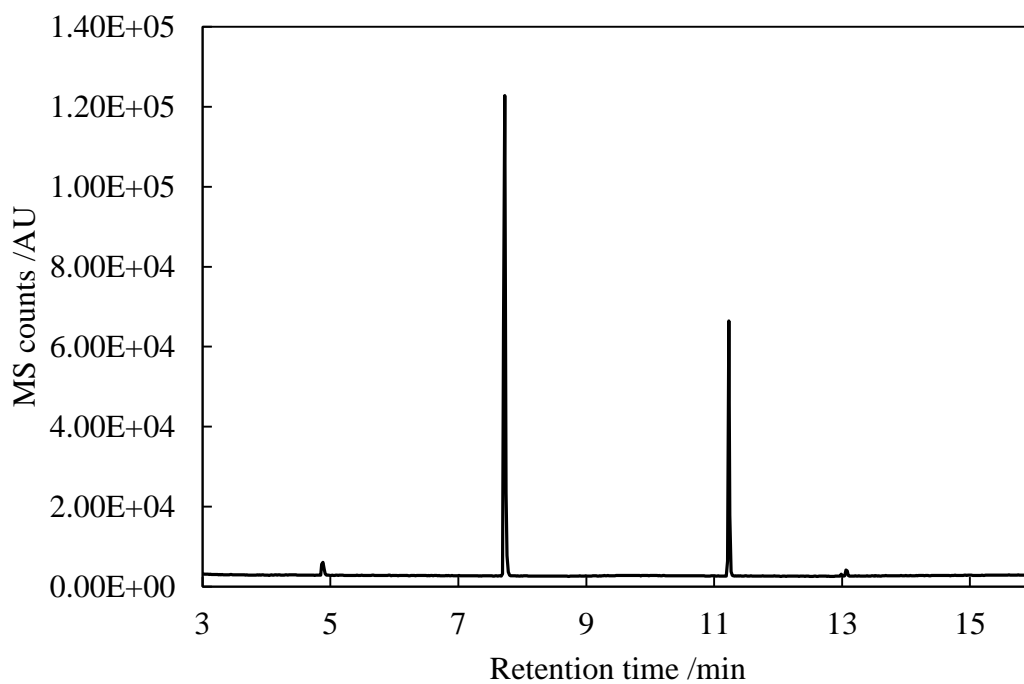
Appendix 14 GC-MS chromatograph of the batch Suzuki reaction of 0.025 M 4-bromobenzonitrile, 0.026 M phenyl boronic acid and 0.121 M potassium carbonate in 66.7% aqueous DMF. The catalyst for the reaction was palladium on a silica monolith. Reaction solution was held for 10 minutes at 80 °C.



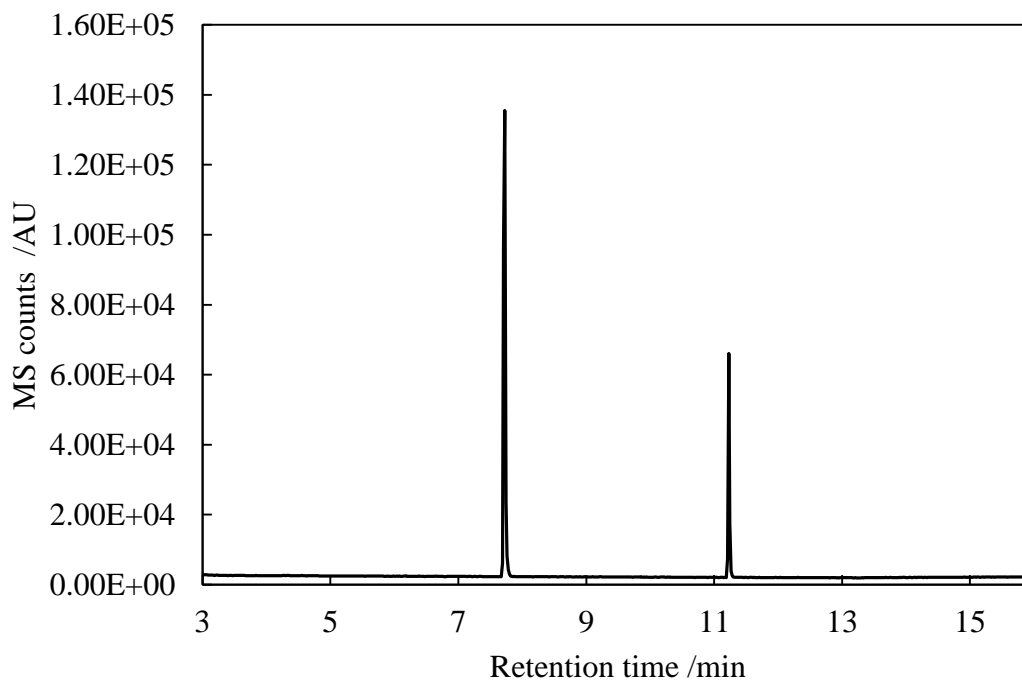
Appendix 15 GC-MS chromatograph of the batch Suzuki reaction of 0.025 M 4-bromobenzonitrile, 0.026 M phenyl boronic acid and 0.121 M potassium carbonate in 66.7% aqueous DMF. The catalyst for the reaction was palladium on a silica monolith. Reaction solution was held for 15 minutes at 80 °C.



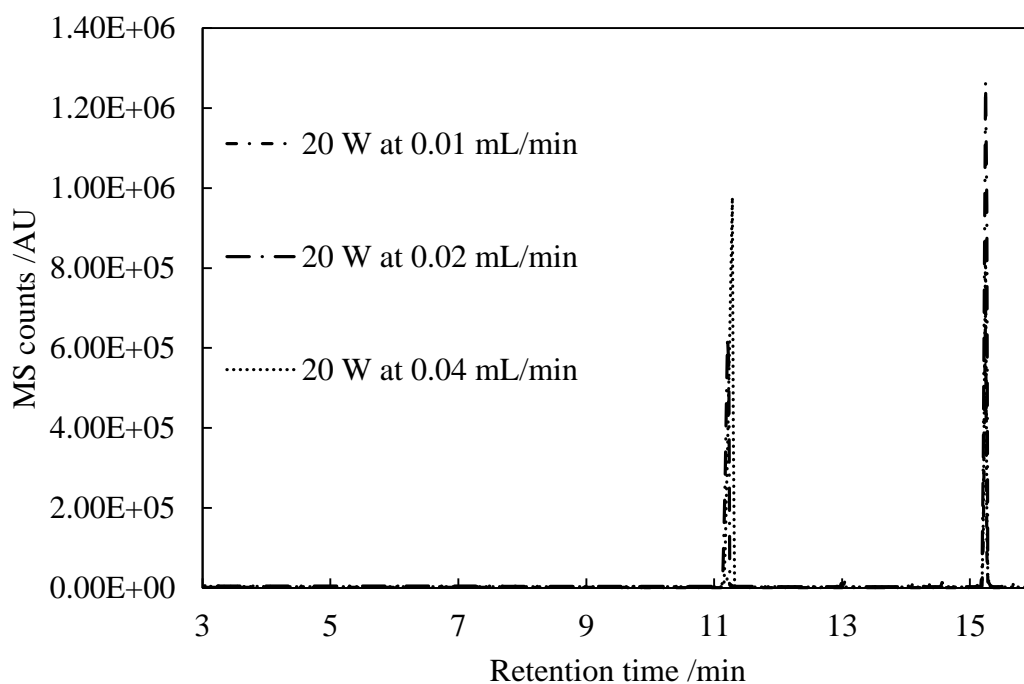
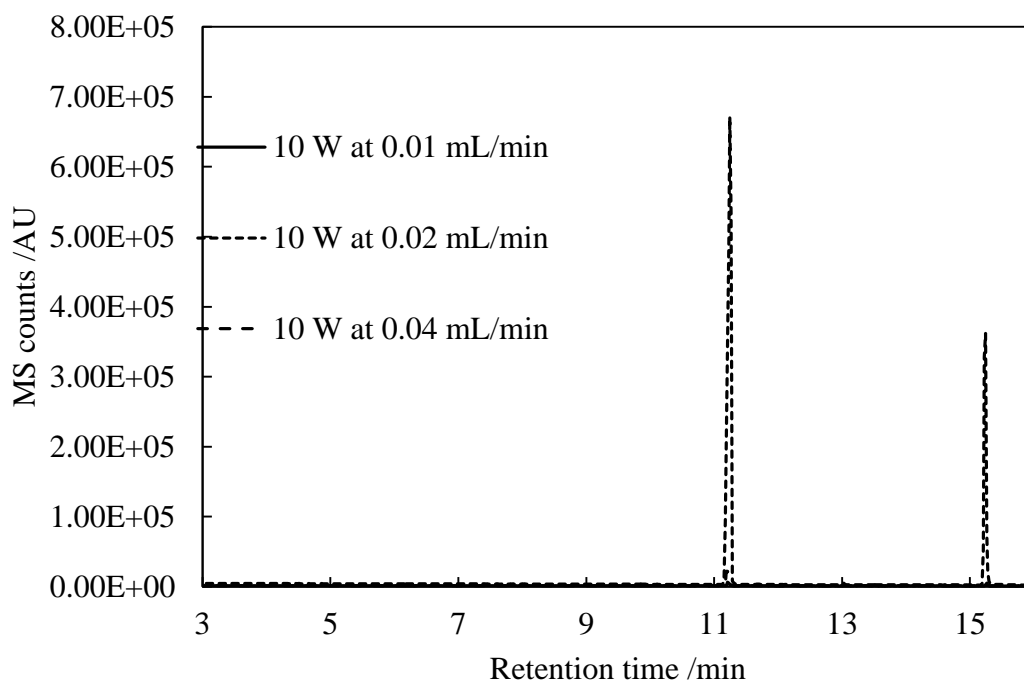
Appendix 16 GC-MS chromatograph of the batch Suzuki reaction of 0.025 M 4-bromobenzonitrile, 0.026 M phenyl boronic acid and 0.121 M potassium carbonate in 66.7% aqueous DMF. The catalyst for the reaction was palladium on a silica monolith. Reaction solution was held for 30 minutes at 80 °C.



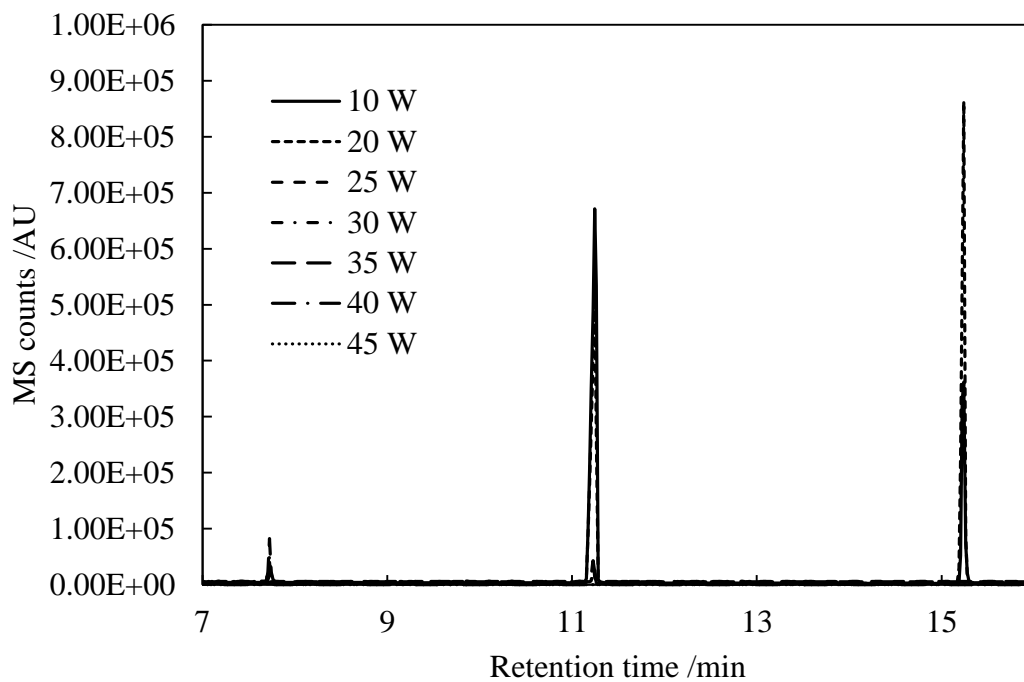
Appendix 17 GC-MS chromatograph of the flow Suzuki reaction of 0.1 M 4-bromobenzonitrile, 0.12 M phenyl boronic acid and 0.24 M potassium carbonate in 66.7% aqueous DMF. The catalyst for the reaction was palladium on a silica monolith. Reaction solution was flowed at $20 \mu\text{L min}^{-1}$ for 12 minutes at 20 W microwave power reaching $80 \text{ }^\circ\text{C}$.



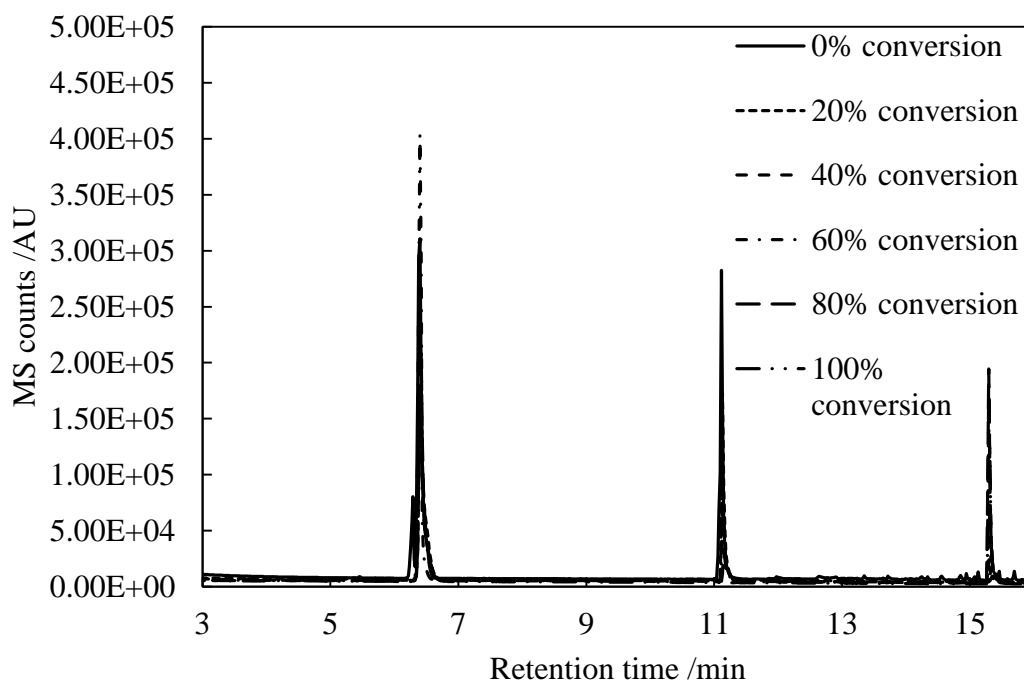
Appendix 18 GC-MS chromatograph of the flow Suzuki reaction of 0.1 M 4-bromobenzonitrile, 0.12 M phenyl boronic acid and 0.24 M potassium carbonate in 66.7% aqueous dioxane. The catalyst for the reaction was palladium on a silica monolith. Reaction solution was flowed at $20 \mu\text{L min}^{-1}$ for 12 minutes at 20 W microwave power reaching 59°C .



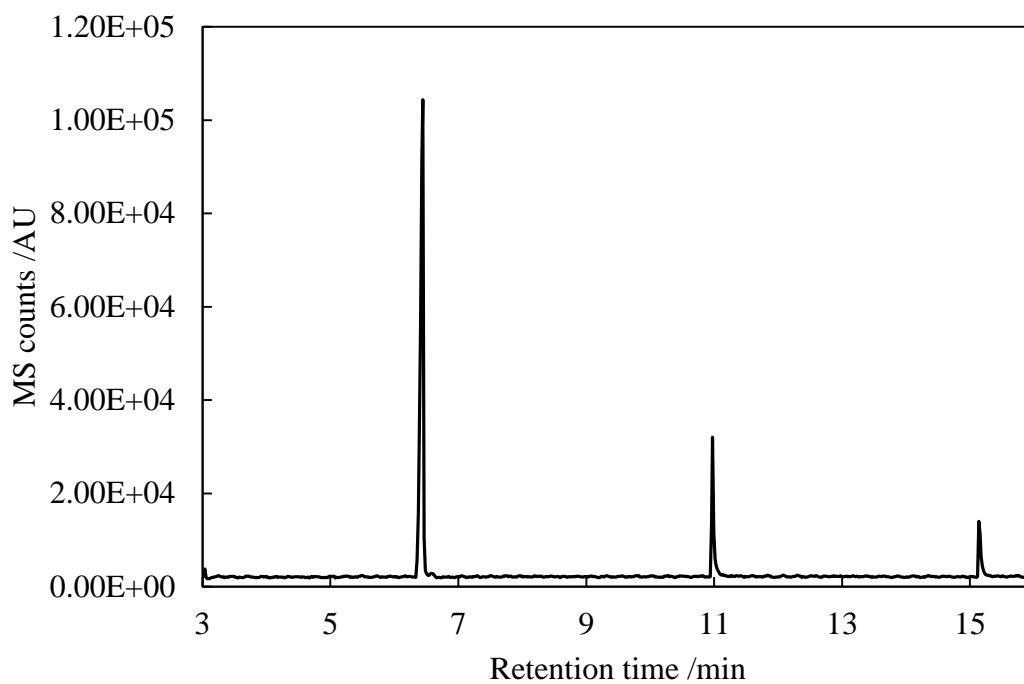
Appendix 19 GC-MS chromatograms of the flow Suzuki reaction of 0.1 M 4-bromobenzonitrile, 0.12 M phenyl boronic acid and 0.24 M potassium carbonate in 66.7% aqueous dioxane. The catalyst for the reaction was palladium on a silica monolith. Reaction solution was flowed at 10, 20 and 40 $\mu\text{L min}^{-1}$ for 15 minutes at 10 and 20 W of microwave power.



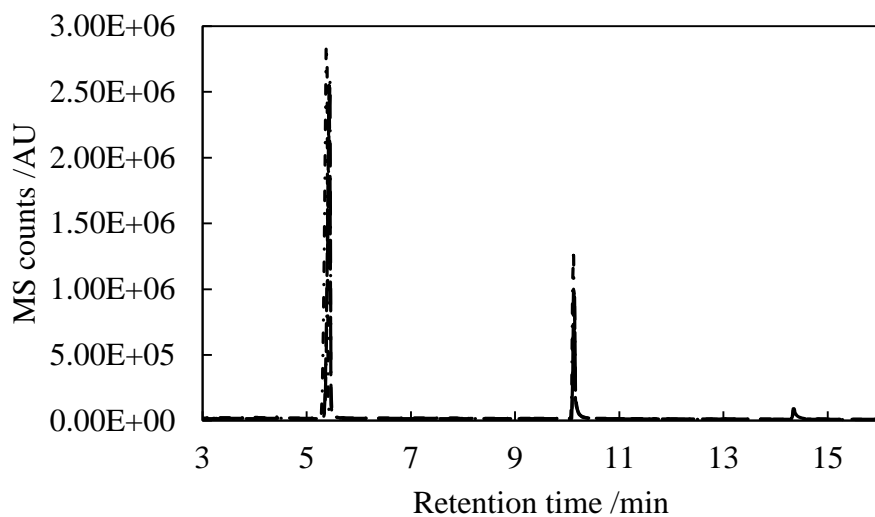
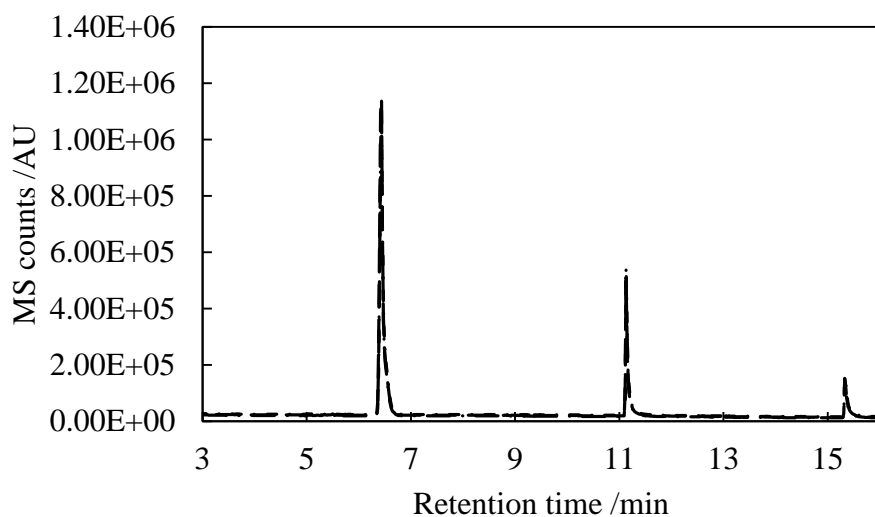
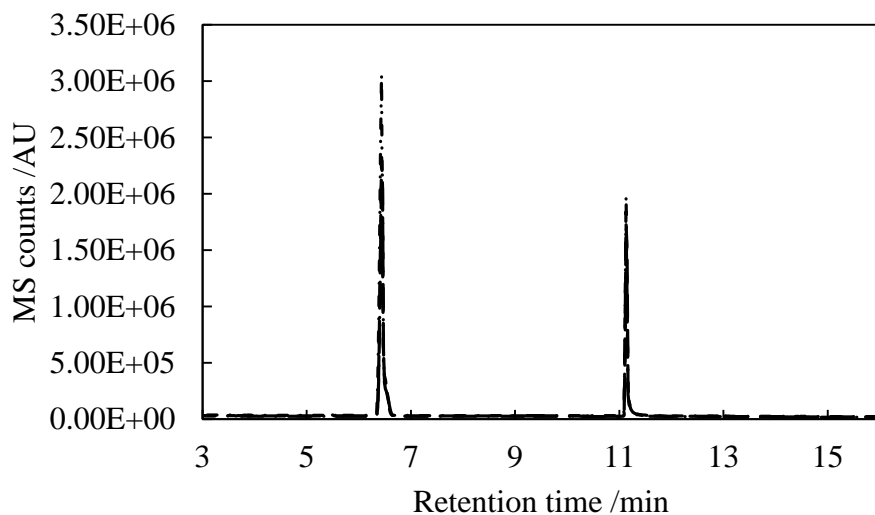
Appendix 20 GC-MS chromatograms of the flow Suzuki reaction of 0.1 M 4-bromobenzonitrile, 0.12 M phenyl boronic acid and 0.24 M potassium carbonate in 66.7% aqueous dioxane. The catalyst for the reaction was palladium on a silica monolith. Reaction solution was flowed at $20 \mu\text{L min}^{-1}$ for 12 minutes at 10, 20, 25, 30, 35, 40 and 45 W of microwave power respectively

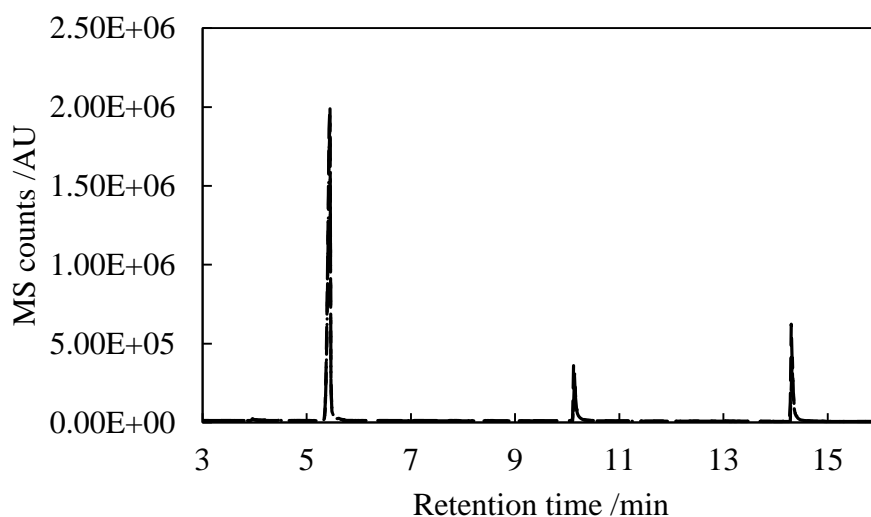
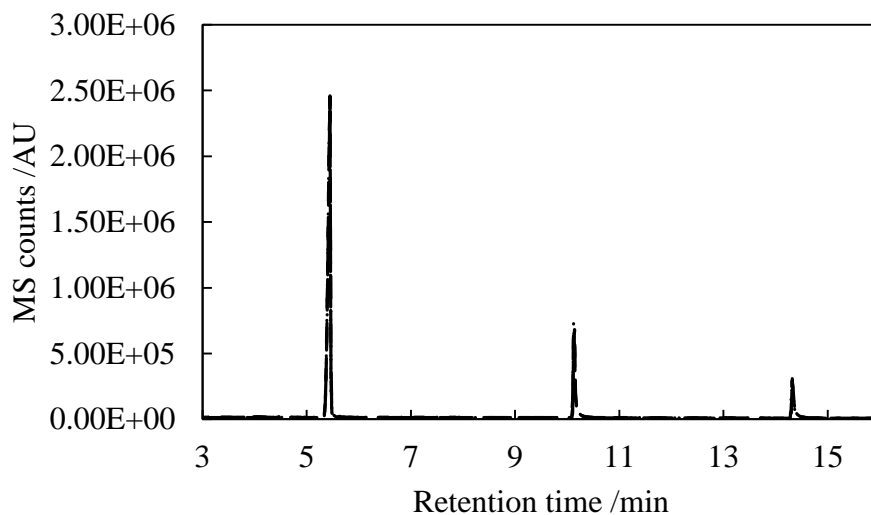


Appendix 21 GC-MS chromatograms of the standard calibration solutions for the Suzuki reaction. The solutions were produced with 0.0994, 0.0764, 0.0579, 0.0397, 0.0193, 0.000 M 4-bromobenzonitrile, 0.1156, 0.0957, 0.0802, 0.0677, 0.0413, 0.0205 M phenylboronic acid, 0.2485, 0.2544, 0.2440, 0.2394, 0.2400, 0.2438 M potassium carbonate, and 0.0000, 0.0220, 0.0391, 0.0598, 0.0797, 0.0989 M 4-cyanobiphenyl in 66.7% DMF respectively. The GC-MS method for analysis was described in *GC-MS analysis B*.

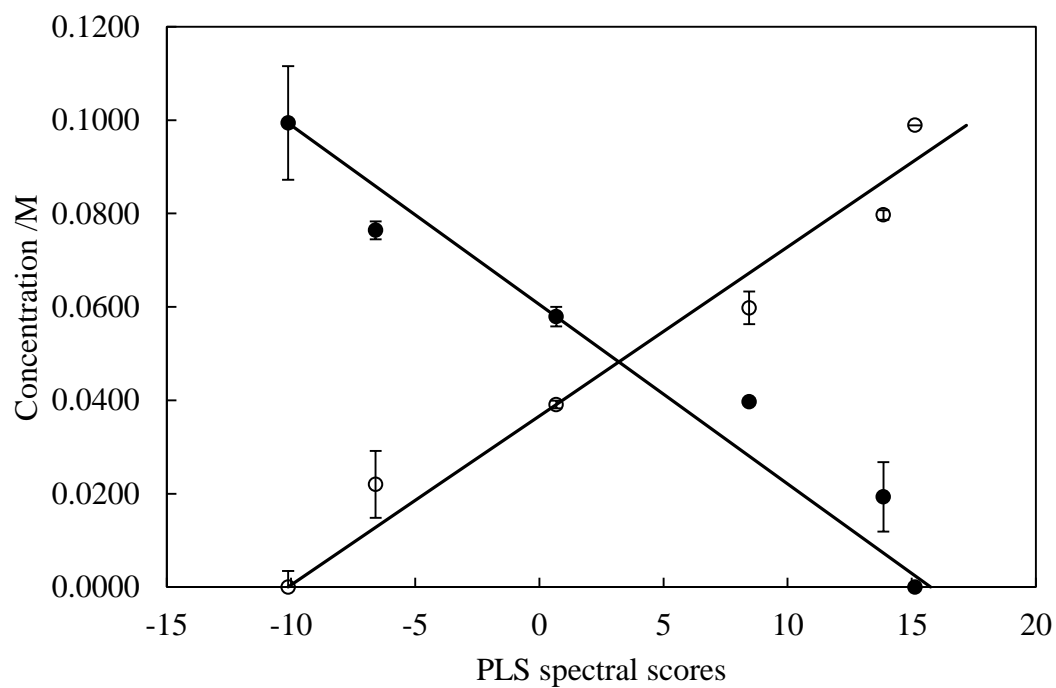


Appendix 22 GC-MS chromatograph of the flow Suzuki reaction of 0.1 M 4-bromobenzonitrile, 0.12 M phenyl boronic acid and 0.24 M potassium carbonate in 66.7% aqueous DMF. The catalyst for the reaction was palladium on a silica monolith with a void volume of 560 μL . Reaction conditions were set to a 7 minute catalyst residence time at 80 $\mu\text{L min}^{-1}$ at 2 W of microwave power.





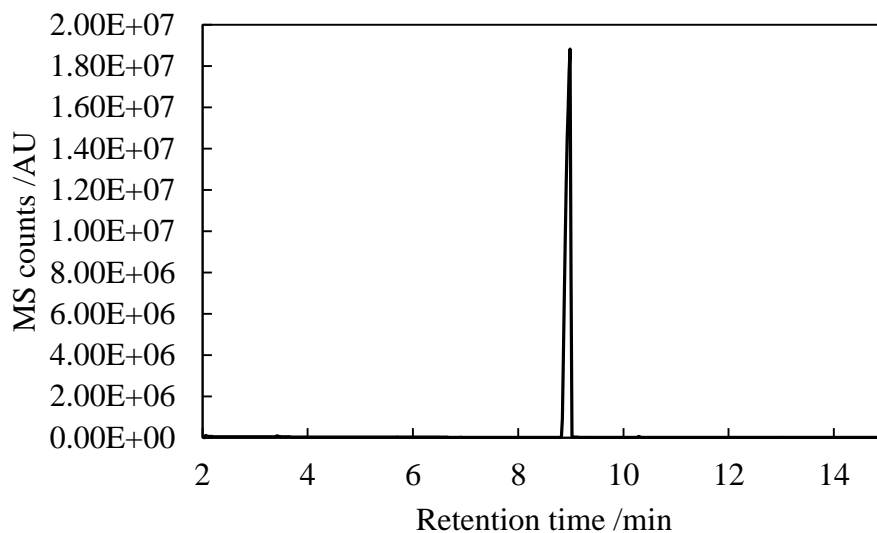
Appendix 23 GC-MS chromatograms of the flow Suzuki reaction of 0.1 M 4-bromobenzonitrile, 0.12 M phenyl boronic acid and 0.24 M potassium carbonate in 66.7% aqueous DMF. The catalyst for the reaction was palladium on a silica monolith with void volumes of 560 or 2700 μL . The heating method for the reaction was a water bath set at 78, 93, 90, 90 and 90 $^{\circ}\text{C}$ respectively. The flow rates of the reactions were 80, 40, 100, 50 and 50 $\mu\text{L min}^{-1}$ equating to a catalyst residence time of 7, 14, 27, 54 and 54 minutes respectively. Each chromatograph demonstrates 3 spectra from the same sample. The chromatograms are ordered for the reactions described in Table 7 as A, B, C, D and E respectively.



Appendix 24 GC-MS calibration of 4-bromobenzonitrile (•) and 4-cyanobiphenyl (○). The chromatographic region of interest was between 5 to 20 minutes. The data was subject to mean centring normalisation, auto scaling and a 5 point moving average smoothing before PLSR analysis.

Residence time /s	Concentration /M				
	Measured		Calculated		
	[CBP]	[BBN]	[CBP]	[BBN]	[PBA] remaining
41	0.0592	0.0375	0.0572	0.0392	0.0593
26	0.0434	0.0541	0.0465	0.0499	0.0759
19	0.0404	0.0572	0.0392	0.0572	0.0790
14	0.0330	0.0649	0.0317	0.0647	0.0867
12	0.0254	0.0728	0.0281	0.0683	0.0946
10	0.0260	0.0722	0.0253	0.0711	0.0940
8	0.0240	0.0743	0.0210	0.0754	0.0961
6	0.0228	0.0756	0.0180	0.0784	0.0974
4	0.0193	0.0792	0.0132	0.0832	0.1010
3	0.0114	0.0875	0.0089	0.0875	0.1093
0	0.0015	0.0978	0.0000	0.0964	0.1196

Appendix 25 Original reaction data obtained from Raman spectral results from Flow reaction monitoring 4.37. Suzuki cross-coupling reaction results between 4-bromobenzonitrile (0.10 M) and phenyl boronic acid (0.12 M) in the presence of potassium carbonate (0.24 M). The CMR used was produced from *monolith 2.5* with *palladium loading 2.14* with a void volume of 1.0961 mL. The reaction temperature was controlled with a column heater set at 80 °C. 4-Cyanobiphenyl (CBP) and 4-bromobenzonitrile (BBN) concentrations and reaction conversions were determined *Raman calibration 4.20*. Phenyl boronic acid (PBA) concentrations were calculated in accordance to 4-bromobenzonitrile concentrations.



Appendix 26 GC-MS chromatograph of the acetylation reaction between 0.3 M 4-bromophenol and excess acetic anhydride using tungstosilicic acid catalyst. The reaction was batch and the peak observed at was 4-bromophenyl acetate.